Cold Collisions of Ultracold Atoms

Ryan James Thomas

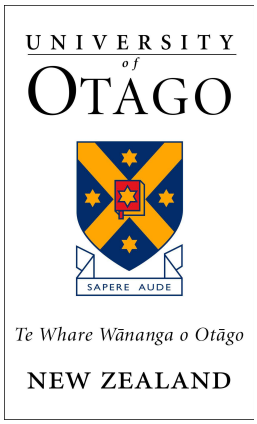

A thesis submitted for the degree of Doctor of Philosophy

at the University of Otago, Dunedin, New Zealand.

November 2017

Primary academic supervisor:	*Niels Kjærgaard*
Secondary supervisor:	*Jevon Longdell*

Original version submitted for examination:	*June 2017*
Revised version post-examination:	*November 2017*

Abstract

This thesis describes experiments investigating the collisions of alkali metal atoms at energies between $10 - 2000$ μK, measured in units of the Boltzmann constant. The atoms are accelerated towards each other using a purpose-built collider comprised of a crossed-beam optical dipole trap, which enables us to collide dense ensembles of ultracold atoms in any internal state at relatively high energies. I present the results of two experiments centered around resonant enhancement of the collisions. The first is between homonuclear ^{40}K atoms near a shape resonance where the fermionic nature of the atoms determines the character of multiple scattering effects. The second experiment involves heteronuclear ^{40}K^{87}Rb collisions near a magnetically-tunable Feshbach resonance where we measure parameters describing the resonance as a function of collision energy. Theoretical models are developed that let us describe the collisions using published empirical interaction potentials, and we find good agreement between these models and the experiment.

Acknowledgements

In the long-ago and halcyon days of my youth, I had a high school physics teacher named Norm Funnell. He was everything that a teacher should be: courteous, encouraging, approachable, intelligent, energetic, and enthusiastic about physics. He insisted, and demonstrated, that physics was fun – or "phun" as he would have spelled it – and I believed him. I still believe it. It is safe to say that his tutelage and enthusiasm for the subject were what made me pursue an undergraduate degree in physics, although somewhat ironically he thought I would not have the patience for a PhD. More than a decade later, I have proved him wrong.

I have had the benefit over that decade of being taught by some truly excellent professors, especially in my undergraduate days at Simon Fraser University. When I made the transition from the classroom to research, I likewise was fortunate to have outstanding supervisors who added immeasurably to my education. Paul Haljan taught me the practicalities of an optics lab and how to program in LabVIEW: a skill which has turned out to be more useful than expected. Jeff McGuirk introduced me to cold atoms, gave me the responsibility of running the day-to-day operations in his lab, and started me on an honours project of simulating evaporative cooling using the direct simulation Monte Carlo method, a numerical technique which constitutes an important part of this thesis. Alex Lvovsky provided me with a thorough grounding in light-atom interactions and taught me self-reliance in the lab.

Finally, there is Niels Kjærgaard, my PhD supervisor. I first contacted Niels when I brushed off an old dream of going to New Zealand for postgraduate research, and he was one of the few people doing interesting (to me, at least) experimental research in the country. When I asked Niels about his future research plans, he gave a list of possibilities and then immediately impressed me with his own research philosophy:

> *I don't know where all this is going to end. In my experience, it is of course important to have plans and goals, but much of the fun (and perhaps the best science) is what happens on the path there. All the unexpected phenomena which you did not see coming.*

It was exactly what I wanted to do for my degree: fundamental science with an appreci-

ation that the weird stuff you see along the way is the most interesting. Since my arrival, Niels has been unbelievably supportive, from encouraging pet projects, to sending me to all manner of international conferences, to spending countless hours polishing journal articles for publication.[1] Most importantly, Niels essentially turned me loose in his lab to make what I would of my time with little direct supervision, and I sincerely appreciate that independence.

Past and present members of the lab have also been very helpful. Amita Deb helped to get me started, has served as an incredibly useful repository of knowledge about the experiment, and provided innumerable valuable physics discussions. Kris Roberts likewise provided invaluable help with the ^{40}K system, both when we first started trying to see collisions, and when we took serious data for publications. Bianca Sawyer introduced me to dispersive probing and provided a lot of debugging help on the experiment. Milena Horvath forced me to be much more precise in my physics arguments, making me walk back or qualify a lot of statements I have made. Craig Chisholm helped install the photonic crystal fibre. Matthew Chilcott provided a lot of electronics help for various servo boards and also convinced me that FPGA programming really isn't that hard.

A big thank you also goes out to Dr. Eite Tiesinga, who generously hosted me during my visit to the University of Maryland. Eite provided significant theoretical support for the ^{40}K multiple scattering work, and he also helped me with the coupled-channels code that I wrote, especially with debugging it. Being able to compare numerical results with those from an expert in the field makes validation of code almost too easy.

I would also like to thank all of the people who got me out of the lab, especially those who got me out onto the crags or into the mountains. The Tuesday night rock climbing crew, especially Lindsay and Riley, introduced me to a great bunch of people. Matteo, Lara, and Juliet got me out for some epic skiing in the backcountry.[2] Juliet and Lara also accompanied me on a number of summer tramping and climbing trips, and Lara finally convinced me that there is a difference between tramping and hiking.[3]

On a personal note, I also thank my parents for being incredibly supportive of my decision to come to New Zealand and of my rather esoteric career path in general. Finally, I thank Alex, who decided that I was worth sticking with through a three year long-distance relationship. I could not have done it without you.

[1] No mean feat from Dunedin, where every international conference not in Australia costs at least $2000 just to get there.

[2] By epic, I mean both the traditional kind and the kind where you ski 200 m below snowline.

[3] The difference is that tramping is hiking with extra suffering.

Contents

Chapter 1

Introduction

In 1909, the importance of the scattering experiment in physics was demonstrated by Geiger and Marsden in the now-famous "gold-foil" experiment, where α-particles that impinged on a thin sheet of gold foil were deflected in unexpected ways[1]. Rutherford used these measurements in 1911 to infer that the atom was organized into a sparse cloud of negatively charged electrons and an incredibly dense, positively charged nucleus[2]. In other words, he used the results of a scattering experiment to deduce properties of the interaction between the gold nuclei and the α-particles. Such was the import of this and other work that no less than three different countries – New Zealand, Canada, and the UK – claim him as their own. A scant three years later, Franck and Hertz demonstrated the quantization of atomic energy levels in the scattering of electrons from mercury vapour. The scattering experiment was here to stay. In the century that has passed, the scattering experiment has only become more central to our understanding of the fundamental physics of nature, and it has moved away from the compact experiments of the early twentieth century to epitomize the idea of Big Science where billions of dollars are spent on projects that require the joint effort of thousands of scientists.

This thesis is not the story of high-energy collision physics. Instead, it takes a different path, starting in 1925 with the prediction by Bose and Einstein of a new phase of matter: what we now call a Bose-Einstein condensate (BEC). A BEC forms when the temperature of a sample of "bosons" – particles with integer spin – is lowered enough that all the bosons clump together in the ground state of the system. As each boson occupies the same quantum state, a BEC is a macroscopic quantum object. Fast-forwarding to the 1970s, after Hecht[3] predicted that a BEC of spin-polarized hydrogen would exhibit superfluidity, Stwalley and Nosanow[4] predicted the transition temperature and advocated for creating a BEC, saying, "It is our opinion that the study of the Bose-Einstein condensation is the most important experiment that can be done with [spin-polarized hydrogen]." As it turned out, spin-polarized hydrogen was a poor choice for studies of condensation due to unfavourable collisional

properties: the elastic cross section, a number encapsulating the effect of the inter-atomic potential, is anomalously low. Efficient cooling of spin-polarized hydrogen, and all other atoms, relies on a large ratio of elastic collisions, which are those that conserve the kinetic energy, to inelastic collisions, which do not, and it took until 1998 before condensation was achieved in hydrogen[5]. A similar problem plagued the creation of a BEC in cesium, except in this case the cross section was anomalously high and it suffered from a high rate of molecule formation through three-body collisions[6]. Cesium was not condensed until 2003[7]. The two species that eventually won the race to BEC in 1995 were ^{87}Rb[8] and ^{23}Na[9] due primarily to their favourable collision properties at cold temperatures. ^{7}Li was also condensed in the same year, but it suffered from attractive interactions at low energies which limited the density of atoms that could be achieved[10].

Not long after the first observation of BEC in ultracold atomic gases of alkali atoms, researchers turned to the possibility of creating a degenerate gas of fermions. Whereas a BEC consists of all atoms in the ground state, a degenerate Fermi gas consists of placing one atom in the lowest available energy state until there are no more atoms left to place. Cooling a gas of fermions is more difficult than cooling a gas of bosons, because fermions in the same internal state stop colliding with each other at low temperatures due to the Pauli exclusion principle[11]. Instead, either two different internal states[12] or a separate coolant[13, 14, 15, 16] must be used. One of the major motivations for producing a Fermi gas was to investigate the Bardeen-Cooper-Schrieffer model of superconductivity[17]. Attractive interactions between two different spin states of the fermions are needed, and for this reason ^{6}Li was the first species to be tried[18, 19, 20]. However, at low magnetic fields the elastic cross-section for ^{6}Li inter-state collisions is relatively low which necessitates a long evaporation sequence. Combined with unfavourable optical cooling properties, a number of technical advances were required to reach quantum degeneracy in ^{6}Li[21, 22], which was first accomplished in 2001[16]. In the end, the first species to form a degenerate Fermi gas was ^{40}K in 1999[12].

The collision properties of atoms at very low energies – less than 100 μK measured in units of the Boltzmann constant – were therefore of prime importance in determining not just whether a particular species could be condensed, but also what behaviour it would exhibit once condensed. Even before the first observation of BEC, the possibility was raised of *controlling* the scattering properties of ultracold atoms through a phenomenon known as a Feshbach resonance[23]. Feshbach resonances, or sometimes Fano-Feshbach resonances, were described theoretically by Hermann Feshbach and Ugo Fano in the context of nuclear[24, 25] and atomic physics[26] as a modification of scattering properties due to the presence of an quasi-bound state having an energy equal to the energy of a collision. The interference of the two scattering paths – a background contribution and a resonant contribution from the decay of the quasi-bound state – produces marked changes in the scattering

properties of a system. In the original studies, the locations of the resonances were considered to be fixed by nature; in the context of the new field of ultracold atomic physics, the resonance positions could be tuned at will. Three years after the first observation of BEC, the first demonstration of the effect of a tunable Feshbach resonance occurred in ^{23}Na[27]. Since then, Feshbach resonances have been indispensable tools in ultracold atomic systems.

But how does one study the collisions of ultracold atoms? Depending on the state of the atoms and the type of collision to be probed, a number of techniques have been used. Measurements of thermalization times, where the sample is perturbed and the time taken to reach equilibrium is measured, have proven very useful in inferring the cross section for non-degenerate atoms[28, 29, 30, 31, 32]. Cross-dimensional thermalization measurements were used for degenerate Fermi gases to demonstrate the Wigner threshold law[33, 34]. Loss spectroscopy is particularly popular for locating Feshbach resonances, and the first observation of a Feshbach resonance in an atomic gas demonstrated this technique[27]. Other measurements work best with degenerate samples, such as measuring the interaction energy[35, 36]. Photoassociation spectroscopy, where a two-photon process is used to transfer colliding atoms to a deeply bound molecular state, has been instrumental in mapping out inter-atomic potentials[37].

However, all of the above methods for studying cold collisions are indirect and lack angular resolution. Only a few experiments have been devised that use a collider geometry with a well-defined collision axis. One of the earliest examples in ultracold atoms was by Gibble *et al.*[38] using a cesium fountain to launch atoms upwards, a technique that was later refined to measure the p-wave threshold[39] and map out Feshbach resonances[40]. Two research groups implemented magnetic colliders for spin-polarized ^{87}Rb which allowed them to observe a d-wave shape resonance[41, 42] and to directly measure the phase shifts; this work was later extended to ^{87}Rb atoms in different states allowing the observation of s, p, and d-wave scattering[43]. A more limited technique that works well with degenerate samples of atoms is to use Kapitza-Dirac diffraction to transfer momentum from optical standing waves to atoms; its limitation is that the energy cannot be easily tuned. However, it has been used to great effect to measure a Feshbach resonance in ^{40}K[44], to generate scattering halos up to g-wave[45], to measure atom-atom correlations[46, 47], and to explore highly-anisotropic collisions in strongly dipolar atoms[48].

The major constraints of these studies are that they have a limited range of energies, a limited collisional opacity, and a limited number of states that can be collided. The energies have been typically limited to less than 150 μK, with the magnetic collider experiments reaching 500 μK[41] and 1200 μK[42]. These, however, could only collide magnetically trappable states. Here at the University of Otago, we have developed an ultracold atom collider that addresses all of these limitations[49, 50, 51]. It uses optical dipole traps, so it can trap any ground state atom, and the maximum collision energy of 2000 μK is limited

only by the amount of power in the trapping beams. Additionally, the experimental system has been designed to produce a large number of two species of ultracold atoms which can be collided, ^{87}Rb and ^{40}K[49], with possible extensions to ^{85}Rb, ^{39}K, and ^{41}K. This versatility allows us to investigate a hitherto unexplored region of heteronuclear collisions between the ultracold (< 1 μK) regime, probed using degenerate gases, and the cold (> 10 mK) regime, probed using atomic beams[52].

In this thesis, I present some of the first results from our optical collider, and they run the gamut of cold atom scattering topics: homonuclear and heteronuclear collisions, single and multichannel scattering theory, shape and Feshbach resonances, and primary and multiple scattering. In addition to the experimental work, I have developed a complete suite of software that can predict not only the scattering properties of a particular pair of atoms, but also use those properties to predict the effects of colliding dense ensembles of those atoms. Comparisons between the experimental data and the theoretical predictions show good agreement.

This thesis is laid out as follows. In Chapter 2 I provide a relatively detailed theoretical foundation of this work, including a description of the numerical methods for modeling the experiment. In Chapter 3, I provide a description of the experimental apparatus. Chapters 4 and 5 discuss the particular experiments of homonuclear ^{40}K collisions near a shape resonance and heteronuclear ^{40}K^{87}Rb collisions near a Feshbach resonance, respectively. Pertinent theoretical, experimental, and analysis details are given in their respective chapters. Finally, in Chapter 6 I discuss the future of the optical collider.

A couple of conventions are worth noting at the start. First, I exclusively measure collision energies in units of the Boltzmann constant, so an energy will be quoted in μK or mK. This is a convention that is used in most (but not all) papers on ultracold atom collisions, and it serves to highlight an important figure-of-merit of our collider; namely, that the collision energy is much larger than the temperature of the clouds. For those with different backgrounds, the conversions to other units are

$$1\ \mu\text{K} = 1.38 \times 10^{-29}\ \text{J} = 8.62 \times 10^{-11}\ \text{eV} = 6.95 \times 10^{-7}\ \text{cm}^{-1}.$$

I also exclusively use Gauss as the unit of magnetic field, keeping with the tradition of atomic physics for which the S.I. Tesla is far too large: 10^4 G $= 1$ T. I write uncertainties on numbers using parentheses as, for example, $3.502(42)$, where the number in parentheses indicates the 1-σ uncertainty in the last digits; this is equivalent to 3.502 ± 0.042.

Finally, the careful reader will notice that I do not use either "I" or "we" exclusively. Physics is a collective endeavour, and experimental physics even more so, so the use of "I" alone seems, to me at least, rather pretentious. The use of "we," however, is vague as to what my contributions to this work are. By changing between the different pronouns, I have tried to separate my contributions to the experiment from contributions made by the many

people who have made this work possible.

Chapter 2

Theoretical background

The theory behind this work, namely non-relativistic quantum scattering theory, is a mature subject. Most textbooks on quantum mechanics will include at least one chapter on the subject, and there have been a number of in-depth monographs penned regarding both relativistic and non-relativisitic scattering theory. The treatment of scattering theory is consequently quite varied and ranges from introductory[53] to more in-depth[54] to a veritable orgy of mathematical abstraction[55, 56]. As one can imagine, each approach has its own utility. Often, the more abstract versions focus on time-dependent scattering theory which, while more rigourous, is not particularly useful for *calculating* quantities that can be measured in the lab. Harald Friedrich's approach[54], using almost exclusively time-independent scattering theory, might lack the rigour of the time-dependent approach, but one also does not need to read ten dense chapters before starting to learn how to calculate scattering properties of quantum systems (as must be done with John R. Taylor's book[55]). As a result, I have a chosen to follow Friedrich's treatment.

Recognizing that a thesis is not meant to be a textbook, and that it would be a colossal duplication of effort, I will not reproduce the entirety of scattering theory in this chapter. However, I also acknowledge that theses, and especially PhD theses, are used as references by the research groups where they are written, and it is very convenient to have a compact description of the theoretical background of a particular experiment in one location. To balance out these two competing forces, I will give a reasonably detailed discussion of time-independent scattering theory and will leave extraneous derivations to the appendices.

2.1 The basic time-dependent scattering problem

Consider the classical scattering problem: a particle comes in from infinity with a specific asymptotic trajectory (the "in" asymptote), interacts with a fixed potential, and then leaves and asymptotically approaches a different trajectory (the "out" asymptote). In classical

mechanics, the in and out asymptotes can be specified by the limits of the position and momentum as time goes to negative and positive infinity, respectively. Determining how in asymptotes map to out asymptotes is the fundamental question of scattering theory.

The quantum scattering problem is very similar, except rather than an incoming particle one has an incoming wavepacket, and instead of Hamiltonian dynamics we have the time-dependent Schrödinger equation

$$i\hbar\partial_t|\psi(t)\rangle = \hat{H}|\psi(t)\rangle = \left(\frac{\hat{\mathbf{p}}^2}{2m} + V(\hat{\mathbf{r}})\right)|\psi(t)\rangle \tag{2.1}$$

where $\hat{\mathbf{r}}$ is the position operator, $\hat{\mathbf{p}}$ is the momentum operator, m is the mass of the particle, and $V(\hat{\mathbf{r}})$ is the potential energy.[1] If two particles with positions $\hat{\mathbf{r}}_1$ and $\hat{\mathbf{r}}_2$ and momenta $\hat{\mathbf{p}}_1$ and $\hat{\mathbf{p}}_2$ scatter from each other instead of one particle scattering from a fixed potential, then I can rewrite the position operators in terms of the center of mass position $\hat{\mathbf{R}}$ and relative position $\hat{\mathbf{r}}$

$$\hat{\mathbf{R}} = \frac{m_1\hat{\mathbf{r}}_1 + m_2\hat{\mathbf{r}}_2}{m_1 + m_2} \qquad \hat{\mathbf{r}} = \hat{\mathbf{r}}_1 - \hat{\mathbf{r}}_2 \tag{2.2}$$

and the momentum operators in terms of the center of mass momentum $\hat{\mathbf{P}}$ and the relative momentum $\hat{\mathbf{p}}$

$$\hat{\mathbf{P}} = \hat{\mathbf{p}}_1 + \hat{\mathbf{p}}_2 \qquad \hat{\mathbf{p}} = \frac{m_2\hat{\mathbf{p}}_1 - m_1\hat{\mathbf{p}}_2}{m_1 + m_2}. \tag{2.3}$$

I assume that the potential depends only on the relative coordinate, which means that I can write it as Eq. (2.1) where $\hat{\mathbf{p}}$ is the relative momentum operator, $m = m_1m_2/(m_1 + m_2)$ is the reduced mass of the system, and $V(\hat{\mathbf{r}})$ is the interaction potential between the particles. The quantum problem can be represented schematically as in Fig. 2.1. A wavepacket that

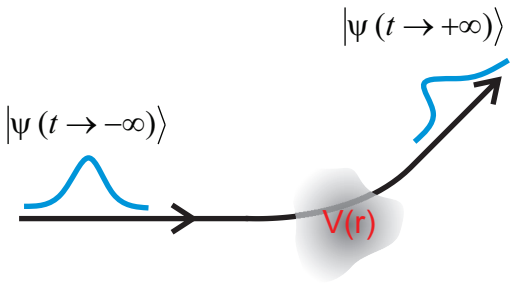

Figure 2.1: Diagram of time-dependent scattering. A free-particle wavepacket interacts with a fixed potential and has both its momentum and its shape changed.

evolves as a free particle as $t \to -\infty$ interacts with the potential and leaves, approaching a different free particle solution as $t \to +\infty$. The problem of time-dependent scattering theory is to find the so-called scattering operator, $\hat{S}$, which maps incoming states (in

[1] Some notational confusion is inevitable, as I use $\hat{\mathbf{r}}$ to represent both the position operator and the unit vector pointing in the direction of the vector $\mathbf{r}$. It should be clear from context which one is meant.

asymptotes) to outgoing states (out asymptotes). Such a picture, however, is fraught with complications. Does every in asymptote have a corresponding out asymptote and vice versa (asymptotic completeness)? Do wavepackets truly behave as free particles far enough away from the potential (asymptotic condition)? The answer to both of these questions is, perhaps unsurprisingly, it depends on the potential. Potentials that do not decay fast enough, such as the Coloumb potential, do not admit free particle asymptotes at infinity. In a similar vein, highly attractive potentials such as a potential that scales as r^{-3} near the origin may have in asymptotes but not out asymptotes because particles can come from infinity and become bound to the potential. In the case of a single particle with no internal structure interacting with a fixed potential (or two particles with a mutual interaction) one can impose certain conditions on the potential which ensure that particles evolve freely at infinity and that all in asymptotes will map one-to-one to all out asymptotes. These conditions are:

1. $V(r) = \mathcal{O}(r^{-3-\epsilon})$ as $r \to \infty$ for $\epsilon > 0$. The potential falls off faster than r^{-3} at infinity.

2. $V(r) = \mathcal{O}(r^{-2+\epsilon})$ as $r \to 0$ for $\epsilon > 0$. The potential is less singular than r^{-2} at the origin.

3. $V(r)$ is continuous except for a finite number of finite discontinuities.

The above conditions are more restrictive than is necessary, and they apply only to the case of particles with no internal structure (so that $V(r)$ operates only on the spatial degrees of freedom). In this work, I will be primarily interested in the case of particles (atoms) with internal structure, and for this situation, "[it is not] possible to enumerate the class of interactions V for which the asymptotic condition and asymptotic completeness hold."[55] Therefore, I will not concern myself with the details of what class of potentials allow for the development of scattering theory beyond an appeal to "reasonableness." Put another way, as an experimentalist I am concerned with whether I can accurately predict the results of an experiment, and I will assume that the scattering theory developed in the remainder of this chapter works unless proven otherwise.

Under these conditions, one can define a scattering operator, $\hat{S}$, which maps in asymptotes $|\psi_{\text{in}}\rangle$ to out asymptotes $|\psi_{\text{out}}\rangle$

$$\hat{S}|\psi_{\text{in}}\rangle = |\psi_{\text{out}}\rangle \tag{2.4}$$

where the in and out asymptotes are defined (loosely) as the limits of a scattering orbit $|\psi(t)\rangle$ as $t \to \pm\infty$.[2] The scattering operator can also be written in terms of the $\hat{T}$-operator,

[2]The more rigourous definition of the in and out asymptotes requires that they evolve as free particle solutions as $t \to \pm\infty$.

which is defined as

$$\hat{T} = \hat{S} - 1 \tag{2.5}$$

which is useful because it removes the part of the scattering operator that does nothing to the incoming state. Indeed, by defining the scattering state as $|\psi_{\text{sc}}\rangle = |\psi_{\text{out}}\rangle - |\psi_{\text{in}}\rangle$ we see that

$$\hat{T}|\psi_{\text{in}}\rangle = |\psi_{\text{sc}}\rangle.$$

In other words, the $\hat{T}$-operator acting on the in asymptote gives us the scattering state, which is arguably of more interest than the total out asymptote. The problem of scattering theory is thus to find the scattering operator $\hat{S}$ (or alternatively the $\hat{T}$-operator) for a given potential. Not surprisingly, it is far easier to calculate $\hat{S}$ using time-independent scattering theory. While the connection between time-dependent and time-independent scattering theory can be made fully rigourous[55], I shall simply embrace the wisdom of ages that this is so and proceed with time-independent scattering theory.

2.2 The basic time-independent scattering problem

2.2.1 The scattering amplitude

My starting point here is the time-independent Schrödinger equation in the position basis ($\psi(\mathbf{r}) = \langle \mathbf{r}|\psi\rangle$)

$$\hat{H}\psi(\mathbf{r}) = \left(-\frac{\hbar^2}{2m}\nabla^2 + V(\mathbf{r})\right)\psi(\mathbf{r}) = E\psi(\mathbf{r}) \tag{2.6}$$

for fixed total energy E and no internal structure. Let me rewrite Eq. (2.6) in a slightly different form

$$\left(E + \frac{\hbar^2}{2m}\nabla^2\right)\psi(\mathbf{r}) = V(\mathbf{r})\psi(\mathbf{r}) \tag{2.7}$$

which resembles an inhomogeneous Helmholtz equation, and this equation can be solved using a Green's function. For Eq. (2.7) I define the Green's function $G(\mathbf{r}, \mathbf{r}')$ as

$$\left(E + \frac{\hbar^2}{2m}\nabla^2\right)G(\mathbf{r}, \mathbf{r}') = \delta(\mathbf{r} - \mathbf{r}') \tag{2.8}$$

where $\delta(\mathbf{r} - \mathbf{r}')$ is the Dirac delta function. I solve for the Green's function as follows. Equation (2.8) is clearly invariant with respect to translations in space, so I can, without loss of generality, set $\mathbf{r}' = 0$. Furthermore, since $\delta(\mathbf{r})$ is radially symmetric, the Green's function must be a function of $|\mathbf{r}| = r$ only. I can therefore ignore the θ and ϕ derivatives in the Laplacian to get

$$\left(E + \frac{\hbar^2}{2m}(\partial_r^2 + \frac{2}{r}\partial_r)\right)G(r) = 0 \tag{2.9}$$

for $r > 0$. This has the solution $G(r) = Ae^{ikr}/r$ with $k = \sqrt{2mE/\hbar^2}$, which can be easily checked by substitution. To determine the constant A, I integrate Eq. (2.8), with $\mathbf{r}' = 0$, over a small spherical volume with radius ϵ about $\mathbf{r} = 0$. I then take the limit of $\epsilon \to 0$, which in full looks like

$$\lim_{\epsilon\to 0}\int_{\mathcal{V}_\epsilon}\left(E + \frac{\hbar^2}{2m}\nabla^2\right)G(\mathbf{r})d^3\mathbf{r} = 1.$$

The integral over $EG(\mathbf{r}) \to 0$ as $\epsilon \to 0$, and the second term can be integrated using the divergence theorem

$$\lim_{\epsilon\to 0}\int_{\mathcal{V}_\epsilon}\frac{\hbar^2}{2m}\nabla^2 G(\mathbf{r})d^3\mathbf{r} = \lim_{\epsilon\to 0}\int_{\partial\mathcal{V}_\epsilon}\frac{\hbar^2}{2m}\nabla G(\mathbf{r})\cdot d\mathbf{S} = 1$$

where

$$\nabla G(\mathbf{r}) = Ae^{ikr}\hat{\mathbf{r}}\left(\frac{ik}{r} - \frac{1}{r^2}\right)$$

with $d\mathbf{S} = \epsilon^2 d\Omega$ and $d\Omega = \sin\theta d\theta d\phi$ the element of solid angle. The term proportional to $1/r$ gives a vanishing contribution to the integral in the limit of $\epsilon \to 0$, and the term proportional to $1/r^2$ gives $-2\pi A\hbar^2/m$ in the same limit. Therefore, the Green's function is

$$G(\mathbf{r},\mathbf{r}') = -\frac{m}{2\pi\hbar^2}\frac{e^{ik|\mathbf{r}-\mathbf{r}'|}}{|\mathbf{r}-\mathbf{r}'|} \tag{2.10}$$

where I have reintroduced $\mathbf{r}'$. The solution to Eq. (2.7) is then the sum of the part that solves the inhomogeneous equation and a part that solves the homogeneous equation with $V(\mathbf{r}) = 0$. I can choose any function that satisfies Eq. (2.7) with $V(\mathbf{r}) = 0$, which means I can choose any linear combination of plane waves as my homogeneous solution. Given that I am interested in scattering problems, where particles travel in from infinity, it makes sense to choose just one plane wave; without loss of generality, I choose that plane wave to be propagating along the z axis. The full solution is thus

$$\psi(\mathbf{r}) = e^{ikz} + \int G(\mathbf{r},\mathbf{r}')V(\mathbf{r}')\psi(\mathbf{r}')d^3\mathbf{r}' \tag{2.11}$$

which is known as the Lippman-Schwinger equation. It looks like an explicit solution to Eq. (2.7), but the solution itself is under the integral sign, so one cannot do the integral without already knowing the solution.

Now consider the large r limit where $r \gg r'$. I can approximate $G(\mathbf{r},\mathbf{r}')$ from Eq. (2.10) as

$$G(\mathbf{r},\mathbf{r}') \overset{r\to\infty}{\to} -\frac{m}{2\pi\hbar^2}\frac{e^{ikr}}{r}e^{-ik\hat{\mathbf{r}}\cdot\mathbf{r}'}$$

which changes Eq. (2.11) to

$$\psi(\mathbf{r}) \overset{r\to\infty}{\sim} e^{ikz} - \left[\frac{m}{2\pi\hbar^2}\int e^{-ik\hat{\mathbf{r}}\cdot\mathbf{r}'}V(\mathbf{r}')\psi(\mathbf{r}')d^3\mathbf{r}'\right]\frac{e^{ikr}}{r}, \tag{2.12}$$

where I am using the $\sim$ notation to indicate that I am not including the overall normalization. Note that regardless of the solution or potential, as long as the integral converges in Eq. (2.12) the term in brackets depends only on the direction of $\mathbf{r}$. If the potential is such that $r^2V(\mathbf{r}) \overset{r\to\infty}{\to} 0$ (falls off faster than r^{-2}) and $r^2V(\mathbf{r}) \overset{r\to 0}{\to} 0$ (less singular than r^{-2} at the origin), then the integral will converge for all values of k. I can replace the entire bracket with a single function of the direction of $\mathbf{r}$ and the wavenumber and rewrite Eq. (2.12) as

$$\psi(\mathbf{r}) \overset{r\to\infty}{\sim} e^{ikz} + f(k,\theta,\phi)\frac{e^{ikr}}{r} \tag{2.13}$$

where the *scattering amplitude* $f(k,\theta,\phi)$ is defined as

$$f(k,\theta,\phi) = -\frac{m}{2\pi\hbar^2}\int e^{-ik\hat{\mathbf{r}}\cdot\mathbf{r}'}V(\mathbf{r}')\psi(\mathbf{r}')d^3\mathbf{r}'.$$

The interpretation of Eq. (2.13) is that one sends in a plane wave which interacts with the potential and produces, in the far field, a spherical wave that has some angle-dependent amplitude as seen in Fig. 2.2. The total outgoing asymptotic state is the sum of these two states. The information about the potential is captured by the scattering amplitude. Typically, the scattering amplitude is written only as $f(\theta,\phi)$, with the k-dependence hidden; I shall use this convention throughout this thesis.

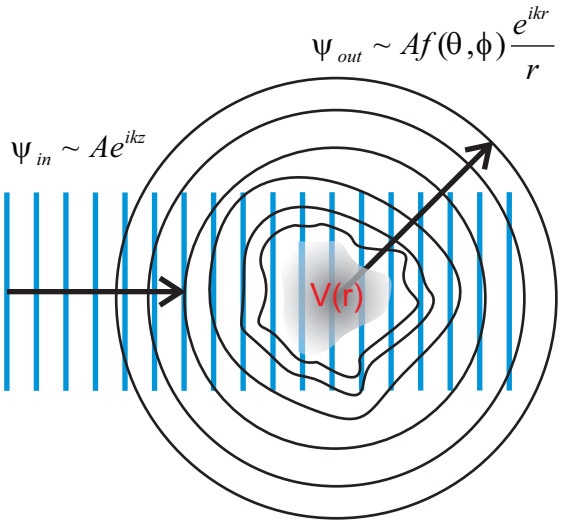

Figure 2.2: Illustration of scattering as described by Eq. (2.13).

By comparing Eq. (2.13) with Eqs. (2.4) and (2.5) one can immediately see the parallels. The in asymptote is specified in Eq. (2.13) to be a plane wave, and the out asymptote is the sum of the in asymptote and a scattered wave. Clearly, the scattering amplitude must have some direct relationship with the $\hat{T}$-operator, and this relationship will become apparent in later sections. Going forward, I will use Eq. (2.13) as the basic ansatz for single-channel scattering theory, and I will build on it for multichannel scattering theory.

2.2.2 Measurements and cross sections

In the ur-scattering experiment the experimentalist fires particles at a fixed target, or possibly two particles at each other, and then measures the directions into which those incident particles are scattered. What one measures in this way is what I will call the scattering distribution

$$\frac{dN_{\rm sc}}{d\Omega}$$

which is the number of scattered particles $N_{\rm sc}$ found in an element of solid angle $d\Omega$. The scattering distribution is implicitly a function of direction. The questions are: how does the scattering distribution relate to the scattering amplitude, and can one quantify the strength of the interaction with a single number?

To answer the first question, recall that the flux of probability is given by the current density $\mathbf{j}(\mathbf{r})$, defined as

$$\mathbf{j}(\mathbf{r}) = \Re\left[\psi^*(\mathbf{r})\frac{\hat{\mathbf{p}}}{m}\psi(\mathbf{r})\right] = \frac{\hbar}{2im}\psi^*(\mathbf{r})\nabla\psi(\mathbf{r}) - \frac{\hbar}{2im}\psi(\mathbf{r})\nabla\psi^*(\mathbf{r}). \tag{2.14}$$

Using Eq. (2.13) the incoming density, represented by the part of the wavefunction e^{ikz}, is $\mathbf{j}_{\rm in}(\mathbf{r}) = \hbar k/m\hat{\mathbf{z}}$. The current density for the outgoing spherical wave is more complicated, but the leading term as $r \to \infty$ is

$$\mathbf{j}_{\rm out}(\mathbf{r}) = \frac{\hbar k}{m}|f(\theta,\phi)|^2\frac{\hat{\mathbf{r}}}{r^2} + \mathcal{O}\left(\frac{1}{r^3}\right). \tag{2.15}$$

The number of particles escaping the potential is given by $\lim_{r\to\infty}\int \mathbf{j}_{\rm out}(\mathbf{r})\cdot d\mathbf{S}$ where $d\mathbf{S} = \hat{\mathbf{r}}r^2 d\Omega$, so the scattering distribution is

$$\frac{dN_{\rm sc}}{d\Omega} = \lim_{r\to\infty}\mathbf{j}_{\rm out}(\mathbf{r})\cdot r^2\hat{\mathbf{r}} = A\frac{\hbar k}{m}|f(\theta,\phi)|^2$$

where A is a normalization constant to fix the number of particles. The normalization constant can be eliminated using the incoming flux $|\mathbf{j}_{\rm in}(\mathbf{r})| = I_{\rm in} = A\hbar k/m$. Normalizing to the incoming flux of particles the scattering distribution is

$$\frac{dN_{\rm sc}}{d\Omega} = \lim_{r\to\infty}\mathbf{j}_{\rm out}(\mathbf{r})\cdot r^2\hat{\mathbf{r}} = I_{\rm in}|f(\theta,\phi)|^2.$$

This in turn defines the differential cross section, $d\sigma/d\Omega$, which relates the incoming flux of particles to the outgoing flux of particles

$$\frac{d\sigma}{d\Omega} = |f(\theta,\phi)|^2. \tag{2.16}$$

Given that it only references the scattering amplitude, it is generally the preferred quantity with which to work.

The second question – is there a single number which quantifies the strength of an interaction – can be answered by integrating the differential cross section over all directions. The resulting quantity is the cross section

$$\sigma = \int \frac{d\sigma}{d\Omega} d\Omega \tag{2.17}$$

which is so-called because it can be considered as an effective geometrical cross section for a "soft" target. If a uniform flux I_{in} of projectiles impinges on the potential then

$$N_{\text{sc}} = \sigma I_{\text{in}}$$

particles will be scattered by the potential. The cross section, calculated in this way, can be substituted into calculations involving collision integrals, rate equations, or anywhere a geometrical cross section might apply. In particular, both the differential cross section and the total cross section will be used later in numerical simulations of the optical collider.

There is a very important theorem, known as the optical theorem, which relates the total cross section to the scattering amplitude in the forward direction. To derive it, first note that the total flux passing through a surface must be zero for all stationary states

$$\oint_{\partial \mathcal{V}} \mathbf{j} \cdot d\mathbf{S} = 0, \tag{2.18}$$

which can be proven by applying the divergence theorem to the above and using $\nabla \cdot (f \nabla g) = \nabla f \cdot \nabla g + f \nabla^2 g$ for functions f and g. The total number of incoming particles passing through any sphere centered on the origin is zero, as $\hat{\mathbf{r}} \cdot \hat{\mathbf{z}} = \cos\theta$ and the integration of $\cos\theta$ over all solid angles is zero. The outgoing number of particles is easily calculated to be $I_{\text{out}} = \hbar k \sigma / m$. To satisfy Eq. (2.18), I must include the interference term between incoming and outgoing waves

$$\mathbf{j}_{\text{int}} = \frac{\hbar}{2im} \left\{ e^{-ikz} \nabla \left(f(\theta, \phi) \frac{e^{ikr}}{r} \right) + f(\theta, \phi)^* \frac{e^{-ikr}}{r} \nabla \left(e^{ikz} \right) \right\} + \text{c.c.}$$

where c.c. stands for the complex conjugate. I only care about the terms that are not orthogonal to $\hat{\mathbf{r}}$ and those that remain when integrated over a sphere of infinite radius. Ergo, I can neglect terms that fall off faster than $1/r^2$ and those that are proportional to $\hat{\phi}$ or $\hat{\theta}$. I get that

$$\mathbf{j}_{\text{int}} \cdot d\mathbf{S} = \frac{\hbar}{2m} f(\theta, \phi) e^{ikr(1-\cos\theta)} [kr(1+\cos\theta) + i] d\Omega + \text{c.c.}.$$

Letting $kr = \gamma$ and $x = \cos\theta$, I use the identity $\lim_{\gamma \to \infty} \int_{-1}^{1} f(x) e^{i\gamma(1-x)} dx = 0$ and also the identity

$$\lim_{\gamma \to \infty} \gamma \int_{-1}^{1} (1+x) f(x) e^{i\gamma(1-x)} dx = 2i f(1)$$

to derive

$$I_{\text{int}} = \lim_{r \to \infty} \oint \mathbf{j}_{\text{int}} \cdot d\mathbf{S} d\Omega = 2\pi i \frac{\hbar}{m} f(\theta = 0) + \text{c.c.}.$$

Solving $I_{\text{out}} + I_{\text{int}} = 0$, I get (with $\Im(x)$ being the imaginary part of x)

$$\sigma = \frac{4\pi}{k}\Im\left[f(\theta = 0)\right] \tag{2.19}$$

which is the optical theorem. Note that the scattering amplitude must have an imaginary part in order for there to be a non-zero cross section.

2.2.3 Radially/rotationally symmetric potentials

An important class of potentials are those that are radially symmetric; i.e. they do not depend on orientation. The mutual interaction of a pair of alkali metal atoms in their ground states is, to an excellent approximation, rotationally symmetric. For such systems, the Hamiltonian $\hat{H}$ commutes with all the components of the angular momentum operator $\hat{\mathbf{L}}$ and its square $\hat{\mathbf{L}}^2$. Therefore, I can use as a basis the simultaneous eigenvectors of $\hat{H}$, $\hat{\mathbf{L}}^2$, and $\hat{L}_z$:

$$\begin{aligned}
\hat{H}|E\ell m_\ell\rangle &= E|E\ell m_\ell\rangle \\
\hat{\mathbf{L}}^2|E\ell m_\ell\rangle &= \hbar^2\ell(\ell+1)|E\ell m_\ell\rangle \\
\hat{L}_z|E\ell m_\ell\rangle &= \hbar m_\ell|E\ell m_\ell\rangle.
\end{aligned} \tag{2.20}$$

Symmetries with respect to $\hat{\mathbf{L}}^2$ and $\hat{L}_z$ imply that the interaction cannot change the value of m_ℓ or ℓ. Furthermore, $\hat{H}$ commutes with the raising and lowering operators $\hat{L}_\pm = \hat{L}_x \pm i\hat{L}_y$. From this, one can show that

$$\begin{aligned}
\langle \ell m_\ell|\hat{L}_-\hat{H}\hat{L}_+|\ell m_\ell\rangle &= \langle \ell m_\ell|\hat{H}\hat{L}_-\hat{L}_+|\ell m_\ell\rangle \\
(\ell - m_\ell)(\ell + m_\ell + 1)\langle \ell, m_\ell + 1|\hat{H}|\ell, m_\ell + 1\rangle &= \sqrt{(\ell - m_\ell)^2(\ell + m_\ell + 1)^2}\langle \ell m_\ell|\hat{H}|\ell m_\ell\rangle \\
\langle \ell, m_\ell + 1|\hat{H}|\ell, m_\ell + 1\rangle &= \langle \ell m_\ell|\hat{H}|\ell m_\ell\rangle
\end{aligned} \tag{2.21}$$

which implies that the matrix elements of $\hat{H}$, and by extension $\hat{S}$, do not depend on m_ℓ.[3] Equations (2.20) and (2.21) also apply to more general rotationally invariant potentials involving spin if one simply replaces $\hat{\mathbf{L}}$ with the total angular momentum of the system $\hat{\mathbf{J}}$.

For a fixed energy E, I can expand any wavefunction $\psi(\mathbf{r}) = \langle \mathbf{r}|\psi\rangle$ in terms of $|E\ell m_\ell\rangle$ using the identity

$$\int dE \sum_{\ell m_\ell} |E\ell m_\ell\rangle\langle E\ell m_\ell| = 1$$

[3] The extension to $\hat{S}$ requires that $\hat{\mathbf{p}}^2/2m$ and $V(\mathbf{r})$ commute separately with $\hat{\mathbf{L}}$.

as follows

$$\begin{aligned}\psi(\mathbf{r}) &= \langle \mathbf{r}|\psi\rangle \\ &= \int dE \sum_{\ell m_\ell} \langle \mathbf{r}|E\ell m_\ell\rangle\langle E\ell m_\ell|\psi\rangle \\ &= \int dE \sum_{\ell m_\ell} f_{\ell m_\ell}(r,E) Y_{\ell m_\ell}(\theta,\phi) c_{\ell m_\ell}(E) \\ &= \sum_{\ell m_\ell} \psi_{\ell m_\ell}(r) Y_{\ell m_\ell}(\theta,\phi) \\ &= \sum_{\ell m_\ell} \frac{u_{\ell m_\ell}(r)}{r} Y_{\ell m_\ell}(\theta,\phi) \end{aligned} \tag{2.22}$$

where the integral over basis functions $f_{\ell m_\ell}(r,E)$ is $\int dE f_{\ell m_\ell}(r,E) c_{\ell m_\ell}(E) = \psi_{\ell m_\ell}(r)$. Here, $Y_{\ell m_\ell}(\theta,\phi)$ are the spherical harmonics, which are eigenfunctions of $\hat{\mathbf{L}}^2$ and $\hat{L}_z$, and the $u_{\ell m_\ell}(r)$, known as the radial wavefunctions, are the expansion coefficients of $\psi(\mathbf{r})$ in the basis of the spherical harmonics. Since angular momentum is conserved and I am assuming that the particles do not have any spin, then the outgoing wave must have the same angular momentum as the incoming plane wave. The plane wave has $m_\ell = 0$ because it is azimuthally symmetric about the z-axis, so the outgoing wave must also have $m_\ell = 0$. Therefore, I can replace the spherical harmonics with their $m_\ell = 0$ equivalents, the Legendre polynomials $P_\ell(\cos\theta)$[57], to get

$$\psi(\mathbf{r}) = \sum_\ell \frac{u_\ell(r)}{r} P_\ell(\cos\theta). \tag{2.23}$$

Now, the kinetic energy operator $-\hbar^2/(2m)\nabla^2$ can be written using the operator $\hat{\mathbf{L}}^2$ as

$$-\frac{\hbar^2}{2m}\nabla^2 = -\frac{\hbar^2}{2m}\left(\partial_r^2 + \frac{2}{r}\partial_r\right) + \frac{\hbar^2}{2mr^2}\hat{\mathbf{L}}^2$$

but since I am expanding $\psi(\mathbf{r})$ in terms of eigenfunctions of $\hat{\mathbf{L}}^2$, I can replace

$$\hat{\mathbf{L}}^2 P_\ell(\cos\theta) = \hbar^2\ell(\ell+1)P_\ell(\cos\theta)$$

to get the radial Schrödinger equation

$$\left(-\frac{\hbar^2}{2m}\partial_r^2 + \frac{\hbar^2\ell(\ell+1)}{2mr^2} + V(r)\right) u_\ell(r) = E u_\ell(r). \tag{2.24}$$

Equation (2.24) involves only the second derivative of r rather than both the first and second derivatives, and this is the reason for including the factor of $1/r$ in the expansion of $\psi(\mathbf{r})$. Thus, Eq. (2.24) has exactly the same form as the Schrödinger equation with an effective potential

$$V_{\text{eff}}(r) = V(r) + V_{\text{cent}}(r) = V(r) + \frac{\ell(\ell+1)}{2mr^2}$$

which includes the centrifugal term arising from non-zero angular momentum. I have plotted an example of the effect of the centrifugal potential on a pure van der Waals potential in Fig. 2.3. The effect of $V_{\text{cent}}(r)$ is to add a "centrifugal barrier" to the effective poten-

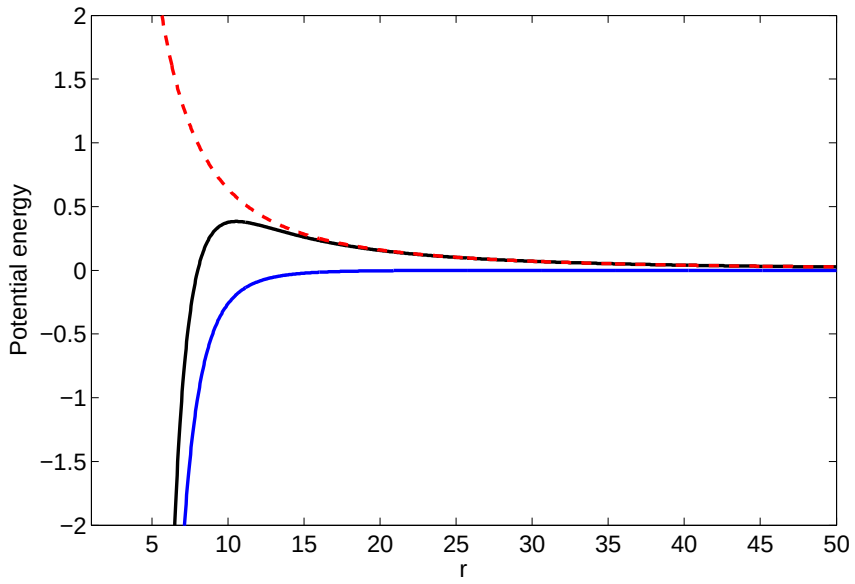

Figure 2.3: Effect of centrifugal potential. Blue curve is $V(r) \propto r^{-6}$, red dashed curve is V_{cent}, and the black curve is the sum of the two.

tial; particles with energies less than the height of the barrier will either tunnel through the barrier or be reflected. The barrier thus suppresses higher angular momentum scattering. Furthermore, the region behind the barrier may support long-lived states with energies $E > 0$ which decay by tunneling through the barrier; these states are the origin of so-called shape resonances which will be discussed in detail in Sec. 2.5.

2.2.4 Scattering phase shifts

Suppose that the potential $V(r)$ is zero. The radial Schrödinger equation Eq. (2.24) can be written as

$$\left[r^2\partial_r^2 - \ell(\ell+1) + k^2r^2\right] u_\ell(r) = 0 \tag{2.25}$$

where $k^2 = 2mE/\hbar^2$. The solutions to Eq. (2.25) are the Riccati-Bessel functions, denoted as u_ℓ^s and u_ℓ^c, which can be written in terms of Bessel functions of the first and second kind, $J_\nu(kr)$ and $Y_\nu(kr)$ respectively[58], or the spherical Bessel functions $j_\nu(kr)$ and $y_\nu(kr)$, as

$$\begin{aligned} u_\ell^s(r) &= krj_\ell(kr) = \sqrt{\frac{\pi kr}{2}} J_{\ell+1/2}(kr) \\ u_\ell^c(r) &= -kry_\ell(kr) = -\sqrt{\frac{\pi kr}{2}} Y_{\ell+1/2}(kr). \end{aligned} \tag{2.26}$$

As $kr \to \infty$ they have the asymptotic forms

$$\begin{aligned} u_\ell^s(r) &\overset{r\to\infty}{=} \sin(kr - \ell\frac{\pi}{2}) + \mathcal{O}\left(\frac{1}{kr}\right) \\ u_\ell^c(r) &\overset{r\to\infty}{=} \cos(kr - \ell\frac{\pi}{2}) + \mathcal{O}\left(\frac{1}{kr}\right) \end{aligned} \tag{2.27}$$

which is why I have chosen the superscripts s and c for the functions, to stand for sine and cosine behaviour at infinity. As $kr \to 0$ they behave as

$$\begin{aligned} u_\ell^s(r) &\overset{kr\to 0}{=} \frac{\sqrt{\pi}(kr)^{\ell+1}}{2^{\ell+1}\Gamma(\ell+\frac{3}{2})}\left[1 - \frac{(kr)^2}{4\ell+6}\right] \\ u_\ell^c(r) &\overset{kr\to 0}{=} \frac{2^\ell\Gamma(\ell+\frac{1}{2})}{\sqrt{\pi}(kr)^\ell}\left[1 + \frac{(kr)^2}{4\ell-2}\right]. \end{aligned} \tag{2.28}$$

The function u_ℓ^c cannot be a physical solution to Eq. (2.25) because it is not square-integrable, which leaves the "regular" solution u_ℓ^s as the only solution.

Now suppose that there is a potential $V(r)$ that falls off with distance faster than $1/r^2$. Then as $kr \to \infty$, the centrifugal potential dominates – see Fig. 2.3 – and the asymptotic solution is a superposition

$$u_\ell(r) \overset{r\to\infty}{=} Au_\ell^s(r) + Bu_\ell^c(r) \propto \sin(kr - \ell\frac{\pi}{2} + \delta_\ell) \tag{2.29}$$

where $\tan\delta_\ell = B/A$. The presence of the irregular solution $u_\ell^c(r)$ is both allowed, as I am not considering regions near the the origin, and necessary to match the asymptotic behaviour of the true solution $u_\ell(r)$. The scattering phase shift, induced by the potential on the asymptotic states, is δ_ℓ and it is a function of energy E and is indexed by orbital angular momentum ℓ. Importantly, δ_ℓ is a strictly real quantity if $V(r)$ is real-valued which is a consequence of the unitarity of the scattering process.[4] The scattering phase shifts are related to the scattering amplitude encountered in Eq. (2.13) as follows. It is well known[5] that a plane wave can be expanded using Legendre polynomials using Rayleigh's formula

$$e^{ikz} = \sum_\ell (2\ell+1)i^\ell j_\ell(kr)P_\ell(\cos\theta), \tag{2.30}$$

and, defining the ℓth scattering amplitude f_ℓ by

$$f(\theta,\phi) = \sum_\ell f_\ell P_\ell(\cos\theta), \tag{2.31}$$

[4] If $V(r)$ is real then the operators of Eq. (2.24) are all real, which means that one can choose the solution itself to be strictly real. An alternative proof of the reality of δ_ℓ uses the optical theorem.

[5] ...to those who know it well. For a proof, see appendix A.1.

I use it to express the asymptotic behaviour of $\psi(\mathbf{r})$ in Eq. (2.13) as

$$\begin{aligned}\psi(\mathbf{r}) &\overset{r\to\infty}{\sim} \left(\sum_\ell (2\ell+1) i^\ell j_\ell(kr) P_\ell(\cos\theta)\right) + f(\theta,\phi)\frac{e^{ikr}}{r} \\ &\overset{r\to\infty}{\sim} \sum_\ell i^\ell P_\ell(\cos\theta)\left((2\ell+1)j_\ell(kr) + f_\ell \frac{e^{i(kr-\ell\pi/2)}}{r}\right) \\ &\overset{r\to\infty}{\sim} \sum_\ell i^\ell P_\ell(\cos\theta)\left((2\ell+1)\frac{\sin(kr-\ell\pi/2)}{kr} + f_\ell \frac{e^{i(kr-\ell\pi/2)}}{r}\right).\end{aligned}$$

Using the definition of $u_\ell(r)$ from Eq. (2.23) the asymptotic behaviour of $u_\ell(r)$ is

$$u_\ell(r) \overset{r\to\infty}{\sim} i^\ell \left[\frac{2\ell+1}{k}\sin(kr-\ell\frac{\pi}{2}) + f_\ell e^{i(kr-\ell\pi/2)}\right].$$

I can rewrite the asymptotic behaviour of $u_\ell(r)$ in a form more similar to Eq. (2.29)

$$u_\ell(r) \overset{r\to\infty}{\sim} i^\ell \left[\left(\frac{2\ell+1}{k} + i f_\ell\right)\sin(kr-\ell\frac{\pi}{2}) + f_\ell\cos(kr-\ell\frac{\pi}{2})\right]$$

which clearly identifies the coefficients A and B, indicating that the phase shift is

$$\tan\delta_\ell = \frac{B}{A} = \frac{k f_\ell}{2\ell+1+ikf_\ell}$$

which can be rewritten as

$$f_\ell = \frac{2\ell+1}{k} e^{i\delta_\ell}\sin\delta_\ell = \frac{2\ell+1}{2ik}\left(e^{2i\delta_\ell}-1\right). \tag{2.32}$$

The factor $e^{2i\delta_\ell}$ is in fact the eigenvalue of the S-matrix, defined component-wise as $S^{\ell m_\ell}_{\ell' m'_\ell} = \langle \ell' m'_\ell|\hat{S}|\ell m_\ell\rangle = S_\ell(E)\delta_{\ell\ell'}\delta_{m_\ell m'_\ell}$, which is another (and much more compelling) reason why the phase shift in this case must be real: the eigenvalues of a unitary matrix have unit modulus. The factor $e^{2i\delta_\ell}-1$ is the matrix element of the T-matrix (defined similarly to the S-matrix), and it will appear in a similar form when discussing the multichannel problem.

The differential cross section can now be expressed as the unholy mess

$$\frac{d\sigma}{d\Omega} = |f(\theta)|^2 = \frac{1}{k^2}\sum_{\ell,\ell'}(2\ell+1)(2\ell'+1)e^{i(\delta_\ell-\delta_{\ell'})}\sin\delta_\ell\sin\delta_{\ell'}P_\ell(\cos\theta)P_{\ell'}(\cos\theta) \tag{2.33}$$

whereas the total cross section can be easily computed using the orthogonality of the Legendre polynomials $\int_{-1}^{1} P_\ell(x)P_{\ell'}(x)dx = 2\delta_{\ell,\ell'}/(2\ell+1)$

$$\begin{aligned}\sigma &= \int \frac{d\sigma}{d\Omega}d\Omega \\ &= \frac{4\pi}{k^2}\sum_\ell (2\ell+1)\sin^2\delta_\ell = \sum_\ell \sigma_\ell.\end{aligned} \tag{2.34}$$

The partial cross sections, σ_ℓ, defined as

$$\sigma_\ell = \frac{4\pi}{k^2}(2\ell+1)\sin^2\delta_\ell, \tag{2.35}$$

have the property that they can never be larger than

$$\sigma_\ell \leq \frac{4\pi(2\ell+1)}{k^2}. \tag{2.36}$$

This limit is known as the unitarity limit because it arises from the restriction that the phase shifts be real quantities. The total cross section, on the other hand, has no limit because $\sum_\ell(2\ell+1)=\infty$.

In ultracold collisions, we are generally concerned with the behaviour of the scattering phase shifts as the collision energy approaches zero, which is termed the threshold energy or just threshold. To derive this behaviour, consider a potential that falls off faster than any power of r, such as e^{-r}. At a very large, but still finite, r one can describe the solution of Eq. (2.24) by the superposition Eq. (2.29). Considering the case of $k\to 0$, I can use the leading order approximation of the regular and irregular solutions from Eq. (2.28) to get

$$\begin{aligned} u_\ell(r) &\overset{kr\to 0}{\propto} u_\ell^s(kr) + \tan\delta_\ell u_\ell^c(kr) \\ &\overset{kr\to 0}{\propto} \frac{\sqrt{\pi}k^{\ell+1}}{2^{\ell+1}\Gamma(\ell+\frac{3}{2})}\left[r^{\ell+1} + \tan\delta_\ell \frac{2^{2\ell+1}\Gamma(\ell+\frac{1}{2})\Gamma(\ell+\frac{3}{2})}{\pi k^{2\ell+1}r^\ell}\right]. \end{aligned} \tag{2.37}$$

At threshold, where $k=0$, and in the limit where $V(r) \ll V_{\text{cent}}(r)$, the solutions to Eq. (2.24) are $r^{\ell+1}$ and $r^{-\ell}$. Therefore, Eq. (2.37) must approach a k-independent superposition of these two solutions as $k\to 0$. As the $k^{\ell+1}$ prefactor can be normalized away, the only way for Eq. (2.37) to be k-independent as $k\to 0$ is for the prefactor of the $r^{-\ell}$ term to be k-independent. Therefore, the scattering phase shift must obey

$$\tan\delta_\ell \overset{k\to 0}{=} -\frac{\pi}{\Gamma(\ell+\frac{1}{2})\Gamma(\ell+\frac{3}{2})}\left(\frac{a_\ell k}{2}\right)^{2\ell+1} \tag{2.38}$$

where I have introduced the k independent scattering length a_ℓ. Equation (2.38) is referred to as Wigner's threshold law[33], and it demonstrates a growing suppression of higher-ℓ scattering at low energies. Since $f_\ell(k) = \frac{2\ell+1}{k}e^{i\delta_\ell}\sin\delta_\ell$, the scattering amplitude behaves as

$$f_\ell(k) \overset{k\to 0}{\propto} k^{2\ell}a_\ell^{2\ell+1} \tag{2.39}$$

and the partial cross sections as

$$\sigma_\ell \overset{k\to 0}{\propto} k^{4\ell}a_\ell^{4\ell+2} \propto E^{2\ell}a_\ell^{4\ell+2}. \tag{2.40}$$

For these short-ranged potentials, only s-wave ($\ell=0$) scattering can occur at threshold, and in this case

$$\tan\delta_0 = -a_0 k = -ak \tag{2.41}$$

where I have dropped the subscript 0 for the s-wave scattering length, as is customary. At low energies, the total cross section is then simply

$$\sigma = 4\pi a^2.^{6} \tag{2.42}$$

Wigner's threshold law, especially in the form Eq. (2.40), illustrates the utility of the partial wave expansion. At low energies, one can succinctly describe the scattering process using a small number of parameters.

Of course, the dominant long-range interaction between alkali-metal atoms (the focus of this work) is the van der Waals interaction which behaves asymptotically[7] as

$$V(r) = -\frac{C_6}{r^6}.$$

Clearly, the van der Waals interaction does not fall off faster than any power of r, so it is unclear whether the derivation above for near-threshold phase shifts should apply. The proof is somewhat laborious, and I have relegated it to appendix A.2, but the result is simple: for any potential $V(r) \overset{r\to\infty}{=} \pm C_\alpha r^{-\alpha}$ Eq. (2.38) applies for

$$2\ell + 3 < \alpha. \tag{2.43}$$

For the van der Waals potential, with $\alpha = 6$, only $\ell = 0$ and 1 obey Eq. (2.38). When $2\ell + 3 > \alpha$ the phase shifts behave as

$$\tan\delta_\ell \overset{k\to 0}{\sim} \mp(k\beta_\alpha)^{\alpha-2} \tag{2.44}$$

where

$$\beta_\alpha = \left(\frac{2m|C_\alpha|}{\hbar^2}\right)^{1/(\alpha-2)}$$

is a quantum-mechanical length scale; the negative sign applies to repulsive potentials and the positive to attractive potentials. For $\alpha = 6$ this means that $\ell \geq 2$ partial waves all have $\tan\delta_\ell \overset{k\to 0}{\propto} k^4$.

Lastly, I should comment on what "near-threshold" means. How close to $k = 0$ should one be in order to apply these near-threshold relationships? The derivations are not particularly clear on this matter, but a convenient rule of thumb is that the phase shift should be much less than unity: $\delta_\ell \ll 1$. Consequently, the condition for a collision to be sufficiently low energy to be classified as "near-threshold" depends on which partial wave is being considered. In the absence of shape resonances, s-wave collisions might be near-threshold for energies lower than about 10 μK, p-wave collisions below about 300 μK, and d-wave and above below about 600 μK. If a shape resonance is present, as for homonuclear collisions of ^{40}K or ^{87}Rb, then these energy limits must be adjusted downwards accordingly.

[6] For distinguishable particles. As is described in Sec. 2.4, indistinguishable particles get an extra factor of 2.

[7] Neglecting retardation effects which for very large r change the r^{-6} dependence to r^{-7} [59, 60].

2.3 Time-independent multichannel scattering theory

Only in rare circumstances can one apply the basic scattering theory of Sec. 2.2 directly. Most problems of interest involve the scattering of particles that have internal degrees of freedom such as spin or principle quantum number. The low energy scattering of alkali metal atoms in a magnetic field, for example, involves internal states defined by the atoms' spin states, the energy of which are non-degenerate at infinite separation. Ergo, in order to deal with the multichannel problem, one must account for both multiple internal states and non-degenerate energies for those states.

Suppose that I have an "internal" Hamiltonian $\hat{H}_{\rm int}$ that acts only on the internal degrees of freedom, such as spin or principal quantum number. It has orthonormal eigenstates denoted by $|a\rangle$ which obey

$$\hat{H}_{\rm int}|a\rangle = E_a|a\rangle \tag{2.45}$$

with energy E_a. Note that the state $|a\rangle$ can be the internal state of one particle, in the case of a single particle scattering from a fixed potential, or the internal state of a two particle system. The internal states $|a\rangle$ define scattering *channels*. The total state vector can be expanded in terms of products between the internal states and the motional states

$$|\psi\rangle = \sum_a |\psi_a\rangle|a\rangle \tag{2.46}$$

where $\langle \mathbf{r}|\psi_a\rangle = \psi_a(\mathbf{r})$ is the spatial wavefunction for channel a. Suppose now that there is some potential $\hat{W}(\hat{\mathbf{r}})$ that acts on both the spatial coordinates and the internal coordinates. The total Hamiltonian for this system is

$$\left[\frac{\hat{\mathbf{p}}^2}{2m} + \hat{H}_{\rm int} + \hat{W}\right]|\psi\rangle = E|\psi\rangle \tag{2.47}$$

for a state with energy E. Taking the inner product of Eq. (2.47) with $\langle \mathbf{r}|\langle a|$ I get the coupled-channel equations

$$-\frac{\hbar^2}{2m}\nabla^2\psi_a(\mathbf{r}) + \sum_b V_{ab}(\mathbf{r})\psi_b(\mathbf{r}) = (E - E_a)\psi_a(\mathbf{r}) \tag{2.48}$$

where $V_{ab}(\mathbf{r}) = \langle a|\hat{W}|b\rangle$ are the matrix elements of $\hat{W}$ in the space of internal excitations. Crucially, I assume that $V_{ab}(\mathbf{r}) \to 0$ as $r \to \infty$ for all a and b, and I further assume that this fall-off is faster than r^{-2}. Note that in Eq. (2.48) the channels where $E < E_a$ decay exponentially as $e^{-\kappa_a r}/r$ with $\kappa_a = \sqrt{2m(E_a - E)}/\hbar$: these channels contain bound states and are referred to as closed channels. The corresponding open channels are those with $E > E_a$ and approach free-particle states with wavevector $k_a = \sqrt{2m(E - E_a)}/\hbar$. Only the open channels can contribute to the state in the far-field, so we look for solutions to

Eq. (2.48) that satisfy the ansatz

$$\langle \mathbf{r}|\psi\rangle \overset{r\to\infty}{\sim} e^{ik_a z}|a\rangle + \sum_{b\in\text{open}} f_{ab}(\theta,\phi)\frac{e^{ik_b r}}{r}|b\rangle \tag{2.49}$$

which corresponds to

$$\psi_b(\mathbf{r}) \overset{r\to\infty}{\sim} e^{ik_a z}\delta_{ab} + f_{ab}(\theta,\phi)\frac{e^{ik_b r}}{r} \tag{2.50}$$

when b is an open channel.

The spatial wavefunction for any channel a can be expanded in terms of the spherical harmonics:

$$\psi_a(\mathbf{r}) = \sum_{\ell m_\ell} \frac{u_{a\ell m_\ell}(r)}{r} Y_{\ell m_\ell}(\theta,\phi) \tag{2.51}$$

or, by taking the inner product with $\langle r|$ rather than $\langle \mathbf{r}|$,

$$\langle r|\psi_a\rangle = \sum_{\ell m_\ell} \frac{u_{a\ell m_\ell}(r)}{r}|\ell m_\ell\rangle. \tag{2.52}$$

Taking the inner product of Eq. (2.47) with $\langle r|\langle \ell m_\ell|\langle a|$ I get the radial coupled channels equations

$$\left[-\frac{\hbar^2}{2m}\partial_r^2 + \frac{\hbar^2\ell(\ell+1)}{2mr^2}\right] u_{a\ell m_\ell}(r) + \sum_{b\ell' m'_\ell} V^{b\ell' m'_\ell}_{a\ell m_\ell}(r) u_{b\ell' m'_\ell}(r) = (E-E_a)u_{a\ell m_\ell}(r) \tag{2.53}$$

with radial potential $V^{b\ell' m'_\ell}_{a\ell m_\ell}(r) = \langle a\ell m_\ell|\hat{W}|b\ell' m'_\ell\rangle$. To determine the S-matrix, and hence the scattering amplitude, one needs "simply" to solve Eq. (2.53) for the channel wavefunctions $u_{a\ell m_\ell}(r)$. There is, however, a catch. The value of the channel functions at $r = 0$ are known: all of them are 0. What is not known are the initial derivatives at $r = 0$. Indeed, one knows nothing else about the channel functions except that as $r \to \infty$ the functions $u_{a\ell m_\ell}(r)$ tend to a superposition of the regular and irregular solutions $u^s_\ell(k_a r)$ and $u^c_\ell(k_a r)$ with unknown coefficients. In fact, the coefficients are exactly what I am interested in! How does one solve this problem?

If the situation was that I had N equations for N channels, but I knew both boundary conditions for each channel, then there would be a single column vector of solutions $\mathbf{u}(r)$ comprised of channel functions $u_{a\ell m_\ell}(r)$ that would solve the system of equations. In my case, however, I know only one of each pair of boundary conditions which gives me N degrees of freedom. Essentially, I am solving N different systems of differential equations, which means that there are N possible solution vectors $\mathbf{u}(r)$. The solution to these N systems of equations can be represented by a matrix $U(r)$ whose N columns are the solutions to each of the N different systems of equations. As $r \to \infty$, the matrix asymptotically approaches

$$U(r) \overset{r\to\infty}{=} u^s(kr)A + u^c(kr)B \tag{2.54}$$

for constant matrices A and B, and $u^s(kr)$ and $u^c(kr)$ are diagonal matrices of the regular and irregular solution to the free-particle Schrödinger equation.[8] Each diagonal entry of $u^s(kr)$ and $u^c(kr)$ corresponds to a channel defined by the labels a, ℓ, and m_ℓ and are given by

$$u^s_\ell(k_a r) = \sqrt{k_a} r j_\ell(k_a r) \overset{r\to\infty}{\sim} k_a^{-1/2} \sin(k_a r - \ell\frac{\pi}{2}) \tag{2.55a}$$

$$u^c_\ell(k_a r) = -\sqrt{k_a} r y_\ell(k_a r) \overset{r\to\infty}{\sim} k_a^{-1/2} \cos(k_a r - \ell\frac{\pi}{2}). \tag{2.55b}$$

Note the difference between these functions and those defined by Eq. (2.26): there is a factor of $k_a^{-1/2}$ in Eq. (2.55b) compared to Eq. (2.26). I have tacitly assumed that the channel wavefunctions are all Dirac orthonormalized, and in order for this normalization to be compatible across channels with different wavevectors the extra factor of $k_a^{-1/2}$ is necessary[54].

Suppose now that one wants a quantity analogous to $\tan\delta_\ell$ in the single channel case. If I right-multiply Eq. (2.54) by A^{-1} then I get a new matrix of solutions

$$UA^{-1} = X \overset{r\to\infty}{=} u^s(kr) + u^c(kr)K. \tag{2.56}$$

The matrix $K = BA^{-1}$ is called the *reactance* matrix, and it must be Hermitian if the potential $\hat{W}$ is Hermitian. With the components written out explicitly, I have

$$X^{a\ell m_\ell}_{b\ell' m'_\ell} \overset{r\to\infty}{=} \delta_{ab}\delta_{\ell\ell'}\delta_{m_\ell m'_\ell} u^s_\ell(k_a r) + K^{a\ell m_\ell}_{b\ell' m'_\ell} u^c_{\ell'}(k_b r).[9] \tag{2.57}$$

In the case of a single radial equation the reactance matrix reduces to

$$K^{a\ell m_\ell}_{a\ell m_\ell} = K_\ell = \tan\delta_\ell$$

as expected.

I need not choose the functions $u^s_\ell(kr)$ and $u^c_\ell(kr)$ as the asymptotic forms of the solution. Instead, I can choose a superposition of the two to produce functions analogous to incoming and outgoing spherical waves

$$u^\pm_\ell(k_a r) = u^c_\ell(k_a r) \pm i u^s_\ell(k_a r) = \pm i\sqrt{k_a} r h^\pm_\ell(k_a r) \overset{r\to\infty}{\sim} k_a^{-1/2} e^{\pm i(k_a r - \ell\pi/2)} \tag{2.58}$$

where $h^\pm_\ell(kr) = j_\ell(kr) \pm i y_\ell(kr)$ are the spherical Hankel functions. I can rewrite the matrix of solutions $U(r)$ as

$$\begin{aligned} U(r) &\overset{r\to\infty}{=} \left[u^+(kr) - u^-(kr)\right]\frac{A}{2i} + \left[u^+(kr) + u^-(kr)\right]\frac{B}{2} \\ &\overset{r\to\infty}{=} \frac{u^+(kr)}{2i}(A + iB) - \frac{u^-(kr)}{2i}(A - iB) \\ -2iU(r)(A - iB)^{-1} = \Phi &\overset{r\to\infty}{=} u^-(kr) - u^+(kr)(A + iB)(A - iB)^{-1} \\ &\overset{r\to\infty}{=} u^-(kr) - u^+(kr)S \end{aligned} \tag{2.59}$$

[8] Whether A and B left-multiply or right-multiply is irrelevant as long as the algebra that follows is consistent.

[9] As a matrix, the upper three indices together specify the column and the lower three the row.

where the S-matrix is equivalent to

$$S = (A + iB)(A - iB)^{-1} = (1 + iK)(1 - iK)^{-1}. \tag{2.60}$$

The S-matrix defined here is the same S-matrix that appears in time-dependent multichannel scattering theory. It is unitary, which reflects conservation of particle number/probability. The corresponding matrix Φ has components

$$\Phi^{a\ell m_\ell}_{b\ell' m'_\ell} = \delta_{ab}\delta_{\ell\ell'}\delta_{m_\ell m'_\ell} u^-_\ell(k_a r) - S^{a\ell m_\ell}_{b\ell' m'_\ell} u^+_{\ell'}(k_b r). \tag{2.61}$$

To obtain the scattering matrix from a matrix of solutions U, I suppose that, as above, I can write it as

$$U = g_1 C + g_2 D$$
$$U' = g'_1 C + g'_2 D$$

where g_1 and g_2 are any two linearly independent solutions (in appropriate matrix form) of the uncoupled free particle equations and the primes denote differentiation. One can show that

$$(g'_2 U - g_2 U') = (g'_2 g_1 - g_2 g'_1)C = W_{2,1} C$$
$$(g'_1 U - g_1 U') = (g'_1 g_2 - g_1 g'_2)D = W_{1,2} D$$

with the Wronskian defined as $W_{a,b} = g'_a g_b - g_a g'_b$. Suppose that $g_1 = u^+(k_a r)$ and $g_2 = u^-(k_b r)$. Then as $r \to \infty$, the Wronskians approach $W_{2,1} \overset{r\to\infty}{=} -2i$ and $W_{1,2} \overset{r\to\infty}{=} 2i$.[10] Now, it is straightforward to prove for any two solutions of the free-particle equation that the Wronskian is independent of r, which means that the asymptotic versions of the Wronskians are equal to the Wronskians everywhere.[11] Therefore, for all r, I have that $W_{2,1} = -2i$ and $W_{1,2} = 2i$ for the pair of solutions $u^+(kr)$ and $u^-(kr)$. The scattering matrix $S = -CD^{-1}$ can then be calculated as

$$S = (g'_2 U - g_2 U')(g'_1 U - g_1 U')^{-1} \tag{2.62}$$

which references only directly calculated quantities.

Finally, I want to connect the S-matrix to the scattering amplitudes $f_{ab}(\theta, \phi)$. First, I

[10] There is some sleight of hand here. Without the extra normalization factor of $k_a^{-1/2}$ the Wronskians would depend on the channel wavevectors which would be much more difficult to work with.

[11] This is a consequence of Abel's identity[61].

rewrite the ansatz Eq. (2.50) as

$$\begin{aligned}
\psi_b(\mathbf{r}) &\overset{r\to\infty}{\sim} e^{ik_a z}\delta_{ab} + f_{ab}(\theta,\phi)\frac{e^{ik_b r}}{r} \\
&\overset{r\to\infty}{\sim} 2\sum_\ell \sqrt{\pi(2\ell+1)}i^\ell j_\ell(k_a r)Y_{\ell,0}(\theta,\phi)\delta_{ab} + f_{ab}(\theta,\phi)\frac{e^{ik_b r}}{r} \\
&\overset{r\to\infty}{\sim} -\frac{1}{r}\left(\sum_\ell \sqrt{\frac{\pi(2\ell+1)}{k_a}}i^{\ell-1}(u_\ell^-(k_a r) - u_\ell^+(k_a r))Y_{\ell,0}(\theta,\phi)\delta_{ab} - f_{ab}(\theta,\phi)e^{ik_b r}\right) \\
&\overset{r\to\infty}{\sim} -\frac{1}{r}\left(\sum_\ell \sqrt{\frac{\pi(2\ell+1)}{k_a}}i^{\ell-1}u_\ell^-(k_a r)Y_{\ell,0}(\theta,\phi)\delta_{ab}\right. \\
&\qquad\left. -e^{ik_b r}\left[f_{ab}(\theta,\phi) - i\sum_\ell \sqrt{\frac{\pi(2\ell+1)}{k_a k_b}}Y_{\ell,0}(\theta,\phi)\delta_{ab}\right]\right)
\end{aligned} \tag{2.63}$$

where I have used a modified form of Eq. (2.30) where the Legendre polynomial has been replaced by a spherical harmonic

$$e^{ikz} = 2\sum_\ell \sqrt{\pi(2\ell+1)}i^\ell j_\ell(kr)Y_{\ell,0}(\theta,\phi). \tag{2.64}$$

Now, the matrix Φ defines a basis of vectors with which one can expand radial wavefunctions. The radial wavefunction $u_{b\ell' m'_\ell}$ can be written in the asymptotic limit as a linear combination of basis vectors

$$\begin{aligned}
u_{b\ell' m'_\ell}(r) &\overset{r\to\infty}{\sim} \sum_{\ell m_\ell} C_{\ell m_\ell}\Phi^{a\ell m_\ell}_{b\ell' m'_\ell} \\
&\overset{r\to\infty}{\sim} \sum_\ell C_{\ell m_\ell}\left(\delta_{ab}\delta_{\ell,\ell'}\delta_{m_\ell,m'_\ell}u_\ell^-(k_a r) - S^{a\ell m_\ell}_{b\ell' m'_\ell}u_{\ell'}^+(k_b r)\right) \\
&\overset{r\to\infty}{\sim} \sum_\ell C_{\ell m_\ell}\left(\delta_{ab}\delta_{\ell,\ell'}\delta_{m_\ell,m'_\ell}u_\ell^-(k_a r) - i^{-\ell'}e^{ik_b r}S^{a\ell m_\ell}_{b\ell' m'_\ell}\right)
\end{aligned} \tag{2.65}$$

with unknown expansion coefficients $C_{\ell m_\ell}$. I now write out the wavefunction $\psi_b(\mathbf{r})$ using Eq. (2.51)

$$\begin{aligned}
\psi_b(\mathbf{r}) &= \sum_{\ell' m'_\ell}\frac{u_{b\ell' m'_\ell}}{r}Y_{\ell' m'_\ell}(\theta,\phi) \\
&\overset{r\to\infty}{\sim} \frac{1}{r}\sum_{\ell' m'_\ell \ell m_\ell} C_{\ell m_\ell}\left(\delta_{ab}\delta_{\ell,\ell'}\delta_{m_\ell,m'_\ell}u_\ell^-(k_a r) - i^{-\ell'}e^{ik_b r}S^{a\ell m_\ell}_{b\ell' m'_\ell}\right)Y_{\ell' m'_\ell}(\theta,\phi).
\end{aligned} \tag{2.66}$$

By direct comparison between Eq. (2.63) and Eq. (2.66), one can see that in order for the $u_\ell^-(k_a r)$ terms to match, the expansion coefficients must be

$$C_{\ell m_\ell} = -\sqrt{\frac{\pi(2\ell+1)}{k_a}}i^{\ell-1}\delta_{m_\ell,0}$$

which implies that

$$f_{ab}(\theta,\phi) - i\sum_{\ell}\sqrt{\frac{\pi(2\ell+1)}{k_a k_b}}Y_{\ell,0}(\theta,\phi)\delta_{ab} = \sum_{\ell' m'_\ell \ell}\sqrt{\frac{\pi(2\ell+1)}{k_a k_b}}i^{\ell-\ell'-1}S^{a\ell 0}_{b\ell' m'_\ell}Y_{\ell' m'_\ell}(\theta,\phi).$$

The scattering amplitude is therefore

$$f_{ab}(\theta,\phi) = \sum_{\ell,\ell',m'_\ell}\sqrt{\frac{\pi(2\ell+1)}{k_a k_b}}i^{\ell-\ell'-1}Y_{\ell' m'_\ell}(\theta,\phi)\left[S^{a\ell 0}_{b\ell' m'_\ell} - \delta_{a,b}\delta_{\ell\ell'}\delta_{0m'_\ell}\right]. \tag{2.67}$$

A somewhat more convenient expression is obtained using the T-matrix $T = S - 1$:

$$f_{ab}(\theta,\phi) = \sum_{\ell,\ell',m'_\ell}\sqrt{\frac{\pi(2\ell+1)}{k_a k_b}}i^{\ell-\ell'-1}Y_{\ell' m'_\ell}(\theta,\phi)T^{a\ell 0}_{b\ell' m'_\ell}. \tag{2.68}$$

The scattering amplitude calculated here assumes that the incoming particle is travelling along the z-axis. While this can always be arranged, the necessary rotation of the internal state may be complicated, and it may be easier to consider incidence along an arbitrary direction instead. Changing the incoming wave to $e^{i\mathbf{k}\cdot\mathbf{r}}$ and using the generalized Rayleigh's formula[55]

$$P_\ell(\hat{\mathbf{k}}\cdot\hat{\mathbf{r}}) = \frac{4\pi}{2\ell+1}\sum_{m_\ell}Y_{\ell m_\ell}(\hat{\mathbf{r}})Y^*_{\ell m_\ell}(\hat{\mathbf{k}}) \tag{2.69}$$

the final result for the scattering amplitude from states $a \to b$ and incident direction $\hat{\mathbf{k}}$ to $\hat{\mathbf{r}}$ is

$$f_{ab}(\hat{\mathbf{k}}\to\hat{\mathbf{r}}) = \frac{2\pi}{\sqrt{k_a k_b}}\sum_{\substack{\ell m_\ell \\ \ell' m'_\ell}} i^{\ell-\ell'-1}Y_{\ell' m'_\ell}(\hat{\mathbf{r}})Y^*_{\ell m_\ell}(\hat{\mathbf{k}})T^{a\ell m_\ell}_{b\ell' m'_\ell}. \tag{2.70}$$

Now that I have the scattering amplitude, I need to calculate the differential cross section. I defined the differential scattering cross section using the current density of the outgoing wave relative to the incoming current density, but both of those are proportional to the wavevector. Since the wavevectors for each channel are different, I need to re-evaluate the relationship between the differential cross section and the scattering amplitude. The outgoing current density, in the far field, for channel b is

$$\mathbf{j}_b(\mathbf{r}) = A\frac{\hbar k_b}{m}|f_{ab}(\theta,\phi)|^2\frac{\hat{\mathbf{r}}}{r^2} + \mathcal{O}\left(\frac{1}{r^3}\right) \tag{2.71}$$

which means that the number of pairs of particles in channel b given an incident wave in a is

$$\frac{dN_{ab}}{d\Omega} = \lim_{r\to\infty}\mathbf{j}_b(\mathbf{r})\cdot r^2\hat{\mathbf{r}} = A\frac{\hbar k_b}{m}|f_{ab}(\theta,\phi)|^2 \tag{2.72}$$

where A is a normalization constant. The incident flux is $I_a = |\mathbf{j}_a(\mathbf{r})| = A\hbar k_a/m$, which means that the differential cross section for this process is

$$\frac{d\sigma_{ab}}{d\Omega} = \frac{k_b}{k_a}|f_{ab}(\theta,\phi)|^2 \tag{2.73}$$

and its associated cross section is the integral over all solid angles

$$\sigma_{ab} = \frac{k_b}{k_a} \int |f_{ab}(\theta, \phi)|^2 d\Omega. \tag{2.74}$$

The total cross section is the sum over all open channels

$$\sigma_a = \sum_{b \in \text{open}} \sigma_{ab}. \tag{2.75}$$

I can calculate the $a \to b$ cross sections using Eq. (2.74) and by exploiting the orthonormality of the spherical harmonics get

$$\sigma_{ab} = \frac{\pi}{k_a^2} \sum_{\substack{\ell_1 \ell_2 \\ \ell' m'_\ell}} i^{\ell_2 - \ell_1} \sqrt{(2\ell_1 + 1)(2\ell_2 + 1)} ((S^{a\ell_1 0}_{b\ell' m'_\ell})^* - \delta_{ab}\delta_{\ell_1 \ell'}\delta_{m'_\ell 0})(S^{a\ell_2 0}_{b\ell' m'_\ell} - \delta_{ab}\delta_{\ell_2 \ell'}\delta_{m'_\ell 0}). \tag{2.76}$$

Summing over all open channels b

$$\begin{aligned}
\sigma_a &= \frac{\pi}{k_a^2} \sum_{\substack{b\ell_1 \ell_2 \\ \ell' m'_\ell}} i^{\ell_2 - \ell_1} \sqrt{(2\ell_1 + 1)(2\ell_2 + 1)} ((S^{a\ell_1 0}_{b\ell' m'_\ell})^* - \delta_{ab}\delta_{\ell_1 \ell'}\delta_{m'_\ell 0})(S^{a\ell_2 0}_{b\ell' m'_\ell} - \delta_{ab}\delta_{\ell_2 \ell'}\delta_{m'_\ell 0}) \\
&= \frac{\pi}{k_a^2} \sum_{\ell_1 \ell_2} i^{\ell_2 - \ell_1} \sqrt{(2\ell_1 + 1)(2\ell_2 + 1)} \left[\left(\sum_{b\ell' m'_\ell} (S^{a\ell_1 0}_{b\ell' m'_\ell})^* S^{a\ell_2 0}_{b\ell' m'_\ell} \right) - (S^{a\ell_1 0}_{a\ell_2 0})^* - S^{a\ell_2 0}_{a\ell_1 0} + \delta_{\ell_1 \ell_2} \right] \\
&= \frac{\pi}{k_a^2} \sum_{\ell_1 \ell_2} i^{\ell_2 - \ell_1} \sqrt{(2\ell_1 + 1)(2\ell_2 + 1)} \left[(SS^\dagger)^{a\ell_2 0}_{a\ell_1 0} - (S^{a\ell_1 0}_{a\ell_2 0})^* - S^{a\ell_2 0}_{a\ell_1 0} + \delta_{\ell_1 \ell_2} \right]
\end{aligned} \tag{2.77}$$

where I have used the definition of matrix multiplication

$$\sum_{b\ell' m'_\ell} (S^{a\ell_1 0}_{b\ell' m'_\ell})^* S^{a\ell_2 0}_{b\ell' m'_\ell} = \sum_{b\ell' m'_\ell} (S^\dagger)^{b\ell' m'_\ell}_{a\ell_1 0} S^{a\ell_2 0}_{b\ell' m'_\ell} = (SS^\dagger)^{a\ell_2 0}_{a\ell_1 0}.$$

The optical theorem for multichannel scattering reads[54]

$$\sigma_a = \frac{4\pi}{k_a} \Im \left[f_{aa}(\theta = 0) \right] \tag{2.78}$$

and the forward scattering amplitude, from Eq. (2.67), is

$$f_{aa}(\theta = 0) = \frac{1}{2k_a} \sum_{\ell\ell'} \sqrt{(2\ell' + 1)(2\ell + 1)} i^{\ell - \ell' - 1} \left[S^{a\ell 0}_{a\ell' 0} - \delta_{\ell\ell'} \right] \tag{2.79}$$

since $Y_{\ell m_\ell}(\theta = 0, \phi) = \delta_{m_\ell, 0} \sqrt{(2\ell + 1)/(4\pi)}$. Therefore,

$$\begin{aligned}
\frac{4\pi}{k_a} \Im \left[f_{aa}(\theta = 0) \right] &= \frac{2\pi}{ik_a} \left(f_{aa}(\theta = 0) - f^*_{aa}(\theta = 0) \right] \\
&= \frac{\pi}{k_a^2} \sum_{\ell' \ell} i^{\ell - \ell'} \sqrt{(2\ell' + 1)(2\ell + 1)} \left[2\delta_{\ell\ell'} - (S^{a\ell 0}_{a\ell' 0})^* - S^{a\ell' 0}_{a\ell 0} \right] \\
&= \sigma_a + \frac{\pi}{k_a^2} \sum_{\ell' \ell} i^{\ell - \ell'} \sqrt{(2\ell' + 1)(2\ell + 1)} \left[\delta_{\ell\ell'} - (SS^\dagger)^{a\ell' 0}_{a\ell 0} \right].
\end{aligned} \tag{2.80}$$

Only when S is unitary does the optical theorem hold, which again expresses the relationship between unitarity and particle conservation. If the ansatz is incomplete, in that it does not include all open channels, then in general the S-matrix will not be unitary. In this case one can call the loss of particles absorption and define an absorption cross section

$$\sigma_{\rm abs} = \frac{\pi}{k_a^2}\sum_{\ell'\ell} i^{\ell-\ell'}\sqrt{(2\ell'+1)(2\ell+1)}\left[\delta_{\ell\ell'} - (SS^\dagger)^{a\ell' 0}_{a\ell 0}\right] \tag{2.81}$$

which accounts for those states that are not included during the calculation.

2.4 Identical particles

All that I have done so far applies to particles that scatter from a fixed, external potential and to pairs of different particles that scatter from each other. But in quantum mechanics we have the concept of *identical* particles whose wavefunctions have particular symmetrization requirements. A pair of identical particles occupies only a subspace of the full Hilbert space available to non-identical particles. I can use the results that I have already derived to determine the scattering matrix and amplitude for pairs of identical particles.[12]

Suppose I have two identical particles, either bosons or fermions, in the same internal state. In this case I can factor out the internal state and ignore it, leaving only the spatial coordinates. Suppose that one particle is in the spatial wavefunction $\chi(\mathbf{r})$ and the other in $\xi(\mathbf{r})$. Since the particles are identical, and in the same internal state, one cannot say for sure whether particle 1 is in $\chi(\mathbf{r})$ or $\xi(\mathbf{r})$ and similarly for particle 2. To get around this problem, I construct a wavefunction that is non-committal as to which particle is in which state:

$$\psi(\mathbf{r}_1,\mathbf{r}_2) = \frac{\chi(\mathbf{r}_1)\xi(\mathbf{r}_2) \pm \chi(\mathbf{r}_2)\xi(\mathbf{r}_1)}{\sqrt{2}} \tag{2.82}$$

where the plus sign is for bosons and the minus sign is for fermions. I can also write this in terms of the centre-of-mass coordinate and relative coordinate

$$\mathbf{R} = \frac{\mathbf{r}_1+\mathbf{r}_2}{2} \qquad \mathbf{r} = \mathbf{r}_1 - \mathbf{r}_2,$$

and, when the potential depends only on $\mathbf{r}$, I can write the total wavefunction as a product state

$$\psi(\mathbf{r}_1,\mathbf{r}_2) = A(\mathbf{R})\zeta_\pm(\mathbf{r}), \tag{2.83}$$

where $\zeta_\pm(\mathbf{r}) = \pm\zeta_\pm(-\mathbf{r})$; i.e., the function of the relative coordinate is even or odd for bosons or fermions, respectively. When the internal states are not the same, I can generalize Eq. (2.83) to

$$\psi(\mathbf{R},\mathbf{r}) = A(\mathbf{R})\frac{\zeta(\mathbf{r})|ab\rangle \pm \zeta(-\mathbf{r})|ba\rangle}{\sqrt{2}} \tag{2.84}$$

[12] Inspired by and based on Stoof *et al.*[62].

where the first label in the ket $|ab\rangle$ denotes the internal state of the first particle and the second label the internal state of the second particle. Here, there is no requirement on the symmetry of $\zeta(\mathbf{r})$. Clearly, symmetrization only affects the relative coordinate, so in what follows I can safely ignore the center-of-mass coordinate as I have done in the previous sections.

Let us now consider angular momentum states. The spherical harmonic for direction $\hat{\mathbf{r}}$ behaves under parity transformations $\hat{\mathbf{r}} \to -\hat{\mathbf{r}}$ as[57]

$$Y_\ell^m(-\hat{\mathbf{r}}) = (-1)^\ell Y_\ell^m(\hat{\mathbf{r}}).$$

Therefore, an angular momentum state of identical bosons or fermions, including spins, must be symmetrized as

$$|\psi\rangle = \frac{|\ell m_\ell ab\rangle \pm (-1)^\ell |\ell m_\ell ba\rangle}{\sqrt{2(1+\delta_{ab})}} \tag{2.85}$$

where the denominator accounts for different normalizations when $a = b$ compared to $a \neq b$. I assume that the particles share the same radial state; in the context of scattering theory this means they share the same wavevector/energy. Consequently, I have suppressed the wavevector/energy/radial coordinate labeling. Note that pairs of bosons in the same spin state cannot exist in odd-ℓ angular momentum states, and pairs of fermions in the same spin state cannot exist in even-ℓ angular momentum states. States defined by Eq. (2.85) define a basis for all (anti-)symmetric states, and consequently any state of (fermions) bosons must be a superposition of these states.

The action of the scattering operator $\hat{S}$ on an angular momentum state is

$$\hat{S}|\ell m_\ell ab\rangle = \sum_{\ell' m'_\ell a' b'} S^{\ell m_\ell ab}_{\ell' m'_\ell a' b'} |\ell' m'_\ell a' b'\rangle.$$

This means that its action on a symmetrized state is

$$\hat{S}\left\{\frac{|\ell m_\ell ab\rangle \pm (-1)^\ell |\ell m_\ell ba\rangle}{\sqrt{2(1+\delta_{ab})}}\right\} = \sum_{\ell' m'_\ell a' b'} \frac{S^{\ell m_\ell ab}_{\ell' m'_\ell a' b'} |\ell' m'_\ell a' b'\rangle \pm (-1)^\ell S^{\ell m_\ell ba}_{\ell' m'_\ell b' a'} |\ell' m'_\ell b' a'\rangle}{\sqrt{2(1+\delta_{ab})}}. \tag{2.86}$$

By taking the inner product of Eq. (2.86) with a symmetrized bra, I find the matrix elements of $\hat{S}$ acting on the subspace of symmetrized states:

$$\begin{aligned} S^{\{\ell m_\ell ab\}}_{\{\ell' m'_\ell a' b'\}} &= \left\{\frac{\langle \ell' m'_\ell a' b'| \pm (-1)^{\ell'} \langle \ell' m'_\ell b' a'|}{\sqrt{2(1+\delta_{a'b'})}}\right\} \hat{S} \left\{\frac{|\ell m_\ell ab\rangle \pm (-1)^\ell |\ell m_\ell ba\rangle}{\sqrt{2(1+\delta_{ab})}}\right\} \\ &= \frac{S^{\ell m_\ell ab}_{\ell' m'_\ell a' b'} \pm (-1)^\ell S^{\ell m_\ell ba}_{\ell' m'_\ell a' b'} \pm (-1)^{\ell'} S^{\ell m_\ell ab}_{\ell' m'_\ell b' a'} + (-1)^{\ell'+\ell} S^{\ell m_\ell ba}_{\ell' m'_\ell b' a'}}{2\sqrt{1+\delta_{ab}}\sqrt{1+\delta_{a'b'}}} \end{aligned} \tag{2.87}$$

where the curly brackets $\{.\}$ in the indices of S indicate a symmetrized state. What Eq. (2.87) means in practice is that I can calculate the S-matrix elements initially by ignoring the underlying particle symmetries, and then afterward I can combine the relevant

elements together to create the appropriately symmetrized S-matrix. During numerical calculations one slight complication arises when either one of the symmetrized states defined by Eq. (2.85) is zero. In this case, the symmetrized S-matrix element of Eq. (2.87) is undefined. From a calculational perspective, it makes sense to replace these elements with $\delta_{aa'}\delta_{bb'}\delta_{\ell\ell'}\delta_{m_\ell m'_\ell}$, as the $\hat{S}$ operator has (effectively) no action on these states.

Finally, let me consider the effect of symmetrization on the scattering amplitude and cross section. Remember that the un-symmetrized incoming state was a momentum eigenstate

$$|\mathbf{k}_{ab}ab\rangle$$

whose spatial wavefunction was $\langle\mathbf{r}|\mathbf{k}_{ab}ab\rangle = e^{i\mathbf{k}_{ab}\cdot\mathbf{r}}|ab\rangle$; now, the incoming state must be the appropriately symmetric form

$$|\psi_{\text{in}}\rangle = \frac{|\mathbf{k}_{ab}ab\rangle \pm |-\mathbf{k}_{ab}ba\rangle}{\sqrt{2}}. \tag{2.88}$$

Note that one does not need the state-dependent normalization of Eq. (2.85), as the spatial state $|\mathbf{k}_{ab}\rangle$ does not have well-defined parity. I can decompose the momentum state $|\mathbf{k}_{ab}\rangle$ into a superposition of $|k_{ab}\ell m_\ell\rangle$

$$|\mathbf{k}_{ab}\rangle = \sum_{\ell m_\ell} c_{\ell m_\ell}(k_{ab})|k_{ab}\ell m_\ell\rangle$$

(the $c_{\ell m_\ell}(k)$ are obtained from the generalized Rayleigh's formula) which means that the incoming state is

$$\begin{aligned}
|\psi_{\text{in}}\rangle &= \frac{1}{\sqrt{2}}\left[\sum_{\ell m_\ell} c_{\ell m_\ell}(k_{ab})|k_{ab}\ell m_\ell ab\rangle\right] \pm \frac{1}{\sqrt{2}}\left[\sum_{\ell m_\ell}(-1)^\ell c_{\ell m_\ell}(k_{ab})|k_{ab}\ell m_\ell ab\rangle\right] \\
&= \sum_{\ell m_\ell} c_{\ell m_\ell}(k_{ab})\left[\frac{|k_{ab}\ell m_\ell ab\rangle \pm (-1)^\ell|k_{ab}\ell m_\ell ba\rangle}{\sqrt{2}}\right] \\
&= \sum_{\ell m_\ell} c_{\ell m_\ell}(k_{ab})\sqrt{1+\delta_{ab}}|\{k_{ab}\ell m_\ell ab\}\rangle
\end{aligned} \tag{2.89}$$

where

$$|\{k_{ab}\ell m_\ell ab\}\rangle = \frac{|k_{ab}\ell m_\ell ab\rangle \pm (-1)^\ell|k_{ab}\ell m_\ell ba\rangle}{\sqrt{2(1+\delta_{ab})}} \tag{2.90}$$

is the (anti-)symmetric basis state. The action of the scattering operator $\hat{S}$ is to carry incoming states to outgoing states

$$\begin{aligned}
|\psi_{\text{out}}\rangle &= \hat{S}|\psi_{\text{in}}\rangle \\
&= \sum_{a'b'}\sum_{\substack{\ell m_\ell \\ \ell' m'_\ell}} c_{\ell m_\ell}(k_{ab})\sqrt{1+\delta_{ab}}S^{\{\ell m_\ell ab\}}_{\{\ell' m'_\ell a'b'\}}(k_{ab})|\{k_{a'b'}\ell' m'_\ell a'b'\}\rangle
\end{aligned} \tag{2.91}$$

so that the scattered state is

$$\begin{aligned}|\psi_{\rm sc}\rangle &= |\psi_{\rm out}\rangle - |\psi_{\rm in}\rangle \\ &= \sum_{a'b'}\sum_{\substack{\ell m_\ell \\ \ell' m'_\ell}} c_{\ell m_\ell}(k_{ab})\sqrt{1+\delta_{ab}}T^{\{\ell m_\ell ab\}}_{\{\ell' m'_\ell a'b'\}}(k_{ab})|\{k_{a'b'}\ell' m'_\ell a'b'\}\rangle \end{aligned} \tag{2.92}$$

and the output state can be re-written as

$$|\psi_{\rm out}\rangle = \frac{|\mathbf{k}_{ab}ab\rangle \pm |-\mathbf{k}_{ab}ba\rangle}{\sqrt{2}} + \sum_{a'b'}\sum_{\substack{\ell m_\ell \\ \ell' m'_\ell}} c_{\ell m_\ell}(k_{ab})\sqrt{1+\delta_{ab}}T^{\{\ell m_\ell ab\}}_{\{\ell' m'_\ell a'b'\}}(k_{ab})|\{k_{a'b'}\ell' m'_\ell a'b'\}\rangle. \tag{2.93}$$

Looking at the projection onto $\langle\mathbf{r}|$ gives

$$\begin{aligned}\langle\mathbf{r}|\psi_{\rm out}\rangle &= \frac{e^{ik_{ab}z}|ab\rangle \pm e^{-ik_{ab}z}|ba\rangle}{\sqrt{2}} + \sum_{a'b'}\sum_{\substack{\ell m_\ell \\ \ell' m'_\ell}} c_{\ell m_\ell}(k_{ab})\sqrt{1+\delta_{ab}}T^{\{\ell m_\ell ab\}}_{\{\ell' m'_\ell a'b'\}}(k_{ab})Y_{\ell' m'_\ell}(\hat{\mathbf{r}}) \\ &\qquad \times \left[\frac{|a'b'\rangle \pm (-1)^\ell |b'a'\rangle}{\sqrt{2(1+\delta_{a'b'})}}\right]\frac{e^{ik_{a'b'}r}}{r} \end{aligned} \tag{2.94a}$$

$$\begin{aligned}&= \frac{e^{ik_{ab}z}|ab\rangle \pm e^{-ik_{ab}z}|ba\rangle}{\sqrt{2}} \\ &\qquad + \sum_{a'b'}\frac{\sqrt{1+\delta_{ab}}}{\sqrt{1+\delta_{a'b'}}}\left[\frac{f^{ab}_{a'b'}(\hat{\mathbf{r}})|a'b'\rangle \pm f^{ab}_{a'b'}(-\hat{\mathbf{r}})|b'a'\rangle}{\sqrt{2}}\right]\frac{e^{ik_{a'b'}r}}{r}\end{aligned} \tag{2.94b}$$

where the scattering amplitude for particles going from state $|ab\rangle$ to $|a'b'\rangle$ $f^{ab}_{a'b'}(\hat{\mathbf{r}})$ is

$$f^{ab}_{a'b'}(\hat{\mathbf{r}}) = \sum_{\substack{\ell m_\ell \\ \ell' m'_\ell}} c_{\ell m_\ell}(k_{ab})T^{\{\ell m_\ell ab\}}_{\{\ell' m'_\ell a'b'\}}(k_{ab})Y_{\ell' m'_\ell}(\hat{\mathbf{r}}). \tag{2.95}$$

I will consider two examples involving elastic scattering. The first is the case where $a' = a$ and $b' = b$ but $a \neq b$. The spatial state is

$$\langle\mathbf{r}|\psi_{\rm out}\rangle = \frac{e^{ik_{ab}z}|ab\rangle \pm e^{-ik_{ab}z}|ba\rangle}{\sqrt{2}} + \left[\frac{f^{ab}_{ab}(\hat{\mathbf{r}})|ab\rangle \pm f^{ab}_{ab}(-\hat{\mathbf{r}})|ba\rangle}{\sqrt{2}}\right]\frac{e^{ik_{ab}r}}{r}$$

and I want to know what the differential and total cross sections are. First, I need to know what the probability currents are, and this involves keeping careful track of how I have defined internal state labels in regards to the relative coordinate. From the incoming state, I have one contribution from the $|ab\rangle$ state and one contribution from the $|ba\rangle$ state. The physical meaning of $e^{ik_{ab}z}|ab\rangle$ is that the particle in state a is moving in the positive direction towards the particle in state b. By the same labelling convention, the physical meaning

of $e^{-ik_{ab}z}|ba\rangle$ is that the particle in state b is moving in the negative direction towards the particle in state a. Clearly these are exactly the same physical situation, so the total flux is the sum of these two contributions with appropriate weights from the above equation:

$$|\mathbf{j}_{\text{in}}| = \frac{\hbar k_{ab}}{2m} + \frac{\hbar k_{ab}}{2m} = \frac{\hbar k_{ab}}{m}.$$

Similarly, the outgoing current density has two contributions from the $|ab\rangle$ and $|ba\rangle$ states; $f(\hat{\mathbf{r}})|ab\rangle$ describes the situation when a particle in state a is scattered in direction $\hat{\mathbf{r}}$ and the particle in b is scattered in direction $-\hat{\mathbf{r}}$ and *exactly the same* for the state $f(-\hat{\mathbf{r}})|ba\rangle$. Thus, the outgoing current density for state a going out in direction $\hat{\mathbf{r}}$ and opposite for b is

$$\begin{aligned}\mathbf{j}_{\text{out}}(\mathbf{r}) &= \frac{\hbar k_{ab}}{m}\left[\frac{|f_{ab}^{ab}(\hat{\mathbf{r}})|^2}{2} + \frac{|f_{ab}^{ab}(\hat{\mathbf{r}})|^2}{2}\right]\frac{\hat{\mathbf{r}}}{r^2} + \mathcal{O}\left(\frac{1}{r^3}\right) \\ &= \frac{\hbar k_{ab}}{m}|f_{ab}^{ab}(\hat{\mathbf{r}})|^2\frac{\hat{\mathbf{r}}}{r^2} + \mathcal{O}\left(\frac{1}{r^3}\right).\end{aligned}$$

The *number of pairs of scattered particles* into either $|ab\rangle$ or $|ba\rangle$ is then

$$\frac{dN_{\text{pairs}}}{d\Omega} = \frac{\hbar k_{ab}}{m}|f_{ab}^{ab}(\hat{\mathbf{r}})|^2$$

meaning that the differential cross section is

$$\frac{d\sigma}{d\Omega} = |f_{ab}^{ab}(\hat{\mathbf{r}})|^2 \tag{2.96}$$

and the cross section is

$$\sigma = \int \frac{d\sigma}{d\Omega}d\Omega.$$

Aside from a symmetry requirement on the scattering amplitude, there is no difference in the cross sections for the case with identical particles and without.

Now suppose that both particles are in state a and remain so. Then

$$\langle\mathbf{r}|\psi_{\text{out}}\rangle = \frac{e^{ikz} \pm e^{-ikz}}{\sqrt{2}}|aa\rangle + \left[\frac{f_{aa}^{aa}(\hat{\mathbf{r}}) \pm f_{aa}^{aa}(-\hat{\mathbf{r}})}{\sqrt{2}}\right]|aa\rangle\frac{e^{ikr}}{r}$$

where, again, the total incoming flux in $|aa\rangle$ is $\hbar k/m$. The outgoing flux in state $|aa\rangle$ is

$$\begin{aligned}\mathbf{j}_{\text{out}}(\mathbf{r}) &= \frac{\hbar k}{2m}\left|f_{aa}^{aa}(\hat{\mathbf{r}}) \pm f_{aa}^{aa}(-\hat{\mathbf{r}})\right|^2 \\ &= \frac{2\hbar k}{m}|f_{aa}^{aa}(\hat{\mathbf{r}})|^2\end{aligned}$$

where $f_{aa}^{aa}(\hat{\mathbf{r}})$ has the necessary symmetry for bosons (even) or fermions (odd) by the construction of the matrix elements of $\hat{T}$ in Eq. (2.95). The outgoing flux is now twice as large as it was before. The number of scattered pairs is

$$\frac{dN_{\text{pairs}}}{d\Omega} = \frac{2\hbar k}{m}|f_{aa}^{aa}(\hat{\mathbf{r}})|^2$$

which means that the differential cross section is

$$\frac{d\sigma}{d\Omega} = 2|f_{aa}^{aa}(\hat{\mathbf{r}})|^2 \tag{2.97}$$

and the cross section is

$$\sigma = \int \frac{d\sigma}{d\Omega} d\Omega = 2 \int |f_{aa}^{aa}(\hat{\mathbf{r}})|^2 d\Omega. \tag{2.98}$$

Due to interference between the two possible paths that particles can take and still end up in the same state, the cross sections are now twice as large as for the case of identical particles in different states. Therefore, the probability of a collision is twice as large under the same circumstances.

One last comment about fluxes and cross sections. The fluxes measure the movement of the probability of finding the *pair* of particles in the state $|aa\rangle$. It does not measure the probability of finding **a** particle in state a. So when I talk about $dN_{\text{pairs}}/d\Omega$ being the number of scattered pairs, it means just that: pairs of particles. For both cases of different and same states, the total number of individual particles that are scattered into solid angle $d\Omega$ is twice that number.

2.5 Scattering resonances

Arguably the most interesting observation in a scattering experiment is a resonance: where the cross section for a process changes rapidly. In many cases, and certainly the cases which this work examines, resonances can be thought of as arising from coupling between the incoming scattering state and a quasi-bound state when the kinetic energy and bound state energies are nearly equal. There are two primary types of resonances: shape (or potential) resonances and Feshbach resonances[24, 25, 26, 63]. Shape resonances occur when the quasi-bound state is trapped behind a barrier in the potential for a *single* channel, whereas Feshbach resonances occur when the quasi-bound state occurs in a closed channel and only decays due to coupling between the incoming and closed channel. Therefore, shape resonances can occur in both single and multichannel problems while Feshbach resonances are restricted to multichannel problems. Illustrations of the two types of resonances are shown in Fig. 2.4.

To see how a quasi-bound state can affect the elements $S_\ell(E)$ of the $\hat{S}$-operator, I will first consider the relationship between a truly bound state and $S_\ell(E)$. For $E > 0$, the asymptotic behaviour of the radial wavefunction in the single channel case is

$$u_\ell(r) \overset{r\to\infty}{\sim} e^{-i(kr-\ell\pi/2)} - S_\ell(E) e^{i(kr-\ell\pi/2)}.$$

However, this asymptotic form is still mathematically valid for $E < 0$ where $k = i\kappa$ ($\kappa > 0$) is purely imaginary:

$$u_\ell(r) \overset{r\to\infty}{\sim} e^{\kappa r + i\ell\pi/2} - S_\ell(E) e^{-\kappa r - i\ell\pi/2}.$$

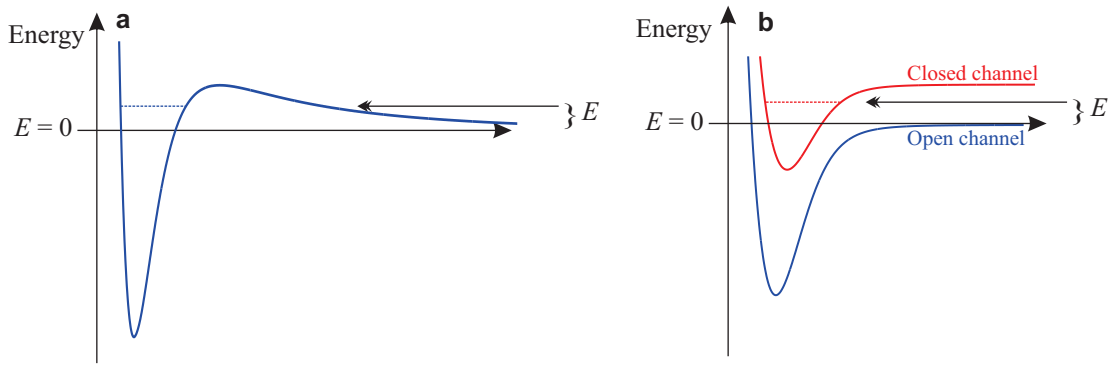

Figure 2.4: Two types of scattering resonances. **a** Shape resonance, where the quasi-bound state (dashed line) is trapped behind a potential barrier. **b** Feshbach resonance, where the quasi-bound state occurs in a closed channel.

To get a physical, square-integrable solution, only the exponentially decreasing term can be part of the solution; therefore, $S_\ell(E_b)$ must diverge at every bound state energy $E_b = -\frac{\hbar^2\kappa^2}{2m}$. In fact, $S_\ell(E)$ has a simple pole at E_b[55]

$$S_\ell(E) = \frac{A}{E - E_b}$$

where A is a normalization constant. Note that this does not violate any unitary conditions on $\hat{S}$ because the scattering operator is only unitary for $E \geq 0$. By extending the domain of $S_\ell(E)$ to $E < 0$ one acquires more information on the potential, namely its bound states.

To investigate quasi-bound states, I again extend the domain of $S_\ell(E)$, only this time to the lower complex half-plane with $E = E_R - i\frac{\Gamma}{2}$ where I assume that $\Gamma \geq 0$. The reason for this restriction is that if one considers the time-evolution of the probability of being in the quasi-bound state, one has $|e^{-iEt/\hbar}|^2 = e^{-\Gamma t/\hbar}$; i.e., the probability decays with time as one would expect.[13] In the same way that bound states are associated with poles in $S_\ell(E)$, one associates a quasi-bound state with a pole at the complex energy $E_R - i\frac{\Gamma}{2}$. For real, positive energies the scattering operator must be unitary so I write the element as

$$S_\ell(E) = S_{\text{bg}} \frac{E - E_R - i\frac{\Gamma}{2}}{E - E_R + i\frac{\Gamma}{2}} \tag{2.99}$$

where S_{bg} is the scattering matrix element far from resonance and has unit modulus. Since $|S_\ell(E)| = 1$, I can write it as the exponential of a phase

$$\begin{aligned} \delta_\ell(E) &= \delta_{\text{bg}} + \delta_{\text{res}} \\ &= \delta_{\text{bg}} - \tan^{-1}\left(\frac{\Gamma/2}{E - E_R}\right) \end{aligned} \tag{2.100}$$

[13] More advanced mathematical analysis[55] requires $\Gamma \geq 0$ based on the choice of branch cuts in the analytic continuation of $S_\ell(E)$.

which shows interference between the background phase shift $\delta_{\rm bg}$ and a resonant contribution $\delta_{\rm res}$ arising from the decay of the discrete bound state into the continuum. The partial cross section defined in Eq. (2.35) is thus

$$\sigma_\ell(E) = \frac{4\pi(2\ell+1)}{k^2}\sin^2\left(\delta_{\rm bg} - \tan^{-1}\left[\frac{\Gamma/2}{E-E_R}\right]\right) \tag{2.101a}$$

$$= \frac{4\pi(2\ell+1)}{k^2}\frac{(\epsilon+q)^2}{1+\epsilon^2}\sin^2\delta_{\rm bg} \tag{2.101b}$$

with $\epsilon = 2(E-E_R)/\Gamma$ and $q = -\cot\delta_{\rm bg}$. The last fraction in Eq. (2.101b) is known as the Beutler-Fano function, and it was first observed in auto-ionization data[64]; it appears in many different branches of physics where discrete states can decay into the continuum[65, 66, 67, 68]. For $\delta_{\rm bg} = 0$ the cross section reduces to a familiar Breit-Wigner, or Lorentzian, function. In physical systems, it may be difficult to observe a "pure" Beutler-Fano profile because of the energy dependence of $\delta_{\rm bg}$. Indeed, if $\delta_{\rm bg}$ varies on the same energy scale as Γ then it makes little sense to factor $S_\ell(E)$ as in Eq. (2.99) and the idea of a resonance loses its meaning. As an example of shape resonances, Fig. 2.5 shows the scattering phase shifts and partial cross sections for the four lowest partial waves of ^{87}Rb-^{87}Rb scattering in the hyperfine spin state $|f_1 m_{f1}\rangle|f_2 m_{f2}\rangle = |22\rangle|22\rangle$. These properties were calculated using the methods described in the next two sections. In creating these plots, I have neglected the

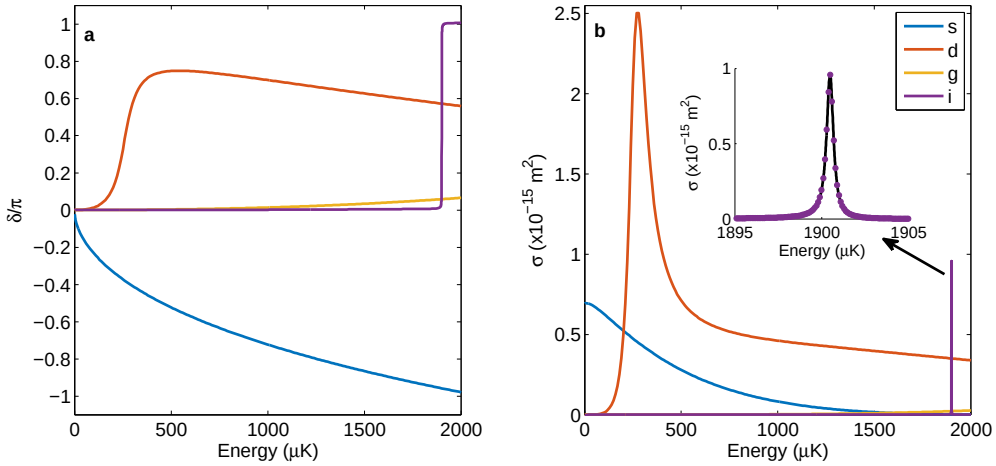

Figure 2.5: Scattering phase shifts **a** and partial cross sections **b** for ^{87}Rb-^{87}Rb scattering in the hyperfine spin state $|22\rangle|22\rangle$. Inset is an enlargement of the i-wave scattering resonance; the black curve is a fit to Eq. (2.101a) with $\Gamma = 0.47$ μK and $\delta_{\rm bg} = 0.0192$.

dipole-dipole interaction for simplicity (Eq. (2.131)). ^{87}Rb has shape resonances in both the d ($\ell = 2$) and i ($\ell = 6$) partial waves.[14] Note, however, that the d-wave shape resonance

[14] That these shape resonances are separated by $\Delta\ell = 4$ is a consequence of an approximate $\Delta\ell = 4$ periodicity in the bound state energies of the asymptotic van der Waals potential[69].

does not change the phase from 0 to π; this reduction occurs because of variations in the background phase shift at a similar rate. The i-wave shape resonance, however, is narrow enough that the background phase shift does not change appreciably over the width of the resonance, so the phase shift here does change from 0 to π. It is well described by a Beutler-Fano profile given by Eq. (2.101a).

The above discussion applies to the single-channel problem and hence to shape resonances, but it does not necessarily apply to Feshbach resonances and the multichannel problem. To that end, I will consider the case of a single isolated Feshbach resonance as shown in Fig. 2.4b where the closed channel supports a single bound state at energy E_0 in the absence of coupling between the open and closed channel.[15] Let $V_1(r)$ and $V_2(r)$ be the potentials for channels 1 and 2, respectively, which also contain the centrifugal potential. The radial coupled channel equations are

$$\left[-\frac{\hbar^2}{2m}\partial_r^2 + V_1(r)\right] u_1(r) + V_{12}(r)u_2(r) = Eu_1(r) \tag{2.102a}$$

$$\left[-\frac{\hbar^2}{2m}\partial_r^2 + V_2(r)\right] u_2(r) + V_{21}(r)u_1(r) = Eu_2(r) \tag{2.102b}$$

where $V_{12}(r) = V_{21}^*(r)$ are the coupling potentials. I assume that $\lim_{r\to\infty} V_{12}(r) = 0$ and $\lim_{r\to\infty} V_i(r) = E_i$ where E_i are the channel thresholds. I also assume that $E_1 < E < E_2$. The existence of a bound state at energy E_0 in the absence of coupling means that

$$\left[-\frac{\hbar^2}{2m}\partial_r^2 + V_2(r)\right] u_0(r) = E_0 u_0(r) \tag{2.103}$$

where I assume that $\langle u_0|u_0\rangle = 1$; i.e., $u_0(r)$ is normalized to unity. Suppose that the channel function $u_2(r)$ is restricted to be a multiple of u_0. The vector of solutions for Eqs. (2.102a) and (2.102b) is then

$$\mathbf{u}(r) = \begin{pmatrix} u_1(r) \\ Au_0(r) \end{pmatrix}.$$

I can simplify Eq. (2.102b) using Eq. (2.103)

$$V_{21}(r)u_1(r) = A(E - E_0)u_0(r), \tag{2.104}$$

so that Eq. (2.102a) can be written as the inhomogeneous differential equation

$$\left[E + \frac{\hbar^2}{2m}\partial_r^2 - V_1(r)\right] u_1(r) = AV_{12}(r)u_0(r). \tag{2.105}$$

I can solve Eq. (2.105) by defining the Green's function

$$\left[E + \frac{\hbar^2}{2m}\partial_r^2 - V_1(r)\right] G(r, r') = \delta(r - r') \tag{2.106}$$

where the Green's function $G(r, r')$ has the important properties:

[15] This section borrows heavily from [54].

1. $G(r, r')$ is continuous in r, r'.

2. $G(r, r')$ satisfies the boundary conditions, namely that $G(0, r') = 0$ and $G(r, r')$ approaches the free-particle solution as $r \to \infty$.

3. $G(r, r') = G(r', r)$.

$G(r, r')$ must be comprised of the regular and irregular solutions of the homogeneous part of Eq. (2.106) when $r \neq r'$ as $\delta(r - r') = 0$. Defining the regular and irregular solutions by their asymptotic behaviour as

$$u_1^{\text{reg}}(r) \overset{r\to\infty}{\sim} \sqrt{\frac{2m}{\pi\hbar^2 k}} \sin(kr - \ell\frac{\pi}{2} + \delta_{\text{bg}}) \tag{2.107a}$$

$$u_1^{\text{irr}}(r) \overset{r\to\infty}{\sim} \sqrt{\frac{2m}{\pi\hbar^2 k}} \cos(kr - \ell\frac{\pi}{2} + \delta_{\text{bg}}) \tag{2.107b}$$

it is straightforward to use Eq. (2.106) and additional properties to show that the Green's function must be

$$G(r, r') = -\pi \begin{cases} u_1^{\text{reg}}(r) u_1^{\text{irr}}(r'), & r < r' \\ u_1^{\text{reg}}(r') u_1^{\text{irr}}(r), & r > r' \end{cases} \tag{2.108}$$

where the overall constant factor $-\pi$ can be found by integrating Eq. (2.106) in a small region around $r = r'$. The solution to Eq. (2.102a) is then

$$u_1(r) = u_1^{\text{reg}}(r) + A \int_0^\infty G(r, r') V_{12}(r') u_0(r') dr' \tag{2.109a}$$

$$\overset{r\to\infty}{\sim} u_1^{\text{reg}}(r) - \pi A \langle u_1^{\text{reg}} | \hat{V}_{12} | u_0 \rangle u_1^{\text{irr}}(r) \tag{2.109b}$$

where the second line follows because I assume that $V_{12}(r)$ decays to zero as $r \to \infty$. One can clearly see that the prefactor $-\pi A \langle u_1^{\text{reg}} | \hat{V}_{12} | u_0 \rangle$ plays the role of the K matrix element from Eq. (2.57). The K matrix is related to the tangent of the scattering phase shift, so I define a resonant phase shift as

$$\tan \delta_{\text{res}} = -\pi A \langle u_1^{\text{reg}} | \hat{V}_{12} | u_0 \rangle \tag{2.110}$$

where the total phase shift acquired by the wave is $\delta = \delta_{\text{bg}} + \delta_{\text{res}}$. The amplitude A is found by taking Eq. (2.109b) and substituting it into Eq. (2.104) to get

$$A(E - E_0) u_0(r) = V_{21} u_1^{\text{reg}}(r) + A V_{12}(r) \int_0^\infty G(r, r') V_{12}(r') u_0(r') dr'.$$

Taking the inner product of the above with $\langle u_0 |$ and solving for A I get that

$$A = \frac{\langle u_0 | \hat{V}_{21} | u_1^{\text{reg}} \rangle}{E - E_0 - \langle u_0 | \hat{V}_{21} \hat{G} \hat{V}_{21}^\dagger | u_0 \rangle}$$

and the resonant phase must be

$$\begin{aligned}\tan\delta_{\rm res} &= -\frac{\pi|\langle u_0|\hat{V}_{21}|u_1^{\rm reg}\rangle|^2}{E-E_0-\langle u_0|\hat{V}_{21}\hat{G}\hat{V}_{21}^\dagger|u_0\rangle}\\ &= -\frac{\Gamma(E)/2}{E-E_0-\delta E(E)}\end{aligned} \tag{2.111}$$

which has the same form as for the single channel shape resonance in Eq. (2.100). The key differences here are that Γ is a function of energy, and one sees explicitly that the resonance energy E_R is shifted from that of the "true" bound state E_0 by an amount $\delta E(E)$, which itself depends on the energy. Using the threshold behaviour of the regular solution from Eq. (2.28) and the normalization in Eq. (2.107a) the threshold behaviour of Γ is

$$\Gamma(E) = 2\pi|\langle u_0|\hat{V}_{21}|u_1^{\rm reg}\rangle|^2 \propto k^{2\ell+1} \propto E^{\ell+1/2} \tag{2.112}$$

which is a similar energy dependence as for the scattering phase shifts near threshold. At high energies the width becomes energy-independent[70].

What about the more general situation, applicable to alkali metal atoms, where there are many possible open channels to which the quasi-bound state can decay? I start from the description of a resonance as a pole in the complex energy Eq. (2.99) and rewrite it as[54, 55]

$$S = S_{\rm bg}S_{\rm res} = S_{\rm bg}\left[1-\frac{iA}{E-E_R+i\Gamma/2}\right]. \tag{2.113}$$

If I have a multichannel system, then if I replace $S_{\rm bg}$ and A with matrices/operators I have the most general description of a simple, isolated pole. Unitarity of S implies that $S_{\rm bg}$ must be unitary and also that

$$i(E-E_R)(\hat{A}^\dagger-\hat{A}) - (\hat{A}+\hat{A}^\dagger)\frac{\Gamma}{2} + \hat{A}^\dagger\hat{A} = 0.$$

Since I have assumed that there is only a simple, isolated pole, then neither $\hat{A}$ or $\hat{A}^\dagger$ can have a pole, so the only way for the above to be equal to zero for all E is for $A = A^\dagger$ which implies that

$$\hat{A}^2 = \Gamma\hat{A}. \tag{2.114}$$

If I define an operator $\hat{B} = \Gamma^{-1}\hat{A}$ then I have instead that

$$\hat{B}^2 = \hat{B};$$

i.e., $\hat{B}$ is a projection operator. Not only is it a projection operator, but for an isolated, non-degenerate quasi-bound state at E_R it must also have rank 1[55] which means that for some normalized vector $|b\rangle$ it can be written as

$$\hat{B} = |b\rangle\langle b|.$$

The reasoning is as follows: suppose we have an initial state which is the bound state wavefunction and let it evolve. It will decay into a single, unique superposition of open-channel wavefunctions. It is reasonable to assume that the projection operator $\hat{B}$ will project our incoming open-channel wavefunction onto this unique superposition of outgoing waves, implying that it must have the form of the above[54]. As a result, I know that

$$B_{nm} = \langle n|\hat{B}|m\rangle = \langle n|b\rangle\langle b|m\rangle = b_n b_m^*, \qquad \sum_n |b_n|^2 = 1.$$

The elements of the scattering matrix can thus be written as

$$S_{nm} = S_{\mathrm{bg},nm} - \frac{i c_n b_m^* \Gamma}{E - E_R + i\Gamma/2} \tag{2.115}$$

where $|c\rangle = S_{\mathrm{bg}}|b\rangle$ and $\sum_n |c_n|^2 = 1$. The quantity $|b_n|^2$ is known as the branching ratio for entering the resonance from channel n, and $|c_n|^2$ is the branching ratio for leaving the resonance by channel n.

Suppose that the background scattering is purely elastic with $S_{\mathrm{bg},nm} = e^{2i\delta_n}\delta_{nm}$ and $c_n = e^{2i\delta_n} b_n$. If I consider only a single partial wave the inelastic cross section is

$$\sigma_{\mathrm{inel}} = \frac{\pi}{k_n^2}\left(1 - |S_{nn}|^2\right) \tag{2.116}$$

where n is the entrance channel.[16] Since $|S_{\mathrm{bg},nn}| = 1$, I can write that

$$1 - |S_{nn}|^2 = \frac{\Gamma^2 |b_n|^2 (1 - |b_n|^2)}{(E - E_R)^2 + \Gamma^2/4} \tag{2.117}$$

which is a Breit-Wigner curve as a function of E. If there is only one open channel then $|b_n| = 1$, so there is no inelastic loss and the elastic cross section follows Eq. (2.101b). If instead there are other open channels, and in particular if the branching ratios to those channels are non-zero, then one can have resonant inelastic loss to those channels.

A last comment on the widths. If I define the partial widths $\Gamma_n = \Gamma|b_n|^2$, then each Γ_n will depend on a matrix element similar to Eq. (2.112) where the $|u_i^{\mathrm{reg}}\rangle$ is replaced with $|u_n^{\mathrm{reg}}\rangle$. As a result, each partial width will have the same energy dependence near their respective channel thresholds. Open channels whose thresholds are well below that of the entrance channel, as in Fig. 2.6, will have partial widths that are nearly energy-independent when the energy is near the threshold of the entrance channel as long as E_{open} is large compared to E since $\Gamma(E + E_{\mathrm{open}}) \approx \Gamma(E_{\mathrm{open}})$. The partial width associated with elastic scattering will still have the energy dependence of Eq. (2.112).

As an example, I have plotted in Fig. 2.7 $|T_{nm}|^2$ for two different Feshbach resonances in ^{87}Rb. In Fig. 2.7a, the ^{87}Rb absolute ground state is both atoms in the $|1,1\rangle$ state, so there are no other open channels to which the quasi-bound state can decay, and only the

[16] Eq. (2.116) is a consequence of Eq. (2.81).

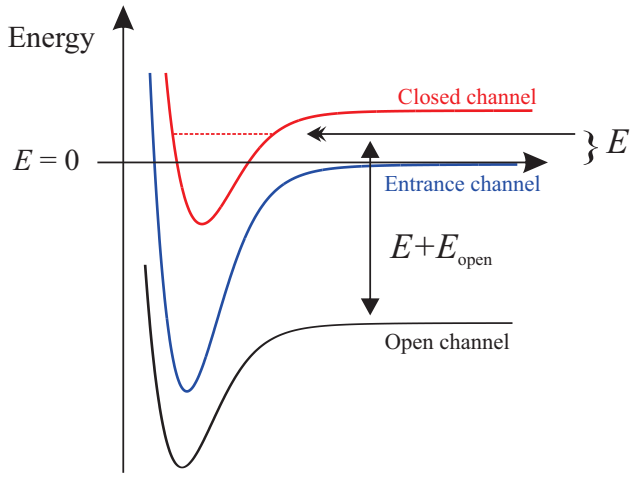

Figure 2.6: Potential energy curves for a Feshbach resonance with an additional open channel.

elastic element of the $\hat{T}$-operator is non-zero. This resonance is well-described by the simple asymmetric Beutler-Fano profile of Eq. (2.101b). In contrast, the resonance in the $|1,1\rangle|2,0\rangle$ state at 9.05 G has many open channels to which it can decay, some of which have different values of ℓ due to dipole-dipole coupling (Eq. (2.133)). Regardless, the inelastic curves are well-described by Lorentzian lineshapes.

To close out this section on resonances, let me relate the behaviour of the $\hat{S}$ operator derived above to standard expressions for the s-wave scattering length a near a Feshbach resonance[63]. From Eq. (2.57) I can express the $\hat{K}$ operator in terms of $\hat{S}$ as

$$\hat{K} = i(1-\hat{S})(1+\hat{S})^{-1}.$$

Recalling that for the single-channel problem at threshold $K = \tan\delta \overset{k\to 0}{=} -ak$ I define the scattering length for the multichannel problem as[71]

$$a(k) = \frac{1}{ik_n}\frac{1-S_{nn}}{1+S_{nn}} \tag{2.118}$$

where a is, in general, complex. Using $S_{\mathrm{bg},nn} = e^{2i\delta_n} \approx 1 + 2i\delta_n = 1 - 2ik_n a_{\mathrm{bg}}$ for real δ_n one can show that in the limit of $k_n \to 0$ ($E \to 0$),

$$a = a_{\mathrm{bg}}\left(1 + \frac{\gamma_n}{-E_R + i\Gamma/2}\right) \tag{2.119a}$$

$$= a_{\mathrm{bg}}\left(1 - \frac{\gamma_n E_R}{E_R^2 + \Gamma^2/4} - \frac{i\gamma_n\Gamma/2}{E_R^2+\Gamma^2/4}\right) \tag{2.119b}$$

where $\gamma_n = \Gamma_n/(2k_n a_{\mathrm{bg}})$ is a reduced resonance width. Note that Γ is the total resonance width, and as $k_n \to 0$ the elastic contribution $\Gamma_n \to 0$ leaving only the inelastic contributions. Calculating the elastic cross section one gets

$$\sigma_{nn} = 4\pi|a|^2 = 4\pi a_{\mathrm{bg}}^2\left(1 - \frac{\gamma_n E_R}{E_R^2+\Gamma^2/4}\right)^2 + \frac{4\pi a_{\mathrm{bg}}^2\gamma_n^2\Gamma^2/4}{(E_R^2+\Gamma^2/4)^2} \tag{2.120}$$

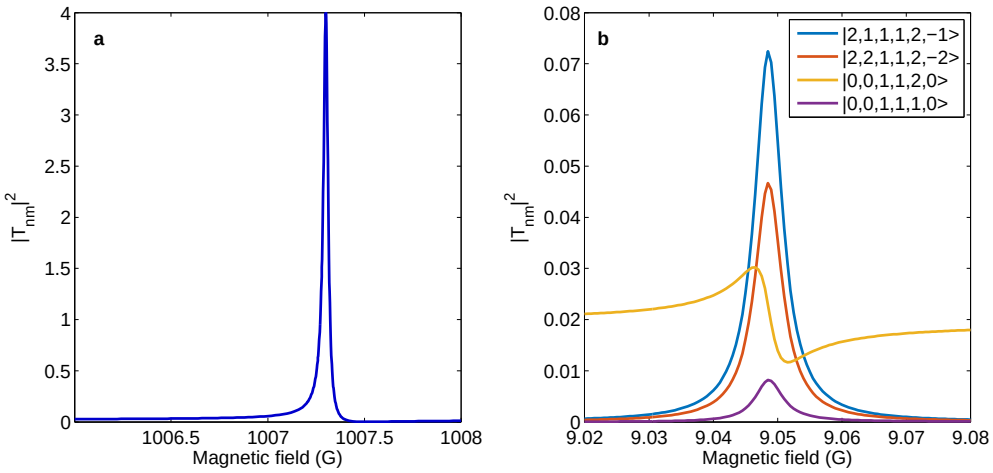

Figure 2.7: Feshbach resonances in ^{87}Rb as a function of magnetic field at a collision energy of 1 μK. **a** Resonance in the $\ell = 0$ and $|1,1\rangle|1,1\rangle$ entrance channel. Only the elastic element of the $\hat{T}$-operator is plotted as there are no other open channels. **b** Resonance in the $\ell = 0$ and $|1,1\rangle|2,0\rangle$ entrance channel. The four channels with the largest $|T_{nm}|^2$ values are plotted and labeled with the notation $|\ell m_\ell f_1 m_{f1} f_2 m_{f2}\rangle$.

whereas the inelastic cross section is obtained from Eq. (2.117) as

$$\sigma_{\text{inel}} = \frac{2\pi}{k_n} \frac{a_{\text{bg}} \gamma_n \Gamma}{E_R^2 + \Gamma^2/4} \tag{2.121}$$

which is proportional to the imaginary part of a. In the event that there is no inelastic loss, so that $\Gamma = \Gamma_n$, the scattering length becomes

$$a = a_{\text{bg}} \left(1 - \frac{\gamma_n}{E_R}\right) \tag{2.122}$$

which is the standard form for the scattering length near a Feshbach resonance in the absence of inelastic channels. One advantage of using the complex scattering length is that it appears in the expression for the mean-field interaction energy of degenerate quantum gases described by the Gross-Pitaevskii equation. The imaginary part causes a decay of the total number of atoms in time in accordance with two-body loss as described by the inelastic cross section Eq. (2.121).

2.6 Collisions of alkali metal atoms

Alkali metal atoms are perhaps the simplest atoms to describe. They have one valence electron, which means that those electrons occupy hydrogen-like orbitals. High precision values for atomic parameters exist, and one can calculate scattering properties of these atoms to high accuracy. As this thesis is concerned with the collisions of ^{87}Rb and ^{40}K, both alkali metal atoms, I will lay out the relevant Hamiltonian.

The first piece of the Hamiltonian that I need is the internal part, $\hat{H}_{\rm int}$. While the internal energy of each particle is governed by the electron-nucleus and electron-electron Coulomb force and various perturbations to these, I will consider only collisions between atoms in states with the lowest principal quantum number and angular momentum. As long as the collision energy is low enough, it is a good approximation to ignore other degrees of freedom and focus only on the ground state. For alkali metal atoms experiencing no external magnetic field, the ground state is perturbed by the hyperfine interaction

$$\hat{H}_{\rm hf} = a\hat{\mathbf{I}}\cdot\hat{\mathbf{S}}, \tag{2.123}$$

which arises from the contact term of the dipole-dipole interaction between the electron and the nucleus. By coupling the nuclear spin $\hat{\mathbf{I}}$ and the electron spin $\hat{\mathbf{S}}$ to form the total angular momentum $\hat{\mathbf{F}} = \hat{\mathbf{S}} + \hat{\mathbf{I}}$, I can write the hyperfine interaction as

$$\hat{H}_{\rm hf} = \frac{a}{2}\left(\hat{\mathbf{F}}^2 - \hat{\mathbf{S}}^2 - \hat{\mathbf{I}}^2\right) \tag{2.124}$$

which shows that the angular momentum eigenstates of $\hat{\mathbf{F}}^2$ and $\hat{F}_z$, labeled by $|f, m_f\rangle$, are eigenstates of $\hat{H}_{\rm hf}$. The total angular momentum can take the two values of $f = i \pm 1/2$, so the ground state of the alkali atom is split into two manifolds each with degeneracy of $2f + 1$, corresponding to the different values of $m_f = m_i + m_s$. The energy difference between the two states is $E_{\rm hfs} = a(i + 1/2)$. To extend to two alkali atoms, I simply add their internal energies

$$\hat{H}_{\rm hf} = a_1\hat{\mathbf{I}}_1\cdot\hat{\mathbf{S}}_1 + a_2\hat{\mathbf{I}}_2\cdot\hat{\mathbf{S}}_2 \tag{2.125}$$

where I have assumed that the atoms are not the same species. Symmetries prove to be very important in solving coupled channels equations because they allow one to restrict the solution to smaller subspaces of interest, so let us consider what symmetries Eq. (2.125) has. $\hat{H}_{\rm hf}$ commutes with $\hat{\mathbf{F}}_1$ and $\hat{\mathbf{F}}_2$ separately, and thus with their sum $\hat{\mathbf{F}} = \hat{\mathbf{F}}_1 + \hat{\mathbf{F}}_2$. Therefore, f_1, f_2, m_{f_1} and m_{f_2} are all separately conserved. $\hat{H}_{\rm hf}$ is an example of a scalar operator: it commutes with the total angular momentum of the system and its matrix elements are thus unchanged upon global rotations[57].

Adding an external magnetic field $\mathbf{B} = B\hat{\mathbf{z}}$ along the z-axis adds the following Hamiltonian to the system

$$\begin{aligned}\hat{H}_B &= g_S\mu_B\mathbf{B}\cdot(\hat{\mathbf{S}}_1 + \hat{\mathbf{S}}_2) + g_{I_1}\mu_B\mathbf{B}\cdot\hat{\mathbf{I}}_1 + g_{I_2}\mu_B\mathbf{B}\cdot\hat{\mathbf{I}}_2 \\ &= \left[g_S(\hat{S}_{z1} + \hat{S}_{z2}) + g_{I_1}\hat{I}_{z1} + g_{I_2}\hat{I}_{z2}\right]\mu_B B\end{aligned} \tag{2.126}$$

where μ_B is the Bohr magneton, g_S is the electron g-factor (approximately 2)[17], and the g_I are the nuclear g-factors for the different atoms. $\hat{H}_B$ is an example of a vector operator

[17] For simplicity I have used g_S, but it is more correct to use the ground-state g_J values here for each atom.

because it does not commute with the total angular momentum: its matrix elements change depending on the choice of quantization axis. Therefore, $\hat{\mathbf{F}}_1$, $\hat{\mathbf{F}}_2$, and $\hat{\mathbf{F}}$ do not commute with $\hat{H}_B$ (as can be easily seen) although their projections along the z-axis do. Therefore, the quantities $m_{s(1,2)}$ and $m_{i(1,2)}$ are separately conserved.

Combining the two contributions $H_{\rm hf}$ and H_B, we get the total internal Hamiltonian

$$\hat{H}_{\rm int} = a_1 \hat{\mathbf{I}}_1 \cdot \hat{\mathbf{S}}_1 + a_2 \hat{\mathbf{I}}_2 \cdot \hat{\mathbf{S}}_2 + \left[g_S (\hat{S}_{z1} + \hat{S}_{z2}) + g_{I_1} \hat{I}_{z1} + g_{I_2} \hat{I}_{z2} \right] \mu_B B. \tag{2.127}$$

This Hamiltonian conserves neither the total angular momentum nor the individual projections. It does, however, commute with $\hat{F}_{z(1,2)}$, so the individual quantum numbers $m_{f(1,2)} = m_{s(1,2)} + m_{i(1,2)}$ and the total spin projection $m_f = m_{f1} + m_{f2}$ remain good quantum numbers. The application of a magnetic field evidently mixes states of different $f_{1,2}$ that have the same $m_{f(1,2)}$.

Now that the internal Hamiltonian has been dealt with, let us move to the interaction Hamiltonian of the two atoms. The interaction of the two atoms is dominated by their valence electrons, and therefore the combined spin state of these spin 1/2 fermions matters. If the valence electrons are in the singlet state, then their spatial wavefunction must be symmetric and the electrons can be found in between the two atoms, leading to a strong covalent bond. On the other hand, if the electrons are in the triplet state then the wavefunction must be anti-symmetric, and the resulting bond will be much weaker. Based on symmetry alone the interaction potential must depend on the magnitude of the total spin $\mathbf{S} = \mathbf{S}_1 + \mathbf{S}_2$. Let $V_1(r)$ be the potential for the triplet state with $s = 1$ and $V_0(r)$ be the potential for the singlet state with $s = 0$ in the Born-Oppenheimer (BO) approximation; the potential operator which projects out the appropriate potential for an arbitrary spin state is

$$\begin{aligned} \hat{V}(r) &= \frac{1}{4}\left[3V_1(r) + V_0(r)\right] + \left[V_1(r) - V_0(r)\right] \hat{\mathbf{S}}_1 \cdot \hat{\mathbf{S}}_2 \\ &= V_D(r) + J(r) \hat{\mathbf{S}}_1 \cdot \hat{\mathbf{S}}_2 \end{aligned} \tag{2.128}$$

where $V_D(r)$ is referred to as the direct potential and $J(r)$ the exchange potential. This potential energy operator commutes with the total spin $\hat{\mathbf{S}}$, and hence conserves both the total spin quantum number s and the spin projection $m_s = m_{s1} + m_{s2}$.

High-precision parametrization of the singlet and triplet potentials can be obtained from photo-association spectroscopy, and the potentials for ^{40}K^{87}Rb obtained in this manner are shown in Fig. 2.8[72]. These potentials are typically separated into three regions: inner, intermediate, and outer. The inner region contains the part of the interaction that represents the repulsive core of the potential and is parametrized using an inverse power law with exponent from 4-6. The intermediate region contains the actual potential well and is parametrized using a power series in a non-linear variable. The outer region is dominated by the long-range dispersion forces from induced multipole moments, typically expressed

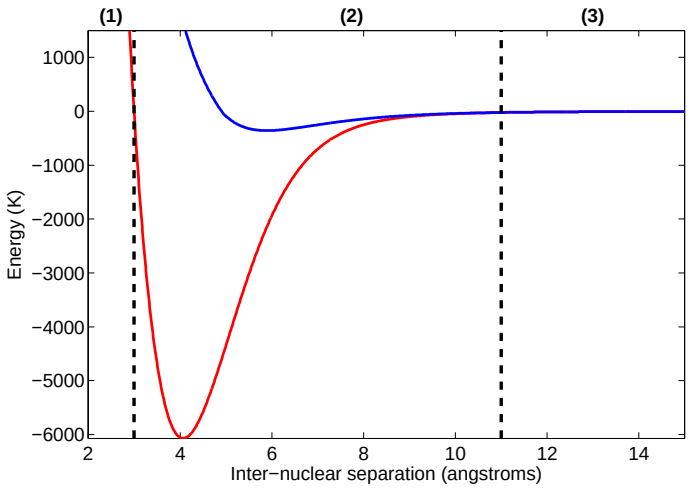

Figure 2.8: Plot of the KRb Born-Oppenheimer potentials for the spin singlet (red) and triplet (blue) states. Vertical black dashed lines delineate the inner **(1)**, intermediate **(2)**, and outer **(3)** regions for the singlet potential.

as a power series

$$V_{\mathrm{LR}}(r) = -\frac{C_6}{r^6} - \frac{C_8}{r^8} - \frac{C_{10}}{r^{10}} \pm E_{\mathrm{exch}}(r) \tag{2.129}$$

where the r^{-6} term is the typical van der Waals interaction. While the van der Waals interaction arises from induced dipole-dipole coupling, the higher powers arise from dipole-quadrupole, dipole-octopole and quadrupole-quadrupole coupling[60, 73]. The exchange term, $E_{\mathrm{exch}}(r)$, is an exponentially decaying term that accounts for the difference in the potential due to the spins being in the singlet (negative sign) or triplet (positive sign) state[72, 74, 75]. As ultracold collisions and Feshbach resonances are most sensitive to the last bound state in a potential, the shape of the long-range tail of the potential has a significant impact on the location and strengths of resonant features.

Let us now combine all the terms with the centrifugal term to get the total potential energy for the system:

$$\begin{aligned}\hat{H} &= \hat{H}_{\mathrm{hf}} + \hat{H}_B + \hat{V}(r) + \hat{H}_{\mathrm{cent}} \\ &= a_1 \hat{\mathbf{I}}_1 \cdot \hat{\mathbf{S}}_1 + a_2 \hat{\mathbf{I}}_2 \cdot \hat{\mathbf{S}}_2 + \left[g_S(\hat{S}_{z1} + \hat{S}_{z2}) + g_{I_1} \hat{I}_{z1} + g_{I_2} \hat{I}_{z2} \right] \mu_B B \\ &\qquad + V_D(r) + J(r) \hat{\mathbf{S}}_1 \cdot \hat{\mathbf{S}}_2 + \frac{\hbar^2}{2mr^2} \hat{\mathbf{L}}^2. \end{aligned} \tag{2.130}$$

First, consider the symmetries of Eq. (2.130) when $B = 0$. By judicious use of the associative property, one can show that $[\hat{H}, \hat{\mathbf{F}}] = 0$, which means that both the total internal angular momentum f and its projection m_f are conserved quantities. Such a symmetry makes solving of the coupled channels equations easier as one can break the set of equations down into blocks with the same f and m_f and solve them independently. If $B \neq 0$, then $\hat{H}$ no longer commutes with all components of $\hat{\mathbf{F}}$, but it still commutes with $\hat{F}_z$, so m_f remains a good

quantum number. This is a far more typical situation than collisions without a magnetic field, especially as Feshbach resonances are typically accessed by tuning external magnetic fields. The solution of the coupled channels equations is slightly more time-consuming because now one can only restrict the subspace of states to those with the same m_f but not the same f. Note that $\hat{H}$ commutes with $\hat{\mathbf{L}}$, so ℓ and m_ℓ are conserved separately to the internal degrees of freedom. Therefore, one can separately solve for not only each partial wave, but each component of each partial wave, which significantly reduces computing time.

Equation (2.130) is the leading contribution to the potential energy. Depending on the situation, next order corrections can be included. The most important next order correction, especially for $\ell \neq 0$ partial waves, is the magnetic dipole-dipole interaction between the valence electrons. The electrons have magnetic dipole moments of $\hat{\boldsymbol{\mu}}_{1,2} = g_S \mu_B \hat{\mathbf{S}}_{1,2}$, which means that their interaction energy is[57]

$$\begin{aligned}\hat{V}_{dd}(\mathbf{r}) &= \frac{\mu_0}{4\pi r^3}[\hat{\boldsymbol{\mu}}_1 \cdot \hat{\boldsymbol{\mu}}_2 - 3(\hat{\boldsymbol{\mu}}_1 \cdot \hat{\mathbf{r}})(\hat{\boldsymbol{\mu}}_2 \cdot \hat{\mathbf{r}})] \\ &= \frac{\mu_0 (g_S \mu_B)^2}{4\pi r^3}[\hat{\mathbf{S}}_1 \cdot \hat{\mathbf{S}}_2 - 3(\hat{\mathbf{S}}_1 \cdot \hat{\mathbf{r}})(\hat{\mathbf{S}}_2 \cdot \hat{\mathbf{r}})] \end{aligned} \tag{2.131}$$

where μ_0 is the permeability of free space, $\mu_0 = 4\pi \times 10^{-7}$ NA^{-2}. Unlike the other contributions to the energy that I have described, Eq. (2.131) depends explicitly on the spatial orientation, so one should expect that it does not preserve ℓ or m_ℓ. By writing both the spin components and the position components in the spherical basis $\hat{\mathbf{e}}_\pm = (\hat{\mathbf{x}} \pm i\hat{\mathbf{y}})/\sqrt{2}$ and $\hat{\mathbf{e}}_0 = \hat{\mathbf{z}}$, one can show that

$$\hat{V}_{dd}(\mathbf{r}) = \frac{\mu_0 (g_S \mu_B)^2}{4\pi r^3} \sum_{q=-2}^{2} \hat{T}_q(\hat{\mathbf{r}}) \tag{2.132}$$

where

$$\begin{aligned}\hat{T}_0 &= 4\sqrt{\frac{\pi}{5}} Y_2^0(\hat{\mathbf{r}}) \left[\hat{S}_{1z}\hat{S}_{2z} - \frac{1}{4}(\hat{S}_{1+}\hat{S}_{2-} + \hat{S}_{1-}\hat{S}_{2+})\right] \\ \hat{T}_{\pm 1} &= \mp 3\sqrt{\frac{2\pi}{15}} Y_2^{\pm 1}(\hat{\mathbf{r}}) \left[\hat{S}_{1z}\hat{S}_{2\mp} + \hat{S}_{1\mp}\hat{S}_{2z}\right] \\ \hat{T}_{\pm 2} &= 3\sqrt{\frac{2\pi}{15}} Y_2^{\pm 2}(\hat{\mathbf{r}}) \left[\hat{S}_{1\mp}\hat{S}_{2\mp}\right]. \end{aligned} \tag{2.133}$$

One can see that the terms $\hat{T}_q$ conserve the z-projection of the total angular momentum $\hat{\mathbf{F}} + \hat{\mathbf{L}}$. Additionally, I can compute the matrix element $\langle \ell_f m_f | Y_\ell^q(\hat{\mathbf{r}}) | \ell_i m_i \rangle$ to get[57]

$$\begin{aligned}\langle \ell_f m_f | Y_\ell^q(\hat{\mathbf{r}}) | \ell_i m_i \rangle &= \int (Y_{\ell_f}^{m_f})^*(\hat{\mathbf{r}}) Y_\ell^q(\hat{\mathbf{r}}) Y_{\ell_i}^{m_i}(\hat{\mathbf{r}}) d\Omega \\ &= \sqrt{\frac{(2\ell+1)(2\ell_i+1)}{4\pi(2\ell_f+1)}} \langle \ell_i \ell 00 | \ell_f 0 \rangle \langle \ell_i \ell m_i q | \ell_f m_f \rangle \end{aligned} \tag{2.134}$$

which says that, for $\ell = 2$, **(a)** the dipole-dipole interaction has no effect on $\ell_i = \ell_f = 0$ states, and **(b)** only states with $\ell_f - \ell_i = \pm 2$ and $\ell_f = \ell_i > 0$ are connected. The dipole-dipole interaction is a significant complication in that it makes the number of states that have to be simultaneously solved for unbounded, although in practice one only needs to include the states $|\ell_f - \ell_i| = 2$ and not those of higher order.[18] It also allows for transitions between states of different m_f by changing the value of m_ℓ, which is the origin of so-called "dipolar relaxation" of maximum spin states like $|22\rangle$ in ^{87}Rb to lower internal angular momentum states[76, 77].

Other contributions to the potential energy depend on what was included in the parametrization of the BO potentials; depending on the atomic species, different effects have different strengths. Spatial variation of the hyperfine constants due to perturbation of the core electrons can be included[74], as well as second-order spin coupling[74, 72] (which adds an extra r-dependence to Eq. (2.132)), or retardation effects yielding spatially varying dispersion constants[74]. As the location of Feshbach resonances are quite sensitive to the details of the potential (especially the long-range part), any coupled-channels solver must include all effects included in the parametrization of the BO potentials.[19]

2.7 Coupled-channels solver

At first glance, it might seem that the most difficult part about solving for the multichannel S-matrix is solving Eq. (2.53) numerically. In fact, due to a great deal of research on various different types of numerical integrators, this step is almost trivial. The difficult part of solving for S is book-keeping: transforming between different basis sets and keeping track of states. In this section, I will outline the function of the coupled-channels solver for alkali metal atoms that I wrote in the MATLAB programming language. I have summarized the steps of the solver in Fig. 2.9.

The first step is defining the basis sets used in the calculation. As it is much easier to calculate operator matrix elements in the basis in which the operators are diagonal, I use more basis sets than are strictly necessary for the actual integration. For instance, the hyperfine Hamiltonian Eq. (2.125) is most easily defined using the $|\ell m_\ell f_1 m_{f1} f_2 m_{f2}\rangle$ basis.[20] Calculating the matrix elements of the BO potential is best performed in the basis where the electron spins are coupled, which is $|\ell m_\ell s m_s m_{i1} m_{i2}\rangle$. Both the dipole-dipole

[18] For highly magnetic atoms, such as chromium or erbium, more orders would need to be included.

[19] In the case of the Rb potentials in [74], the authors neglected to mention that they include retardation corrections from [60] in their long-range potential. These must be included to accurately predict the location of Feshbach resonances.

[20] As electronic and nuclear total spins $s_{1,2}$ and $i_{1,2}$ do not change during collisions, it suffices to specify basis vectors by six labels only, so I drop the individual electronic and nuclear spin labels.

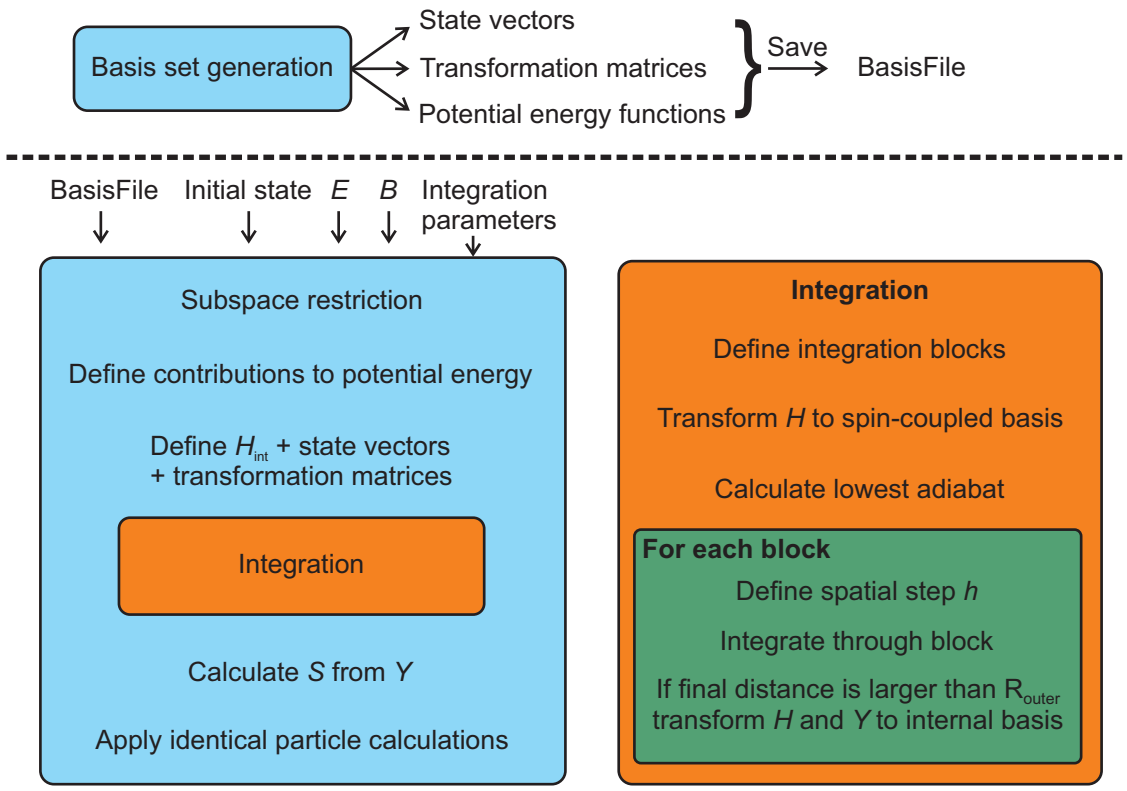

Figure 2.9: Flowchart outlining the different steps in solving the coupled channels equations. Y is the matrix of log-derivatives defined in Eq. (2.137).

interaction and the energy shift due to the magnetic field are most conveniently calculated in the fully uncoupled basis $|\ell m_\ell m_{s1} m_{i1} m_{s2} m_{i2}\rangle$. Finally, there is what I call the "internal" basis, which is the basis that diagonalizes Eq. (2.127). Asymptotic states are eigenstates of Eq. (2.127), and collision energies must be referenced to the eigen-energies of these states. I label these states as $|\ell m_\ell a b\rangle$ where a and b each start at 1 for the lowest energy state and increase to a maximum of $(2s_n + 1)(2i_n + 1)$, the total number of states for atom n.

Obviously one must be able to transform easily between these basis sets, and the liberal application of Clebsch-Gordan coefficients is especially useful. Elements of the transformation matrices B are defined as

$$B_{\alpha_i \beta_j} = \langle \alpha_i | \beta_j \rangle$$

where $|\alpha_i\rangle$ and $|\beta_j\rangle$ stand for vectors i or j in basis sets α or β, respectively. For one step of coupling, such as coupling individual electronic spins to total spin, the elements of B are just Clebsch-Gordan coefficients:

$$B_{\alpha_i \beta_j} = \langle s m_s |_i | m_{s1} m_{s2} \rangle_j .$$

More complicated transformations, such as from the spin-coupled basis to the internal basis, can be achieved by multiplying the relevant B matrices together. All of these transformations (with the exception of those to the internal basis, more on that later) and basis sets can be calculated in advance, and as there can be a lot of states, it pays to store them in a file and load them as necessary instead of re-calculating them every time one solves the coupled-channel equations.

The next step, once the basis sets are defined and their respective transformations are calculated, is to restrict the calculation to the subspace that is coupled to the incoming state. This is a critical step, as the number of possible channels otherwise becomes unmanageably large: ^{40}K-^{40}K s-wave collisions involve 324 channels, and this number rapidly grows for higher ℓ. The extent to which the full Hilbert space can be restricted depends on the Hamiltonian and its symmetries. In the absence of dipole-dipole coupling and a magnetic field, the Hamiltonian in Eq. (2.130) commutes with $\hat{\mathbf{F}}$ and $\hat{\mathbf{L}}$, which means that only states with the same f, m_f, ℓ, and m_ℓ as the initial state need to be considered. In the presence of a magnetic field but no dipole-dipole coupling $\hat{H}$ commutes with $\hat{F}_z$ and $\hat{\mathbf{L}}$, so only states with the same m_f, ℓ, and m_ℓ as the initial state need to be considered. Lastly, if dipole-dipole coupling is included, then all channels with the same $m_f + m_\ell$ and same parity (even or odd ℓ) as the initial channel need to be considered.

The different contributions to the potential in Eq. (2.130) are first defined within the most convenient basis in the restricted subspace before being transformed into the basis used for calculation. At this point, it is necessary to construct the transformation matrix between the internal basis and the uncoupled basis by numerically solving for the eigenvectors and eigenvalues of Eq. (2.127). Diagonalizing H_{int} cannot be done in advance because the eigenvectors and eigenvalues depend on the magnetic field, which is a parameter and not a constant in the calculation. These values then have to be reconciled with the labeling of the internal states.[21] Using the internal Hamiltonian, one also redefines the zero-point of energy such that the initial state has only kinetic energy.

At this point, much of the book-keeping is done and it is time to start integrating Eq. (2.53). This equation can be recast in the simple-looking matrix ordinary differential equation

$$U''(r) = M(r)U(r) \tag{2.135}$$

where $U(r)$ is the matrix of solutions and $M(r)$ is the coupling matrix whose components are defined as

$$M_{nm}(r) = \left[\frac{2m}{\hbar^2}V_{nm}(r) + \frac{\ell_n(\ell_n+1)}{r^2}\delta_{nm} - k_n^2\delta_{nm}\right] \tag{2.136}$$

[21] On a technical note, the MATLAB eigenvalue function will not produce a unitary transformation matrix for Eq. (2.127), and it is necessary to find the eigenvectors of the internal Hamiltonians for each atom separately before putting them together.

where $k_n^2 = \frac{2m}{\hbar^2}(E - E_n)$ and δ_{nm} is the Kroenecker delta. The difficulty in numerically solving Eq. (2.136) is that if there are closed channels ($k_n^2 < 0$), then the solutions for those channels tend to explode exponentially as the equation is integrated outwards. There are a number of different methods[78] for dealing with this problem, but perhaps the simplest method is the improved log-derivative method of D. E. Manolopoulos[79]. Instead of solving for $U(r)$, one solves for the log-derivative

$$Y(r) = U'(r)U^{-1}(r) \tag{2.137}$$

(note the order of operations) which approaches a constant for exponentially increasing or decreasing functions of r. Of course, this introduces a new problem; namely that the inverse $U^{-1}(r)$ does not exist when the determinant of $U(r)$ vanishes.

I can write down a differential equation for $Y(r)$ by differentiating Eq. (2.137) and using Eq. (2.136) to eliminate the second derivative

$$\begin{aligned}(Y(r)U(r))' = Y'U + YU' &= U'' \\ &= MU \\ Y'(r) &= M(r) - Y^2(r).\end{aligned} \tag{2.138}$$

One solves this equation using invariant imbedding, which works by defining matrices $\mathcal{Y}_n(r', r'')$ on an arbitary interval $[r', r'']$ through

$$\begin{aligned}U'(r') &= -\mathcal{Y}_1(r', r'')U(r') + \mathcal{Y}_2(r', r'')U(r'') \\ U'(r'') &= -\mathcal{Y}_3(r', r'')U(r') + \mathcal{Y}_4(r', r'')U(r'').\end{aligned} \tag{2.139}$$

I right-multiply the first of Eq. (2.139) with $U^{-1}(r')$ and the second with $U^{-1}(r'')$ and use some algebra to eliminate the mixed terms $U(r')U^{-1}(r'')$ and $U(r'')U^{-1}(r')$ to get the recurrence relationship

$$Y(r'') = \mathcal{Y}_4(r', r'') - \mathcal{Y}_3(r', r'')\left[Y(r') + \mathcal{Y}_1(r', r'')\right]^{-1}\mathcal{Y}_2(r', r''). \tag{2.140}$$

As this is a numerical integration, I will divide the total interval into sectors $[a, b]$. In fact, I will divide it further into half-sectors with midpoint $c = (b + a)/2$ and step size $h = (b - a)/2$. The improved log-derivative method then solves the additional homogeneous problem of

$$X''(r) = M_{\text{ref}}(r)X(r) \tag{2.141}$$

for a particular choice of reference potential $M_{\text{ref}}(r)$. I choose a piecewise constant diagonal reference potential

$$(M_{\text{ref}}(r))_{nm} = \delta_{nm}p_n^2 = \delta_{nm}M_{nn}(c) \quad r \in [a, b] \tag{2.142}$$

with p_n^2 equal to the diagonal elements of the coupling matrix $M(r)$ evaluated at the sector midpoint. I then define propagators $y_n(r', r'')$ for the log-derivative of $X(r)$ in the same way as in Eq. (2.139), and by solving the resulting system of equations I derive the propagators

$$y_1(r', r'')_{nm} = y_4(r', r'')_{nm} = \delta_{nm} \begin{cases} |p_n| \coth |p_n| h, & p_n^2 \geq 0 \\ |p_n| \cot |p_n| h, & p_n^2 \leq 0 \end{cases}$$
$$y_2(r', r'')_{nm} = y_3(r', r'')_{nm} = \delta_{nm} \begin{cases} |p_n| \operatorname{csch} |p_n| h, & p_n^2 \geq 0 \\ |p_n| \csc |p_n| h, & p_n^2 \leq 0 \end{cases}. \tag{2.143}$$

Finally, I define the residual coupling matrix

$$\tilde{M}(r) = M(r) - M_{\text{ref}}(r) \tag{2.144}$$

and I calculate corrections to the above propagators ("quadratures") from a modified Simpson's rule

$$\begin{aligned} Q(a) &= \frac{h}{3} \tilde{M}(a) \\ Q(c) &= \frac{4}{h} \left[1 - \frac{h^2}{6} \tilde{M}(c) \right]^{-1} - \frac{4}{h} \\ Q(b) &= \frac{h}{3} \tilde{M}(b). \end{aligned} \tag{2.145}$$

Using these, I construct so-called "effective" half-sector propagators

$$\begin{aligned} \hat{\mathcal{Y}}_1(r', r'') &= y_1(r', r'') + Q(r') \\ \hat{\mathcal{Y}}_2(r', r'') &= y_2(r', r'') \\ \hat{\mathcal{Y}}_3(r', r'') &= y_3(r', r'') \\ \hat{\mathcal{Y}}_4(r', r'') &= y_4(r', r'') + Q(r'') \end{aligned} \tag{2.146}$$

which have to be applied twice using the effective recurrence relation

$$\hat{Y}(r'') = \hat{\mathcal{Y}}_4(r', r'') - \hat{\mathcal{Y}}_3(r', r'') \left[\hat{Y}(r') + \hat{\mathcal{Y}}_1(r', r'') \right]^{-1} \hat{\mathcal{Y}}_2(r', r''). \tag{2.147}$$

One application propagates from a to c, and a second time propagates from c to b. In this way I have

$$\hat{Y}(a) = Y(a)$$

which carries to

$$\hat{Y}(b) = Y(b) + \mathcal{O}(h^4).$$

Once I have integrated $Y(r)$ far beyond the range of the potentials, I can extract the scattering matrix using a variation of Eq. (2.62):

$$S = (g_2' - g_2 Y)(g_1' - g_1 Y)^{-1} \tag{2.148}$$

with the basis functions (as matrices) $g_{1,2}(r)$ defined in Eq. (2.58). The last step is only for identical particles, and that is to transform the S-matrix into its (anti-)symmetrized version using Eq. (2.87).

Three questions remain: what basis should one integrate in, what are the initial values, and what step size should one use? For the question of basis, the numerical method outlined above is not specific to a particular basis, so one can in principle integrate in any basis. In practice, however, numerical artifacts are avoided by integrating in the basis for which the coupling matrix M is most nearly diagonal. Thus, for separations less than R_{outer} I integrate in the basis which couples the electronic spins together $|\ell m_\ell s m_s m_{i1} m_{i2}\rangle$. For larger separations I transform the matrix into the basis of internal states[36].

Regarding initial values, it doesn't really matter much what values are used for the initial condition, as the log-derivative is either undefined or infinite at $r = 0$. A diagonal matrix with large values or a diagonal matrix with the WKB amplitudes $\sqrt{M_{nm}}\delta_{nm}$ work equally well in practice when starting at a very small, but non-zero, r. The question of step size is slightly more difficult. In practice, the step size should be much smaller than the local de Broglie wavelength. I numerically calculate the eigen-energies of the potential at every position r – the adiabats – and use the lowest energy to estimate the de Broglie wavelength, from which I choose a step size. I integrate the coupled-channels equations in blocks of $5-15$ angstroms, the sizes of which are defined mostly by the amount of memory available on the computer, and I use a constant step size for each block that is calculated from the lowest adiabat. Each block, therefore, has a different step size.[22]

As of writing, the coupled-channels solver can determine the scattering properties for ground-state collisions of ^{87}Rb, ^{40}K, and ^{40}K^{87}Rb. Hyperfine parameters such as g_J, g_I, and a are found in [80], although more recent values are compiled in the online resources [81, 82]. Born-Oppenheimer interaction potentials are taken from photo-association data for Rb[74], K[75], and KRb[72]. As the parametrization of the Born-Oppenheimer potentials generally does not depend on the hyperfine structure, one can calculate the scattering properties of any combination of isotopes of the above atoms by using their specific hyperfine parameters, such as from Arimondo *et al.*[80]. Retardation effects for Rb and K are from Marinescu *et al.*[60]. Physical constants are sourced from the United States National Institute of Standards and Technology[83] and atomic masses from Audi *et al.*[84]. Extensions to combinations of different atomic species is a matter of finding BO potentials for that combination; for instance, sodium potentials can be found in Knoop *et al.*[85].

[22] This method of calculating the step size was suggested to me by Dr. Eite Tiesinga at the University of Maryland.

2.8 Direct-simulation Monte Carlo for an optical collider

While the calculation of the collision cross section must be done quantum mechanically, once the cross section and differential cross section are known one can calculate the effect of collisions on a sample of non-degenerate atoms classically. The appropriate equation here is the Boltzmann equation which has the unfortunate problem of being very difficult to solve in out-of-equilibrium situations, and there are few further-from-equilibrium situations than a collision of two cold atomic clouds at energies tens to thousands of times larger than their thermal energy. Therefore, one needs a numerical method for solving the Boltzmann equation.

In this work, I use one of the most common and versatile methods for integrating the Boltzmann equation: the so-called Direct Simulation Monto-Carlo (DSMC) method. Originally developed by G. A. Bird for the simulation of gaseous fluid dynamics[86], it has been successfully used to model ultracold atomic gases – most notably during evaporation[87, 88, 89]. DSMC works by decoupling the motion of the atoms from their collisions in a time step that is short compared to the mean collision time, so it only works when the atoms can be considered to be "free" most of the time. This situation occurs when the mean free path of the atoms is much larger than the inter-particle spacing. Qualitatively, DSMC is appropriate when **(a)** the cross section is finite (no Coulomb interaction) so atoms are asymptotically free after collisions, and **(b)** the sample is better described as a gas than a liquid.

DSMC calculates collisions between atoms by dividing space into a 3D grid with cubic cells of volume V_c. Collisions between pairs of atoms only occur between atoms that are in the same cell. The probability that a collision occurs between a given pair of atoms is

$$P_{\text{coll}} = \frac{\sigma v_{\text{rel}} dt}{V_c} \tag{2.149}$$

where $v_{\text{rel}} = |\mathbf{v}_1 - \mathbf{v}_2|$ is the magnitude of the relative velocity of the atom pair and dt is the time-step. For each possible collision partner, I calculate P_{coll} and compare it to a randomly generated number distributed uniformly on the interval $[0, 1]$; if that value is less than P_{coll} the collision succeeds and I calculate new velocities. For N_c atoms in a cell, the number of possible collision partners is $N_c(N_c - 1)/2$, which means that for the simulation as a whole the computational resources scale as the square of the total number of atoms. Such scaling would quickly limit the utility of this method to only very small samples.

Bird's method uses a re-scaling trick to make the resource scaling linear with the total number of atoms. Firstly, one works with so-called "test" particles instead of real particles. Each test particle represents F real particles but has the same mass as a single particle, so they have the same positions and velocities that real particles would have. The number of

collisions of test particles in a cell during a time dt is

$$N_{\text{coll}} = \frac{FN_c(N_c-1)\sigma v_{\text{rel}}dt}{2V_c} \tag{2.150}$$

where N_c is now the number of *test* particles in a particular cell. The probability for any pair of test particles to collide is evidently

$$P_{\text{coll}} = \frac{F\sigma v_{\text{rel}}dt}{V_c} \tag{2.151}$$

and one needs to test $N_{\text{pairs}} = N_c(N_c-1)/2$ pairs of particles. The problem here is that the probability for a collision is low – it has to be or the sample is not gaseous – so most of the atom pairs will not succeed in a collision and represent wasted computational resources. Instead, I select

$$N_{\text{sel}} = \left\lceil \frac{FN_c(N_c-1)[\sigma v_{\text{rel}}]_{\max}dt}{2V_c} \right\rceil \tag{2.152}$$

pairs of atoms to test for collisions, where $[\sigma v_{\text{rel}}]_{\max}$ is a running maximum of the product of σv_{rel} and $\lceil x \rceil$ rounds x up to the next integer. I then rescale the collision probability such that the correct number of collisions succeed by using the new probability

$$\tilde{P}_{\text{coll}} = P_{\text{coll}}\frac{N_{\text{pairs}}}{N_{\text{sel}}}. \tag{2.153}$$

This ensures that the collision probability for each selected pair is nearly 1 so there are no wasted resources. Typically N_{sel} is near 1, so the total number of collisions that need to be tested for collision scales with the total number of cells which itself is proportional to the total number of test particles. Hence, the method scales approximately linearly with the number of test particles.

The DSMC procedure is summarized in Fig. 2.10. Cross sections and T-matrix elements are loaded from the coupled-channels solver for each possible collision pair. I interpolate these values over a dense, uniformly spaced grid of collision energies, so that I can quickly perform a look-up of the cross section and T-matrix elements for a particular collision energy. I then define the trap, cloud, and cell parameters. Test particles are initialized in the simulation according to the Boltzmann distribution of positions and velocities

$$f(\mathbf{r}) \propto e^{-\frac{U_i(\mathbf{r})}{kT_i}} \qquad f(\mathbf{v}) \propto e^{-\frac{m_i\mathbf{v}^2}{2kT_i}}$$

for atoms in species i at temperature T_i in a potential $U_i(\mathbf{r})$. The movement phase is performed using the second-order Verlet method[90] which has the property that it conserves the total energy over time; for a test particle with position $\mathbf{r}(t)$, velocity $\mathbf{v}(t)$ and mass m, I update its position and velocity using

$$\begin{aligned} \mathbf{q} &= \mathbf{r}(t) + \mathbf{v}(t)dt \\ \mathbf{v}(t+dt) &= \mathbf{v}(t) - \frac{dt}{m}\nabla U(\mathbf{q},t) \\ \mathbf{r}(t+dt) &= \mathbf{q} + \mathbf{v}(t+dt)dt \end{aligned} \tag{2.154}$$

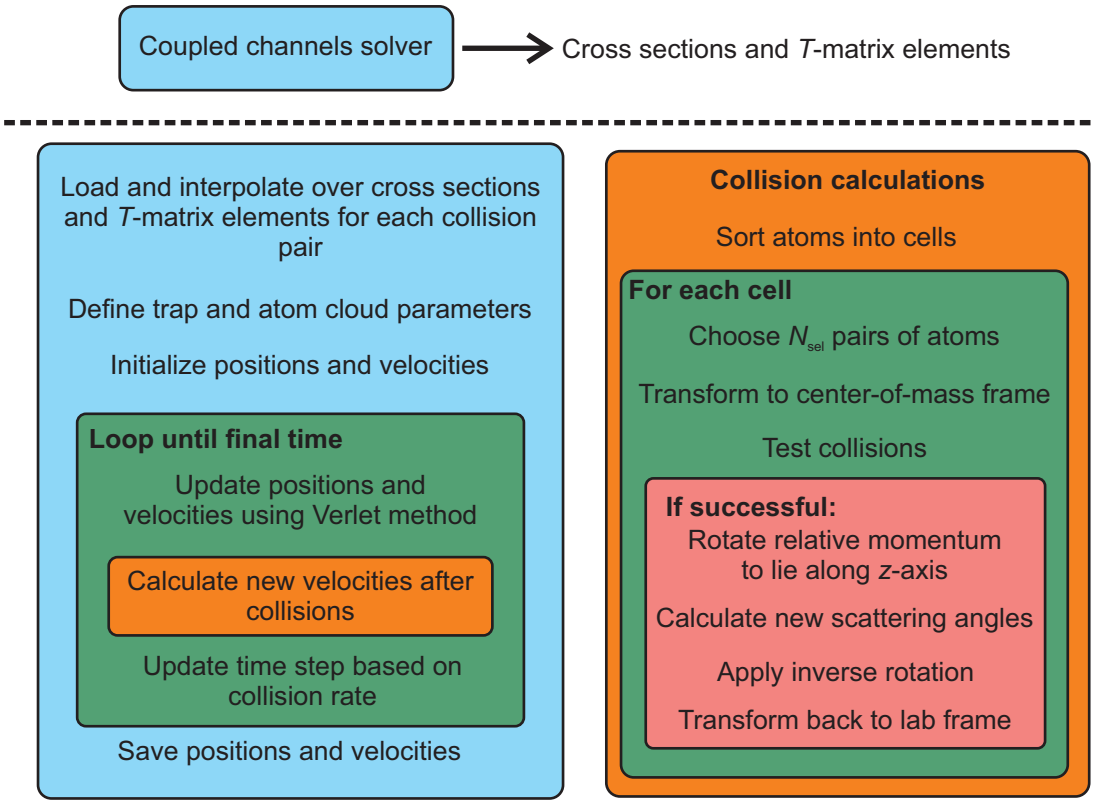

Figure 2.10: Flowchart describing the procedure for simulating collisions using DSMC.

where $U(\mathbf{r}, t)$ is the time-dependent potential energy for the atoms. Following the movement phase, I calculate whether or not a collision occurs and update the velocities of the test particles. First, the momenta are transformed into the center-of-mass frame; second, they are rotated by a matrix R so that the relative momentum lies along the z-axis. The probability of a collision occurring is calculated using Eq. (2.153); if the collision is successful, then new relative momenta are calculated. The cumulative distribution function $F(\theta, \phi)$ for angles θ and ϕ for an arbitrary differential cross section is defined by

$$\frac{dF(\theta, \phi)}{d\Omega} = \sigma^{-1} \frac{d\sigma}{d\Omega}, \tag{2.155}$$

and I can use the probability integral transform to calculate the correct distributions of θ and ϕ from a uniform distribution[91]. The transform works as follows: suppose I have a random variable X that has a cumulative distribution function F_X. Then the random variable $Y = F_X(X)$ is uniformly distributed over $[0, 1]$. What this means in practice is that if I generate a sample of random numbers Y that are uniformly distributed over $[0, 1]$ – using, for instance, the MATLAB `rand` function – then if I apply the inverse function F_X^{-1} to Y the resulting sample of random numbers $X = F_X^{-1}(Y)$ will be distributed according to the cumulative distribution function F_X. As an example, consider pure s-wave scattering;

here,

$$\frac{dF(\theta,\phi)}{d\Omega} = \frac{1}{4\pi}$$

or

$$dF(\theta,\phi) = \frac{1}{4\pi}\sin\theta d\theta d\phi.$$

Clearly, θ and ϕ are independent variables with ϕ already uniformly distributed on $[0, 2\pi]$. The cumulative distribution for θ can be obtained by integrating over ϕ to get

$$dF_\theta(\theta) = \frac{1}{2}\sin\theta d\theta,$$

which means that

$$F_\theta(\theta) = \frac{1}{2}\left(1-\cos\theta\right).$$

By the probability integral transform, if I calculate θ as

$$\theta = \cos^{-1}\left(1-2U\right)$$

where U is a random variable uniformly distributed over $[0, 1]$, then the random variable θ will have the cumulative distribution F_θ. Similarly, for pure p-wave scattering I calculate the random variable θ from

$$\theta = \cos^{-1}\left(\mathrm{sgn}(1-2U)|1-2U|^{\frac{1}{3}}\right),$$

with $\mathrm{sgn}(x)$ returning the sign of x; θ will have a cumulative distribution function defined by

$$\frac{dF_\theta(\theta)}{d\theta} = \frac{1}{2}\cos^2\theta\sin\theta.$$

The probability integral transform is, therefore, very useful for simulating the low-energy scattering of bosons from bosons or bosons from fermions, where the scattering is pure s-wave, and for simulating the scattering of indistinguishable fermions, where the scattering is pure p-wave.

For all other distributions, $F(\theta,\phi)$ is defined using Eqs. (2.155), (2.68) and (2.73), and it is difficult to analytically invert the cumulative distribution function in order to use the probability integral transform. A numerical method for generating samples from arbitrary distributions is needed. For the experiments in this thesis, ϕ is always uniformly distributed on $[0, 2\pi]$, so I only need to sample θ. To this end, I use rejection sampling[91] to calculate the value of θ based on the known distribution $F(\theta,\phi)$. This works by generating a uniformly distributed random value of θ on the interval $[0,\pi]$ and calculating the value of the probability density function $dF_\theta(\theta)/d\theta$. I then generate another uniformly distributed random value on the interval $[0, \max_{\theta\in[0,\pi]}(dF_\theta(\theta)/d\theta)]$; if this value is less than the value of the density function at θ, then the value for θ is accepted as being from the desired distribution. Otherwise, it is rejected. This method allows for relatively efficient sampling of

any given distribution of θ. Once the scattering angles are calculated, I compute the new relative momentum, keeping the magnitude the same. I then apply the inverse rotation R^{-1} to the new relative momentum vector and then transform the individual momenta back to the lab frame.

Finally, I should note that there are a number of ways by which one can improve the simulation accuracy by changing parameters either in space or in time during the simulation. A number of these are locally adaptive (such as time-steps[92] or sub-cell size[93]) and require that one not only keep track of each test particle but also store information regarding each cell. In the simulation of a collision event, many cells might be occupied at one moment and empty the next, and keeping track of all the cells can be costly in terms of memory. I have chosen not to implement these local improvements due to the memory cost, which means that my DSMC code can run on a decent desktop computer for up to 10^6 test particles. Comparisons with more advanced code[94] indicate that as long as the number of test particles is $> 10^4$ my simulation is accurate enough to be reliably compared to experiment. One improvement I do make is to check that the time-step remains much smaller than the inverse of the global collision rate, and as this influences only a global parameter it has no memory penalty.

Chapter 3

Experimental design

The experimental apparatus is a variant of what might be called a "standard" BEC machine, if such a standard can be said to exist. It is based on the design put forth by Lewandowski[95] and Lewandowski *et al.*[96], with the added complication of a ^{40}K magneto-optical trap and associated optics. Much of the credit for the design, construction, and testing of the apparatus belongs to my predecessors in the lab. Aside from what I would call general experiment maintenance (keeping everything running), my major contributions to the apparatus are the dark SPOT and depumping system for K (Sec. 3.2), K microwave and K and Rb radio-frequency state preparation (Sec. 3.5), re-tooling of the imaging system (Sec. 3.6), improving the FPGA control system (Sec. 3.7), and the Helmholtz current servo (Sec. 3.8). In this chapter, I will give an overview of the apparatus; more details can be found in Ana Rakonjac's PhD thesis[49], Thomas McKellar's MSc thesis[97], and Kris Roberts' honours thesis[98].[1] Where different, this work should be taken as the more up-to-date version.

3.1 Rubidium MOT

Our experiment starts by collecting ^{87}Rb atoms in a 3D magneto-optical trap (MOT). Much ink has been spent on describing the physics and implementation of MOTs, so for those interested in the details I direct you to the following references[99, 100, 101, 102, 103]. Briefly, a MOT is a combination of a 3D optical molasses and a magnetic quadrupole field, typically obtained by placing two current-carrying coils in an anti-Helmholz configuration. Optical molasses works by using the Doppler effect to induce a velocity-dependent force on the atoms; combining it with a magnetic field gradient (and the correct polarization of light) makes the force both velocity and position dependent. If the laser has a frequency lower

[1] Honours theses written in the Department of Physics at the University of Otago are not available online. Contact Niels Kjærgaard for a copy.

than the transition frequency (red-detuned), the atoms will be both cooled and trapped near the magnetic field minimum. Since there are states to which atoms can be off-resonantly excited and then decay to states unaddressed by the cooling beams an additional "repump" laser is needed to re-populate the ground state of the cooling transition. Our laser setup for the ^{87}Rb MOT is shown in Fig. 3.1. We derive our cooling beams from a Toptica DL Pro laser that is locked to the $F = 2 \rightarrow F' = 2 - 3$ cross-over line of a saturated absorption spectroscopy signal of the ^{87}Rb D2 line. The structure of the D2 line is shown in Fig. 3.2.

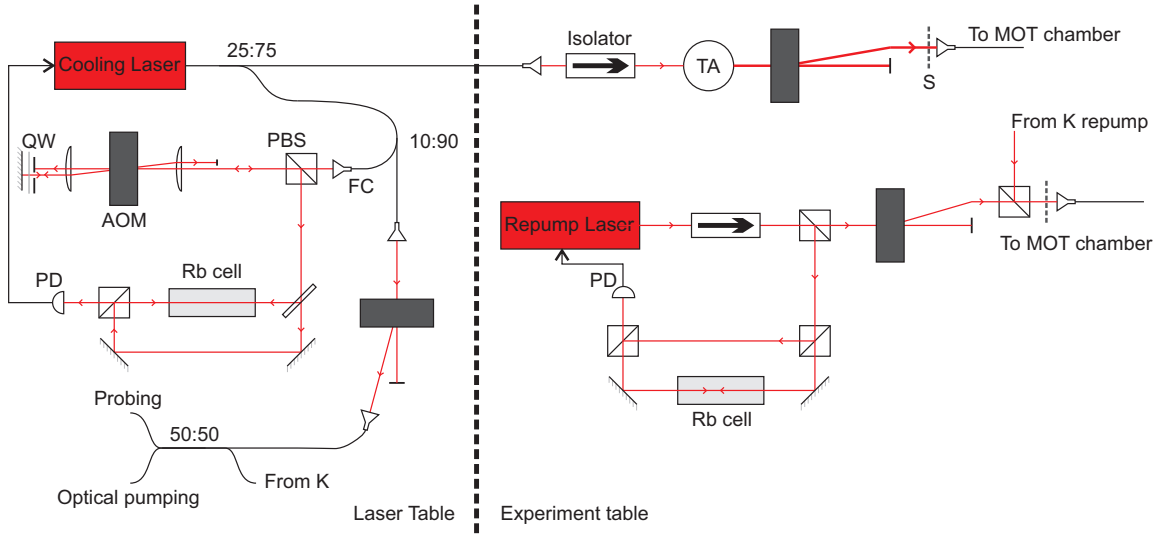

Figure 3.1: Simplified schematic of the Rb laser setup. AOM: Acousto-optic modulator, PD: Photodiode, TA: Tapered amplifier, FC: Fibre coupler, PBS: Polarizing beam-splitter, S: Shutter, QW: quarter-wave plate. Both lasers are Toptica DL Pro models, although the cooling laser has an internal isolator.

We pass the beam used for locking through a double-pass acousto-optic modulator (AOM) which lets us tune the frequency of the laser over approximately 60 MHz while remaining locked to the same line. The power of the cooling beam is boosted by a tapered amplifier (TA) and sent through to the MOT optics via an optical fibre. There it is split into six beams whose polarizations are set to σ^+ before entering the MOT chamber. Deriving six beams from the original path instead of using three and retro-reflecting mirrors avoids shadows cast by light scattering and lets us capture more atoms. The cooling beams are red-detuned from the $F = 2 \rightarrow F' = 3$ transition, and, because of off-resonant excitations, we also need light to repump atoms that decay to the $F = 1$ manifold. The repump laser is also a Toptica DL Pro laser which is locked, via saturated absorption spectroscopy, to the $F = 1 \rightarrow F' = 1-2$ cross-over line. We switch the repump light on and off using a fixed-frequency AOM. As the hyperfine splitting between the two ground states and between the excited states is relatively large we do not need much power in the repump beam, and hence we do not need a TA for this path. The repump beam is split only into two and enters the MOT chamber

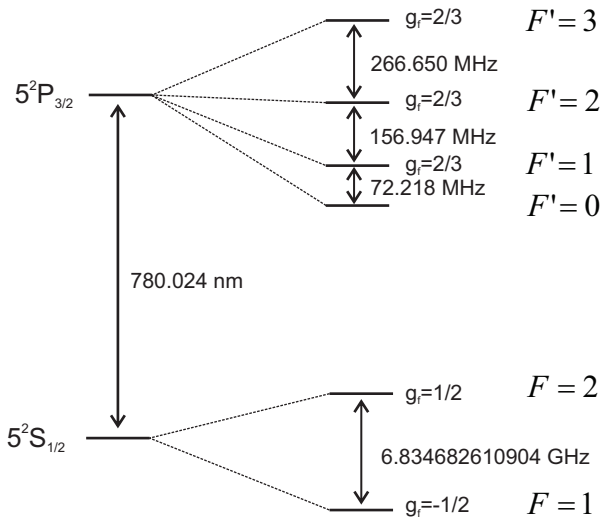

Figure 3.2: ^{87}Rb D2 line structure with hyperfine splittings and g_f values.

from the top and bottom.

We typically saturate the atom number of our MOT after 20 s of loading, but to allow the transistors used to servo the Ioffe-Pritchard trap (Sec. 3.3) to cool down between experimental runs we load for closer to 50 s. At this point we reduce the repump power to pump more atoms to the $F = 1$ manifold to compress the atom cloud – the so-called "compressed-MOT" or CMOT stage[95] – and then switch the quadrupole field off for 30 ms of optical molasses and polarization-gradient cooling, which significantly improves the number of atoms loaded into the Ioffe-Pritchard trap. Finally, we apply a small bias field along with circularly polarized light to optically pump atoms to the $|F = 2, m_F = 2\rangle$ ground state. At this point we work with purely magnetic traps as described in Sec. 3.3.

3.2 Potassium MOT

The ^{40}K MOT is similar to the ^{87}Rb MOT, in that we use a 3D MOT with six beams to collect ^{40}K atoms and we need a repump laser to pump atoms out of the dark ground state. The laser system is shown in Fig. 3.3 and the structure of the ^{40}K D2 line in Fig. 3.4. There are significant differences in the two MOT systems, however. Whereas ^{87}Rb occurs with 27.8% natural abundance, so we can get a good absorption signal without the need for enriched cells, ^{40}K has a natural abundance of only 0.012%. Enriched ^{40}K salt, as a result, is incredibly expensive and not worth using in a vapour cell for locking a laser. It is, however, worth using in the MOT dispensers.[2] Instead of locking to a ^{40}K absorption line, we lock to the $F = 1 - 2$ cross-over line between ground state levels in ^{39}K. We derive the beam

[2]Thanks to Ina Kinski for manufacturing the enriched dispensers.

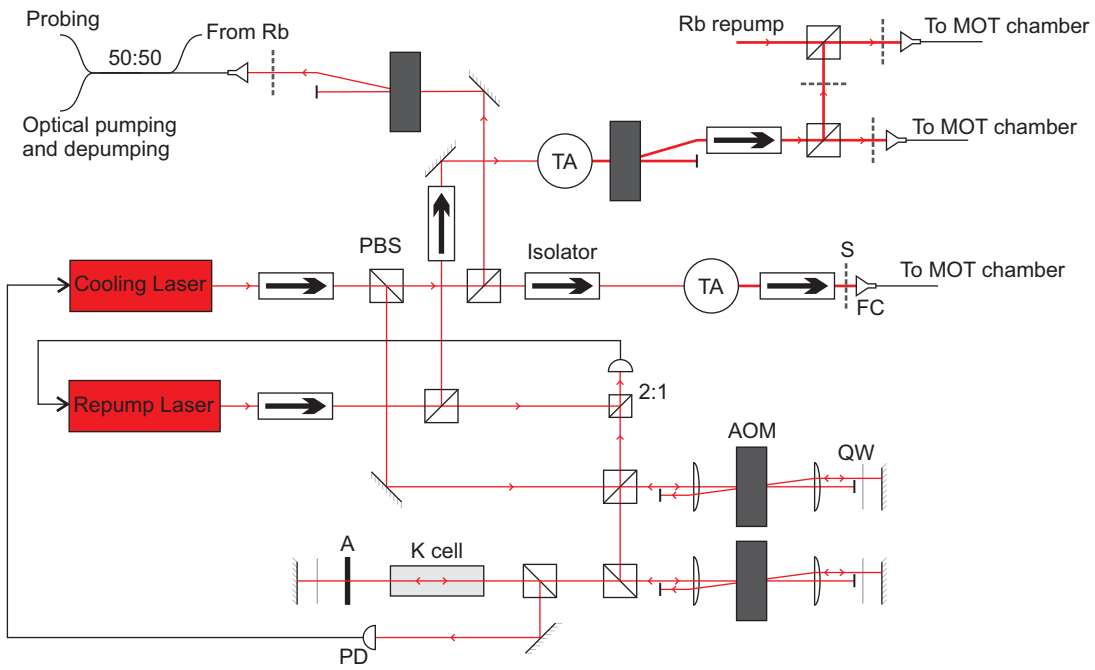

Figure 3.3: Simplified schematic of the K laser setup. AOM: Acousto-optic modulator, PD: Photodiode, TA: Tapered amplifier, FC: Fibre coupler, PBS: Polarizing beam-splitter, A: Attenuator, S: Shutter, QW: quarter-wave plate. The 2:1 cube is a non-polarizing beam-splitting cube. The cooling laser is a Toptica DL Pro, and the repump laser is a New Focus StableWave.

used for locking from a Toptica DL Pro and pass it through two double-pass AOMs, one of whose frequency we tune, to offset the beam's frequency by approximately 600 MHz. This puts the cooling beam frequency red-detuned from the ^{40}K $F = 9/2 \rightarrow F' = 11/2$ transition. The cooling beam is then amplified by a TA and sent to the MOT chamber, where it is combined with the Rb MOT beam using custom $\lambda/2$ waveplates – which act as half-waveplates for 780 nm light and full-waveplates for 767 nm light – on custom rotation mounts[104] just before it is split into six.

Due to the relatively small hyperfine splittings of ^{40}K, optical pumping of atoms into $F = 7/2$ dark ground state occurs at a higher rate than for ^{87}Rb. This necessitates a TA for the repump beam in addition to the MOT beam. The amplified repump beam is also split into six beams and sent to the MOT chamber, although only about half of the power of the MOT beam is necessary for effective repumping. Given the number of optical components needed for locking a ^{40}K laser, we do not use saturation absorption spectroscopy to lock the repump laser. Instead, we combine the repump beam and the MOT beam on a non-polarizing beam-splitting cube and measure the resulting interference signal on a photodiode. When locked, this beat-note signal should be near the hyperfine splitting. We generate a second electrical signal at that frequency and use a phase-comparator to phase lock the measured interference signal to the generated signal. This lets us tune the repump

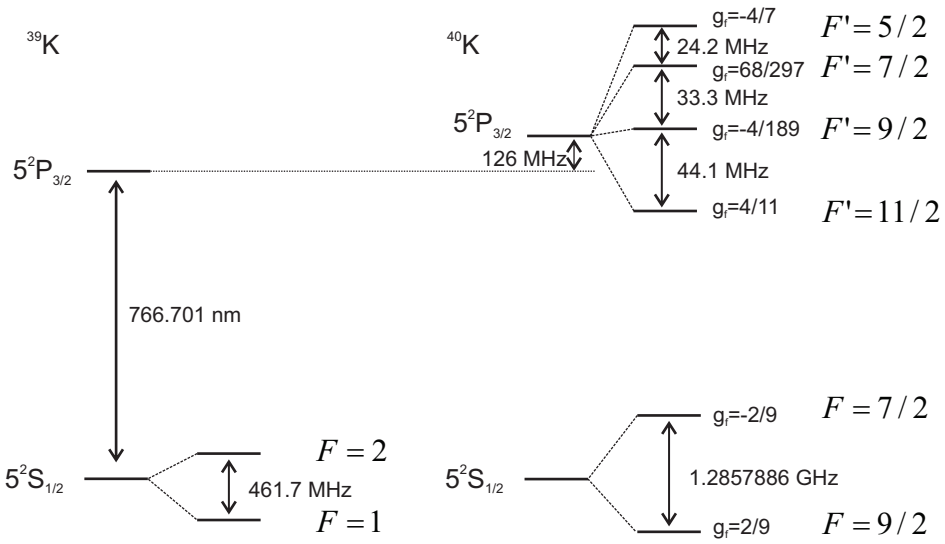

Figure 3.4: ^{39}K and ^{40}K D2 line structure with hyperfine splittings and g_f values. For clarity, I have omitted the excited state hyperfine structure of ^{39}K.

frequency over a wide range.

So far, the system as I have described it does not yield a great deal of ultra-cold ^{40}K at the end of evaporation. To improve the yield, we implemented two changes. The first was to use a dark SPOT[3] technique to improve the K MOT numbers[105, 106]. This involves placing an opaque, round disk in the center of the repump beam path which means that atoms in the center of the MOT see far less repump intensity. These atoms spend more time in the dark state and scatter much less light, leading to higher densities of atoms in the MOT as re-radiation pressure is reduced. This turned out to be insufficient for increasing the number of atoms, so we used the K optical pumping path as a "depumper" [105] which actively pumps atoms from the $F = 9/2$ manifold to the $F = 7/2$ manifold by exciting atoms to the $F' = 9/2$ and $F' = 7/2$ excited state manifolds. The size of the depumper beam is the same as the optical pumping beam, so it covers the entire cloud with more intensity being at the center of the MOT. These two improvements led to a factor of 2.5 times increase of ultracold K atoms.

The K MOT is loaded simultaneously with the Rb MOT. We compress the K MOT at the same time as the Rb MOT and then optically pump K atoms to the $|\frac{9}{2}, \frac{9}{2}\rangle$ state. Since we have blocked the central part of the repump beam, however, we needed to add an extra K repump beam to ensure efficient pumping. To this end, we combined a fraction of the K repump light with the Rb repump light which is unimpeded.

[3] SPontaneous force Optical Trap.

3.3 Magnetic trap and evaporation

Once sufficient atoms are optically pumped to their maximally spin stretched states they are loaded into a purely magnetic quadrupole trap obtained by increasing the MOT gradient coil current to approximately 390 A which produces a magnetic field gradient of 105 G/cm in the vertical direction[49]. While one can evaporatively cool atoms in a quadrupole trap, these traps are known to suffer from losses at low temperatures due to Majorana spin flips at the zero of magnetic field[107]. Instead, we shuttle the atoms from the MOT chamber to a lower vacuum pressure chamber – the science cell – where the trap lifetime of the atoms is higher: on the order of seconds. There, we transfer the atoms from the quadrupole trap to a Ioffe-Pritchard (IP) trap which is approximately harmonic and has no magnetic field zero. Ergo, no Majorana spin flips can occur.

An IP trap is formed by combining a 2D magnetic quadrupole configuration in the $x-y$ plane formed from four current carrying "Ioffe bars" with a pair of Helmholtz (HH) coils and "pinch" coils. The pinch coils are a pair of coils whose separation distance is larger than their radii, and they provide curvature in the z direction as well as a large offset field. The HH coils produce a uniform magnetic field in the opposite direction of the pinch coils to partially cancel the large offset field from the pinch coils; the low field enables easy generation of radio-frequency radiation for evaporative cooling. The magnitude of the magnetic field near the center of the trap is

$$|\mathbf{B}(\mathbf{r})| = \sqrt{(\eta s)^2 + (B_0 + \frac{\beta}{2} z^2)^2} \tag{3.1}$$

where $s = \sqrt{x^2 + y^2}$, B_0 is the minimum magnetic field magnitude, and η and β determine the strength of the quadrupole and pinch fields. We can approximate $|\mathbf{B}|$ as harmonic near the center of the trap:

$$|\mathbf{B}(\mathbf{r})| \approx B_0 + \frac{\eta^2 s^2}{2B_0} + \frac{\beta}{2} z^2. \tag{3.2}$$

The potential energy of an atom depends on both its species and its particular Zeeman state. Assuming that the bias field B_0 is low enough that f and m_f remain good quantum numbers the potential energy for an atom with magnetic quantum number m_f and g-factor g_f is

$$U(\mathbf{r}) = m_f g_f \mu_B |\mathbf{B}(\mathbf{r})|. \tag{3.3}$$

The trapping frequencies are evidently $\omega_s = \sqrt{\frac{m_f g_f \mu_B}{m_i B_0}}\eta$ and $\omega_z = \sqrt{\frac{m_f g_f \mu_B \beta}{m_i}}$ for $m_f g_f > 0$, where m_i is the mass of the atom. For $m_f g_f < 0$ the atoms are anti-trapped and are expelled from the trapping region. Atoms in the spin-stretched state have $m_f g_f = 1$, so while both K and Rb atoms sit in the same potential, the K trapping frequency is $\frac{m_{\mathrm{Rb}}}{m_{\mathrm{K}}}$ larger than the Rb trapping frequency. Currently, $\omega_s = 2\pi \times 160$ Hz and $\omega_z = 2\pi \times 16.9$ Hz for ^{87}Rb.

When we load the atoms into the IP trap they are generally at a temperature of a few hundred μK which is much too hot for our experiments. We employ radio-frequency (RF) forced evaporative cooling to reduce the temperature of the atoms down to $\sim$1 μK. Much has been written on the subject of evaporative cooling[108, 109, 110, 88, 89], so I will only give a brief overview. We consider a sample of atoms that can be described by Maxwell-Boltzmann statistics; namely, the probability of finding an atom of energy E is $P(E) \sim e^{-\frac{E}{kT}}$ where T is the temperature. Since the temperature is defined by the average energy per atom of the cloud, if we preferentially remove atoms with higher than average energies then the temperature of the cloud as a whole will be reduced. If we remove atoms above a certain energy $E_{\rm ev}$, then, as the temperature is lowered, we will have exponentially fewer atoms of sufficiently high energy and cooling will stall. Therefore, we force evaporation by lowering $E_{\rm ev}$ as the temperature decreases. Radio-frequency evaporation works by transferring atoms from magnetically trappable states with $m_f g_f > 0$ to anti-trapped states with $m_f g_f < 0$. For ^{87}Rb, this involves transitions from the desired state of $|2, 2\rangle$ to $|2, -1\rangle$ where the atoms are ejected from the trap. As higher energy atoms access higher magnetic fields we can use the change in transition frequencies with magnetic field to select only the highest energy atoms to be removed. This process must be slow enough to allow the cloud to rethermalize but fast enough to avoid significant losses from other processes (collisions with background gases and three-body recombination, for instance). We typically start removing atoms using $E_{\rm ev} \approx 2$ mK and reduce it to near zero in about 45 s.

Of course, the re-thermalization process after high energy atoms are removed only works when the atoms actually interact with each other. For bosons, such as ^{87}Rb, this does not present a problem because they can collide via s-wave channels, and according to the Wigner threshold law Eq. (2.40) the cross section for this process is non-zero at threshold. For ^{40}K this is a problem because ^{40}K is a fermion, and at low energies it can only collide via p-wave channels which have a vanishing cross section at threshold. There are two main methods for cooling fermions to ultra-low temperatures. The first involves using two different spin states of the atom which can collide via s-wave channels[111]. However, this generally means that one loses a significant fraction of the fermions. The other method is to use another species as a coolant[112, 113].[4] In our case, we use ^{87}Rb as the coolant; we evaporatively cool the Rb atoms, and the large inter-species cross section between ^{87}Rb and ^{40}K ensures that the K atoms have the same temperature as the Rb atoms. Conveniently, ^{40}K atoms are not removed by the RF radiation because the transition frequencies between Zeeman states with $\Delta m_f = 1$ are about half of those for ^{87}Rb atoms at the same magnetic field, as $g_{9/2} = 2/9$ for ^{40}K atoms and $g_2 = 1/2$ for ^{87}Rb. We lose K atoms during evaporation primarily from two and three-body losses over the long evaporation time-scales.

[4] One can cool strongly dipolar fermionic atoms directly because Eq. (2.40) does not apply.

Typical maximum numbers of atoms are 5×10^6 ^{87}Rb atoms at $T = 1$ μK in the absence of ^{40}K, and 6×10^6 ^{40}K atoms at $T = 1.5$ μK; when simultaneously evaporating both ^{87}Rb and ^{40}K we lose much of the Rb sample at the very end due to the high final densities. When investigating KRb mixtures we need useful numbers of both types of atoms, so we reduce the K cooling beam power during the MOT loading stage so that we initially load fewer K atoms and hence finish with comparable numbers of Rb and K atoms.

3.4 Optical tweezers

Arguably the most important part of the experiment is the optical tweezer system, which allows us to manipulate samples of atoms and smash them together. The basics of off-resonant optical dipole traps are well-described in [114], but I shall give a brief overview. Consider a two-level quantum system whose levels are separated by an energy $\hbar\omega_0$; the total Hamiltonian in the interaction picture with a coupling field oscillating at ω is

$$H = -\hbar \begin{pmatrix} 0 & \Omega^* \\ \Omega & \Delta \end{pmatrix} \tag{3.4}$$

where Ω is the Rabi frequency and $\Delta = \omega - \omega_0$ is the detuning of the optical field from resonance. I have applied the rotating-wave approximation, which requires $\Omega \ll \omega, \omega_0$. The eigenvalues of Eq. (3.4) are $E_- = \frac{|\hbar\Omega|^2}{\Delta}$ (which connects to the ground state when $\Omega = 0$) and $E_+ = -\hbar\Delta - \frac{\hbar|\Omega|^2}{\Delta}$ (which connects to the excited state). If the optical field is red-detuned ($\Delta < 0$) then regions with a high intensity (proportional to $|\Omega|^2$) will have a lower energy then those with lower intensities. Atoms will thus be attracted to regions of high optical power. By using a large enough detuning, the photon scattering rate can be made arbitrarily small compared to the trap depth, as the scattering rate scales as $\frac{|\Omega|^2}{\Delta^2}$. By this mechanism one can trap atoms in their ground states near the focus of intense, far off-resonant laser beams.

Of course, my simplistic derivation of the dipole potential neglected the so-called counter-rotating terms and glossed over the relationship between the Rabi frequency Ω and the intensity of the optical field. The correct form of the optical dipole potential for an approximately two-level atom is[114]

$$\begin{aligned} U(\mathbf{r}) &= -\frac{3\pi c^2}{2\omega_0^3}\left[\frac{\Gamma}{\omega_0 - \omega} + \frac{\Gamma}{\omega_0 + \omega}\right] I(\mathbf{r}) \\ &= -\kappa I(\mathbf{r}) \end{aligned} \tag{3.5}$$

where $I(\mathbf{r})$ is the intensity of the optical field and Γ is the full-width at half-maximum (FWHM) of the optical transition. For a Gaussian laser beam propagating in the $\hat{\mathbf{z}}$ direction,

the intensity is

$$I(\mathbf{r}) = \frac{2P}{\pi w_x w_y} e^{-\frac{2x^2}{w_x^2} - \frac{2y^2}{w_y^2}} \tag{3.6}$$

with power P and waists w_x and w_y. Expanding Eqs. (3.5) and (3.6) to second order in space we get

$$\begin{aligned} U(\mathbf{r}) &\approx -\frac{2\kappa P}{\pi w_x w_y} + \frac{4\kappa P}{\pi w_x^3 w_y} x^2 + \frac{4\kappa P}{\pi w_x w_y^3} y^2 \\ &= -U_0 + \frac{1}{2} m\omega_x^2 x^2 + \frac{1}{2} m\omega_y^2 y^2 \end{aligned} \tag{3.7}$$

where

$$\omega_x^2 = \frac{8\kappa P}{\pi m w_x^3 w_y} \tag{3.8}$$

is the harmonic trapping frequency for an atom of mass m in the $\hat{\mathbf{x}}$ direction and similarly for ω_y.[5]

Our optical trap is formed from two 1064 nm laser beams which intersect at right-angles.[6] Both beams are derived from the same 50 W laser and are transmitted to their respective locations via optical fibres. The power delivered to the atoms is controlled using AOMs, which also provide very fast (< 1 μs) switching times. To improve reproducibility of the experiment, the output power from the fibres is measured using custom 99/1 beam-splitters and photodiodes; this power is then servoed using analog proportional-integral control boards.[7] The reproducibility of the output power from the fibres is better than 1%.

The horizontal beam propagates parallel to the surface of the optical table in the $\hat{\mathbf{z}}$ direction and supports the atoms against gravity and provides confinement in the $\hat{\mathbf{x}}$ and $\hat{\mathbf{y}}$ directions, as shown in Fig. 3.5. Additionally, it acts as a guide for the atoms by restricting

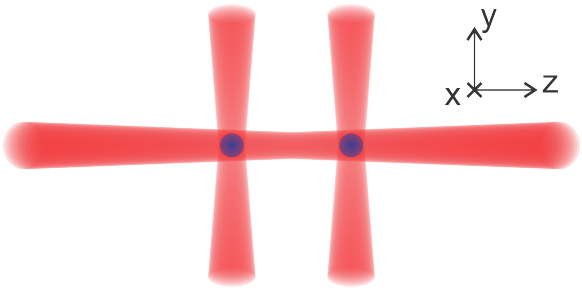

Figure 3.5: Diagram of the crossed-beam dipole trap. The horizontal beam propagates in the $\hat{\mathbf{z}}$ direction and the two vertical beams propagate in the $\hat{\mathbf{y}}$ direction. Atoms (blue) are trapped at the intersection of the horizontal and vertical beams.

[5] I have ignored the variation of the waists along the direction of propagation, which itself leads to a weak harmonic trap, because the geometry of our crossed-beam dipole trap renders this contribution insignificant.

[6] Laser source is an YLR-50-1064-LP-SF from IPG Photonics: http://www.ipgphotonics.com/en/products/lasers/low-power-cw-fiber-lasers/0-98-1-1-micron/ylr-lp-sf-1-100-w

[7] A joint project between Matthew Chilcott and myself.

the path that they can move to be a line: this defines the collision axis. The beam itself is focused onto the center of the IP trap with a waist of $w_{x,y} = 60$ μm. Gravity distorts the trap in the vertical direction causing a reduction in trap depth and a shift in the equilibrium position of the two clouds that depends on the atom species. Using the Gaussian form of the potential Eq. (3.6), the force experienced by the atoms in the y-direction at $x = 0$ is

$$F = -m\omega_y^2 y e^{-\frac{2y^2}{w_y^2}} - mg.$$

Equilibrium is when $F = 0$, and the two points y_n where this occurs are given by

$$y_n = \frac{w_y}{2}\sqrt{-W_n\left(-\frac{4g^2}{\omega_y^4 w_y^2}\right)} \tag{3.9}$$

where $W_n(x)$ is the Lambert W function, defined implicitly by $x = W_n(x)e^{W_n(x)}$[115]. The stable equilibrium position for the atoms is evaluated on the principal branch $W_0(x)$ and the unstable position on the other real branch $W_{-1}(x)$. The modified trap frequency is then

$$(\omega_y')^2 = \omega_y^2\left(e^{-\frac{2y_0^2}{w_y^2}} - \frac{4y_0^2}{w_y^2}\right) \tag{3.10}$$

and the trap depth can be calculated using the difference in the potential energy at the stable and unstable equilibrium positions. I have plotted both the ratio ω_y'/ω_y and the trap depth for our system in Fig. 3.6. Due to the larger force of gravity, Rb has a lower trap depth than K, and this difference can be exploited to evaporatively cool the atoms in the dipole trap without losing K atoms.

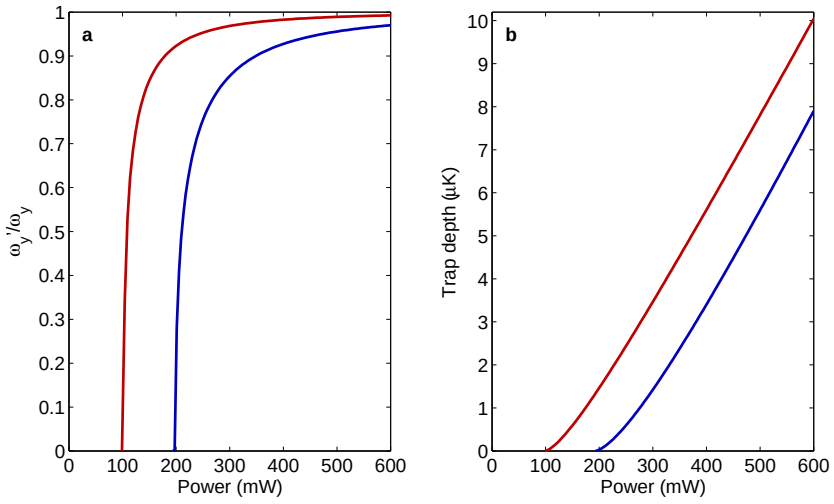

Figure 3.6: Effect of gravity on a horizontally-oriented optical dipole trap. **a** Ratio of trapping frequencies with and without gravity for ^{87}Rb (blue curve) and ^{40}K (red curve). **b** Trap depths for ^{87}Rb (blue) and ^{40}K (red).

Higher power is required in the vertical beam, so it is transmitted using a photonic crystal fibre (PCF) which has a significantly larger mode-field diameter than a typical single-mode fibre and hence can carry more power without deleterious effects. A slight downside is that the output mode of the PCF is not Gaussian: it more resembles a hexagon, reflecting the shape of the PCF core. However, a focused spot approximates a Gaussian for our purposes. The beam from the PCF is expanded to about 2 mm diameter and passed through a two-axis acousto-optic deflector (AOD)[8], a special kind of AOM that is optimized for large deflection angles.[9] By adjusting the frequencies of the RF signals driving the two AODs we can scan the vertical laser beam in a two dimensional plane: both along the direction of the horizontal beam and perpendicular to it. This two-dimensional motion lets us track the position of the waveguide even if it is misaligned relative to the axis of the AOD. The vertical beam is focussed onto the horizontal beam using a so-called f-theta lens[51], which has a flat imaging field in contrast to normal lenses which have spherical imaging fields; this keeps the beam waist the same regardless of the position of the vertical beam.

To implement an optical collider we need to have two vertical beams, not one. The most obvious method of generating two vertical beams using an AOD is to drive the AOD with two frequencies. This works reasonably well if only one AOD frequency needs to be changed to track the waveguide[50]; more generally, one needs to drive each AOD with two frequencies in order to track the position of the waveguide. Suppose that the central point of the optical tweezers (overlapping with the IP trap) is associated with wavevector $k_{z0}\hat{\mathbf{z}} + k_{x0}\hat{\mathbf{x}}$, and the desired position of the atoms is associated with additional wavevectors $\pm\Delta k_z$ and $\pm\Delta k_x$ as shown in Fig. 3.7a. Driving each AOD with two frequencies each will

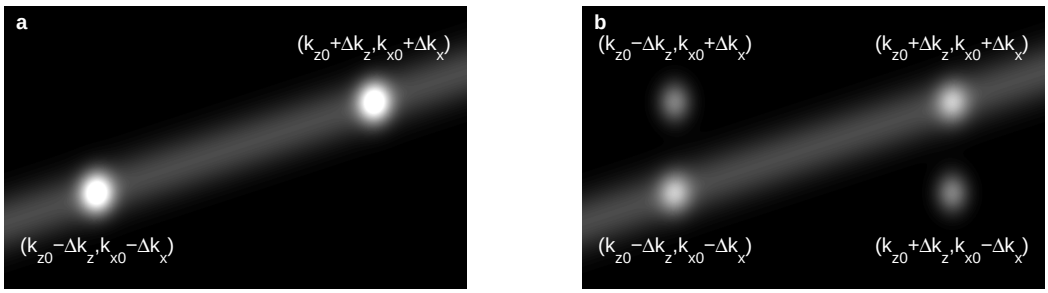

Figure 3.7: Difference between idealized version of two vertical beams **a** and reality when summing two frequencies for each AOD **b**. The long diagonal stripe represents the waveguide.

yield beams that have wavevectors $(k_{z0} + \Delta k_z)\hat{\mathbf{z}} + (k_{x0} + \Delta k_x)\hat{\mathbf{x}}$, $(k_{z0} - \Delta k_z)\hat{\mathbf{z}} + (k_{x0} + \Delta k_x)\hat{\mathbf{x}}$, $(k_{z0} + \Delta k_z)\hat{\mathbf{z}} + (k_{x0} - \Delta k_x)\hat{\mathbf{x}}$, and $(k_{z0} - \Delta k_z)\hat{\mathbf{z}} + (k_{x0} - \Delta k_x)\hat{\mathbf{x}}$ as in Fig.3.7b.

[8] AA Optoelectronics, part number DTSXY-250-1064 http://www.aaoptoelectronic.com/Documents/DTSX-DTSXY-2014.pdf

[9] This is achieved by using shear waves in the crystal rather than longitudinal waves, which have a lower wave speed and hence a larger deflection angle, but at the cost of strong polarization sensitivity.

Only two of these beams overlap with the waveguide, and hence the atoms, while the other two represent wasted power at best and, at worst, can lead to loss of atoms via their partial overlap with the waveguide[116].

Instead, we rapidly toggle between two (x, z) frequency pairs, each of which corresponds to a vertical beam location that overlaps with the waveguide[51]. If we switch between frequency pairs quickly enough the atoms will not have time to respond, and they will behave as though the vertical beams are always on, albeit with half the power (assuming a 50% duty cycle). How fast must this toggling be? The harmonic trapping frequency of the atoms sets the scale, and as long as the toggling frequency is much faster than the trapping frequency we can consider this to be a time-averaged trap.

However, there are some extra considerations that must be taken into account. We are not toggling the positions of beams directly; we are shifting the frequency of the driving signal to the AOD. This rapid toggling produces sidebands on the carrier frequency that themselves deflect some of the laser beam in different directions than desired. As the toggling frequency increases, the distance between the desired beam position and these sidebands becomes comparable to the beam waist, and this leads to an effective broadening of the beam waist and a reduction in the trapping frequency. At very high toggling frequencies the sidebands become resolved and can themselves trap atoms. I have included a derivation of the effects of such toggling on an acousto-optic device in Appendix B for reference. In Fig. 3.8a I show time-averaged trapping potentials generated from the phase-continuous toggling of an AOD through which a Gaussian beam of focal waist 40 μm passes for different toggling frequencies. The trapping potentials are calculated from Eq. (B.29). For toggling frequencies below 100 kHz the traps remain mostly Gaussian, but for higher frequencies the sidebands become resolved and the traps become very structured. The effect of toggling on the trapping frequency is shown in Fig. 3.8b where I have plotted the ratio of the effective trapping frequency as calculated from Eq. (B.30) to the trapping frequency for a single beam with the same total power at the expected location of the right-hand trap. As expected, at low toggling frequencies there is a reduction in the trapping frequency by $2^{-1/2}$ due to halving the amount of power in each beam (Eq. (3.8)). As the toggling frequency increases the effective trapping frequency decreases until oscillations start to appear. At high enough toggling frequencies ω_{trap} does not exist because there is a maximum rather than a minimum of the potential at the expected trap location. Clearly, we wish to avoid using toggling frequencies above 150 kHz so that the sidebands are not resolved, but if we use too low of a toggling frequency then we will have poor timing resolution for changing the trapping potential on the fly. By trial and error, we have found that a toggling frequency of 100 kHz works the best.

We generate the two driving signals for the two-axis AOD using a commercially avail-

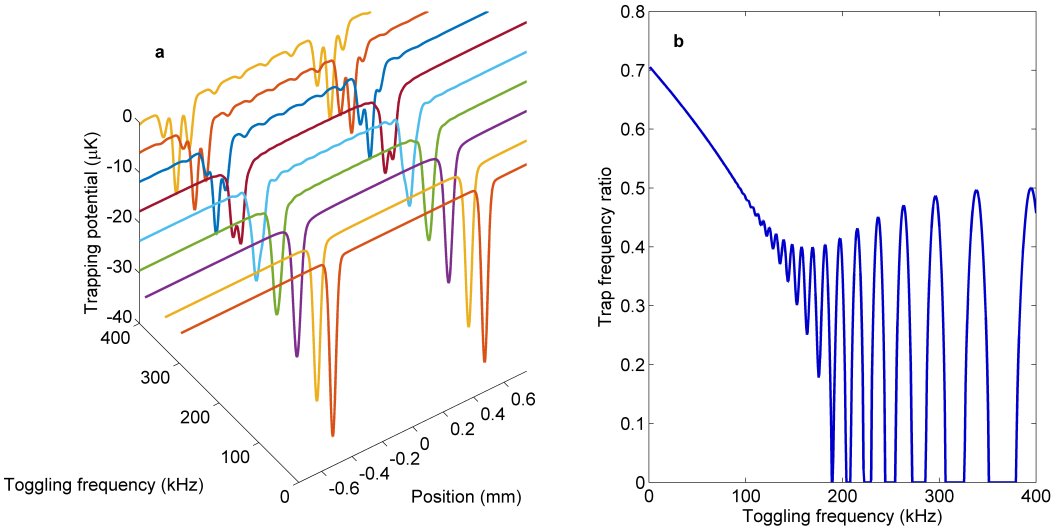

Figure 3.8: Effect of phase-continuous toggling between two driving frequencies of an acousto-optic device. **a** Time-averaged trapping potentials at discrete toggling frequencies for a 40 μm beam waist and ± 0.5 mm trap separation. The scaling factor between position and toggling frequency is 211 μm/MHz. **b** Ratio of actual trapping frequency to trapping frequency in the case of no toggling (a single beam).

able direct digital synthesis (DDS) system – the FlexDDS system from WieserLabs[10] – which allows for phase-continuous toggling between different frequencies; see Appendix B.3.[11] A MATLAB script combined with LabVIEW drivers provided by the vendor uploads a bitstream to the FlexDDS which allows us to program arbitrary frequency and amplitude trajectories into the device. The two channels are updated synchronously using trigger pulses from the imaging controller FPGA (Sec. 3.7). We can dynamically control the driving strength, and hence the optical power at the atoms, at the same time to compensate for changes in the diffraction efficiency as a function of deflection angle. This flexibility enables us to effectively manipulate multiple atom clouds.

A typical collision sequence starts by transferring atoms from the IP trap to the dipole trap. Since the IP trap is elongated in the z direction it turns out to be inefficient to transfer atoms directly from the IP trap to a single dipole trap due to poor mode matching of the two traps. Instead, we have found experimentally that it is most efficient to transfer atoms from the IP trap to a double well dipole trap where the two wells have a separation distance of ± 40 μm. We then separate the two wells to the desired positions using minimum jerk

[10] http://www.wieserlabs.com/products/WL-FlexDDS

[11] Phase-continuous toggling is also a natural extension of how DDS chips work. See [97] for details.

trajectories; these are specified using the fifth-order polynomial[97]

$$z(t) = z_0 + (z_f - z_0)\left[10\left(\frac{t}{T}\right)^3 - 15\left(\frac{t}{T}\right)^4 + 6\left(\frac{t}{T}\right)^5\right] \tag{3.11}$$

where T is the movement duration, and z_0 and z_f are the initial and final positions, respectively. Equation (3.11) is designed to minimize the magnitude of the jerk, or third derivative of z with time. This in turn reduces sloshing of the atom clouds within their potentials and hence reduces heating of the clouds. Once at their final position, we hold the atoms in order to do state and trap preparation/purification. We then accelerate the two traps towards each other, turning off the dipole trap just before the traps overlap to allow the collision to occur in free space. Typically this is done when the traps are separated by $\pm 40 - 60$ μm, depending on the experiment.

From the atoms' reference frame, as the Gaussian traps accelerate they deform due to inertial forces. At high enough acceleration the traps will not provide enough restoring force to retain the atoms, and this defines the maximum acceleration for our system. The maximum force exerted on the atoms by a Gaussian trap is

$$F_{\max} = \frac{m\omega_z^2 w_z}{2\sqrt{e}}$$

which means that the maximum acceleration is $a_{\max} = F_{\max}/m$, and the maximum kinetic energy of a single cloud after accelerating over a distance d from a standstill is

$$E_{\max} = m a_{\max} d = \frac{m\omega_z^2 w_z}{2\sqrt{e}} d = \frac{8\kappa P}{\pi\sqrt{e} w_x w_z^2} d \tag{3.12}$$

which is nearly the same for both ^{40}K and ^{87}Rb due to their similarity in κ (see Eq. (3.5)). Of course, this assumes that the atoms are at zero temperature; due to their thermal energy, the practical maximum collision energy is lower. In practice, our maximum energy is approximately 2 mK. Since we have a limit to the acceleration that our atoms can undergo, we use a collision trajectory that quickly increases the acceleration to a maximum value and holds it there for the duration of the collision trajectory. We use a sigmoid profile whose mathematical form is

$$a(t) = a_{\text{coll}} \frac{t^7}{k^7 + t^7} \tag{3.13}$$

where k is a constant value (typically 16 ms) and a_{coll} is the desired maximum acceleration which approximately sets the collision energy through $E = m a_{\text{coll}} d$. This profile typically works well at minimizing the amount of sloshing that the atoms experience during acceleration, and the collision energy (measured using cloud position versus time) is reproducibile to the level of about 2%.

3.5 State preparation

State preparation refers to both the act of preparing atoms in particular hyperfine ground states and preparing those states in particular wells of the optical tweezers. The latter is particularly important for investigating Feshbach resonances with the optical collider, as one wants the scattering halo to be the result of only the collisional process of interest. State preparation is done using three different frequency ranges corresponding to the different hyperfine splittings of ^{87}Rb and ^{40}K and the energy differences between magnetic Zeeman levels within the same hyperfine manifold. Hyperfine transitions in ^{87}Rb at low magnetic field occur near 6.8 GHz, in ^{40}K near 1.3 GHz, and intra-manifold transitions for both atoms occur between 1-100 MHz. Due to the vast difference in wavelength between these frequency ranges each frequency requires (mostly) its own electronics and antennae. All state preparation frequency sources are referenced to the same 10 MHz clock, derived from a GPS time reference.

For the experiments performed in this work, we used one of the FlexDDS output channels as an input frequency for each frequency range. As we were already using the FlexDDS for the optical tweezers, this was a convenient use of the extra channel. For frequency sweeps the FlexDDS uses the built-in sweep generator of the internal AD9910 DDS chip, so one needs only specify the ramp end points, speed, and increment. The FlexDDS can generate frequencies from near DC to 400 MHz, providing a large tuning range for microwave and RF state preparation. By judicious use of high-frequency switches[12] one can direct the signal to the appropriate set of electronics as shown in Fig. 3.9

For RF state preparation the bare FlexDDS signal covers an appropriate frequency range. To send the signal to the RF coil, the signal `MW_pulse` is kept low and the signal `RF_pulse` is kept high. The Rabi frequency that one obtains at low frequencies (~ 10 MHz) for maximum input power is quite high: $\Omega \approx 2\pi \times 100$ kHz. Depending on the application it is sometimes necessary to insert attenuators between the two RF switches.

For microwave state preparation, the frequency of the FlexDDS signal needs to be increased, and we do this in two ways. For ^{87}Rb, the FlexDDS signal is mixed with a signal at 6.532 GHz to produce sidebands above and below the carrier. The resulting signal is then sent through a sharp bandpass filter with a passband from 6.6 - 7.0 GHz, which is roughly centered on the zero field hyperfine splitting. Only the higher frequency sideband remains, and this is amplified and sent to the Rb antenna. As both the carrier and the lower frequency sideband are very far off resonance, the filter is not strictly necessary; however, the amplifier is typically saturated with power and hence adding another input frequency decreases the amount of output power at the desired frequency. We use a rectangular end-fire antenna designed for 6.5 GHz to direct the microwaves onto the atoms. On the $|22\rangle \rightarrow |11\rangle$

[12] Minicircuits ZASW-50DR+

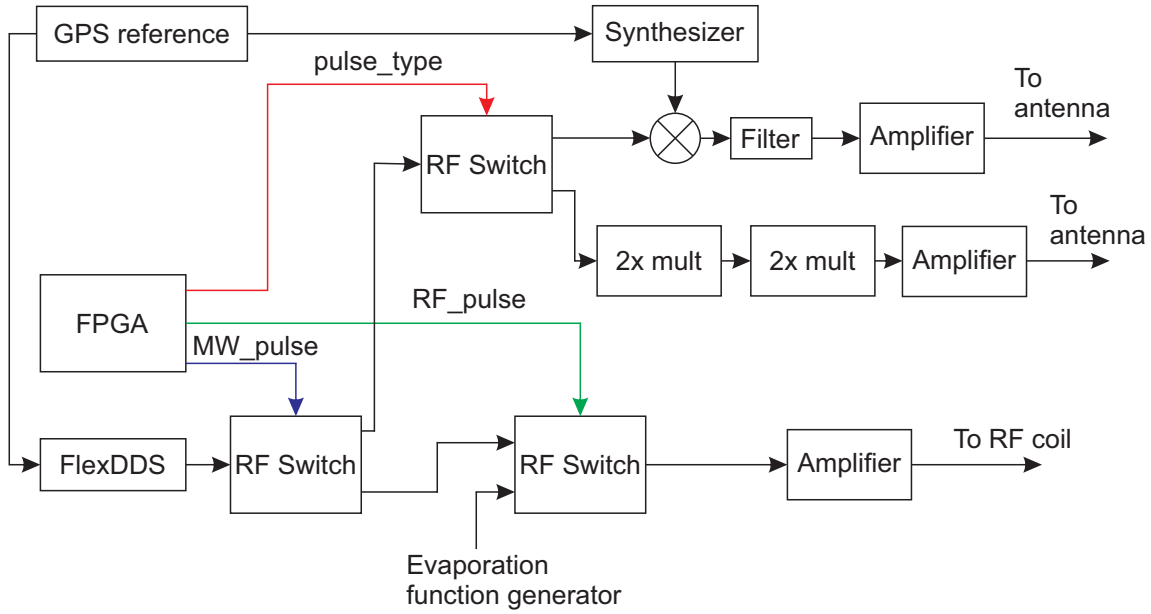

Figure 3.9: Connections between FPGA, FlexDDS, and state preparation electronics. Some components, such as signal amplifiers, are not shown. State preparation frequency sources are referenced to a GPS time base via a 10 MHz clock signal.

transition at 9 G the Rabi frequency is typically about $\Omega = 2\pi \times 16$ kHz.

For ^{40}K we use a different system for increasing the FlexDDS frequency to near 1.3 GHz, as bandpass filters at that frequency were not available when we set up the system. Instead, we use two x2 multipliers with additional signal amplifiers to implement a x4 multiplier. Input frequencies near 320 MHz yield output frequencies near the zero-field hyperfine transition frequency of ^{40}K. The antenna here is a dipole antenna used for communication with aerial drones and is designed for 1.2 GHz. Typical Rabi frequencies for the $|\frac{9}{2}\frac{9}{2}\rangle \rightarrow |\frac{7}{2}\frac{7}{2}\rangle$ transition are near $\Omega = 2\pi \times 13$ kHz.

State preparation is done only in the optical trap, and as such a stable bias field is required. In most cases, state preparation is easiest at relatively low magnetic fields because the microwave frequencies required only need to vary by small amounts. We use the so-called "z-coils"[49], a pair of coils in an approximate Helmholtz configuration, as the magnetic field coils for state preparation. The current is sourced from a custom High Finesse 15V/10A bipolar current source which has a stability of about 1 ppm; the stability of the magnetic field in this case is limited by fluctuations in ambient fields which shift the field experienced by the atoms by a few mG from day to day. We use both π pulses and adiabatic rapid passage (ARP) to prepare atoms of both species in arbitrary spin states.

When colliding atoms, the analysis is much simpler if there is only one state in each of the separated optical traps; for same-species collisions this means that each trap should

contain a unique spin state, and for different-species collisions each trap should contain only Rb or K. Conveniently, the z-coils produce a small magnetic field gradient (≈ 8.7 mG/mm at 5 A of current) which we use to individually address optical traps that are sufficiently far apart (more than 1 mm). For example, to prepare both traps with Rb atoms in the $|2,0\rangle$ state we would first load only Rb into the dipole trap, then apply a magnetic bias field with the z-coils, and then use ARP to transfer atoms from the $|2,2\rangle$ state, which is resonant to our probe beams, to the $|1,1\rangle$ state, which is far off-resonant. We then apply a pulse of light resonant to the $F = 2 \rightarrow F' = 3$ transition which will remove all the atoms in the $F = 2$ hyperfine state. We finish by using ARP to transfer atoms from $|1,1\rangle \rightarrow |2,0\rangle$. By using more targeted π-pulses instead of ARP, we can address individual traps and thus collide atoms in different spin states.

Finally for KRb collisions, if one naively separates the initial double-well into two wells and then purifies the traps 50% of the atoms will be lost. We can do better if we preferentially push different states into different wells by using a strong magnetic field gradient and differing magnetic moments of atomic states. The ^{87}Rb $|22\rangle$ and ^{40}K $|\frac{9}{2}\frac{9}{2}\rangle$ states both have the same magnitude and sign of their magnetic moments, but if we transfer the Rb atoms to the $|11\rangle$ state they have a magnetic moment of the opposite sign to the K atoms. As shown in Fig. 3.10, applying a magnetic field gradient to the sample imparts a differential mechanical force on the two species of atoms, and we can push K atoms preferentially into one well and Rb atoms into the other. For this to work properly we need

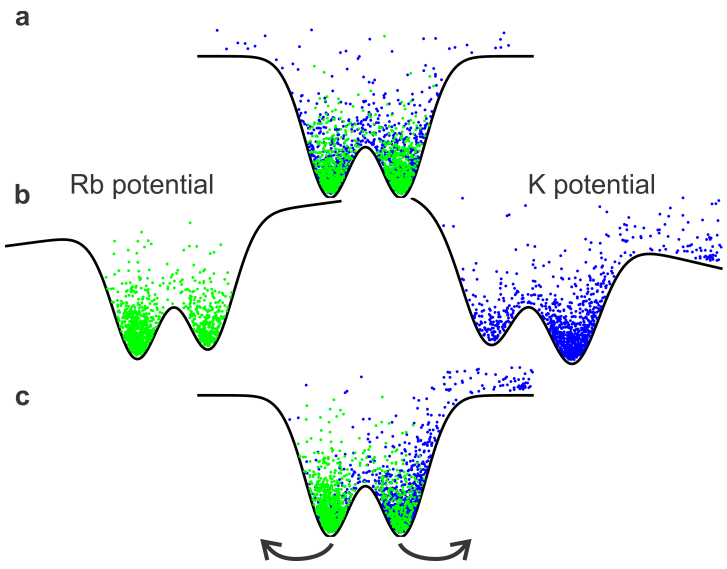

Figure 3.10: Trap preparation using a magnetic field gradient. **a** Rb (green dots) and K (blue dots) jointly occupy a double-well dipole trap. **b** A magnetic field gradient is applied and atoms are preferentially pushed into one of the wells based on their magnetic moment. **c** The magnetic field gradient is slowly turned off as the traps are separated, leaving predominately one species in each trap.

to bring the optical traps closer than their typical double-well separation of ± 40 μm. Using this technique we can retain 60-70% of the initial number of atoms of both species instead of just 50%.

3.6 Imaging

All of the experiments described in this work rely on absorption imaging to provide a spatial description of the atoms. Absorption imaging is conceptually simple. Consider a two-level atom with a dipole-allowed transition at a frequency of ω_0. If a cloud of such atoms is illuminated with low-intensity light at the resonant frequency, the cloud will absorb the light in an amount related to the local density of the atoms integrated along the direction of propagation of the light. The shadow cast by the atoms can be imaged onto a camera and a map of the 2D atom column density can be obtained. The evolution of the light intensity $I(\mathbf{r})$ when $I(\mathbf{r})$ is small is[117]

$$\frac{dI(\mathbf{r})}{dz} = -n(\mathbf{r})\sigma I(\mathbf{r}) \tag{3.14a}$$

$$I(\mathbf{r}) = I(x, y, -\infty)e^{-\sigma \int_{-\infty}^{z} n(x,y,z')dz'} \tag{3.14b}$$

where $n(\mathbf{r})$ is the density of atoms, z is the direction of propagation of the light, and σ is the absorption cross section equal to $\frac{3\lambda_0^2}{2\pi}$ with $\lambda_0 = 2\pi c/\omega_0$ the vacuum wavelength.

Of course, two-level atoms do not exist in nature, and imaging with low-intensity light may yield too little signal-to-noise, so one must be able to account for these two effects. In order to obtain the highest signal-to-noise, one wants to use a transition that mimics a two-level atom as closely as possible; these are known as cycling transitions because the atom can only cycle between two states. Selection rules for electric-dipole transitions are that $\Delta f = 0, \pm 1$ and $\Delta m_f = 0, \pm 1$, so cycling transitions are only between the highest m_f ground state and the highest m_f excited state, which is the $|f = 2, m_f = \pm 2\rangle \rightarrow |f' = 3, m'_f = \pm 3\rangle$ transition for ^{87}Rb and the $|f = 9/2, m_f = \pm 9/2\rangle \rightarrow |f' = 11/2, m'_f = \pm 11/2\rangle$ transition for ^{40}K. These transitions can only be driven by $\sigma^{\pm}$ light: circularly polarized light propagating along the quantization axis defined by the magnetic field.

Our magnetic field is aligned with the axis of the optical collider, and we image at right angles to the collider axis in order to obtain maximum information about the scattering halo, so we cannot drive the cycling transitions exclusively. Instead, we use linearly polarized light in the y-direction which is a superposition of $\sigma^{\pm}$ light. This breaks the cycling transition and allows atoms to shuffle to different ground state levels if the light is present for long enough; the effect is a reduced absorption cross section with time. As long as the number of photons per light pulse is small enough, this redistribution can be neglected.

The major effect of not using a cycling transition is that the optical cross section changes depending on the orientation of the polarization relative to the quantization axis.

Assuming that all optical transitions have the same resonant frequency, the evolution of the light intensity on-resonance is given by[117]

$$\frac{dI(\mathbf{r})}{dz} = -n(\mathbf{r})\frac{\sigma_0}{\alpha}\frac{I(\mathbf{r})}{1+\frac{I(\mathbf{r})}{\alpha I_{\text{sat}}}} \tag{3.15}$$

where σ_0 is the two-level cross section, I_{sat} is the saturation intensity of the cycling transition, and α is a dimensionless parameter that accounts for the change in cross section due to polarization. The value of α can, in general, be calculated using angular momentum addition rules and the Wigner-Eckart theorem[81, 118], but for transitions between ground and excited states of maximum f one can write[13]

$$\alpha^{-1} = \sum_q |\epsilon_q|^2 |\langle f m_f 1 q | f', m'_f\rangle|^2$$

where ϵ_q is the component of the polarization unit vector in the direction of spherical basis vector $\hat{\mathbf{e}}_q$[14] and $\langle j_1 m_{j1} j_2 m_{j2} | j m_j\rangle$ is the Clebsch-Gordan coefficient. For light polarized in the $\hat{\mathbf{y}}$ direction and a quantization axis in the $\hat{\mathbf{z}}$ direction, $\alpha = 15/8$ for ^{87}Rb atoms in the $|f = 2, m_f = \pm 2\rangle$ states and $\alpha = 55/28$ for ^{40}K atoms in the $|f = 9/2, m_f = \pm 9/2\rangle$ states.

Equation (3.15) can be easily integrated to extract the column density of atoms from the measured intensities

$$\sigma_0 \int_{-\infty}^{\infty} n(\mathbf{r}) dz = \sigma_0 n(x,y) = \alpha \log\left(\frac{I_i(x,y)}{I_f(x,y)}\right) + \frac{I_i(x,y) - I_f(x,y)}{\alpha I_{\text{sat}}} \tag{3.16}$$

where $I_f(x,y) = I(x,y,+\infty)$ and $I_i(x,y) = I(x,y,-\infty)$. If the light field is collimated as it passes through the atoms, then one can infer $I_i(x,y)$ by measuring the intensity of the light without atoms present at the same location that one measures I_f: i.e., at the camera. In our system, we take three images: one with atoms I_{atoms}, one without atoms $I_{\text{no atoms}}$ and one with no light I_{dark} to account for background light and dark counts on the camera CCD. The values $I_{f,i}$ are calculated as $I_{\text{atoms}} - I_{\text{dark}}$ and $I_{\text{no atoms}} - I_{\text{dark}}$, respectively, and the density of atoms is calculated from Eq. (3.16). The value of I_{sat} is converted to CCD counts using the camera specifications[15] and the known magnification and pixel size[16], measured by dropping ^{87}Rb atoms in the $|20\rangle$ state and measuring their trajectory.

One question that remains is how reliable is the calculated value of α? If the orientation of the polarization relative to the quantization axis is wrong, or if the model does not necessarily apply, then by using the calculated values of α we may under or overestimate the

[13] For instance, transitions between states with $f = 2$ and $f' = 3$ in ^{87}Rb.

[14] $\hat{\mathbf{e}}_{\pm 1} = \frac{1}{\sqrt{2}}(\hat{\mathbf{x}} \pm i\hat{\mathbf{y}})$ and $\hat{\mathbf{e}}_0 = \hat{\mathbf{z}}$.

[15] Obtained from the test data sent with the camera.

[16] Currently, the pixel size is 16×16 μm and the magnification is $1.441(3)$ with the Andor iXon camera.

density of atoms, and when attempting to simulate collisions an accurate density of atoms is crucial. It turns out that it is possible to measure α by using a fixed density of atoms and varying the intensity of the probing light. To avoid redistribution effects, it is necessary to keep the number of photons per probe pulse roughly constant, so the duration of the probe pulse must be varied inversely to the intensity. To measure α, I first solve Eq. (3.16) for $I_f(x,y)$

$$I_f(x,y) = \alpha I_{\rm sat} W\left(\frac{I_i(x,y)}{\alpha I_{\rm sat}} \exp\left[\frac{I_i(x,y)}{\alpha I_{\rm sat}} - \frac{n(x,y)\sigma_0}{\alpha}\right]\right) \tag{3.17}$$

where $W(x)$ is the Lambert-W function (Eq. (3.9)) evaluated on the principle branch. Dividing Eq. (3.17) by $I_i(x,y)$ and defining the saturation parameter $\xi = I_i/I_{\rm sat}$ I can write

$$\mathrm{OD} = \log\left(\frac{I_i}{I_f}\right) = -\log\left(\frac{\alpha}{\xi} W\left[\frac{\xi}{\alpha} e^{\frac{\xi}{\alpha} - \mathrm{OD}_0}\right]\right) \tag{3.18}$$

where $\mathrm{OD}_0 = n(x,y)\sigma_0/\alpha$ is the unsaturated optical depth of the sample. The measurement consists of keeping OD_0 fixed by keeping the atom number and temperature constant, imaging that sample of atoms with different values of the saturation parameter ξ, and measuring the resulting values of I_i/I_f. Both OD_0 and α are determined by fitting the data to Eq. (3.18); low saturation parameters will fix the value of OD_0 and high saturation parameters will determine the value of α. The results for ^{40}K are shown in Fig. 3.11a with $\alpha = 1.98(10)$, within the uncertainty of the expected value of $55/28 = 1.9643$.

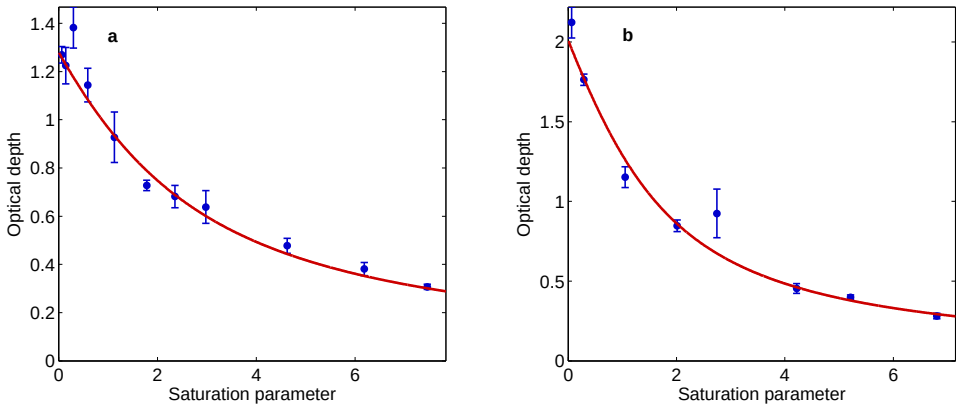

Figure 3.11: Measurement of the optical depth for ^{40}K (**a**) and ^{87}Rb (**b**) atoms as a function of saturation parameter. Circles are measured values, and the line is a fit to Eq. (3.18)

One can do the same measurement but with circularly polarized light and a bias field pointing along the direction of propagation as a sanity check; the results are shown in Fig. 3.11b for ^{87}Rb atoms. Here, I measure $\alpha = 1.006(61)$, within the uncertainty of the expected value of 1.

Finally, when investigating KRb collisions it is useful to be able to image both species of atoms in the same experimental run. For this reason, and also for improved signal-to-noise,

we installed an Andor iXon 897 frame-transfer CCD camera as the main imaging camera.[17] A frame-transfer system consists of two CCD arrays, one of which is permanently masked from exposure to light. During an exposure, the unmasked CCD collects light for the predetermined exposure time, and at the end of that time the charge in the unmasked CCD is transferred to the masked CCD. As charge is transferred row by row, this process takes only number of rows $\times$ 1/shift clock speed ≈ 160 μs to transfer the entire image to the masked CCD. Once the transfer is done a new image can be collected on the unmasked CCD. The data is read from the masked CCD pixel-by-pixel, a process that takes approximately 18 ms to complete. Using the frame-transfer CCD allows us to take two images with a programmable delay between them from 160 μs to 13 ms. Species selectivity is achieved by switching between the appropriate probe lasers. In this way we can take dual images of any combination of K and Rb.

3.7 Experimental control

Much like a Time Lord, computer control of the experiment has two hearts. Most of the experiment is controlled via a LabVIEW program called RebeKa, developed by Callum McKenzie. It provides a graphical interface for setting voltage levels (analog and digital) and times that are fed to National Instruments PCI cards.[18] The signals from these cards are then connected to various electronics which control, for example, voltage-controlled oscillators for AOMs or amplifier levels. RebeKa exclusively controls the setup, MOT, CMOT, transfer, and IP trap loading phases of the experiment. It also provides some of the control for the evaporative cooling phase and the main phase of the experiment when the atoms have been cooled to near their final temperature and are to be loaded into the optical tweezers for a particular experiment. The different phases of RebeKa can be triggered externally, and to synchronize the experiment with the 50 Hz power line we trigger the important phases of RebeKa on a 0-5 V signal generated from the 50 Hz line.[19]

The second heart is the Field Programmable Gate Array (FPGA) based imaging controller, currently implemented using a Xilinx Spartan 3AN evaluation board.[20][21] The master clock of the FPGA is 50 MHz, so it controls all time-sensitive signals where a timing resolution of better than 10 μs is needed. Currently, the FPGA controls the imaging sequence (probe AOMs, shutters, and the camera triggers), microwave and RF pulses, dispersive probing[119, 120, 121, 122] pulses for both Rb and K, optical tweezer on/off signals,

[17] http://bp.andor.com/scientific-cameras/ixon-emccd-camera-series/ixon-ultra-897

[18] PCI-6713, PCI-6733, PCI-6534, and PCI-MIO-16E-1[49]

[19] The electronics for this digital signal were designed and assembled by Matthew Chilcott.

[20] Part number (discontinued) HW-SPAR3AN-SK-UNI-G. See https://www.xilinx.com/products/boards-and-kits/hw-spar3an-sk-uni-g.html for specifications and manuals.

[21] The FPGA imaging controller was developed by Thomas McKellar[97] and later improved by me.

FlexDDS trigger pulses, and the Helmholtz servo (Sec. 3.8). The FPGA sequence is triggered from RebeKa and nearly all signals are timed from that point. The major exception is the dispersive probing subsystem which has its own trigger, allowing the dispersive probe to be used prior to the main experimental sequence – such as during evaporative cooling.

The architecture of the FPGA is defined using the hardware definition language VHDL, and parameters are uploaded to the FPGA using the Universal Asynchronous Receiver and Transmitter (UART) protocol. Parameters are encoded as a 32-bit word which is sent in 1 byte segments to the FPGA using the UART protocol and a USB-to-serial convertor. The FPGA reassembles this information and assigns parameters as needed. The FPGA can also transmit data to the controlling PC using the UART protocol; currently, this is being used exclusively for the Helmholtz servo.

In addition to RebeKa and the FPGA, there are several other control systems necessary for the experiment. Control of evaporation is provided via a GPIB connection to an Agilent function generator, and parameters are set using a LabVIEW interface.[22] A separate LabVIEW interface controls, and reads images from, the Andor camera. This interface also uploads the bitstream to the FlexDDS (see Sec. 3.4), and it provides a method by which a sequence of FPGA parameters can be uploaded to (and measurements downloaded from) the FPGA. Synchronization of these two LabVIEW interfaces, as they reside on a separate computer from RebeKa, is provided by a National Instruments USB-6009 data acquisition device.[23] One digital signal from RebeKa is used to initiate evaporative cooling, and a second one is used to prepare the camera for taking images, upload a new set of parameters to the FPGA, and start downloading the bitstream to the FlexDDS.

3.8 Helmholtz coil current servo

The Saga of the Servo[24] is a textbook example of the golden hammer fallacy: if all one has is a hammer, then everything looks like a nail. So it was with my attempts to stabilize the magnetic field produced by the Helmholtz (HH) coils for use in studies of Feshbach resonances.

The performance requirement of the servo is at first glance straightforward: stabilize the magnetic field sufficiently well that fluctuations of the field from its set point would be much smaller than the scale over which the resonant scattering phase changes significantly. One can estimate this scale by using the threshold resonance parameter Δ as a measure of the resonance's magnetic width (see Chapter 5); clearly, fluctuations of the magnetic field δB must be much smaller than $|\Delta|$. The Helmholtz coils were designed to be able to

[22] As of writing we are currently testing a new system using the FPGA.

[23] This is now a legacy device. A manual can be found at www.ni.com/pdf/manuals/375296a.pdf

[24] Or perhaps Servo-wulf.

reach a field of 1007 G where ^{87}Rb has a Feshbach resonance in its absolute ground state. This resonance has $\Delta = 0.17$ G, so one needs $\delta B \ll 0.17$ G. Suppose that $\delta B \approx \frac{1}{100}|\Delta|$ (certainly qualifying as much less than Δ); the magnetic field would need to be stabilized to a fractional variation of 1.7×10^{-6}. This is quite a stringent requirement, and it is the main reason for investigating other Feshbach resonances as they have less stringent stability requirements. The ground state Feshbach resonance of KRb near 546 G has $\Delta = -3$ G, requiring a fractional stability of only 5.5×10^{-5} – nearly fifty times less stringent. The ab channel Feshbach resonance in ^{40}K near 202 G is even less stringent with $\Delta = 7$ G[36], so it needs a fractional stability of 3.5×10^{-4}.

It is all well and good to have a magnetic field stable enough for Feshbach studies, but how does one *know* what the magnetic field is? The most common method for measuring a magnetic field is to use Rabi spectroscopy, whereby one measures the resonance frequency of a particular hyperfine atomic transition and compares that to a well-known theoretical description. If one can isolate a two-level system within the hyperfine manifolds – and this can nearly always be done – then one can use the celebrated Rabi-flopping equation to describe the population of atoms in the two states[57]

$$P_2 = \frac{\Omega}{(\omega - \omega_0)^2 + \Omega^2} \sin^2\left(\sqrt{\Omega^2 + (\omega - \omega_0)^2}\frac{t_{\text{pulse}}}{2}\right) \tag{3.19}$$

where P_2 is the probability of a single atom being in state 2, ω is the frequency of applied radiation, ω_0 is the resonant frequency of the transition, t_{pulse} is the duration of the radiation pulse, and Ω is the Rabi frequency (assumed to be real), proportional to the square root of the applied power and the matrix element connecting states 1 and 2. By picking a fixed Ω and t_{pulse}, and varying the frequency, one can measure P_2 (or $P_1 = 1 - P_2$) and extract the resonant frequency ω_0. This frequency is determined by the atomic parameters and the strength of the magnetic field through the Breit-Rabi formula[81]

$$\omega_0 = -\frac{\Delta\omega_{\text{hfs}}}{2(2i+1)} + g_i\frac{\mu_B}{\hbar}(m_i \pm m_s)B \pm \frac{\Delta\omega_{\text{hfs}}}{2}\left(1 + \frac{4(m_i \pm m_s)x}{2i+1} + x^2\right)^{1/2} \tag{3.20}$$

where $\Delta\omega_{\text{hfs}}$ is the hyperfine splitting frequency and

$$x = \frac{(g_j - g_i)\mu_B B}{\hbar\Delta\omega_{\text{hfs}}}.$$

The parameters in Eq. (3.20) are known extremely accurately[80, 81, 82], so the magnetic field B can also be accurately determined from a measurement of ω_0.

The problem with measuring the magnetic field via Eq. (3.19) is that there is a trade-off between frequency sensitivity and signal-to-noise. The ideal pulse length to use is one that corresponds to a π pulse, as this yields the greatest signal-to-noise. However, if the Rabi frequency is too low, then variations in the magnetic field will cause variations in

ω_0 that are larger than the width of the Rabi-flopping curve which is approximately $t_{\rm pulse}^{-1}$. These fluctuations will render any attempt to extract ω_0 hopeless. The obvious solution is to increase Ω, but one is typically limited in the amount of power that can be delivered to the atoms and thus limited in the attainable Rabi frequencies. Therefore, one needs to use shorter pulses which are less sensitive to frequency fluctuations but have lower signal-to-noise. Even so, fluctuations in the magnetic field have to be kept small: much smaller than is required for the wider Feshbach resonances. How small depends on the sensitivity of the transition to fluctuations in the magnetic field. For calibrating the Helmholtz coil, I used the ^{87}Rb $|20\rangle \rightarrow |10\rangle$ transition as it is the only transition in ^{87}Rb at 550 G that has a resonant frequency within the bandwidth of the microwave electronics. Given the Rabi frequency in our experiment of approximately $\Omega = 2\pi \times 3$ kHz for this transition the fractional magnetic field stability has to be about 10^{-5} to be able to reliably measure the transition frequency.

Stabilizing a magnetic field to 10 ppm requires that one can measure a magnetic field to better than 10 ppm, and magnetic field probes that can measure 550 G to within 10 mG would be expensive, bulky, and have low bandwidth. Instead, one stabilizes the current which generates the magnetic field and hopes that **(a)** the geometry of the coils does not change, and **(b)** ambient magnetic fields do not change. The HH coils are cooled from the mains supply of water which varies in temperature between experimental runs on the order of 1°C, and, given the coefficient of expansion of copper, these fluctuations probably add run-to-run fluctuations of at most 10 ppm. From re-optimizing π-pulses for state preparation, I estimate that ambient magnetic fields vary by about 2 mG day to day. Consequently, stabilizing the current to stabilize the magnetic field is a reasonable proposition, with most of the error arising from temperature. Stabilizing the temperature of the cooling water will ameliorate this issue.[25]

The current servo, therefore, consists of four major parts: the power supply, the current transducer, the servo electronics, and the actuator. A schematic is shown in Fig. 3.12. Two pairs of high-current relays are used to physically disconnect the HH coils and its actuator from the IP trap power supply and connect the HH coils to a separate power supply.[26] The power supply is an Agilent 6690A capable of supplying 0-15 V and 0-440 A; in most of the work that I have done I have set the voltage to 7.5 V, which is enough to push 200 A through the HH coils and associated connectors. The actuator is three MOSFETs arranged in parallel and connected to the current source and the HH coils.[27]. By varying the gate-source voltage on the MOSFETs, one can adjust the current from drain to source and hence through the HH coils.

[25] We are currently testing a new system for water cooling.

[26] These relays were installed by Milena Horvath and Amita Deb.

[27] MOSFET part number IXFN200N07. Each MOSFET has a transient suppression diode connecting drain and source.

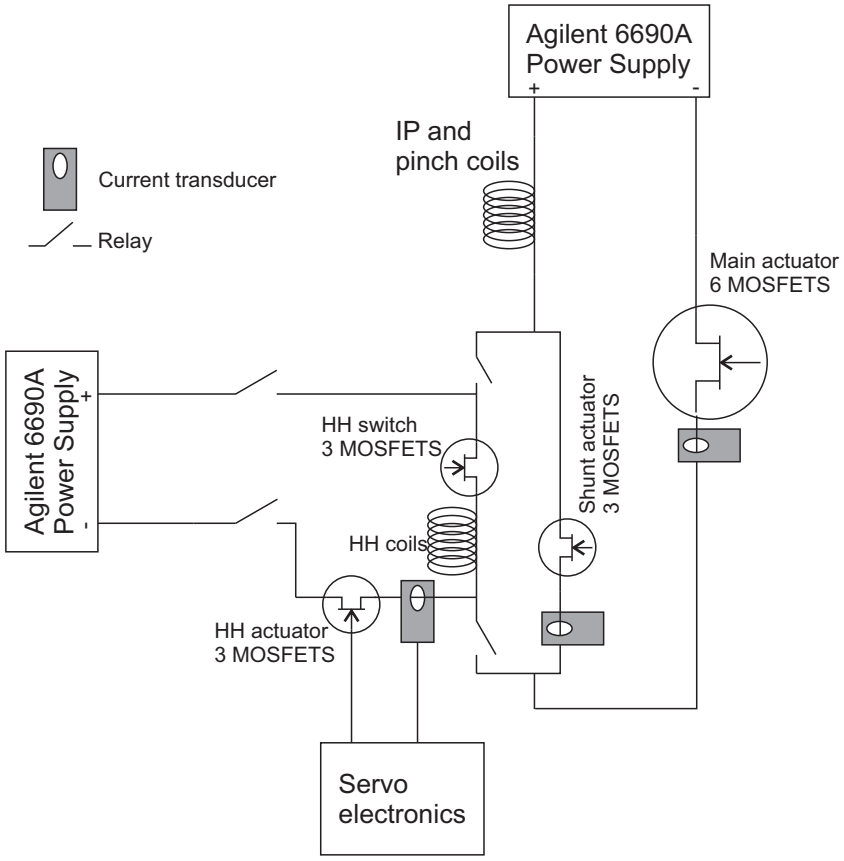

Figure 3.12: Schematic of the IP trap connections including relays for switching between power supplies.

So far, I have used two different models of current transducers in three different configurations with three different servo electronics. In the original servo design I used a Danfysik Ultrastab 866 current transducer with a voltage output module (VOM) that produced ± 10 V for ± 600 A of primary current. While convenient, as it did not require a precision sense resistor, the VOM produced a significant amount of noise which made it impossible to stabilize the current to any better than 10^{-4}. The servo unit itself was a very simple analog PI controller soldered onto a breadboard with voltage output limits and some precision unity-gain differential amplifiers.[28] The control signal was provided by an Agilent 33522A arbitrary function generator. None of the electronic components were particularly low-noise, and combined with the noise inherent to the VOM this limited the current stability.

The next iteration of the servo electronics involved obtaining proper low-noise and low-drift op-amps and making a proper printed circuit board (PCB).[29] A switch was included to reset the integral term to prevent wind-up when the servo was not in use and avoid large

[28] INA105KP

[29] Much of the credit for the servo schematic and PCB design/layout goes to Matthew Chilcott.

current spikes at the beginning of any current ramp. Additionally, due to the noise of the VOM, I chose to use a precision 1 Ω sense resistor[30] to generate a voltage from the current output of the transducer in the hope that this would be much less noisy. Finally, the control voltage was provided by a high-precision 20-bit digital-to-analog convertor (DAC)[31], as the resolution of the Agilent function generator was insufficient. This design had one major flaw in that the sense resistor was far too small for the currents of interest. Noise from the rest of the electronics contributed significantly to noise on the actuator signal and led to poor current stability. This problem was improved when we purchased precision 10 Ω sense resistors[32], but the noise from the rest of the electronics was still rather large.

A number of other issues manifested themselves. First was that the DAC was on an evaluation board that was separate from the servo PCB, and there were ground loops that affected the control signal. These were mostly eliminated by using an isolation amplifier between the DAC output and the PCB input. The second issue was that of controlling the DAC. Originally I used the Serial Peripheral Interface (SPI) on a Raspberry Pi, but this suffered from latency issues which made it an unreliable controller. This particular issue was solved by implementing an SPI interface on the imaging controller FPGA; indeed, this was my major motivation for retooling the FPGA architecture. However, it became clear that it was impossible to actually measure the stability of the current with the equipment that I had available – the noise floor of our oscilloscopes was too high and our $5\frac{1}{2}$ digit multimeter lacked sufficient time resolution – and hence it was impossible to optimize the performance of the servo. To this end, we purchased a 24-bit analog-to-digital convertor (ADC)[33] evaluation board whose digital control interface I also implemented via the FPGA. Using the ADC as a guide, I was able to reduce current fluctuations down to about 10^{-5}. However, it turned out that the settings for the various gain parameters (proportional, integral, and derivative) that reduced the noise the most were also on the edge of stability for the feedback loop. These gains were not themselves stable in time, and within 24 hours of optimizing the current stability to 10^{-5}, I found that the stability was now at about 10^{-2}. Clearly some way of stabilizing the PID gains was needed.

As I already had the FPGA controlling both the DAC and the ADC, it made sense to implement the controller digitally with the ADC measuring the voltage across a sense resistor connected to the current transducer, and the DAC generating the MOSFET gate-source voltage. The ADC itself has built-in filters to reduce noise and these are set by switches on the evaluation board; currently the servo uses the maximum filtration and hence the slowest sampling rate of one sample every 128 μs.[34]

[30] Vishay VHP471R0000.

[31] Analog devices AD5791 chip on evaluation board EVAL-AD5791SDZ.

[32] Vishay Y169010R0000T9L, 10 Ω, 8 W, 0.01% tolerance.

[33] Texas Instruments ADS127L01 chip on evaluation board ADS127L01EVM.

[34] The specifications say that the sampling rate is 8 kS/s, or a sample every 125 μs, but this is simply

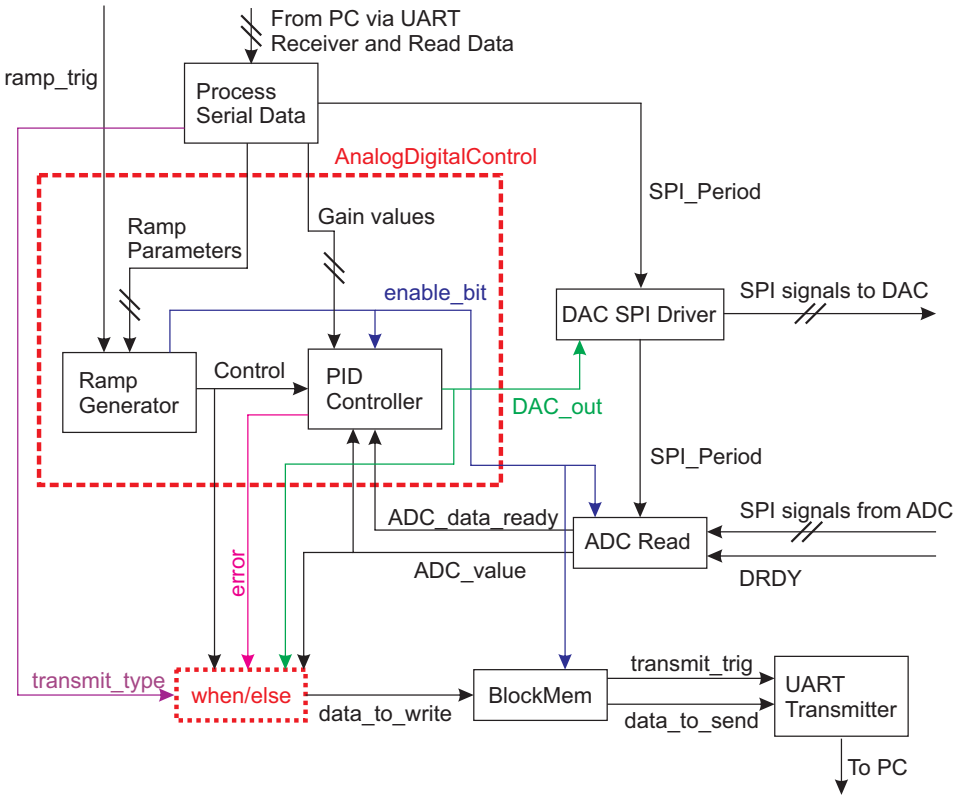

Figure 3.13: Schematic of the FPGA architecture that defines the behaviour of the HH servo. A double slash over a line represents multiple signals. Parameters are set to the FPGA from the PC and are processed by ProcessSerialData, which disperses the signals as necessary. See text for more details.

The current FPGA architecture for the PID controller is schematically shown in Fig. 3.13. The `RampGenerator` module accepts user inputs defining hold times, voltage codes, sample rate, and voltage code derivatives, and it generates linear ramps of the ADC voltage code. These ramps are sent to the `PID_Controller` module. The `ADC_Read` module waits for a falling edge of the `DRDY` signal from the ADC, which signifies that a new converted voltage value is ready, reads this value, and sends it to `PID_Controller`. `PID_Controller` has four main parameters: the proportional, integral, and derivative gains and a global divisor represented by an integer n. The error signal is formed from the difference between the measurement from `ADC_Read` and the control signal from `RampGenerator`, the integral and derivative terms are calculated from repeated summation and differencing (with conditional statements to prevent integral saturation), and the output value is calculated by multiplying each error term with its respective gain. The

rounding on the part of the manufacturer. The ADC requires 2048 clock edges to acquire and filter the data, and for the 16 MHz on-board clock this works out to be 128 μs. This timing can also be checked with an oscilloscope.

resulting value is then bit-shifted to the right by n-bits, approximating division by 2^n.[35] The combination of multiplication and bit-shift allows the FPGA to rapidly approximate any value of a gain parameter. This final value is passed through conditional statements to avoid overflow of the DAC code, and then this code is written to the DAC. A number of values, such as the DAC code, the ADC code, the error signal and so forth, can be stored in internal block RAMs on the FGPA chip, and these are then sent via the UART protocol to the controlling PC. Reading out the ADC code is necessary for optimizing the performance of the servo.

With this digitally controlled servo I use a different, lower-noise current transducer from Danisense.[36] Two terminals of a 10 Ω sense resistor are attached to the input junction box of the ADC evaluation board, and I further place a 22 μF capacitor in parallel with the sense resistor to reduce the amount of noise, which effectively creates a low-pass filter with a corner frequency of about 700 Hz. As the system is non-linear, different gain parameters are needed for different current ranges. Near 546 G the current servo performs as in Fig. 3.14 using a linear ramp of the set point from 0 V to 1.223 V in 75 ms with the start point of the sequence always triggered on the AC line. The primary source of noise is harmonics from the 50 Hz AC line, but, as the experiment is synchronized to that line, the beat-note pattern is stable from run to run. Due to these harmonics, I ensure that collisions near Feshbach resonances occur at the same time (0.755 s) from the start of the main phase of RebeKa to ensure repeatability of the magnetic field. Measuring the fluctuations from run-to-run shows that the servo obtains a fractional stability of better than 10^{-5}.[37,38]

Using the servo to stabilize the current and measuring the magnetic field using Rabi spectroscopy, I get the calibration curves as shown in Fig 3.15. I have shown two calibration curves for different voltage ranges due to the non-linearity of the system requiring different gain parameters. For the lower voltages, the calibration is

$$B = 2.1371(152)\ \text{G} + V_{\text{set}} \times 447.9750(222)\ \text{G/V}$$

and for the higher voltages

$$B = 2.1227(2137)\ \text{G} + V_{\text{set}} \times 448.001(174)\ \text{G/V}.$$

[35] In the same way that shifting a decimal number, such as 546, one place to the right to give 54.6 is equivalent to dividing by 10^1, shifting a binary number one place to the right is equivalent to dividing by 2^1. However, since the bit that was shifted to the right is discarded, this only approximates division by 2^1. Arbitrary powers of two are easily generalized.

[36] Danisense DS600IDSA http://www.danisense.com/images/pdf/0-600A/DS600IDSA.pdf

[37] I would have saved nearly four months if I had taken my father's advice on the matter, who, when told of the performance requirements, said that it would probably need to be digitally controlled.

[38] Similar performance has been achieved using analog circuitry in the PhD thesis of Andreas Marte[123] (only available in German).

The parameters associated with both curves are within their respective uncertainties of each other, indicating a highly linear relationship between B and $V_{\rm set}$ despite the need for different gain values. These two sets of data were taken two days apart which indicates that any drift in the magnetic field is smaller than the fluctuations induced by the stabilization method. Over the course of experiments with Feshbach resonances, I periodically checked the calibration by using adiabatic rapid passage centered on the expected transition frequencies and found that these sweeps always worked to transfer ^{87}Rb atoms from $|20\rangle \rightarrow |10\rangle$. From these checks, I can put an upper bound on the magnitude of the drift of the calibration at less than 40 mG over weeks-long timescales.

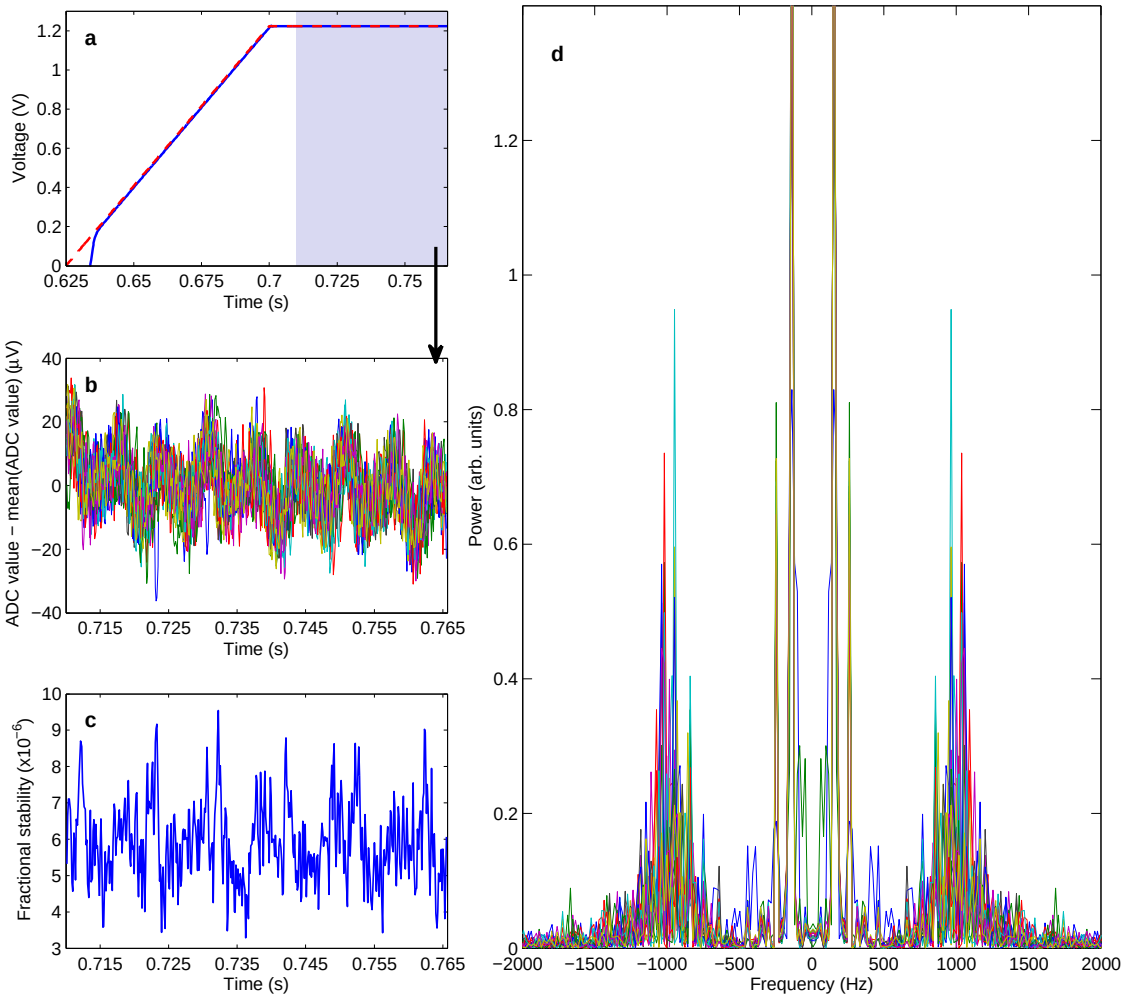

Figure 3.14: Behaviour of the HH servo over 10 repetitions. **a** Mean measured voltage (blue solid line) with behaviour of voltage set point (red dashed line). Blue shaded region indicates the time window plotted in **b**. **b** Voltage as measured by ADC with the mean value subtracted. Note that there is a slow relaxation of the current to its steady state value, but this is highly repeatable. As the experiment is triggered on the 50 Hz AC line, all harmonics due to 50 Hz noise are coherent. **c** Fractional stability of the voltage measured by the ADC as a function of time, calculated as the standard deviation of the ADC value over its mean. **d** Power spectrum of the ADC voltage. At 150 Hz the noise is coherent, and the higher frequency noise clustered at 1 kHz varies from run-to-run.

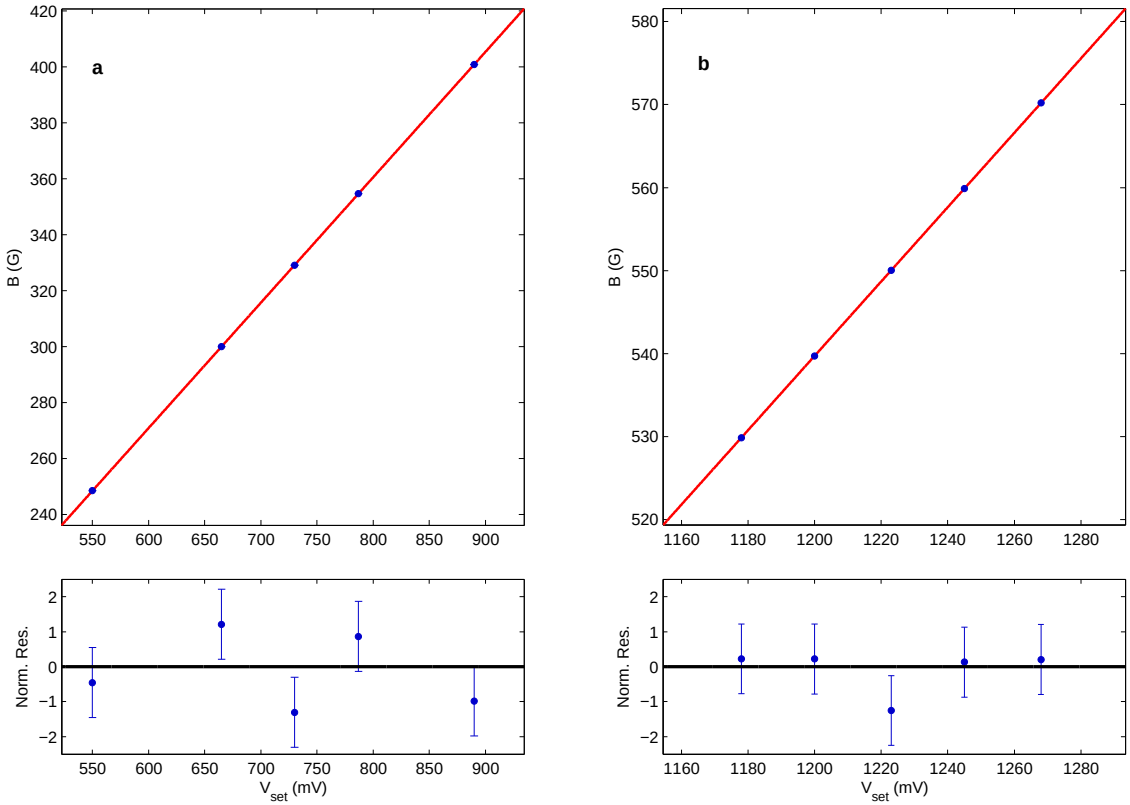

Figure 3.15: Calibration curves for the HH servo. **a** Magnetic field B measured using Rabi spectroscopy as a function of the set voltage V_{set} for the range $550 - 900$ mV. **b** Magnetic field B as a function of V_{set} for the range $1160 - 1280$ mV. Error bars are smaller than the line width of the plots. Lower plots are of fit residuals normalized to the uncertainty on their respective data points.

Chapter 4

Multiple scattering near a p-wave shape resonance

Suppose one has a sample of identical quantum particles prepared in the same internal state and wants to know whether the particles are bosons or fermions. How would one go about determining this fundamental property? One might be tempted to invoke the spin-statistics theorem[124, 57] and use a Stern-Gerlach apparatus to split the cloud into $2s+1$ components, but this only works if all spin states are populated. Since all the particles are in the same internal, but not motional, state, the Stern-Gerlach approach will not work. Instead, one needs to make use of the Pauli exclusion principle[11] and test whether or not the particles can be in the same internal *and* motional state at the same time. A possible test is to look at elastic collisions between the particles; if one divides the sample in twain and then smashes them together, the scattering amplitude will carry a tell-tale sign of the nature of the particles due to the symmetrization requirement in Sec. 2.4

$$f(\theta,\phi) \rightarrow \frac{f(\theta,\phi) \pm f(\pi-\theta,\phi+\pi)}{\sqrt{2}}$$

where the positive and negative signs apply to bosons and fermions, respectively. If the particles are bosons the amplitude will have even parity, and if the particles are fermions the amplitude will have odd parity. A direct measurement of the parity of the scattering amplitude is thus an unambiguous method for determining the particles' nature.

Of course, measuring the scattering amplitude directly is difficult; it is much easier to measure the differential cross section

$$\frac{d\sigma}{d\Omega} = \frac{1}{2}|f(\theta,\phi) \pm f(\pi-\theta,\phi+\pi)|^2$$

by counting the number of particles scattered into a given solid angle. For collisions with rotationally symmetric interactions, no fermions can be scattered at 90° to the collision axis regardless of collision energy– a so-called "forbidden" region. Bosons, in contrast, will

be scattered at $90°$ for nearly all collision energies.[1] If one has some knowledge about the inter-particle interaction, then the particle symmetry is nearly unambiguously determined from the presence or absence of particles scattered at $90°$.

Or is it? All of the theory developed in Chapter 2 applies to the situation when only two particles scatter from each other and then fly off behaving as free particles. Such an experiment rarely occurs in practice; instead, one takes ensembles of particles and smashes them together. For collisionally transparent samples, where the probability of an individual pair of particles colliding is small, the distribution of scattered particles is directly proportional to the differential cross section. For collisionally opaque samples, however, a particle that has experienced one collision has a high probability of experiencing another. This multiple scattering can lead to profound changes in the distribution of scattered particles which will no longer be directly proportional to the differential cross section. For collisionally opaque samples of indistinguishable fermions the resulting scattering halo may appear to violate anti-symmetrization by populating the "forbidden" region. Understanding the dynamics that leads to such apparent violation of fundamental physics is therefore of interest.

In this chapter I will present the results of an experiment involving the collisions of fermionic particles where the collisional opacity varies depending on the collision energy. Multiple scattering reigns over most of the energy range, and the exact energy dependence of the cross section has a dramatic effect on the distribution of scattered particles. I present quantitative comparisons between experimental data and simulations using the DSMC method of Sec. 2.8. This work has been published in [125], and was done in collaboration with Kris Roberts, Andrew Wade, Blair Blakie, Eite Tiesinga, Amita Deb, and Niels Kjærgaard.

4.1 Description of the experiment

In this work the fermions are neutral atoms of ^{40}K with both atoms prepared in the maximum spin state $|\frac{9}{2}\frac{9}{2}\rangle$. As the electron spins for both atoms are aligned, the total electronic spin state must be in the triplet configuration, and hence this experiment is very nearly a perfect single-channel problem.[2] The long-range interaction is dominated by the r^{-6} van der Waals interaction, so the Wigner threshold law Eq. (2.38) applies and we expect that the lowest energy scattering will have exclusively a p-wave distribution. The distribution of scattered particles is then

$$\frac{dN_{\rm sc}}{d\Omega} = \frac{3N_{\rm sc}}{4\pi}\cos^2\theta \tag{4.1}$$

[1] One can imagine that at certain, discrete, energies the different partial waves might interfere such that there is no scattering at $90°$, but this would require a very precise cancellation that would not persist at most collision energies.

[2] The dipole-dipole interaction mixes different channels, but this is a small correction.

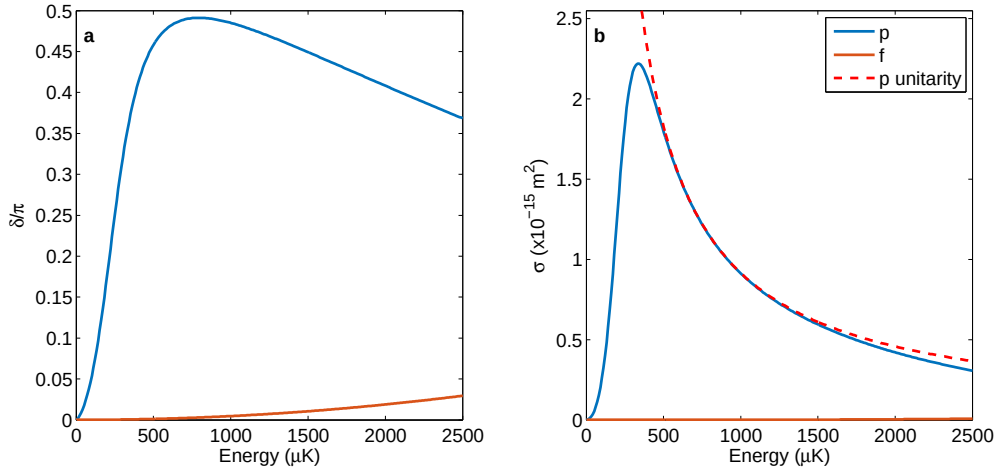

Figure 4.1: Lowest order scattering phase shifts **a** and partial cross sections **b** for ^{40}K-^{40}K scattering with both atoms in the $|\frac{9}{2}\frac{9}{2}\rangle$ state. Dashed red line shows the p-wave unitarity limit.

where $N_{\rm sc} = \int (dN_{\rm sc}/d\Omega) d\Omega$ is the total number of scattered particles. The cross section as a function of energy for p-wave elastic scattering at $B = 0$ is shown in Fig. 4.1. Similarly to the ^{87}Rb d-wave shape resonance in Fig. 2.5, the ^{40}K p-wave phase shift does not change by π across the shape resonance at 350 μK; instead, it reaches a maximum value of $\approx \pi/2$ and then starts to decrease. Dwelling at $\pi/2$ means that the width of the resonance is significantly wider than the ^{87}Rb d-wave resonance. In Fig. 4.1b I have also plotted the the maximum attainable cross section, given by the p-wave unitarity limit, which the p-wave partial cross section meets for a significant energy range, although not, curiously, at the peak cross section. Finally, I have included the f-wave phase shift and cross section; comparing to the p-wave cross section, I claim that all scattering in the energy range of $0 - 2000$ μK is p-wave. This is a crucial claim, because it means that any energy-dependent change in the shape of the inferred differential cross section must be due to multiple scattering effects rather than a change in the differential cross section itself.

The experiment starts by cooling a mixture of ^{87}Rb and ^{40}K atoms in the IP trap to a temperature of $\approx$ 700 nK before loading the atoms into the double well optical dipole trap described in Sec. 3.4. We split the initial double well in 75 ms into two wells that are separated by 5.8 mm, which at the time was the largest separation that we could obtain with the AOD diffraction efficiencies and available optical power. By adjusting the relative power in the two wells as they are split we can control the fraction of K atoms that remain in one well or the other; we aim for a splitting fraction of 50%. At this point we remove the Rb atoms using a resonant light pulse. As we evaporatively cool the K atoms in the $|\frac{9}{2}\frac{9}{2}\rangle$ state, we do not need to perform further state preparation. The temperature of the K atoms at this point is $1.3(1)$ μK with $3.50(35) \times 10^5$ atoms in each well. At this point we accelerate the two atom clouds towards each other using a sigmoidal profile (Sec. 3.4), and

when the two wells are separated by 80 μm we switch off the optical trap so that the atom clouds can collide in free space. We wait until the atom clouds are either separated by 1.65 mm or the time of flight after the trap is turned off is 1.25 ms, whichever has a greater time of flight. This was done because at very short times of flight the unscattered cloud is so dense that one cannot accurately count the number of atoms in the cloud. Very long times of flight, however, reduce the density of scattered atoms to an extent that the signal-to-noise is degraded. The above scheme was chosen as a suitable compromise. At the time of the experiment, we believed that a time of flight of 1.25 ms was sufficient to accurately count the atoms, but this turned out to not be the case.

Finally, for an accurate comparison between the experiment and DSMC we need to know the trap frequencies of the two wells. Depending on the axis, we measured the frequency in three different ways. For the vertical (y) axis we turned the horizontal beam off briefly (between $0.7 - 1.4$ ms) to allow the atoms to acquire momentum due to the force of gravity, and we measured the vertical position of the cloud after turning the beam on as a function of time to extract the frequency. For the z-axis we displaced the two wells suddenly by 5 μm and measured the resulting oscillations in the z-position of the cloud. The x-axis is more difficult to measure, and we settled on periodically modulating the horizontal trapping power and looking for parametric heating of the cloud. From these measurements, and assuming that the horizontal beam is symmetric, we can calculate the trapping frequencies due to all of the beams. The horizontal beam produces a trap with frequencies $(\omega_x, \omega_y) = 2\pi \times (250, 250)$ Hz, and the vertical beam produces traps with frequencies $(\omega_x, \omega_z) = 2\pi \times (384, 334)$ Hz. The x frequencies sum in quadrature, so the potential in each well is described by trap frequencies $(\omega_x, \omega_y, \omega_z) = 2\pi \times (457, 250, 334)$ Hz, giving in-trap cloud sizes of $(s_x, s_y, s_z) = (5.7, 10.4, 7.8)$ μm.

4.2 Image analysis

An absorption image of the collision halo at $E = 150$ μK is shown in Fig. 4.2a, where I have labeled the salient features. The dense, black circles are the Gaussian profiles of the unscattered atoms which expand and travel as expected for free particles released from a harmonic trap. As the collision partners have the same mass, the collision point is simply midway between the positions of the two unscattered clouds. The 3D collision halo, containing the scattered atoms, surrounds the collision point in a so-called "Newton sphere." It is important to keep in mind that the distributions of scattered and unscattered atoms overlap near the collision axis, so it is not possible to count all the scattered atoms directly: one must interpolate near the collision axis. Finally, as the atoms are fermionic, the image shows that there is no scattering at 90° to the collision axis, an angle marked by the blue

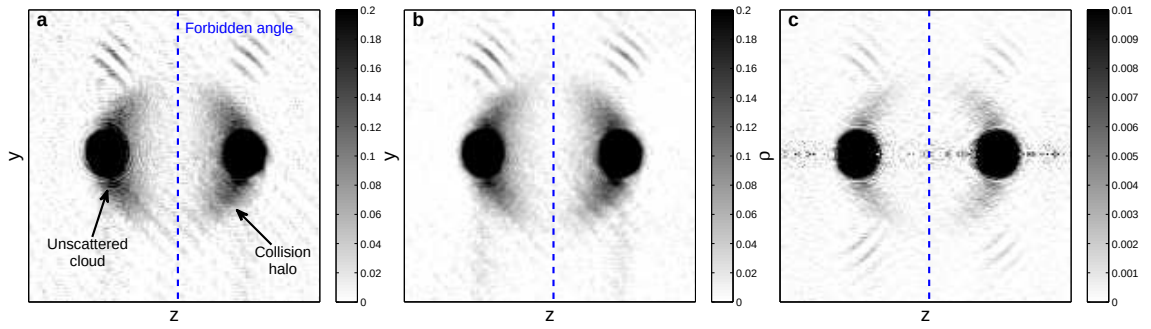

Figure 4.2: Gray scale absorption image of the collision halo formed by the collision of two ^{40}K clouds at $E = 150$ μK at different steps during processing. The collision axis is horizontal. Darker shades indicate more light absorption and hence a higher atom density: scale bars on right indicate optical depth. **a** Raw image. **b** After fringe-removal step. **c** After Abel inversion (note that the gray scale here is different from **a-b**).

dashed line in Fig. 4.2. Moreover, to the eye it appears that the halo follows a typical p-wave pattern with no atoms at $90°$ and the scattered atoms concentrated near the collision axis. Despite its ubiquity in discussions of partial wave scattering of fermions, this may be the first observation of a pure p-wave scattering halo in the collisions of fermions. Other experiments have observed p-wave distributions in the dissociation of p-wave Feshbach molecules[126] or in the ejection of photoelectrons from photoionization[127]; however, neither of these p-wave distributions resulted from the underlying symmetry requirements of the particles. In contrast, the effect of anti-symmetrization on the differential cross section has been observed in Coulomb scattering of fermions[128], but these distributions are not p-wave, and the lack of spin polarization means that there is no extinction of scattering at $90°$.

To demonstrate that the halo is indeed p-wave, we need to extract the scattering distribution from the image. The distribution of atoms in 3D can be described by a function $P(r, \theta, \phi)$ in spherical coordinates whose angular dependence is related to the differential cross section. The absorption image is a projection of this distribution onto a 2D plane; since we image along the x-axis, the absorption image is described by the function

$$\tilde{P}(y, z) = \int_{-\infty}^{\infty} P(r, \theta, \phi) dx = \int_{-\infty}^{\infty} P(\rho, z, \phi) dx,$$

where $\rho = \sqrt{x^2 + y^2}$ is the usual cylindrical coordinate. In our experiment the scattering distribution is azimuthally symmetric, so $P(r, \theta, \phi) = P(r, \theta)$ and $P(\rho, z, \phi) = P(\rho, z)$; i.e., the distribution is independent of ϕ. In that case, the projection associated with absorption imaging is a so-called Abel transform of the 3D distribution[129]. Given the 2D distribution $\tilde{P}(y, z)$, one can invert the Abel transform to get $P(\rho, z)$ in cylindrical co-

ordinates as shown in Fig. 4.2c: from this distribution, $P(r, \theta)$ can be calculated. There are a number of methods that one can use; I have chosen to use the Basis Set EXpansion (BASEX) method[130]. In brief, the BASEX method works by defining a set of Gaussian basis functions whose Abel transforms are known analytically. The 2D distribution is decomposed into the transformed basis and the coefficients of that decomposition are used to reconstruct the 3D distribution. This method has the advantages of handling noisy data with large pixel-to-pixel fluctuations well, of being computationally fast such that it can be employed as the experiment is running, and of confining noise generated during the inversion process to near the $\rho = 0$ line. A key difference between our implementation and that in [130] is we do not assume left-right symmetry; symmetry about the z-axis, however, is enforced by Abel-inversion.[3]

Even though BASEX handles noise well, the input image for Abel-inversion ideally should be as "clean" as possible: there should be a minimum of random noise and other, more structured, technical noise. In this experiment, structured noise in the form of interference fringes was more of an issue than random noise; these fringes can be seen in Fig. 4.2a. The very obvious, upper pair of fringes is due to back-reflection from the surfaces of the science cell of the light field scattered by the dense clouds and are impossible to eliminate entirely without replacing the science cell.[4] Luckily, they generally lie outside of the scattering halo and can be excluded from the analysis by a judicious choice of analysis region. Less prominent, but more problematic, fringes appear throughout the image and overlap with the lower right-hand part of the scattering halo. These fringes arise from imperfect matching between the light field used to image the atoms and the reference field: $I_{\text{atoms}}(y, z)$ and $I_{\text{no atoms}}(y, z)$. As there is a non-zero amount of time between the two images, the position of fringes on these images can shift due to, for instance, air currents in the imaging path. To reduce the effect of these fringes, I use a fringe-removal technique[131] that generates a reference image $I_{\text{no atoms}}(y, z)$ from a set of such images that most closely matches, in the least-squares sense, the image with atoms $I_{\text{atoms}}(y, z)$. The post fringe-removal image is shown in Fig. 4.2b. The result of Abel-inversion of this image using BASEX is shown in Fig. 4.2c.

From the Abel-inverted image, I can extract the scattering distribution with the use of two assumptions regarding the collision halo. First, I ignore the initial spatial extent of the atom clouds and assume that all collisions take place at a single location. As long as the expansion time after the collision is long enough, this assumption is valid and we can ignore the spatial extent. In the experiment, the initial cloud size is approximately 8 μm at $T = 1.3$ μK and a (geometric) mean trapping frequency of 340 Hz. In the time it takes for the clouds to travel from the trap turn-off point to the collision point – a separation distance of 80 μm

[3] Note that in the original paper[130] Eq. A3 should be multiplied by $\sqrt{\pi}$.

[4] Anti-reflection coated glass would significantly reduce the amplitude of these fringes.

– the clouds have expanded to at most 10 μm in size. We let the collision halo expand to a diameter of at least 1.65 mm before we image, so if we look at scattering into $90°$ there will be contributions from the edges of the cloud that actually scatter into $89.65°$ and $90.35°$. If we assume that the edges of the clouds will contribute as many scattered atoms as the centers of the clouds, the offset we will see in the measured scattering distribution will be at most 10^{-4} of the maximum of the distribution, which is well below the noise floor of our measurements.[5]

The second assumption that I make is to ignore the thermal distribution of total momentum between colliding atoms, so that in the laboratory frame the magnitude of the final momentum of both collision partners is the same. The spread in the total momentum will lead to a Gaussian smoothing of the scattering distribution with a width on the order of $\sqrt{kT/E} < 6°$: equivalent to an offset at a scattering angle of $90°$ of 2% of the maximum differential cross section. Again, this is less than the noise level on our measurements, so we can safely ignore the effect of the distribution of total momentum.

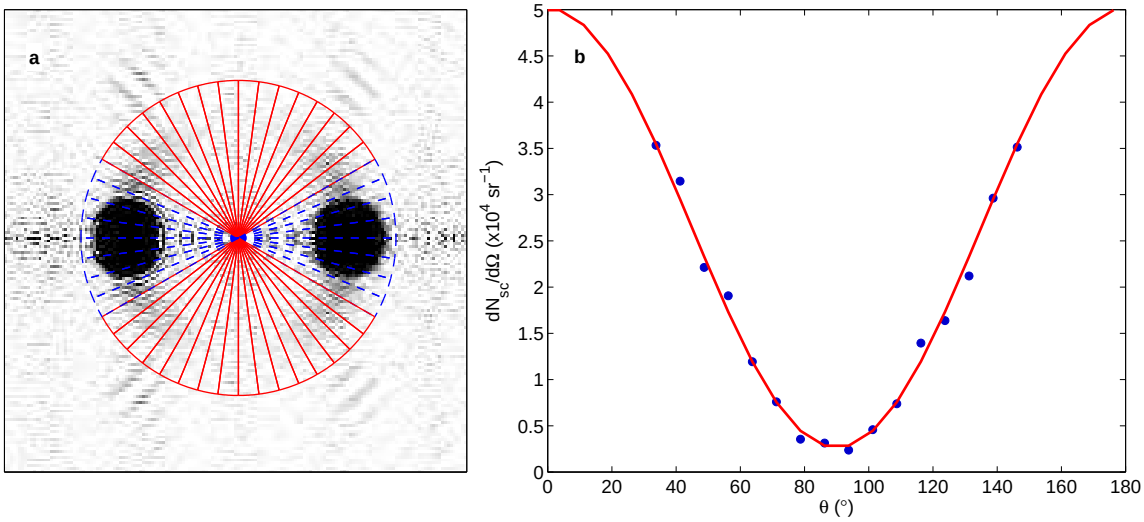

Figure 4.3: Analysis of absorption image of ^{40}K-^{40}K scattering at $E = 150$ μK. **a** Abel-inverted gray scale image with angular bins. Red solid-lined bins are used in the analysis; blue dashed-lined bins are excluded. **b** Scattering distribution extracted from image. Blue circles are experimental data points, solid line is a fit to Eq. (4.2). Only angles in the interval $[0, 180°]$ are plotted because Abel inversion forces reflection symmetry about the z axis.

With these assumptions, I can separate the distribution of atoms into $P(r, \theta) = P_r(r)P_\theta(\theta)$; integrating over all r gives $\int_0^\infty P(r, \theta)r^2 dr = P_\theta(\theta) \propto \frac{d\sigma}{d\Omega}$. I divide the Abel-inverted image

[5]The edges have lower density, so there will be fewer atoms scattered from the edges of the clouds than the centers. Assuming that the rates are the same establishes an upper bound on the systematic error caused by finite cloud size.

into angular sections which start at $r = 0$ and end at a final radial distance $r_{\max}$ that is equal to the position of the unscattered clouds plus three times their width, as shown in Fig. 4.3a. I do not include angular bins near the collision axis in the analysis to avoid contaminating the measurement of the scattering distribution with unscattered atoms. Typically, I exclude angular bins that are within 2.5 times the angular width of the unscattered clouds. The exact values of these analysis parameters, including the total number of bins, do not appreciably influence the final results. I have plotted the extracted scattering distribution in Fig. 4.3b, as well as a fit to a p-wave shape with an offset

$$D(\theta) = a\cos^2\theta + b \tag{4.2}$$

where the offset b captures both technical imperfections[6] and the influence of multiple scattering.

4.3 Scattering distributions

We measured the scattering distribution $\frac{dN_{\rm sc}}{d\Omega}$ as a function of scattering angle θ for a range of collision energies from 50 μK to 1800 μK, and the results are shown in Fig. 4.4.[7] At energies less than 180 μK, the measured scattering distributions are consistent with a pure p-wave halo. Small offsets on the curves are attributable to technical imperfections in the experiment; namely, the influence of noise on the images and, more importantly, impurities in the prepared spin state. An impurity level of 5% of atoms in other spin states would yield offsets of this magnitude. As a result, Eq. (4.2) matches the data very well with a small offset b.

At higher energies, between 180 μK and 800 μK, we observe scattering halos with an energy dependent isotropic component, which manifests itself as a significant offset in the measured particle distribution as can be seen in Figs. 4.4c and h. As a result, there is scattering into angles that are 90° from the collision axis, which is in apparent violation of the anti-symmetrization requirement. This isotropic component is a result of multiple scattering of the atoms due to a combination of high atomic density and a large cross section; this type of multiple scattering only appears when the cross section is near its maximum. The appearance of isotropic scattering from purely p-wave scattering events can be understood by considering the effect of a rotation of the collision axis on the scattering distribution. Suppose that the axis for a collision event is rotated from the nominal collision axis of

[6] These imperfections come from two main sources: structured noise from imperfect matching of probe and reference beams during imaging, and imperfect state preparation leading to some atoms being in different internal states. The latter will lead to s-wave scattering (and an offset) that will generally decrease with energy.

[7] We took data for higher energies, but the loss of atoms from the traps as they accelerated rendered this data mostly useless.

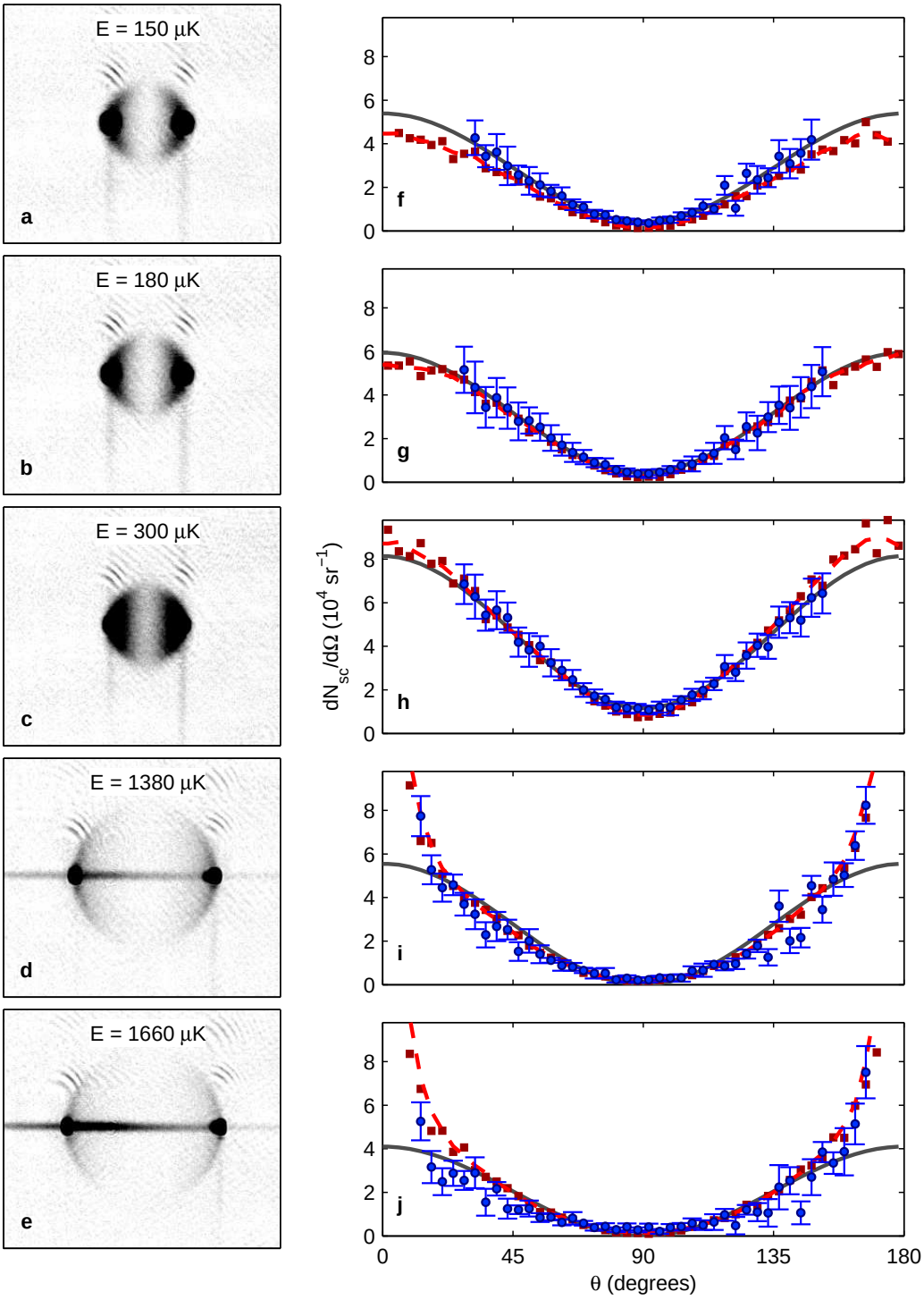

Figure 4.4: Images of ^{40}K collisions and their respective scattering distributions. **a-e** Grayscale absorption images at the specified collision energy. **f-j** Corresponding scattering distributions. Blue circles are mean values measured from five such images, and the error bars are the standard deviation over these images plus a 4% systematic error in determining the number of atoms. The gray line is a fit to Eq. (4.2). The red squares are from a DSMC model of the collisions, and the dashed red line is a smoothed version of the red squares (see Sec. 4.5).

$\theta = 0$ by a small, random angle θ_0. As there is rotational symmetry about the z-axis, the mean of the distribution of θ_0, $\langle\theta_0\rangle$, must be zero. The scattering distribution describing this collision event is

$$\cos^2(\theta - \theta_0),$$

which, when averaged over many realizations, has the form

$$\langle\cos^2(\theta - \theta_0)\rangle = (1 - 2\langle\theta_0^2\rangle)\cos^2\theta + \langle\theta_0^2\rangle.$$

Adding the above to the underlying p-wave distribution we get Eq. (4.2). From where do these rotations in the collision axis arise? A very small fraction are due to the thermal distribution of velocities, but the significant rotations that we observe are due to multiple scattering events involving secondary collisions between an atom that has already had one collision and an atom that has had no previous collisions.

At higher energies yet, above 800 μK, the isotropic component returns to its low-energy value, but the shape of the distribution changes markedly from being described by a p-wave halo. Figs. 4.4d,i and e,j show two examples of the measured distribution and their comparison with Eq. (4.2). The measured distributions have a wider trough at 90° and show enhanced scattering along the axial directions of 0° and 180°. These deviations from the expected behaviour are also due to multiple scattering, but through a different mechanism (see below). The left-right asymmetry seen in Fig. 4.4j is due to a combination of multiple scattering and loss of atoms from the right-hand trap as it accelerates; an imbalance in atom number between two colliding clouds has previously been noted to break left-right symmetry due to multiple scattering[132]. The atoms that are lost from the trap as it accelerates can be seen as the horizontal line of atoms in Figs. 4.4d and e. All images show loss of atoms in the vertical direction as vertical lines of atoms below the unscattered clouds, and these are due to atoms escaping the weaker horizontal trap and falling under the influence of gravity while still being trapped by the strong vertical beams.

The prevalence of multiple scattering and its effect on the scattering distribution is (for fixed atom density) directly related to the energy dependence of the cross section, and we can qualitatively separate the collision energies into three regions. In the region where $E < 180$ μK, the cross section is low and the Wigner threshold law forces it to approach zero as the energy decreases, so multiple scattering – which must occur at a lower energy than the nominal energy – is suppressed and we see a pure p-wave halo: we define this as the *suppression* region. The mid-range of $180 < E < 800$ μK is where the cross section is the highest, and we have *isotropic enhancement* of the scattering distribution. Finally, the high energy region of $E > 800$ μK shows *axial enhancement* of the distribution. To see how the cross section affects multiple scattering and the distribution of scattered particles, let us consider the simplest (and most likely) scenario. A primary collision event will be between

two atoms that have experienced no other collisions. They will initially have diametrically opposed momenta aligned with the collision (p_z) axis as in Fig. 4.5a. The final momenta

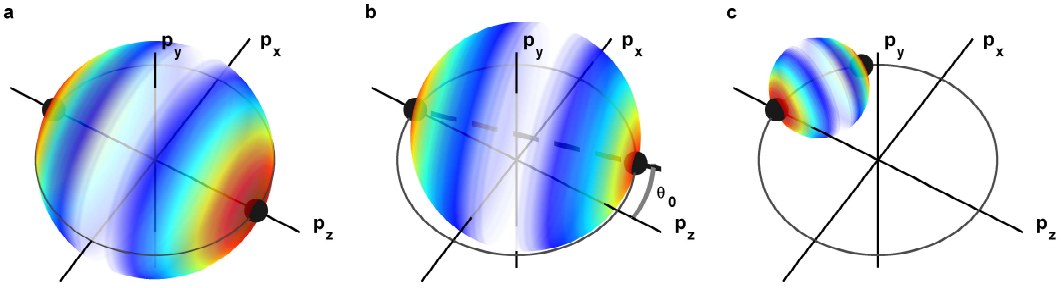

Figure 4.5: Momentum space representation of primary and multiple scattering. **a** Primary scattering event between two atoms (black circles) with opposite momenta on the p_z axis. They scatter onto a momentum shell given by the coloured sphere with a probability of scattering into any given direction given by the colour of the sphere, with white being zero and red an arbitrary maximum. **b** Collisions between atoms that are nearly counter-propagating occur at a slightly smaller collision energy ($E \propto p^2$) and produce collision halos that are slightly rotated from the p_z axis by an amount θ_0. **c** Collisions between atoms that are nearly co-propagating occur at a much lower collision energy and produce two atoms whose momenta lie close to the collision axis.

of these atoms will lie on a momentum shell defined by the initial momentum, and hence the initial collision energy. The direction of the final momenta is determined by the p-wave differential cross section. For sufficiently low cross sections, primary collision events will be the only collision events, and multiple scattering events will be suppressed. For primary collision energies less than 180 μK the cross section is low due to the Wigner threshold law, which is why in this region we see pure p-wave halos.

Higher cross sections will cause some degree of multiple scattering. The most probable secondary collision is between an atom that has had no previous collisions (lies on the z axis) and one that has had one previous primary collision. As there are two dense clouds of atoms traveling in opposite directions along the z axis, this secondary collision is most likely to be either between atoms that are nearly counter-propagating or between atoms that are nearly co-propagating.[8] For atoms that are nearly counter-propagating, as in Fig. 4.5b, the collision axis will be shifted from the nominal collision axis along p_z by a random angle θ_0. As discussed above, over many realizations a small random rotation of the collision axis

[8]This is true in general barring resonances at energies less than $E_{\rm nom}$ with sufficient strength to overcome the significant reduction in atom density off of the collision axis. The resonant cross section here would need to be at least an order of magnitude higher than the p-wave resonant cross section, so such a resonance is highly unlikely.

will appear as an isotropic component on an otherwise pure p-wave halo. The energy of this secondary collision will be nearly as large as the primary collision energy, so this process will be favoured only when the cross section at the primary collision energy is already large. As seen in Fig. 4.1b, the energy range of 180 to 800 μK is associated with a large, resonant cross section, and, as a result, we see an enhancement of the isotropic component in our scattering distributions.

If the secondary collision occurs between atoms that are nearly co-propagating, as seen in Fig. 4.5c, then the final momenta of both atoms will be more closely aligned with the collision axis than for the previous two cases. However, the secondary collision energy will be much lower than the primary collision energy, and the closer the atoms lie to the collision axis the smaller the secondary collision energy. This process is unlikely to occur unless the cross section increases significantly for energies lower than the primary collision energy. This is exactly the case for collisions where the primary collision energy is greater than 800 μK (Fig. 4.1b). Co-propagating collisions, which enhance the scattering distribution along the axial directions, are favoured at high energies because of the isolated p-wave resonance near 350 μK. We therefore expect most of these secondary collisions to occur at or near the resonance energy.

4.4 Total scattered atoms

From the fits of the scattering distributions to Eq. (4.2), we can extract the total number of scattered atoms by integrating over all angles to get

$$N_{\mathrm{sc}} = \frac{4\pi}{3}a + 4\pi b$$

where the coefficient a arises from both primary and secondary collisions and the coefficient b arises solely from the multiple scattering that leads to isotropic enhancement. By using the fit parameters to calculate N_{sc}, rather than summing the data, we can interpolate over the angular regions obscured by the unscattered clouds. Additionally, this approach is more immune to noise on the data. However, I should note that since the axial enhancement region is not well described by Eq. (4.2), the values of N_{sc} extracted in this way may be systematically different from the true value. I will address this point further in Sec. 4.5.

In Fig. 4.6 I plot both the total number of scattered atoms and the number in the isotropic halo. We see that the total number of scattered atoms broadly follows the same trends as the ^{40}K cross section does in Fig. 4.1, as is expected. The inclusion of the isotropically scattered atoms in Fig. 4.6 provides additional information regarding the prevalence of multiple scattering. We see that in the suppression region the total number of scattered atoms increases sharply due to the increase in cross section, but the number of isotropically

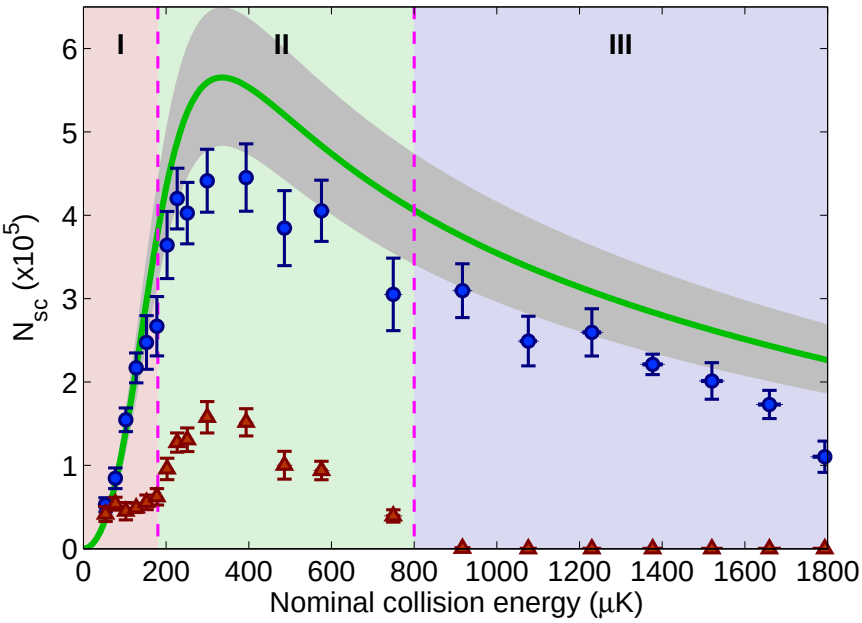

Figure 4.6: Scattered atoms as a function of the nominal collision energy. Blue circles are the total number of scattered atoms; red triangles are only the isotropically scattered atoms. Green line is the prediction based on Eq. (4.10) using the measured total number of atoms of $9.6(1.0) \times 10^5$, and the grey region indicates the uncertainty in the prediction. Coloured sections indicate the different collision regions: **I** suppression, **II** isotropic enhancement, **III** axial enhancement.

scattered atoms remains constant. From this observation, we conclude that this fraction is due to both noise on the image and an energy-independent number of impurity atoms in different spin states. In the isotropic enhancement region, however, we see that the total number of scattered atoms varies more slowly while the number of isotropically scattered atoms peaks near the resonant cross section at 350 μK. In the axial enhancement region the isotropic component drops to zero.[9]

Given knowledge of the cross section and the density of our atomic sample, I can use a simple analytical model to calculate the total number of scattered atoms. The starting point of the model is the classical Boltzmann equation for elastic scattering of equal-mass particles in free space

$$\left[\partial_t + \frac{\mathbf{p}}{m}\cdot\nabla_{\mathbf{r}}\right] f(\mathbf{r},\mathbf{p},t) = \frac{1}{m}\int\left[f(\mathbf{r},\mathbf{p}_1',t)f(\mathbf{r},\mathbf{p}',t) - f(\mathbf{r},\mathbf{p}_1,t)f(\mathbf{r},\mathbf{p},t)\right] \times |\mathbf{p}-\mathbf{p}_1|\frac{d\sigma}{d\Omega}\delta(\mathbf{p}+\mathbf{p}_1-\mathbf{p}'-\mathbf{p}_1')\delta(p^2+p_1^2-(p')^2-(p_1')^2)d^3\mathbf{p}_1 d^3\mathbf{p}' d^3\mathbf{p}_1' \quad (4.3)$$

where $f(\mathbf{r},\mathbf{p},t)$ is the phase-space density of atoms normalized to the total number of atoms and m is the mass of an individual atom. The two Dirac delta functions in Eq. (4.3)

[9] I will note that the actual offset is not exactly zero, as can be seen in Figs. 4.5i and j, but the best fit to Eq. (4.2) has $b = 0$. The actual offset is approximately the same as in the suppression region.

enforce conservation of energy and momentum, and $\frac{d\sigma}{d\Omega}$ is a function of only the energy and the relative initial and final momenta. The interpretation of the collision integral on the right-hand side of Eq. (4.3) is that the first term in the square brackets represents the gain in atoms that scatter into momentum $\mathbf{p}$ while the second term is the loss of atoms that scatter from momentum $\mathbf{p}$. To solve Eq. (4.3), I make three simplifying assumptions[41, 133]:

1. The initial phase-space density is assumed to be $f(\mathbf{r},\mathbf{p},t) = n_1(\mathbf{r},t)\delta(\mathbf{p}-p_0\hat{\mathbf{z}}) + n_2(\mathbf{r},t)\delta(\mathbf{p}+p_0\hat{\mathbf{z}})$; i.e., I ignore the initial Maxwell-Boltzmann momentum distribution of the atoms.

2. The dynamics of the scattered atoms are ignored. This assumption means I ignore the gain term in the collision integral and I integrate Eq. (4.3) over $\mathbf{p}$.

3. The atomic density distributions remain Gaussian throughout the collision.

With these assumptions, I can reduce the Boltzmann equation to a pair of coupled transport equations

$$(\partial_t + v_i\partial_z)n_i(\mathbf{r},t) = -\sigma v n_1(\mathbf{r},t)n_2(\mathbf{r},t) \tag{4.4}$$

where n_i and v_i are the densities and velocities of the two clouds, and $v = |v_1 - v_2| = 2v_0$ is the magnitude of the relative velocity of the clouds with $v_0 = p_0/m = \sqrt{E_{\rm nom}/m}$. I define the densities to be

$$n_i(\mathbf{r},t) = \frac{N_i(t)}{(2\pi)^{3/2}s_{x,i}s_{y,i}s_{z,i}} e^{-\frac{x^2}{2s_{x,i}^2}-\frac{y^2}{2s_{y,i}^2}-\frac{(z-v_it)^2}{2s_{z,i}^2}} \tag{4.5}$$

where $N_i(t)$ is the time-dependent number of atoms and $s_{x,i}$ is the width of the cloud in the x-direction (and similarly for y and z). Equation (4.4) can be integrated over all of x and y to give

$$(\partial_t + v_i\partial_z)n_i(z,t) = -\sigma v \frac{N_1(t)N_2(t)}{(2\pi)^2\xi_x\xi_y s_{z,1}s_{z,2}} e^{-\frac{(z-v_1t)^2}{2s_{z,1}^2}-\frac{(z-v_2t)^2}{2s_{z,2}^2}} \tag{4.6}$$

where $\xi_x = \sqrt{s_{x,1}^2 + s_{x,2}^2}$ and similarly for ξ_y. I can further integrate over all of z by using $\int_{-\infty}^{\infty}\partial_z n(z,t)dz = n(\infty,t) - n(-\infty,t) = 0$ to get an ordinary differential equation for $N_i(t)$

$$\frac{dN_i(t)}{dt} = -\sigma v \frac{N_1(t)N_2(t)}{(2\pi)^{3/2}\xi_x\xi_y\xi_z} e^{-\frac{(vt)^2}{2\xi_z^2}}. \tag{4.7}$$

I make the simplifying assumption that the initial numbers of atoms in each cloud are the same, $N_1(-\infty) = N_2(-\infty)$. Since $dN_1(t)/dt = dN_2(t)/dt$, I have for all time that $N_1(t) = N_2(t)$. Therefore, I need only solve

$$\frac{dN_1(t)}{dt} = -\sigma v \frac{N_1^2(t)}{(2\pi)^{3/2}\xi_x\xi_y\xi_z} e^{-\frac{(vt)^2}{2\xi_z^2}}, \tag{4.8}$$

which can be integrated from $t = -\infty$ to $t = \infty$ to yield

$$\frac{1}{N_{1,i}} - \frac{1}{N_{1,f}} = -\frac{\sigma}{2\pi\xi_x\xi_y} \tag{4.9}$$

where $N_{1,i}$ and $N_{1,f}$ are the initial and final numbers of atoms in cloud 1, respectively. Defining the total number of atoms $N(t) = N_1(t) + N_2(t) = 2N_1(t)$ and the scattered fraction $S = (N_i - N_f)/N_i$, I get

$$S = \frac{\alpha\sigma}{1 + \alpha\sigma} \tag{4.10}$$

where $\alpha = \frac{N_i}{4\pi\xi_x\xi_y}$. For this experiment, the initial cloud temperatures and trapping frequencies are the same, so I assume that the widths are the same and are equal to the in-trap equilibrium values of $s_x = \sqrt{\frac{kT}{m\omega_x^2}}$ and similarly for s_y.

We measured the total number of atoms before accelerating the clouds towards each other to be $9.6(1.0) \times 10^5$ atoms, and using this value (and its uncertainty) I have plotted the prediction of Eq. (4.10) in Fig. 4.6. The prediction significantly and systematically overestimates the number of scattered atoms at nearly every energy except the lowest energies. The most likely explanation of this is that the number of atoms that participate in the collision is not what we have measured. As the atom clouds are accelerated towards each other, some atoms are lost due to deformation of the trap from inertial forces – see Sec. 3.4. Ideally, one would measure the total number of atoms participating in a collision by summing over an entire absorption image, but this turned out to underestimate the total number of atoms by a significant amount and is most likely due to the small, dense nature of the unscattered clouds. Instead, we infer the total number of atoms by assuming that the cross-section is correct and fitting a model with one free parameter to the number of scattered atoms in order to get the total number of atoms participating in the collision. However, as mentioned previously, the manner by which we extract the number of scattered atoms will have systematic errors that may make comparison with the analytic model unreliable. Instead of using Eq. (4.10), we simulate the experiment using the DSMC method described in Sec. 2.8 and use that model for the fit as described in the next section.

4.5 DSMC comparison

In principle, one can simulate the entire collision sequence, including the acceleration phase, using DSMC. While this can be useful, it is also computationally time consuming because the acceleration phase can last up to 80 ms, and the simulation must take time steps that are much less than the shortest trapping period. Instead, we start the simulation at the point where the optical dipole trap is switched off and the clouds are separated by 80 μm. The positions of the atoms are initialized to be in the equilibrium configuration of a harmonic trap with a temperature of of $T = 1.3$ μK and trapping frequencies

$(\omega_x, \omega_y, \omega_z) = 2\pi \times (457, 250, 334)$ Hz. The total number of atoms N_i is divided in half, and each cloud is apportioned an equal number of test particles; we use 2×10^5 test particles for the least-squares determination of N_i, and 10^6 test particles once N_i is known. The velocities of the atoms are initialized to Maxwell-Boltzmann distributions whose mean values are shifted by $\pm v_0 \hat{\mathbf{z}}$ with $v_0 = \sqrt{E_{\mathrm{nom}}/m}$. We let the simulation run until 5 ms past the time at which the cloud centers overlap, at which point the clouds are separated enough that no further collisions take place. For each collision energy, we evolve the positions of the atoms according to their velocities until the final time of the simulation matches the time-of-flight in the experiment.

As DSMC tracks individual particles, we can calculate the number of scattered atoms by counting the number of atoms that have never experienced a collision and subtracting that from the total number. However, this would not be useful for comparing to the experiment because we must analyze absorption images, rather than count individual particles, in the experiment. Such a difference in analysis would lead to systematic errors. Instead, we generate synthetic absorption images by projecting the final test particle distribution onto the $y - z$ plane and then calculating the optical depth from the known absorption cross section, camera pixel size, and imaging magnification.[10] We then analyze these synthetic images using exactly the same algorithm with exactly the same parameters as for the experimental images, including fitting to and integrating over the synthetic scattering distribution to get the total number of scattered atoms.

We perform these simulations over a range of N_i at a fixed temperature for all collision energies and find the value such that the simulation matches the measured data as closely as possible, in a least-squares sense. The best fit is obtained at $N_i = 8.20(15) \times 10^5$. Including the uncertainty in temperature of ± 100 nK, the best fit parameter is $N_i = 8.2(6) \times 10^5$. I plot the results in Fig. 4.7a. As can be seen, both the DSMC simulation and the analytic theory using the fitted value of N_i match the overall data quite well, with some deviations at low and high energies. At low energies we likely have more atoms than average due to loss of atoms during the acceleration phase; additionally, s-wave scattering of impurity atoms will be more pronounced here than at higher energies. This can be seen in the comparison of the isotropically scattered atoms in both measurement and simulation. At high energies, there will be fewer atoms due to loss from deformation of the trap during acceleration.

While the analytic theory is much more quickly evaluated, DSMC provides significant additional information. As shown in Fig. 4.7b, we can also map the distribution of collision energies for each nominal energy that we set in the experiment. We compare this distribution to the one expected in the collision of two thermal atomic clouds of the same species where atoms collide only once. The joint probability distribution for two atoms

[10] We used a different camera than the Andor iXon for this experiment, which had a pixel size of 24×24 μm, and the imaging system had a magnification of 2.901.

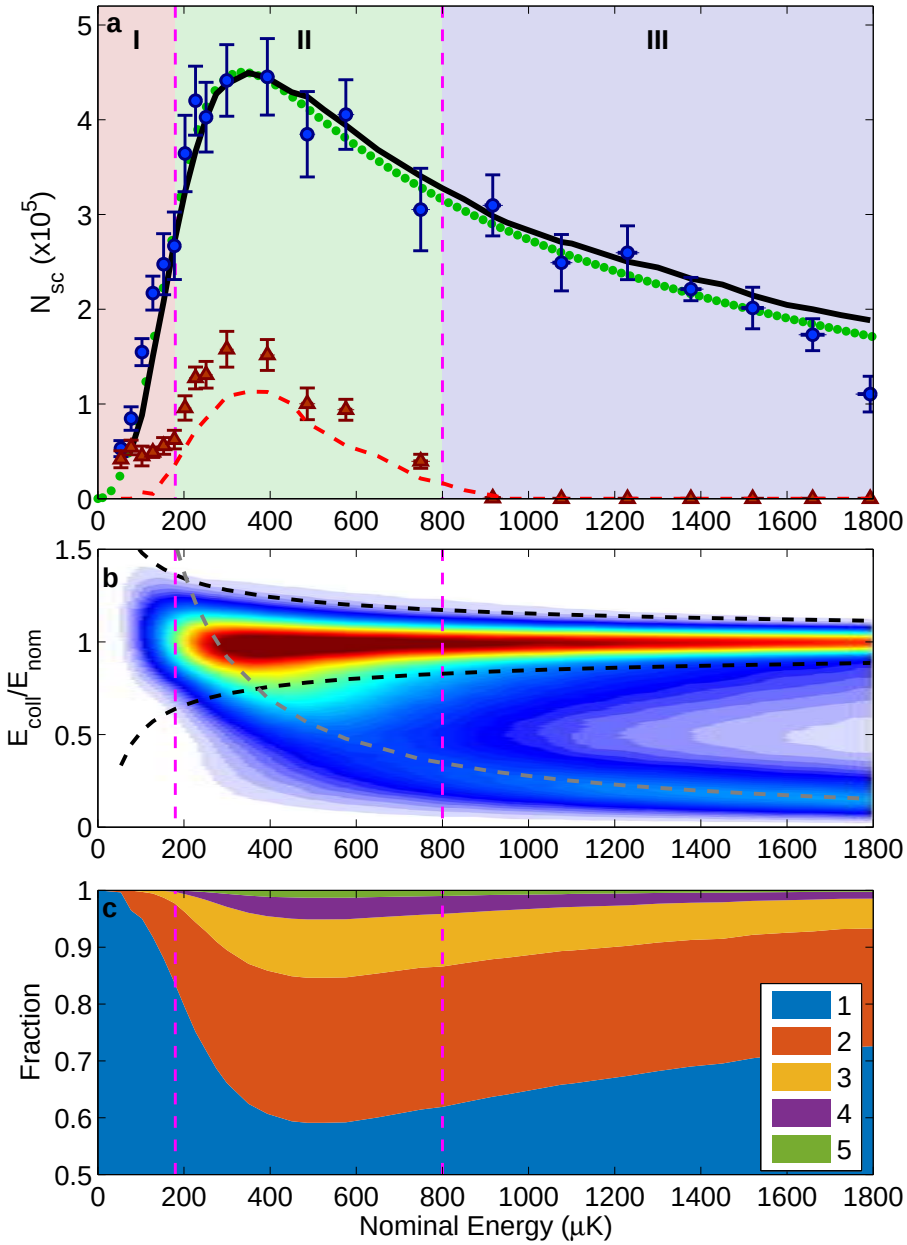

Figure 4.7: Comparison of measured and simulated numbers of scattered atoms. **a** Blue circles are experimental values for total number of scattered atoms; red triangles are only the isotropically scattered atoms. Solid black line is total number of scattered atoms from DSMC simulation with $N_i = 8.2 \times 10^5$; green dotted line is Eq. (4.10) with the same N_i. Red dashed line is DSMC prediction for isotropically scattered atoms. **b** Density plot of the distribution in collision energies E_{coll} normalized to the nominal collision energy E_{nom}, with $E_{\mathrm{coll}}/E_{\mathrm{nom}}$ on the ordinate and E_{nom} on the abscissa. Colour denotes the number of collisions progressing from white indicating zero collisions to red as an arbitrary maximum. Black dashed lines indicate thrice the expected standard deviation of the $E_{\mathrm{coll}}/E_{\mathrm{nom}}$ distribution when only single scattering events are present (Eq. (4.13)). Dashed grey line is the contour $E_{\mathrm{coll}} = 275\ \mu$K. **c** Fraction of scattered atoms that have had at most 1, 2, 3, 4, or 5 collisions as a function of E_{nom}.

with velocities $\mathbf{v}_i$ is

$$\begin{aligned} P(\mathbf{v}_1, \mathbf{v}_2) &= \left(\frac{m}{2\pi kT}\right)^3 \exp\left(-\frac{m(\mathbf{v}_1 - \mathbf{v}_0)^2}{2kT} - \frac{m(\mathbf{v}_2 + \mathbf{v}_0)^2}{2kT}\right) \\ &= \left\{\frac{1}{(\pi/2)^{3/2}\sigma^3} \exp\left(-\frac{2\mathbf{v}_{\rm cm}^2}{\sigma^2}\right)\right\} \left\{\frac{1}{(2\pi)^{3/2}\sigma^3} \exp\left(-\frac{(\mathbf{v}_{\rm rel} + 2\mathbf{v}_0)^2}{2\sigma^2}\right)\right\} \\ &= P_{\rm cm}(\mathbf{v}_{\rm cm}) P_{\rm rel}(\mathbf{v}_{\rm rel} + 2\mathbf{v}_0) \end{aligned} \tag{4.11}$$

where $\mathbf{v}_{\rm cm} = \frac{1}{2}(\mathbf{v}_1 + \mathbf{v}_2)$ is the velocity of the centre of mass, $\mathbf{v}_{\rm rel} = \mathbf{v}_2 - \mathbf{v}_1$ is the relative velocity, and $\sigma^2 = 2kT/m$. The distribution of relative velocities, which determines the distribution of collision energies, is simply a Gaussian offset by the collision velocity $2\mathbf{v}_0$. From Eq. (4.11), it is straightforward to work out the mean collision energy

$$\langle E_{\rm coll} \rangle = \langle \frac{1}{2}\left(\frac{m}{2}\right)(\mathbf{v}_{\rm rel} + 2\mathbf{v}_0)^2 \rangle = \frac{3}{2}kT + E_{\rm nom} \tag{4.12}$$

where the factor $m/2$ is the reduced mass of the two atom system. The standard deviation of the collision energy distribution is somewhat more involved, but it works out to be[134]

$$\mathrm{Std}(E_{\rm coll}) = \frac{1}{2}kT\sqrt{6 + \frac{8E_{\rm nom}}{kT}} \overset{E_{\rm nom}\to\infty}{\to} \sqrt{2E_{\rm nom}kT}. \tag{4.13}$$

One can see in Fig. 4.7b that only in the suppression region is the energy distribution contained within the bounds set by the mean and standard deviation of the distribution of single collision events. In the isotropic enhancement region, the distribution skews towards lower energies as per Fig. 4.5b. At higher energies, in the axial enhancement region, the distribution becomes bimodal with most collisions occurring at the mean nominal collision energy but with a significant fraction clustered around the $E_{\rm coll} = 275$ μK contour. We expect that most secondary collisions will occur near the resonant energy $E_{\rm coll} = 350$ μK; that they occur at a lower value is probably due to the spatial distribution of the primary collision events.

In Fig. 4.7c I have plotted the fraction of scattered atoms that have experienced at most n collisions, where $1 < n < 5$. In the suppression region, almost all scattered atoms are from primary collisions. In the isotropic enhancement region, some atoms experience up to five collisions, and even in the axial enhancement region, where the cross section is relatively low, there are significant numbers of atoms that experience more than one collision.

The DSMC simulation also lets us construct the scattering distributions, and we can compare these to the measured values. These are plotted in Figs. 4.4f-j, and there is quite good agreement between the simulation and the measurements. I should stress again that the simulation has only one free parameter over the entire energy range: the total number of atoms N_i. The scattering distributions in Fig. 4.4f-j are the same simulation results from which we obtain the curves in Fig. 4.7. In particular, the DSMC simulation describes well the non-trivial axial enhancement region.

As a final note, one can also look at the radial distribution of atoms; the radial coordinate is related to the magnitude of the relative collision velocity $|\mathbf{v}_{\rm rel}|$. Using the definition of $P_{\rm rel}(\mathbf{v}_{\rm rel} + 2\mathbf{v}_0)$ from Eq. (4.11), the magnitude of $\mathbf{v}_{\rm rel}$ is distributed according to the probability density

$$P(v_{\rm rel}) = \frac{1}{2v_0\sqrt{2\pi\sigma^2}} \left(e^{-(v_{\rm rel}-2v_0)^2/2\sigma^2} - e^{-(v_{\rm rel}+2v_0)^2/2\sigma^2} \right). \tag{4.14}$$

Equation (4.14) approaches a Gaussian distribution for $v_0 \gg \sigma$, and, since the radial coordinate is simply $v_{\rm rel}$ scaled by the time of flight, we expect that the radial distribution of the atoms should be a Gaussian if only primary collision events are present.

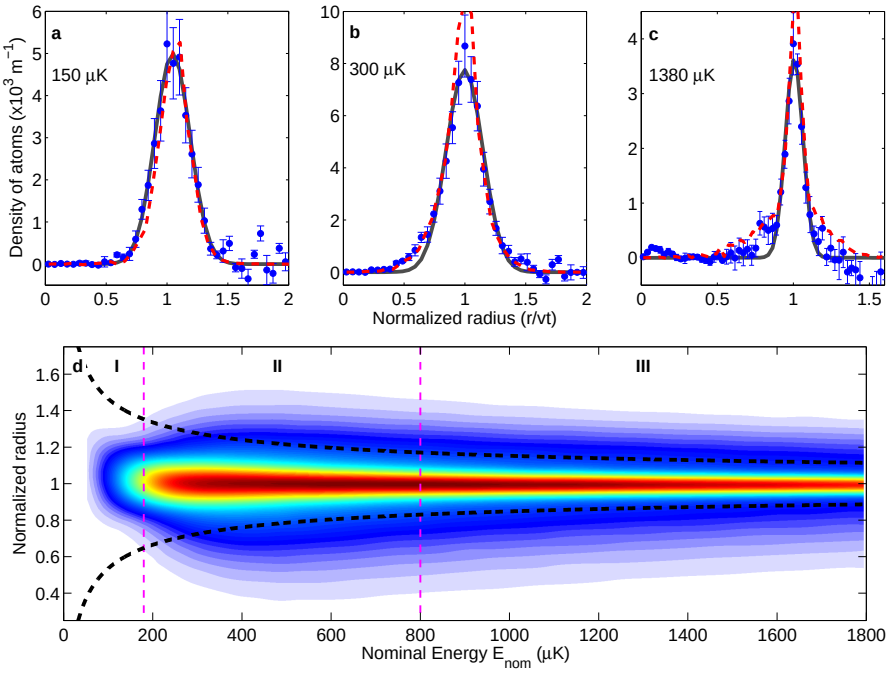

Figure 4.8: Radial distributions of scattered atoms. **a-c** Blue circles are the mean number of atoms in a given radial bin, averaged over five experimental images. The radial bins are normalized as the ratio of the measured position to vt, with v the speed and t the time of flight. Grey line is a fit to a Gaussian. Red dashed line is the result from the DSMC simulation. **d** Density plot of the distribution of normalized radial positions as a function of the nominal collision energy extracted from the DSMC model. Black dashed lines indicate thrice the expected standard deviation of Eq. (4.14).

To generate the radial distributions, we bin the Abel-inverted images by radial distance from the collision midpoint. We remove the strong fringes present in Fig. 4.4 using a Fourier-based filter, and we exclude angles close to the collision axis as before. Also, as for the angular scattering distribution, we analyze the synthetic DSMC absorption images in the same way. To account for differences in the expected collision energy compared to the actual collision energy, we rescale the radial coordinates such that the peaks of the two distributions match. The results are shown in Fig. 4.8. In the suppression region we see

the radial distribution is well-described by a Gaussian. At higher energies the distributions broaden beyond what we would expect from primary collisions only. We also find that the DSMC simulation captures the behaviour of the radial distributions across energy quite well.

4.6 Conclusion

Contrary to a previous work that claimed that fermionic atoms would be unable to attain high enough densities or interactions to easily observe collisional halos[44], we not only observe distinct p-wave halos, but we have sufficient collisional opacity to observe multiple scattering in this fermionic system. We found that the effects of multiple scattering are strongly dependent not only on the cross section at the nominal collision energy, but also on the overall energy dependence of the cross section. At high collisional opacities, the Wigner threshold law that suppresses low energy collisions leads to an apparent s-wave scattering halo in a system of identical fermions. At energies far above an isolated resonance, we observe enhancement of scattering along the collision axis, again leading to a halo that is decidedly not p-wave. While this work has looked exclusively at ^{40}K, our results are more general. Isotropic enhancement will occur for any system of identical fermions. Axial enhancement, on the other hand, will occur for any system where collisions occur at nominal energies above an isolated resonance. Shape resonances in ^{87}Rb fulfill this requirement (see Fig. 2.5), as do any narrow Feshbach resonances[63]. Furthermore, for axial enhancement to occur a resonance is not even needed; all that is required is for the cross section to increase sharply as the collision energy decreases. Indeed, as will be shown in the next chapter, this exact scenario can lead to a rather extreme version of the axial enhancement that has been demonstrated here.

Chapter 5

Collisions near a Feshbach resonance

Feshbach resonances in ultracold atomic physics are, in a word, ubiquitous. A quick search through the American Physical Society's journal publications from 2016 for the words "Feshbach" and "ultracold" alone returns over two hundred entries. And it is no surprise either: Feshbach resonances are an incredibly useful tool for manipulating ultracold atomic samples and investigating many-body states. From the first observations in ^{23}Na[27] and ^{85}Rb[135], Feshbach resonances have been used for studying the BEC-BCS cross-over in degenerate Fermi gases[136, 137, 138, 22, 139], Efimov trimers[140, 141], Anderson localization[142], solitons[143, 144], and ultracold molecule production[145, 146]. Feshbach resonances have also been critical in studying the relatively new field of dipolar quantum gases, especially in regards to their stability[147, 148, 149]. Indeed, the use of a Feshbach resonance was crucial for achieving Bose-Einstein condensation in ^{85}Rb, which has an attractive interaction and hence is not stable against collapse[150], and in ^{133}Cs which has a very large scattering length at zero magnetic field[7, 151, 6].

With all the uses to which Feshbach resonances are put, it is important to be able to accurately predict and characterize them. The vast majority of Feshbach resonances used and studied in ultracold atomic physics are magnetically tunable, although optically tunable resonances exist[152, 153, 63]. Recall from Sec. 2.5 that the resonance position E_R is

$$E_R = E_0 + \delta E(E)$$

where E_0 is the energy of the quasi-bound state and $\delta E(E)$ is the shift of the resonance position due to the coupling between channels. In a magnetically tunable resonance, the channel supporting the quasi-bound state has a different magnetic moment to the entrance channel, and the interaction potentials can thus be tuned relative to each other using a magnetic field. For alkali metal atoms, this tuning arises primarily from the differing magnetic moment of the spin singlet and triplet states. The energy of the quasi-bound state (assuming that the threshold of the entrance channel is at zero) is then[63]

$$E_0 = \delta\mu(B - B_c)$$

where $\delta\mu$ is the difference between the closed and open channel magnetic moments, and B_c is the magnetic field at which the quasi-bound state coincides with the entrance channel threshold. Turning this equation around, for any particular energy E the magnetic field at which the resonance occurs is

$$\begin{aligned} B_{\text{res}} &= \left(B_c - \frac{\delta E(E)}{\delta\mu} \right) + \frac{E}{\delta\mu} \\ &= B_0(E) + \frac{E}{\delta\mu}. \end{aligned} \tag{5.1}$$

In particular, at $E = 0$ the resonance occurs at a magnetic field of $B_0(0) = B_0$. In the low energy limit, the complex scattering length given by Eq. (2.119a) is

$$a(B) = a_{\text{bg}} \left(1 - \frac{\Delta_n}{B - B_0 - i\Gamma_B^{\text{inel}}/2} \right) \tag{5.2}$$

where $\Delta_n = \gamma_n/\delta\mu$ characterizes the elastic width of the resonance and

$$\Gamma_B^{\text{inel}} = \lim_{E\to 0} \frac{\Gamma(E)}{\delta\mu}$$

is the inelastic width. The parameters of interest at threshold then are the $E = 0$ resonance position B_0, the elastic width Δ_n, the background scattering length a_{bg}, and the inelastic width Γ_B^{inel}.

Of these, the most important and easiest to measure is the resonance position. If only the position is of interest, say for a survey of Feshbach resonances in a particular system[154, 36], then the simplest method for determining B_0 is to measure the inelastic loss of atoms from a trapped gas. This technique works both for resonances that have strong two-body loss through energetically open channels and for resonances in the absolute ground state of the system; atoms are lost through three-body decay which scales as a^4[155].[1] A typical measurement sequence is to prepare the atoms in the correct state, wait for a fixed time, and measure the remaining atoms. This procedure is repeated for many magnetic fields. As long as the losses are kept relatively low, a detailed model of the resulting line-shape is not necessary at $E = 0$: the resonance location is at the peak of the loss curve. Finite temperatures of the gas occlude this simple picture, but as a first step this method works very well. As the quasi-bound states of the closed channel are typically near the threshold of that channel, the resonance positions are very sensitive to the details of the long-range dispersion forces given by Eq. (2.129). This sensitivity can be used to refine models of the inter-atomic potential obtained through photoassociation measurements[72], and the results can then be used to predict all the relevant Feshbach parameters. Loss spectroscopy is also the only method by which one can measure the inelastic width; here, one would measure the remaining atoms for several hold times as a function of magnetic field. The

[1] Additionally, Efimov resonances[63] may strongly enhance three-body decay near the resonance.

two-body loss coefficient can then be extracted and a width calculated from its dependence on the magnetic field. Measuring the elastic width is more challenging. One can measure the thermalization time[29, 28, 156], which is related to the cross section ($\propto |a|^2$). Other methods involve measuring the mean-field interaction energy[27, 157] or by measuring the point at which the scattering length is zero[35, 36].

Equation (5.2) is the most widely used model for Feshbach resonances in ultracold atomic gases, and it is worth remarking on the shift in perspective and technique that it implies compared to the original work on Feshbach resonances. The original context that Feshbach[24, 25] and Fano[26] considered were scattering experiments where the energy was varied and the interaction potential was taken as fixed. The ultracold atomic physics community has turned this around and considers the energy to be fixed and the potential to be as malleable as the experimental apparatus allows. Furthermore, experiments done at non-zero energy are done with thermal ensembles of atoms, and these experiments lack a well-defined collision axis. The exceptions to this methodology can be counted with the fingers of one hand. The first study of Feshbach resonances in ultracold systems with a "collider-like" geometry – that is, with a well-defined collision axis – was done by Gensemer *et al.*[40] using an atomic fountain of Cs. This approach allowed the authors to separate overlapping Feshbach resonances based on different values of $\delta\mu$. The second study by Genkina *et al.*[44] used Kapitza-Dirac diffraction to transfer atoms in a degenerate Fermi gas of ^{40}K to differing momentum states and observed the collision halo; measurements of the scattered fraction produced the resonance position and width. However, the design of the experiment restricted the collision energy to a single, relatively low value of ≈ 3 μK. Finally, in our group, M. Horvath investigated the energy dependence of inelastic scattering near a low-field ^{87}Rb resonance[158, 134].

There have been, however, other experiments that might be described as "half-collider" experiments. In these experiments, weakly-bound molecules are created from ensembles of atoms by sweeping a magnetic field adiabatically over a Feshbach resonance. The direction of the field sweep is chosen such that the quasi-bound state's energy is initially higher than the entrance channel threshold, and at the end of the sweep the state's energy is below threshold, which prevents the state from decaying into the entrance channel. It can still decay to other open channels (if present) or to more deeply bound molecular states through collisions with free atoms or other molecules. Sweeping the field in the other direction places the bound state above the threshold of the incident channel, through which it can decay, and the energy of the free pair of atoms is determined by the rate of change of the magnetic field and the decay rate of the quasi-bound state[159]. The first creation of these weakly-bound "Feshbach molecules" was by Regal *et al.*[146] where the authors measured the binding energy of the molecules as a function of magnetic field. Dürr *et al.*[159] demonstrated dissociation halos, and Volz *et al.*[160] used these to probe the ^{87}Rb d-wave shape

resonance. Gaebler *et al.*[126] produced p-wave molecules which, when they decayed, generated p-wave halos of atoms.

In this chapter, I will describe an experiment that we have performed to measure the energy dependence of magnetically tunable Feshbach resonances, marrying the old approach to these resonances with the new. By measuring the scattered fraction of atoms as a function of magnetic field, we can extract the magnetic field dependence of the Feshbach resonance. We compare the parameters describing the resonance to those derived from a coupled-channels model. Near the resonance and at high densities, we see a strong signature of multiple scattering, and this can be understood with the aid of a DSMC model. This work is currently being prepared for publication, and was done in collaboration with Matthew Chilcott, Amita Deb, and Niels Kjærgaard.

5.1 Description of the experiment

In this experiment, we investigate two s-wave Feshbach resonances between ^{40}K and ^{87}Rb. One resonance is between the ^{40}K $|\frac{9}{2}\frac{7}{2}\rangle$ state and the ^{87}Rb $|11\rangle$ state, and it has a threshold resonance position of approximately 300 G and a threshold width of $\Delta = -0.61$ G. The second resonance is between the ^{40}K $|\frac{9}{2}, -\frac{9}{2}\rangle$ state and the ^{87}Rb $|11\rangle$ state, and it is located near 546 G with a width of $\Delta = -3$ G. Both of these resonances have very low inelastic widths; the 300 G resonance has an inelastic width of less than 1 mG, and the 546 G resonance has zero two-body inelastic loss because it is in the absolute ground state of the system. As a result, I can treat both of these resonances using the two-channel model developed in Sec. 2.5 which yields a real-valued resonant phase shift Eq. (2.111) that can be expressed in terms of magnetic field through Eq. (5.1) as

$$\tan \delta_{\text{res}} = \frac{\frac{1}{2}\Gamma_B(E)}{B - B_0(E)}. \tag{5.3}$$

Equation (5.3) is valid for *all* energies, and since we can ignore inelastic decay $\Gamma_B(E)$ is the *elastic* width of the resonance. For a fixed energy, the resonant phase shift changes by π across the resonance. Therefore, the elastic s-wave cross section is described by a pure Beutler-Fano function

$$\sigma(E, B) = \frac{2\pi\hbar^2}{mE} \sin^2 \left[\delta_{\text{bg}}(E) + \tan^{-1} \left(\frac{\frac{1}{2}\Gamma_B(E)}{B - B_0(E)} \right) \right] \tag{5.4}$$

as a function of B for fixed collision energy E. I have plotted an example curve for each resonance in Fig. 5.1. Such a simple description makes it easy to parametrize the resonance as a function of energy since the functional dependence on B is already known. Compare this situation to the typical measurement of varying the energy only; in this scenario, one has to have *a priori* knowledge of the energy dependence of $\Gamma_B(E)$, $\delta_{\text{bg}}(E)$, and $B_0(E)$ in

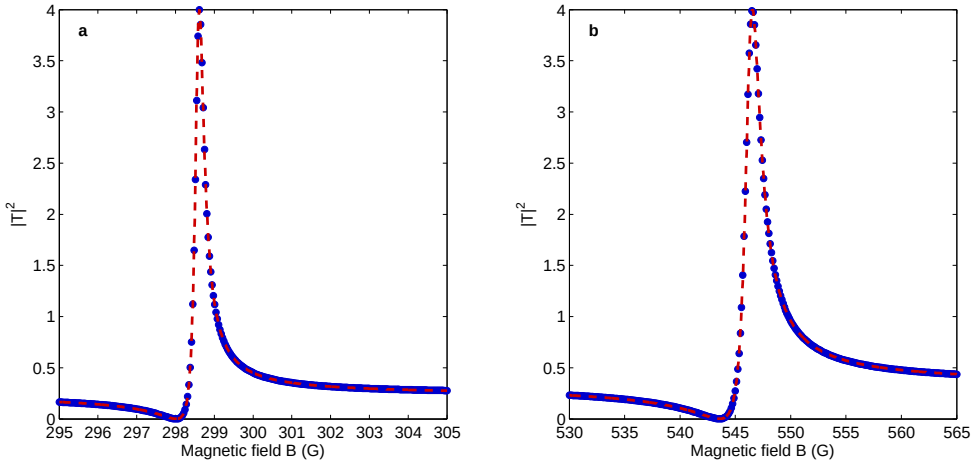

Figure 5.1: Elastic $|T|^2$ values (proportional to σ) for the ^{40}K^{87}Rb Feshbach resonances described in the text at 300 G **(a)** and 546 G **(b)** for $E = 10$ μK. Blue circles are from a coupled-channels calculation and the dashed red line is a fit to Eq. (5.4).

order to adequately describe the measured cross section. In a sense, the measurement of $\sigma(E, B)$ as a function of B for a single energy E comprises an interferometric measurement of both $\delta_{\rm bg}(E)$ and $\Gamma_B(E)$, since it is known that the resonant phase shift must change by π over the resonance. As with any interferometric measurement, one can only determine the relative sign of $\delta_{\rm bg}(E)$ and $\Gamma_B(E)$, but with measurements at several energies one can determine the magnitude and sign of $\delta\mu$, and hence the sign of $\delta_{\rm bg}(E)$.[2]

In addition to the negligible inelastic losses, we chose these resonances because their elastic widths $\Gamma(E)$ over the energy range of interest are larger than the energy spread of the collider, given in Eq. (4.13). This allows us to clearly resolve the features of the resonance, such as the loss-less point where $\sigma = 0$. Their associated large magnetic widths $\Gamma_B(E)$ are also large enough that fluctuations in the magnetic field do not contribute significantly to the uncertainty in parametrizing the resonances.

To begin the experiment, we first transfer a sample of ultracold ^{40}K atoms in the $|\frac{9}{2}\frac{9}{2}\rangle$ state and ^{87}Rb atoms in the $|22\rangle$ state from the IP trap to the optical dipole trap with a well spacing of ± 40 μm. The transfer heats the samples, so we evaporatively cool the combined sample by reducing the power in the horizontal beam, which allows the most energetic atoms to escape. As can be seen in Fig. 3.6, this preferentially removes Rb atoms due to their lower trap depth. Some energetic atoms escape from the double-well trap into the horizontal beam, and these tend to contaminate the scattering halo. To remove them, we apply a weak magnetic field gradient of approximately 2 G/cm in the z-direction to push the atoms in the waveguide to one side; this also acts as an evaporative cooling mechanism.

[2] $\Gamma(E)$ must be non-negative, but since $\delta\mu$ can be either positive or negative $\Gamma_B(E)$ can be positive or negative.

Both cooling procedures occur simultaneously for 350 ms.

At the close of evaporation, we transfer the Rb atoms to the $|11\rangle$ state using adiabatic rapid passage in a 9.2 G field produced by the z-coils. The two species of atoms now have opposite magnetic moments, which means that a strong enough magnetic field gradient will separate the sample into its component species. In practice, this is limited by the temperature of the atoms and the depth of the trap. We bring the two traps closer so that they are separated by 60 μm and then apply a strong (11 G/cm) magnetic field gradient in the z-direction for 5 ms. We then separate the two wells while the gradient remains on; we turn off the gradient 10 ms after the start of separation when the wells are fully separated. Using this method, we retain 60-70% of each species of atoms in one well instead of the 50% that might be expected: see Sec. 3.5 and Fig. 3.10. This procedure also serves to purify the wells of unwanted species, as the remaining 30-40% of atoms are pushed out of the waveguide instead of remaining in one of the wells.

Unlike collision experiments where the detector is fixed, our imaging system is such that our detector effectively moves with the center of mass of the system; if the total momentum is not zero, we do not need to apply corrections to convert measured positions/velocities from the lab frame to the center-of-mass frame[55]. However, it is convenient for the purpose of analyzing the absorption images for the total momentum to be zero. Since the masses of ^{40}K and ^{87}Rb differ, we must impart different velocities to the atom clouds so that the mean momentum of the K cloud is exactly opposite to that of the Rb cloud. To do so, we separate the two clouds such that the K cloud is 2 mm away from the center of the imaging field, and the Rb cloud is $\frac{m_{\mathrm{K}}}{m_{\mathrm{Rb}}} \approx 0.46$ of that distance in the opposite direction, or -0.92 mm. When accelerating the clouds toward each other, we use the same profile given by Eq. (3.13) except that the maximum acceleration a_{coll} for Rb is $\frac{m_{\mathrm{K}}}{m_{\mathrm{Rb}}}$ that of K. This ensures that the mean momentum of the K atoms is exactly opposite to the Rb atoms when the clouds collide.

While the atoms are separated, we finish state preparation as shown in Fig. 5.2. First, we transfer any remaining Rb atoms in the right well (which contains primarily K atoms) from the $|11\rangle$ state (dark) to the $|22\rangle$ state (bright) using a π-pulse; the small magnetic field gradient produced by the z-coils ensures that only those atoms in the right well are transferred. We then remove the $|22\rangle$ atoms using a light pulse resonant with the $F = 2$ hyperfine manifold, leaving us with only Rb atoms in the $|11\rangle$ state in the left well. K atoms in the right well are transferred from the $|\frac{9}{2}\frac{9}{2}\rangle$ state (bright) to the $|\frac{7}{2}\frac{7}{2}\rangle$ state (dark) using adiabatic rapid passage (ARP), and the remaining K atoms in the left well are removed via a resonant light pulse. The final steps of state preparation depend on which resonance we are interested in. For the resonance between the $|\frac{9}{2}, -\frac{9}{2}\rangle$ and $|11\rangle$ states, we then transfer the K atoms in the $|\frac{7}{2}\frac{7}{2}\rangle$ state back to the $|\frac{9}{2}\frac{9}{2}\rangle$ state. The final step is to use adiabatic rapid passage to transfer all K atoms from the $|\frac{9}{2}\frac{9}{2}\rangle$ state to the $|\frac{9}{2}, -\frac{9}{2}\rangle$ state. If we are

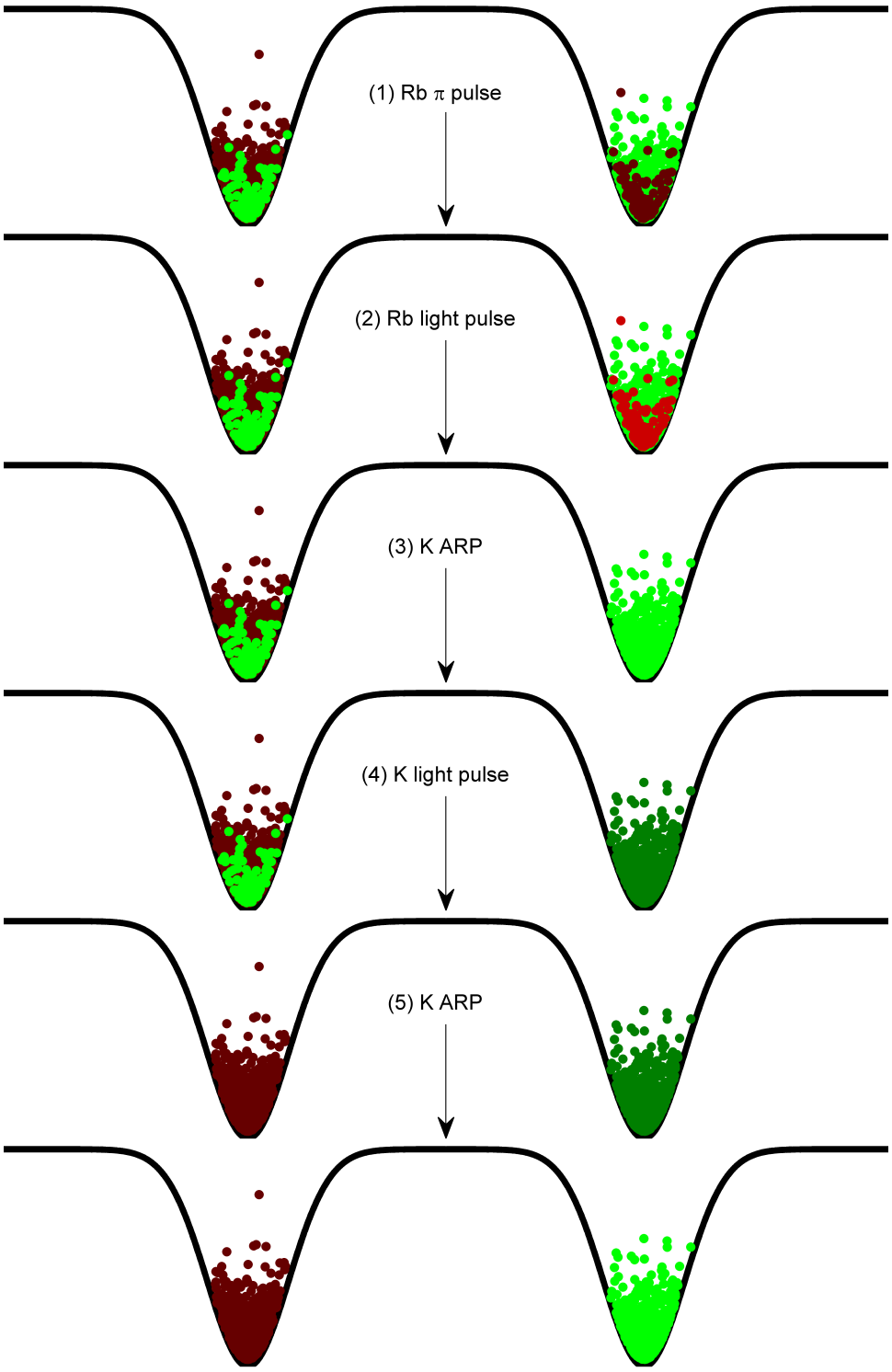

Figure 5.2: State preparation sequence for ^{40}K^{87}Rb Feshbach collisions. Distances are grossly exaggerated for clarity. Green circles are K atoms, red circles are Rb atoms, black solid line is the optical potential. Light colors indicate atoms in a state resonant with the light pulse, dark colors a state far off-resonant from the light pulse. See text for further details.

interested in the resonance between the $|\frac{9}{2}\frac{7}{2}\rangle$ and $|11\rangle$ states, all we do is to transfer K atoms from the $|\frac{7}{2}\frac{7}{2}\rangle$ state to the $|\frac{9}{2}\frac{7}{2}\rangle$ state using RF adiabatic rapid passage. At the end of state preparation, we have approximately 3×10^5 atoms of each species in their respective wells. The temperatures are 0.8 μK for Rb and 1.1 μK for K.

We then reduce the current in the z-coils to zero over 30 ms and increase the current in the Helmholtz coils to the desired set point in 75 ms; the latter time was chosen to minimize the level of transients in the coil response. The ramp is finished at 700 ms after the end of evaporative cooling. We then accelerate the atoms towards each other with a variable maximum acceleration, which determines the collision energy, and we adjust the timing of the penultimate hold time such that collisions occur at $755.0(1)$ ms after the end of evaporative cooling. As the calibration of the magnetic field was performed at this time – see Sec. 3.8 and Figs. 3.14 and 3.15 – we can be assured that our field calibration applies to our collision experiments, regardless of the presence of noise from the AC line. The optical trap is switched off at the time when the K cloud is 60 μm from the collision point, so the atom clouds collide in free space.

Our imaging system was not designed to image either K or Rb atoms at high (> 20 G) magnetic fields, so we switch the current in the Helmholtz coils off when the K atom cloud has traveled 20 μm from the collision point after the collision. Unfortunately, the coils have significant inductance, and combined with likely eddy currents generated by the rapidly changing magnetic field, we image the atoms in an unknown and changing magnetic field. As the timings for each collision energy remain the same, we optimize the optical depth by changing the frequencies of the probe lasers, but the conversion between the optical depth and atom density is unknown. However, this turns out to be unimportant because we work instead with the scattered fraction of atoms, and here we require only a measurement which is proportional to the number of scattered atoms where the proportionality constant is the same at all magnetic fields, although that constant may change between collision energies.

Finally, we do not image the Rb atoms in the $|11\rangle$ state. Instead, after the magnetic field is turned off we use ARP to transfer the atoms from the $|11\rangle$ state to the $|22\rangle$ state, which we then image. The duration and frequency range of the ARP sweep is optimized for every collision energy. We image the two species of atoms at different times using the frame-transfer function of our CCD camera. We first image the K atoms then wait until the Rb atoms have traveled the same distance before imaging the Rb atoms. This ensures that the unscattered clouds are equidistant from the collision point and that the scattering halos are the same size, which makes analysis of the images slightly simpler. We choose the time-of-flight for the K atoms to be such that the unscattered cloud has moved 350 μm from the collision point.

5.2 Image Analysis

A pair of K and Rb images measured near the peak cross section at an energy of 52 μK are shown in Fig. 5.3. In both K and Rb images there are two main structures: the dense,

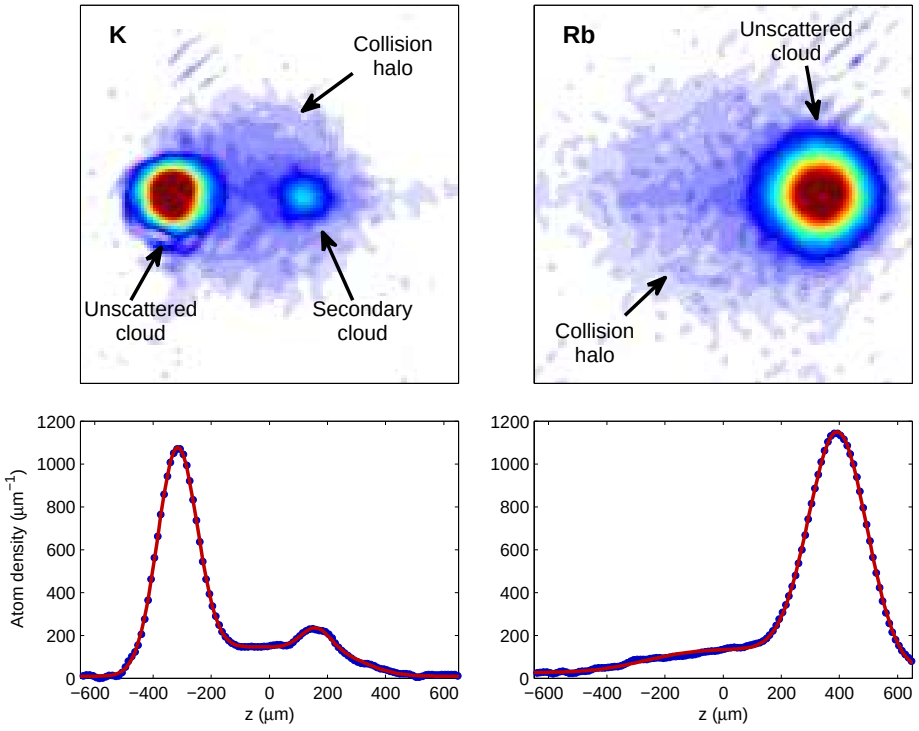

Figure 5.3: Example absorption images and analysis of ^{40}K^{87}Rb scattering near the resonant magnetic field at $E = 52$ μK. **Top:** Absorption images of K and Rb atoms. **Bottom:** Line densities obtained by integrated images along vertical (y) axis. Blue circles are from the image, red line is a fit to Eq. (5.5).

unscattered clouds, and the isotropic s-wave scattering halo.[3] In the K image, however, there is an additional, Gaussian-type structure that is located at the same place as the Rb cloud.[4] Similarly to Chapter 4, this deviation from a pure s-wave halo is due entirely to multiple scattering, which I will discuss in Sec. 5.5. In analyzing our data, we need to take all three structures into account, and it is easier to work with integrated line densities than angular distributions. Compared to Chapter 4, I use a different method for analyzing the images in this experiment for two main reasons. First, most images away from the cross section peak in Fig. 5.1 have few scattered atoms (5-10% of the total) and hence poor signal-to-noise; the angular binning procedure used previously works poorly when signal-to-noise is limited. Second, the presence of the secondary Gaussian cloud in the K cloud significantly complicates the angular model, and I have found that the scattered fraction

[3] At energies above 100 μK p-wave interference with the s-wave halo becomes important.

[4] Recall that the Rb image is taken after the K image.

extracted in this way is unreliable: it depends a great deal on the exact parameters used in analyzing the data. Recall also that the BASEX algorithm for Abel-inversion concentrates noise on the $r = 0$ line, and in this study I am interested in the secondary cloud that lies on the $r = 0$ line. For these reasons, I instead choose to work with linear rather than angular distributions of atoms.

The first step is to apply a 2D fourth order Butterworth bandpass filter to the absorption image, which is defined in the Fourier domain as[161]

$$\left[1 + \left(\frac{\sqrt{k_y^2 + k_z^2}w_{\rm lp}}{2\pi}\right)^8\right]^{-1}$$

where $w_{\rm lp}$ is the low-pass filter width and is typically 5-7 μm. I then integrate each image along the vertical (y) direction to get a line density of atoms $n_i(z)$, where i is either K or Rb. While the integration significantly improves the signal-to-noise, the Butterworth filter reduces noise on the line densities enough to be worth the extra, very minimal, computational effort. Each $n_i(z)$ can be expressed as the sum of three terms

$$n_i(z) = N_i^u P_i^u(z) + N_i^s P_i^s(z) + N_i^m P_i^m(z) \tag{5.5}$$

where each probability density function $P(z)$ is normalized to unity. The first term, $P_i^u(z)$, represents the distribution of unscattered atoms; this is a Gaussian defined by

$$P_i^u(z) = \frac{1}{\sqrt{2\pi s_i^2}} e^{-\frac{(z-z_i)^2}{2s_i^2}} \tag{5.6}$$

where z_i is the center of the unscattered cloud relative to the collision point, and s_i is its width. The third term, $P_i^m(z)$, represents the multiply scattered atoms seen in Fig. 5.3, and we take this to be a Gaussian distribution as well, but with a different width than for the unscattered cloud and a z position that is equal to $-\frac{m_{\rm K}}{m_{\rm Rb}} z_i$; this is a consequence of having collisions occur in the center-of-mass frame. I only include $P_i^m(z)$ for fits to the K distribution, as the multiply scattered atoms are most evident in those images.

The second term, $P_i^s(z)$, represents the scattered atoms whose distribution can be described by the single-event differential cross section.[5] To derive this, I first start from the joint momentum distribution for two species of atoms in the center-of-mass frame

$$P(\mathbf{p}_1, \mathbf{p}_2) = \frac{1}{(2\pi)^3 (m_1 k T_1 m_2 k T_2)^{3/2}} e^{-\frac{(\mathbf{p}_1 - \mathbf{p}_0)^2}{2m_1 k T_1} - \frac{(\mathbf{p}_2 + \mathbf{p}_0)^2}{2m_2 k T_2}} \tag{5.7}$$

where m_i are the masses of the atoms, T_i are the temperatures of the clouds, and $\mathbf{p}_0 = p_0 \hat{\mathbf{z}}$ is the mean relative momentum between the two clouds whose magnitude is defined by the

[5] Note that this does not mean that these atoms have experienced only one collision: they may have experienced more, but the distribution for these higher-order events is experimentally indistinguishable from the single-event distribution. The predominant multiple scattering mode is discussed in Sec. 5.5.

collision energy $E_0 = \frac{p_0^2}{2m}$ with m the reduced mass. Defining the total momentum $\mathbf{P} = \mathbf{p}_1 + \mathbf{p}_2$ and the relative momentum $\mathbf{p} = (m_2\mathbf{p}_1 - m_1\mathbf{p}_2)/M$ with total mass $M = m_1 + m_2$, I can rewrite Eq. (5.7) in terms of $\mathbf{P}$ and $\mathbf{p}$ as

$$P(\mathbf{P},\mathbf{p}) = \frac{1}{(2\pi)^3(m_1 k T_1 m_2 k T_2)^{3/2}} \times \exp\left[-\frac{T_{\text{eff}}}{2MkT_1T_2}\left(\mathbf{P} + \frac{T_2 - T_1}{T_{\text{eff}}}(\mathbf{p} - \mathbf{p}_0)\right)^2 - \frac{(\mathbf{p}-\mathbf{p}_0)^2}{2mkT_{\text{eff}}}\right] \tag{5.8}$$

with an effective temperature $T_{\text{eff}} = (m_1T_2 + m_2T_1)/M$. Integrating over $\mathbf{P}$ gives the distribution of relative momenta

$$P(\mathbf{p}) = \frac{1}{(2\pi m k T_{\text{eff}})^{3/2}} e^{-\frac{(\mathbf{p}-\mathbf{p}_0)^2}{2mkT_{\text{eff}}}} \tag{5.9}$$

which I can integrate over all directions $d\Omega$ to get the distribution of the magnitude of the relative momenta

$$P(p) = \int P(\mathbf{p}) d\Omega = \frac{p}{\sqrt{2\pi} p_0 \sqrt{mkT_{\text{eff}}}} \left(e^{-\frac{(p-p_0)^2}{2mkT_{\text{eff}}}} - e^{-\frac{(p+p_0)^2}{2mkT_{\text{eff}}}}\right). \tag{5.10}$$

The individual momenta for both atoms have the same magnitude p for each collision event but with opposite directions, and the distribution of the direction of $\mathbf{p}$ after the collision is given by the distribution $Q(\theta,\phi) = \sigma^{-1}\frac{d\sigma}{d\Omega}$. For this work I need only consider s and p-wave scattering and the interference between them which gives

$$Q(\theta,\phi) = Q(\cos\theta) = \frac{|T_0 \pm 3T_1\cos\theta|^2}{\pi|T_0|^2 + 3\pi|T_1|^2} \tag{5.11a}$$

$$= \frac{\sin^2\delta_0 + 9\sin^2\delta_1\cos^2\theta \pm 6\sin\delta_0\sin\delta_1\cos(\delta_0-\delta_1)\cos\theta}{4\pi\sin^2\delta_0 + 12\pi\sin^2\delta_1} \tag{5.11b}$$

where T_0 and δ_0 are the s-wave elastic T-matrix element and phase shift, respectively, and T_1 and δ_1 are the p-wave versions of the same.[6] The $+$ sign applies to the Rb halo and the $-$ sign to the K halo.[7]

To determine the distribution of positions of the two atoms after the collision, I relate the final position $\mathbf{r}_i$ to the initial position $\mathbf{r}_i(0)$ and the velocity $\mathbf{v}_i$ by $\mathbf{r}_i = \mathbf{r}_i(0) + \mathbf{v}_i t$ where t is the expansion time after collision. The final distribution of $\mathbf{v}_i$ depends on both the distribution of relative momentum after the collision and on the distribution of total momentum $\mathbf{P}$ before the collision. As in Sec 4.2 I make two simplifying assumptions: I neglect both the total momentum distribution and the distribution of initial positions $\mathbf{r}_i(0)$. The final distribution of positions $\mathbf{r}_i$ is then just a scaled version of the relative momentum

[6] Comparing with Eq. (2.155), $Q(\theta,\phi) = dF(\theta,\phi)/d\Omega$.

[7] This choice, like the choice of coordinate system, is arbitrary.

distribution multiplying the angular distribution Eq. (5.11b)

$$\begin{aligned} P(\mathbf{r}_i) &= P\left(p = \frac{m_i r_i}{t}\right) Q\left(\frac{z}{r_i}\right) \\ &= \frac{r_i}{\sqrt{2\pi} r_{0,i} \tau_i} \left(e^{-\frac{(r_i - r_{0,i})^2}{2\tau_i^2}} - e^{-\frac{(r_i + r_{0,i})^2}{2\tau_i^2}} \right) Q\left(\frac{z}{r_i}\right) \end{aligned} \tag{5.12}$$

where $\tau_i^2 = mkT_{\text{eff}}t^2/m_i^2$ is the width of the distribution and $r_{0,i} = p_0 t/m_i$. By integrating over the x and y coordinates, or more easily over the ϕ and $\sqrt{x^2+y^2}$ coordinates, I get the distribution of scattered atoms along z

$$P_i^s(z) = \frac{\sqrt{2\pi}}{r_{0,i}\tau_i} \int_{|z|}^{\infty} \left(e^{-\frac{(r_i - r_{0,i})^2}{2\tau_i^2}} - e^{-\frac{(r_i + r_{0,i})^2}{2\tau_i^2}} \right) Q\left(\frac{z}{r_i}\right) dr_i. \tag{5.13}$$

When only s-wave collisions need to be considered, Eq. (5.13) can be expressed in terms of the complementary error function $\text{erfc}(q)$ as

$$P_i^s(z) = \frac{1}{4r_{0,i}} \left[\text{erfc}\left(\frac{|z| - r_{0,i}}{2\tau_i}\right) - \text{erfc}\left(\frac{|z| + r_{0,i}}{2\tau_i}\right) \right] \tag{5.14}$$

where $\text{erfc}(q) = 2\pi^{-\frac{1}{2}} \int_q^\infty e^{-q^2} dq$, but otherwise the integral needs to be evaluated numerically.

When fitting Eq. (5.5) to the measured distributions, I allow widths, offsets, and total numbers of atoms in each scattering mode to vary within reasonable bounds. Certain parameters are only allowed to vary as fractions of others; for instance, the multiply scattered cloud's width is defined relative to the unscattered cloud's width to prevent unphysical fit parameters. Similarly, the multiply scattered cloud's position is only allowed to vary a small amount from its expected position as $-\frac{m_K}{m_{Rb}} z_i$. Finally, to ensure the stability of the extracted phase shifts, I simultaneously fit the K and the Rb distributions with the constraint that the scattering phase shifts must be the same for both distributions. Of the extracted parameters, the most important for this study are the number of atoms in each scattering mode: N_i^u, N_i^s, and N_i^m. From these, I calculate the scattered fraction as

$$S = \frac{\sum_i N_i^s + N_i^m}{\sum_i N_i^u + N_i^s + N_i^m}.$$

The scattered fraction can be related to the cross section using Eq. (4.10), repeated here for convenience,

$$S = \frac{\alpha\sigma}{1 + \alpha\sigma} \tag{5.15}$$

where α is a constant that depends on the number of atoms and the geometry of the clouds. I can then fit the combination of Eqs. (5.15) and (5.4) to the measured value of S and extract the parameters defining the Feshbach resonance.

5.3 DSMC validation

If our goal is to use measurements of the scattered fraction as a function of magnetic field to parametrize the Feshbach resonance, it is reasonable to ask how accurate this will be. This question is especially pertinent in light of the effects of multiple scattering observed in Chapter 4 and the clear sign of multiple scattering in Fig. 5.3. Furthermore, one can ask whether the analytic model of Eq. (5.15) is an appropriate model for this experiment. Both questions can be answered by using DSMC to model the collision dynamics. Before proceeding, however, I should highlight the difference in approach to this experiment in comparison to the ^{40}K collisions investigated in Chapter 4. In the previous chapter, the motivation was to measure the elastic p-wave cross section, which controls the number of scattered atoms, as a function of energy. Since we desired an absolute, as opposed to a relative, number, we needed an accurate model of the absolute number of scattered atoms. In contrast, this experiment is not interested in the absolute number of scattered atoms; instead, we are interested in the parameters that control the shape of the curve describing the fraction of atoms scattered as a function of magnetic field. These parameters are independent of the absolute number of scattered atoms, so we only need to verify that our method for extracting these parameters does not have systematic errors.

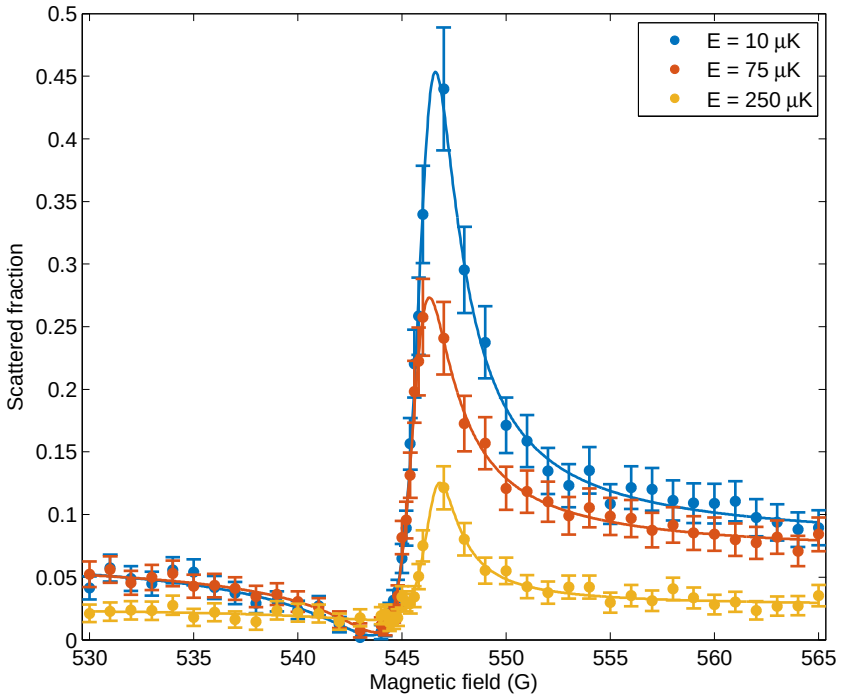

Figure 5.4: Scattered fraction S as a function of magnetic field B for simulated ^{40}K^{87}Rb collisions. Circles are extracted from the synthetic absorption images, and the solid lines are fits. Errors on S are assumed to be the same as in the experiment.

The DSMC model used here is reminiscent of the one used in Sec. 4.5. I initialize one cloud of each species of atom using the distributions for a harmonic trap and a Maxwell-Boltzmann distribution of velocities. Since the atoms have different masses but experience nearly the same optical potential, their trapping frequencies differ. The total ^{87}Rb trapping frequencies from both lasers are approximately $(\omega_x, \omega_y, \omega_z) = 2\pi \times (281, 128, 200)$ Hz, while the ^{40}K trapping frequencies are $(\omega_x, \omega_y, \omega_z) = 2\pi \times (391, 179, 278)$ Hz. The Rb and K cloud temperatures are initialized to their respective values of 0.8 μK and 1.1 μK. The K cloud is given a mean z-velocity of v_{K}, and the Rb cloud is given a mean velocity of $-v_{\mathrm{K}}\frac{m_{\mathrm{K}}}{m_{\mathrm{Rb}}}$, where v_{K} is chosen to give the correct collision energy. I run the simulation until 2 ms after the time at which the cloud centers overlap, and from there I evolve the positions without collisions until the imaging time in the experiment. As we have two different types of atoms, three different cross sections must be used corresponding to the three possible collision partners: Rb-Rb, K-K, and Rb-K. Rb-Rb collisions are assumed to be purely s-wave; our measurement energies and atom densities are such that the d-wave contribution is negligible. K-K collisions are assumed to be purely p-wave. Rb-K collisions can have both s and p-wave contributions, so I use both the total cross section and the T-matrix elements to calculate the appropriate final velocities after any collision via Eqs. (5.11a) and the rejection sampling algorithm described in Sec. 2.8.

Validation involves using the coupled-channels solver to calculate the inter-species cross section as a function of magnetic field and energy, and then using that cross section in the DSMC model to calculate collision probabilities. Each DSMC run is performed for a single magnetic field and nominal energy, and the final position distributions of the atoms are converted into synthetic absorption images. I analyze these synthetic images as described in Sec. 5.2, and I extract the Feshbach parameters B_0, Γ_B, and δ_{bg} by fitting Eqs. (5.15) and (5.4) to the scattered fraction S. An example of the simulated S as a function of B is shown in Fig. 5.4. For this plot, I have used $N_{\mathrm{K}} = N_{\mathrm{Rb}} = 3 \times 10^5$ with 2×10^4 test particles. The synthetic values of S clearly match the expected form with a cross section that is a scaled Beutler-Fano function. For $E = 250$ μK the curve never reaches $S = 0$ because the contribution from p-wave scattering becomes significant at energies of more than 100 μK. To account for this, I add a term to the cross section of Eq. (5.4) that is independent of the magnetic field which accounts for the p-wave cross section. Each of the fits defines a set of parameters, and I compare these parameters to their expected values in Fig. 5.5. For the expected number of atoms in the actual experiment, the extracted parameters closely match the parameters used to generate the DSMC model; this implies that the analysis method that I am using is reliable for that density of atoms. Of course, as the density increases one might expect that the method will be less reliable due to multiple scattering; however, for a 30% increase in the number of atoms in each species, Fig. 5.5 shows that the extracted parameters are still reliable. An imbalance in the number of atoms

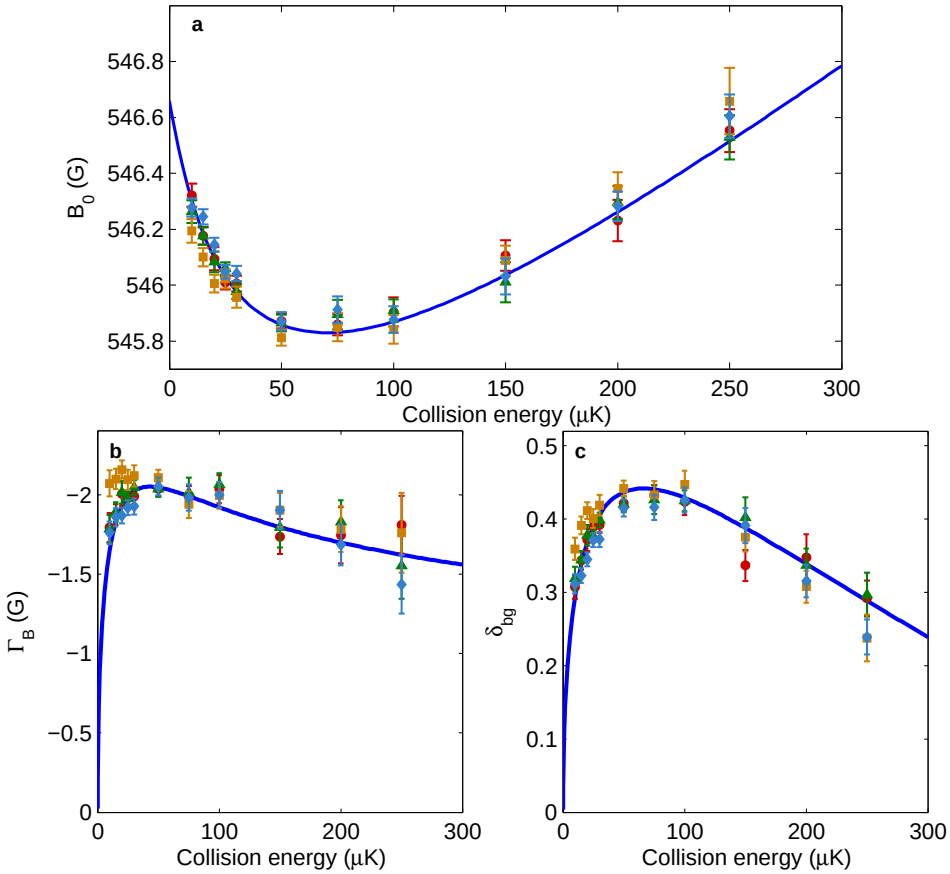

Figure 5.5: Comparison between parameters used to generate DSMC model and parameters extracted from analysis of synthetic absorption images. **a** $B_0(E)$, **b** $\Gamma_B(E)$, **c** $\delta_{\rm bg}(E)$. Red circles are for $N_{\rm K} = N_{\rm Rb} = 3 \times 10^5$, green triangles for $N_{\rm K} = N_{\rm Rb} = 4 \times 10^5$, yellow squares for $N_{\rm K} = 3 \times 10^5$ and $N_{\rm Rb} = 5 \times 10^5$, and blue diamonds for $N_{\rm K} = 5 \times 10^5$ and $N_{\rm Rb} = 3 \times 10^5$.

in each species could potentially cause a systematic difference, as Eq. (5.15) was derived assuming that the number of atoms in each cloud is the same. It is relatively straightforward to show that for a total number of atoms N and an imbalance $\Delta N = N_2 - N_1$ that the scattered fraction is changed from Eq. (5.15) to

$$S = (1 - f^2)\frac{1 - e^{-2\alpha\sigma f}}{(1 - e^{-2\alpha\sigma f}) + f(1 + e^{-2\alpha\sigma f})} \tag{5.16}$$

with $f = \Delta N/N$. One can, in principle, add f as a fitting parameter, but the least-squares fitting of experimental data generally yields implausibly high values for f. Instead, I assume that $f = 0$; the results of fitting with this assumption are also shown in Fig. 5.5 for imbalances in favour of both Rb and K. In the case of more Rb than K, there are some deviations from the expected values; however, I will note that the imbalances used in Fig. 5.5 are implausibly high for our experiment. As a result, I conclude that using the analysis method of Sec. 5.2 should yield accurate values for the Feshbach parameters of interest.

5.4 Results

An example of the experimental data that we obtained is shown in Fig. 5.6 at a collision energy of $E = 52\ \mu$K. We find that the data is well-described by the analytic form of

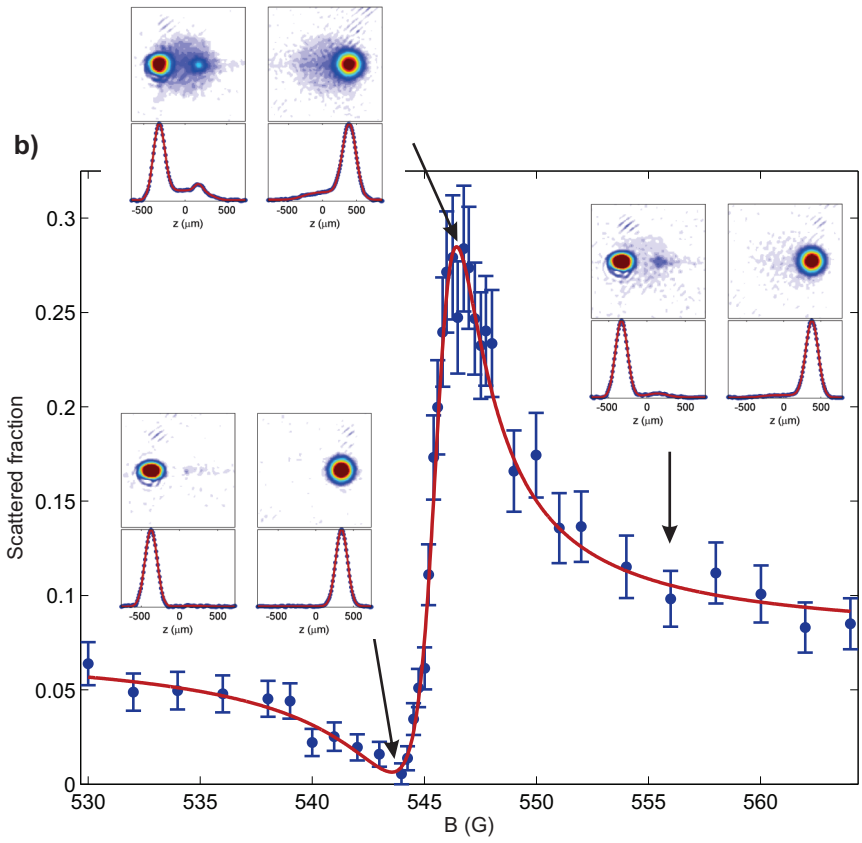

Figure 5.6: Scattered fraction of atoms S as a function of magnetic field B for $E = 52\ \mu$K. Blue circles are experimental data and red line is a fit to Eqs. (5.15) and (5.4). Insets show absorption images and and marginal distributions of K (left) and Rb right) at the indicated magnetic fields.

the scattering fraction with the Beutler-Fano profile of Eq. (5.4). One can clearly see the asymmetry and different features of the Beutler-Fano profile in the data; most notably, there is the resonant magnetic field where the scattering fraction is highest, and the loss-less point where there is almost no scattering. Although Eq. (5.4) predicts that there should be zero collisions at the loss-less point, technical noise on the images that we process means that we inevitably see less-than-perfect extinction. At this relatively low collision energy, we see almost exclusively s-wave scattering, so the shape of the scattering halo does not change as the magnetic field is varied: only the density changes. The multiply scattered K cloud changes density as well, and it is most pronounced at the peak of the resonance.

In contrast, Fig. 5.7 shows data at a collision energy of $E = 196\ \mu$K. Here, the density of the scattering halo follows the same behaviour as for $E = 52\ \mu$K, but the shape

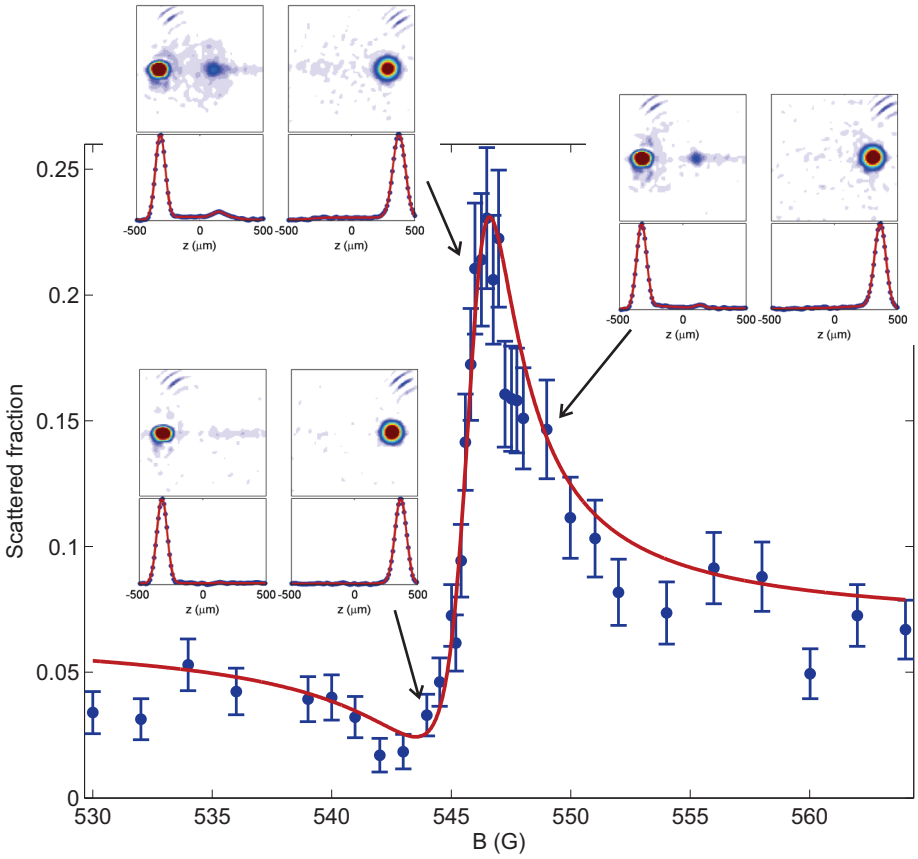

Figure 5.7: Scattered fraction of atoms S as a function of magnetic field B for $E = 196\ \mu$K. Blue circles are experimental data and red line is a fit to Eqs. (5.15) and (5.4). Insets show absorption images and and marginal distributions of K (left) and Rb right) at the indicated magnetic fields.

of the scattering halo changes significantly over the resonance. Near the peak of the resonance, the K scattering halo is nearly isotropic, with a slight skew towards the right. On the high-B side of resonance, the shape is skewed heavily towards the left in an almost "half" p-wave halo. Such behaviour is the result of interference between the s and p-wave scattering phase shifts, which change the asymmetry of the scattering halo through the last term in Eq. (5.11b). Interference of partial waves has been used previously to measure ^{87}Rb scattering phase shifts[42, 43], and one can imagine that the s and p-wave phase shifts could be measured using resonances in a similar fashion by exploiting the phase profile of the resonance. We have attempted this measurement, but the signal-to-noise of our images was not sufficient to obtain reliable values for either phase shift, especially since the p-wave phase shift is expected from coupled-channels calculations to be at most 12°.

Plots of scattering fraction as a function of magnetic field for selected energies are shown in Fig. 5.8. A steady reduction in the peak value of the scattered fraction is seen for increasing energies, which is expected from the E^{-1} scaling of the cross section in

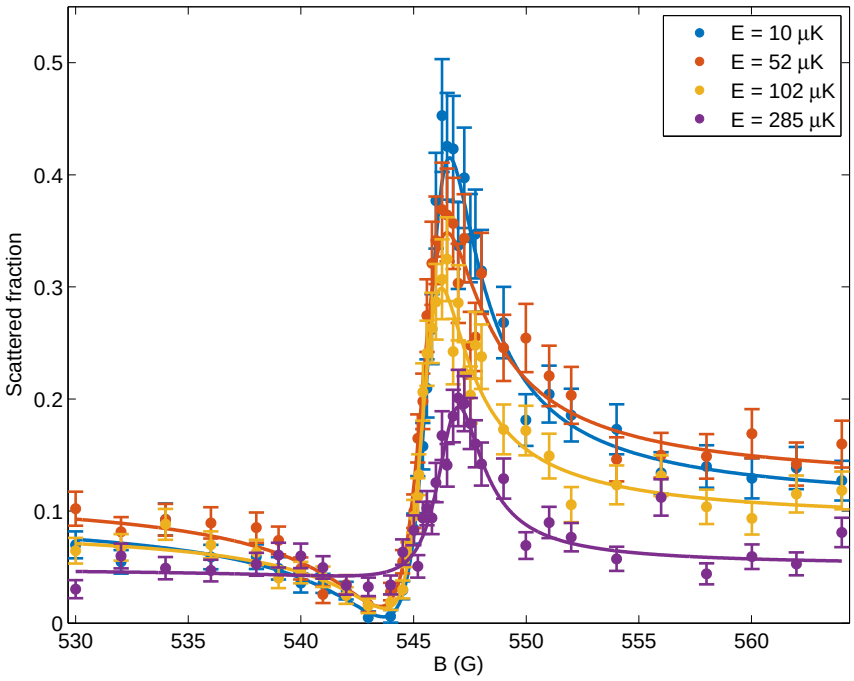

Figure 5.8: Experimentally measured values of the scattered fraction as a function of magnetic field (circles) and fits to Eqs. (5.15) and (5.4) for the specified energies.

Eq. (5.4). Furthermore, the resonance does not appear to shift by much for low energies; it is only as the collision energy is increased beyond 100 μK that a noticeable shift in the resonance position is seen. From the fits of Eq. (5.4) to data such as that in Fig. 5.8, we extract the Feshbach parameters, and these are shown in Fig. 5.9. The most striking feature of this resonance is that the resonance position does not shift monotonically with energy; instead, it has a minimum value at about $E = 70$ μK before increasing and following a linear asymptote. This behaviour is due to a large $\delta E(E)$, which itself arises from the large coupling between the open and closed channels measured by $\Gamma_B(E)$. From multichannel quantum defect theory (MQDT), we expect that $\delta E(E)$ should approach zero for large collision energies[76, 63], leaving $B_0(E)$ to vary linearly with the collision energy, and we see this trend for energies above 100 μK.

Comparing our data to the prediction from the coupled-channels model using the parameters from Pashov *et al.*[72] (blue dashed line), we can immediately see that our measurements of $B_0(E)$ are not consistent with the predictions. Such a shift, however, is to be expected; previous measurements using RF association of molecules have measured $B_0(0) = 546.618(6)$ G [162] and $B_0(0) = 546.669(26)$ G [163].[8] These are to be compared with the coupled-channels prediction of 546.771 G. A likely reason for the mismatch

[8]Technically, all values of $B_0(0)$ are computed at $E = 1$ nK.

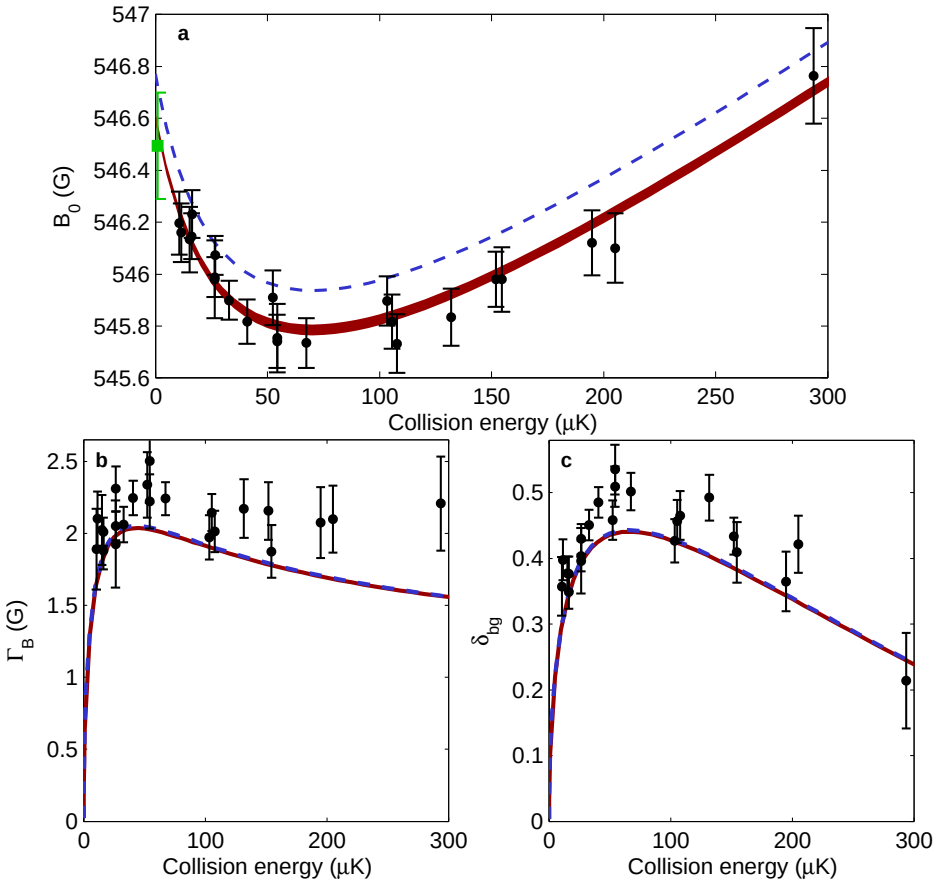

Figure 5.9: Comparison between parameters extracted from experimental data (black circles) and parameters calculated from a coupled-channels model (lines). **a** $B_0(E)$, **b** $\Gamma_B(E)$, **c** $\delta_{\rm bg}(E)$. Green square is the resonance position measured by monitoring inelastic loss. The blue dashed line is calculated based on the parameters described in [72], whereas the red band in **a** is the 1-σ confidence interval obtained by fitting a model potential to the data (see text). In **b** and **c**, the red line is calculated using the optimum model potential.

is that positions of Feshbach resonances are highly sensitive to the long-range tail of the inter-atomic potential. The model potentials in [72] were created largely on the basis of photo-association data, which are less sensitive to long-range interactions, although locations of Feshbach resonances measured in [154] were used to constrain the model. These locations were measured with an uncertainty of ± 0.2 G, and the predictions of the model potential are within that uncertainty of the more precisely measured values.

Unfortunately, an updated model potential is not available, so to compare theoretical predictions and our measurements we make slight adjustments to the long-range potential. We apply retardation corrections in the form of position dependent factors $f_6(r)$, $f_8(r)$, and $f_{10}(r)$[60] such that the new long-range interaction changes from Eq. (2.129) to

$$V_{\rm LR}(r) = -f_6(r)\frac{C_6}{r^6} - f_8(r)\frac{C_8}{r^8} - f_{10}(r)\frac{C_{10}}{r^{10}} \pm E_{\rm exch}(r). \tag{5.17}$$

The retardation correction factors are due to the finite speed of the photons mediating the induced multipole interactions that give rise to Eq. (2.129)[60]. We fix the correction factors to be unity at $r = R_{\text{outer}} = 11$ Å, the distance at which Eq. (5.17) starts to apply in the model potentials of Pashov *et al.*, to ensure that the potential energy is a continuous function of r. The correction factors are proportional to r^{-1} as $r \to \infty$. We calculate the correction factors using the K and Rb values $f_n^{\text{K}}(r)$ and $f_n^{\text{Rb}}(r)$ from [60] as

$$f_n(r) = \frac{1}{2}\left(\frac{f_n^{\text{K}}(\beta r)}{f_n^{\text{K}}(\beta R_{\text{outer}})} + \frac{f_n^{\text{Rb}}(\beta r)}{f_n^{\text{Rb}}(\beta R_{\text{outer}})}\right) \tag{5.18}$$

which ensures that for any value of the parameter β the total potential remains continuous and the long-range potential has the correct behaviour as $r \to \infty$. We then perform a least-squares fit to our data for the resonance position with β as the free parameter, and we find the optimum value to be $\beta = 1.000(65)$. The 1-σ confidence interval for the predicted resonance position as a function of energy is shown as the red band in Fig. 5.9a, and the predictions using the optimized potential for the width and background phase shift are shown as the solid red lines in Figs. 5.9b and c, respectively. There is little change in the latter two parameters because they are mostly determined by the details of the short-range interaction. Using the updated model, we predict $B_0(0) = 546.606(22)$ G which agrees well with the value measured by Klempt *et al.*[162] of $B_0(0) = 546.618(6)$ G.[9]

Our measurements of $\Gamma_B(E)$ and $\delta_{\text{bg}}(E)$ match the predictions less well, and this is likely due to two important factors. First, the values of Γ_B and δ_{bg} extracted from the fit are very sensitive to the ratio of maximum to background scattering fraction. In particular, if the maximum value of S is suppressed, then the measured width will be wider than predicted and the background phase shift will be larger. Such suppression could arise from changes in the measured number of unscattered atoms due to differences in the saturation of the optical depth: at resonance, fewer atoms remain in the unscattered cloud leading to a lower optical depth, less saturation, and a larger estimate of the total number of atoms. A second factor, which is particularly relevant for higher energies, is that the distribution of collision energies becomes wider – see Eq. (4.13) – and as this becomes comparable to the width of the resonance, the measured width of the resonance will become wider. Hints of this can be seen in Fig. 5.5b, where the estimate widths are, on average, higher than expected for larger energies. Our measurement of the background phase shift δ_{bg} matches the predictions more closely, and captures the energy dependence quite well.

We made similar measurements of the narrower Feshbach resonance between the ^{40}K $|\frac{9}{2}\frac{7}{2}\rangle$ and ^{87}Rb $|11\rangle$ states near 300 G. The results of these measurements are shown in Fig. 5.10. This resonance has less exotic behaviour in that its resonance position shifts monotonically

[9] If we optimized the potentials to match just the measurement by Klempt *et al.*, then we find $\beta = 0.960(19)$.

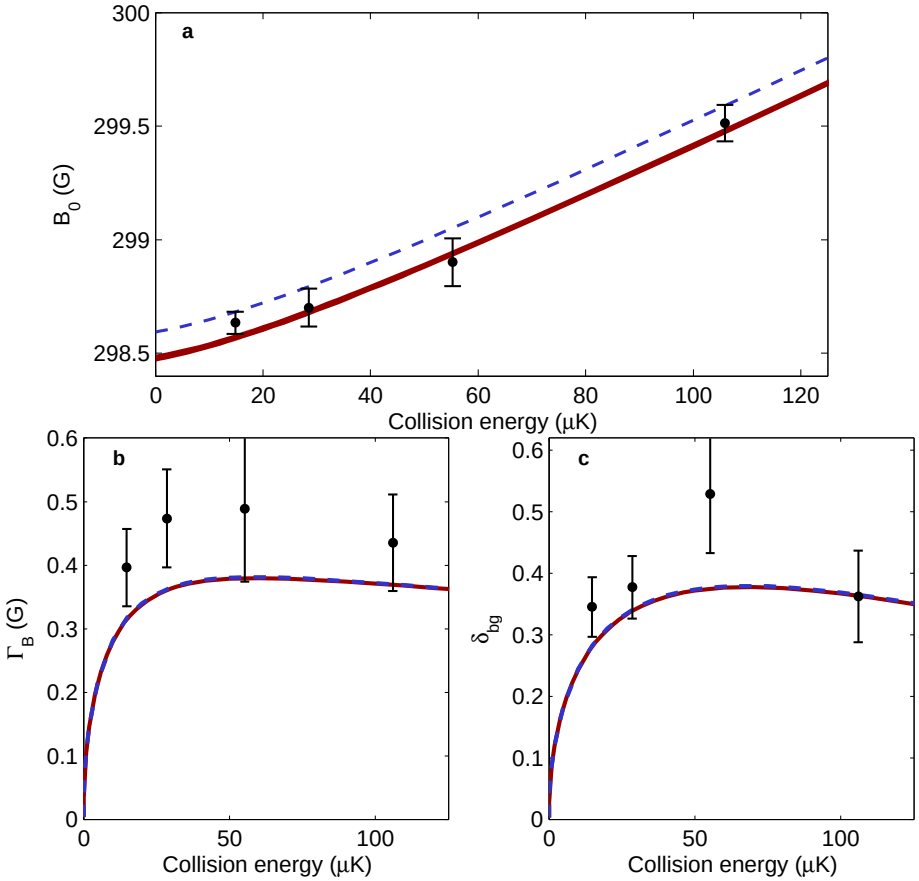

Figure 5.10: Comparison between parameters extracted from experimental data (circles) and parameters calculated from a coupled-channels model (solid lines). **a** $B_0(E)$, **b** $\Gamma_B(E)$, **c** $\delta_{\rm bg}(E)$. The blue dashed line is calculated based on the parameters described in [72], whereas the red band in **a** is the 1-σ confidence interval calculated using parameters optimized to match previous measurements of the 546 G resonance (see text). In **b** and **c**, the red line is calculated using the optimum model potential.

– and nearly linearly – with energy over the entire range of interest. The shift in position $\delta E(E)$ of this Feshbach resonance is much less than that of the 546 G resonance because the coupling between the open and closed channels, measured by $\Gamma_B(E)$, is much less; from multichannel quantum defect theory, one expects that the shift as $E \to 0$ should be proportional to the threshold insensitive width Δ_n[70, 63]. Again, the model described in Pashov *et al.*[72] is not accurate enough to describe the resonance positions that we measure, but using the same modifications as for the resonance at 546 G we find that the coupled channels calculation prediction matches the data well. The other two parameters of interest, $\Gamma_B(E)$ and $\delta_{\rm bg}(E)$, are less well matched by the model. This poor agreement is almost entirely due to the energy spread of the collider relative to the width of the resonance; the maximum width for the 300 G resonance is less than 0.4 G, whereas the maximum width for the 546 G resonance is just over 2 G. The spread of collision energies smears out the

measured resonance, increasing the apparent width of the resonance. In the fits that yield the measurements in Fig. 5.10, we attempt to correct for this spread by averaging the resonance profile over a Gaussian distribution of collision energies with the appropriate widths, but this still fails to produce reliable results. Clearly, our method for measuring Feshbach parameters only works for very wide resonances; in principle, we can measure narrow resonances, but we need much colder samples without sacrificing signal-to-noise.

Lastly, I should comment on our choice to adjust the long-range potentials from Pashov *et al.*[72] by applying retardation corrections estimated from [60]. Two major objections can be raised: why include retardation effects at all, and why obtain ad-hoc estimates of the KRb retardation from [60]? First, we did not need to use retardation corrections; instead, we could have just as easily adjusted the C_6 coefficient directly. While this is commonly done, there is no *a priori* reason why this should be more physically plausible. We initially thought that the shift in the resonance location was due to retardation effects, and so we sought to parametrize a model of this effect; with only small corrections, we obtained predictions that match more precise experimental values well. Additionally, our method of adjusting the long-range interaction ensures that the potential energy function is continuous, which adjusting the C_6 coefficient would not be. The ideal solution to the difference between the model potential of Pashov *et al.* and the measured resonance positions is to fully re-parametrize the interaction potentials, taking into account the new and more precise Feshbach resonance positions. However, to do this properly would require the photoassociation spectra that define the deep, attractive wells of the singlet and triplet potentials. In the future this might be done, but for now reasonable ad-hoc corrections suffice.

The second question, regarding the effects of retardation on the KRb dispersion forces, addresses the fact that Marinescu *et al.*[60] only calculated retardation factors for homonuclear pairs of alkali atoms; heteronuclear pairs were not included. Instead, one should have used the Casimir-Polder potentials described for KRb in [73] or calculated the retardation coefficients directly from the dynamic polarizabilities in [164]. Initially, both of these approaches were attempted, but the long-range potentials that they described resulted in resonance positions that were different from the measured positions by several Gauss. Averaging the K and Rb retardation coefficients from [60] gave resonance positions that were only different from the measured positions by, at most, 100 mG; therefore, this method was chosen as a starting point.[10] More fundamentally, however, is that the model potential from Pashov *et al.*[72] is a phenomenological model: while the terms in the potential and the starting values are inspired by first-principles calculations, the final result is optimized to match observations. The exact values of the various parameters depend on exactly

[10]The careful reader will note that Eq. (5.18) is optimum with the default value of $\beta = 1$ and may be confused by how the resonance positions could be different by 100 mG. Equation (5.18) was the final form that we used for the modification, and other forms had different shifts.

what effects are included, and retardation effects were not included. We have made a phenomenological change to the model but make no claims that the basis for doing so is more correct than the decision of the authors of [72] to leave out retardation effects.

5.5 Multiple scattering

Near the peak of the resonance a second K cloud of Gaussian character appears at the same location as the Rb cloud. The origin of this cloud is multiple scattering of K atoms with Rb atoms, and the mechanism is a more extreme version of the axially enhanced multiple scattering seen in Chapter 4. In the ^{40}K system, primary collisions at a nominal energy that was higher than the resonant energy created pairs of atoms that were nearly co-propagating, and these pairs could collide at the resonant energy of $\sim$350 μK. As a result, the final momenta of these atoms were closely aligned with the collision axis as seen in Fig. 4.5. The crucial requirement there for axial enhancement was a resonance at an energy below the nominal collision energy; here, I will show that axial enhancement persists even when the maximum cross section is at zero energy.

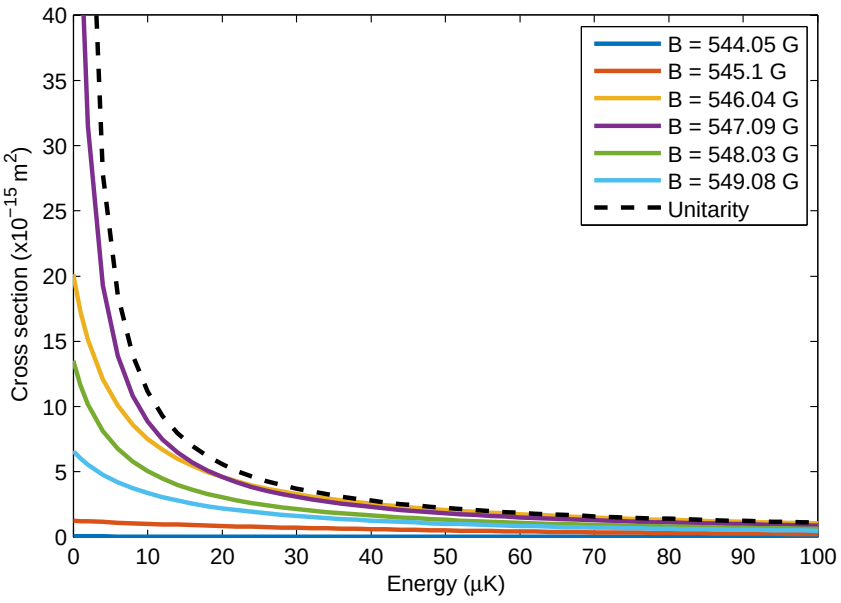

Figure 5.11: Plot of the ^{40}K^{87}Rb cross section in the absolute ground state as a function of energy for the specified magnetic fields. Black dashed line is the unitarity limit.

Despite the presence of a Feshbach resonance in this experiment with KRb collisions, the cross section as a function of energy for fixed magnetic field does not show a distinct resonance as seen in Fig. 5.11. The reason for this lack is that the resonance position shifts very little relative to the width of the resonance as a function of energy. As a result,

the cross section as a function of energy for a magnetic field near the resonant field is very nearly monotonically decreasing as a function of energy, and the lack of a centrifugal barrier allows the cross section to approach very high values as $E \rightarrow 0$. Therefore, secondary collisions between pairs of K and Rb atoms that have vanishingly small collision energies are highly favoured. A diagram of the multiple scattering process is shown in Fig. 5.12. A

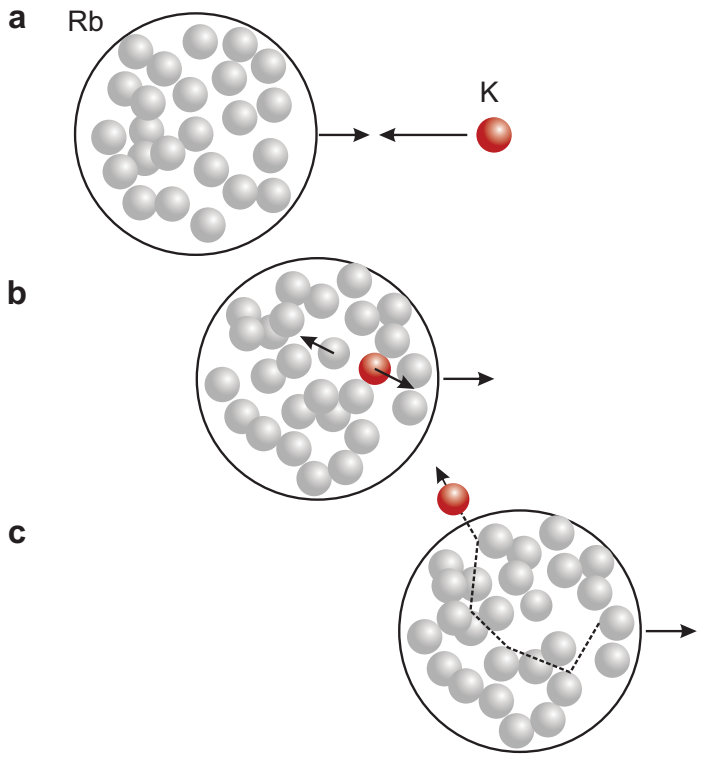

Figure 5.12: Diagram of KRb multiple scattering near resonance for a single K atom. **a** A K atom and a cloud of Rb atoms approach each other. **b** The K atom collides with a Rb atom and the K atoms scatters in the direction that the Rb cloud is moving. **c** The K atom collides many times with Rb atoms before escaping the cloud due to the enhanced cross section at low collision energies.

single K atom collides with an atom in the Rb cloud and scatters in the direction that the Rb cloud is moving. Subsequent collisions between the K atom and the Rb atoms will occur at much lower energies than the initial collision, and the lower the energy of the collision the more favoured it will be[134]. This will tend to trap K atoms that are scattered into velocities that are close to the mean velocity of the Rb cloud. Effectively, the K atoms will perform a random walk through the Rb cloud. If the Rb density is low, then the mean free path of the K atoms through the Rb cloud will be larger than the size of the Rb cloud, and the K atoms will ballistically escape the Rb cloud. If, however, the Rb density is high enough then the mean free path of the K atoms will be smaller than the Rb cloud, and the K atoms will diffuse through the Rb atoms. This process is reminiscent of Schuster *et al.*[165], where the authors concluded that a multiple-scattering energy-cascade was responsible for

a steep increase in the loss of atoms from a condensate when the collisional opacity reached a certain critical value. By using a DSMC model we can count the number of collisions that each atom experiences and map these to spatial locations, and this is done in Fig. 5.13 using experimental parameters. One can see that while the mean number of collisions in the scattering halo is approximately unity, the mean number of collisions in the multiply scattered cloud is up to ten times higher.

As can be seen in Figs. 5.13c and d, a secondary Rb cloud does not exist, although multiply-scattered atoms are preferentially located along the collision axis. The lack of a secondary cloud ultimately stems from a difference between the sizes of the K cloud and the Rb cloud at the time of collision. The K cloud initially has a temperature that is nearly 40% higher than the Rb cloud and, coupled with the difference in mass and therefore expansion rate of the cloud, means that the K cloud is larger than the Rb cloud at the time when the two collide. The collisional opacity of the Rb cloud to K atoms is high enough for the K atoms to diffuse through the Rb cloud, whereas the collisional opacity of the K cloud to Rb atoms is insufficient for diffusion to occur. Rb atoms are still preferentially scattered towards the collision axis due to the energy-dependence of the cross-section, but the density of the K cloud is too low for the Rb atoms to experience enough collisions to diffuse, as can be seen in the difference in the number of collisions shown in Figs. 5.13b and d.

Finally, we can demonstrate that it is the rising nature of the cross section that leads to the secondary cloud. In Fig. 5.14, I have plotted the K spatial distributions calculated by DSMC for three different conditions. In Fig. 5.14a, I have plotted the simulated distributions for parameters as found in the experiment. Keeping the cross section the same as in the experiment but decreasing the density of the Rb atoms reduces, but does not completely eliminate, the secondary K cloud in Fig. 5.14b. Fixing the cross section to be a constant value, however, removes the secondary cloud entirely as in Fig. 5.14c. While secondary collisions occur within the unscattered Rb cloud, there is no preference for collisions that keep the K atoms within its confines.

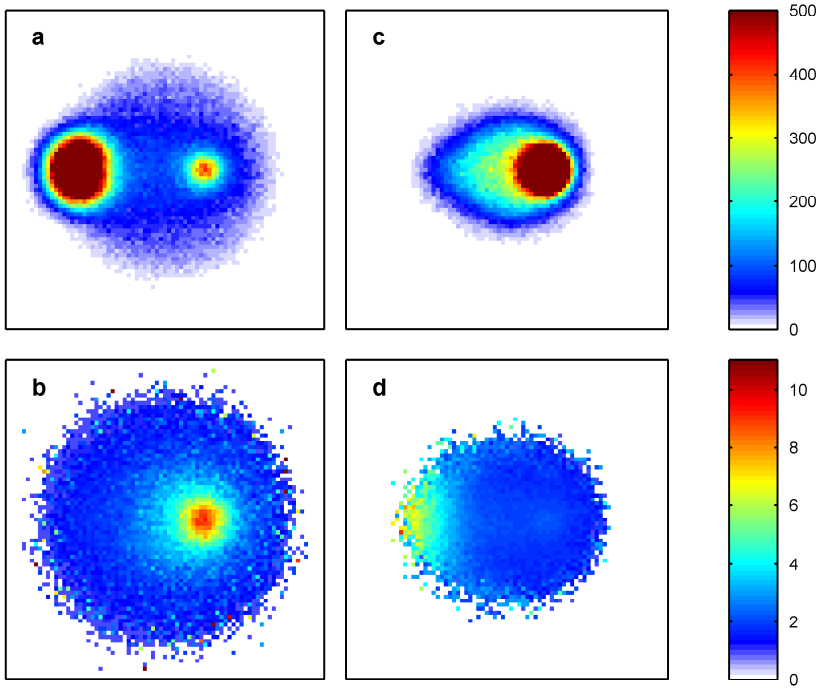

Figure 5.13: Simulated spatial distribution of atoms and mean numbers of inter-cloud collisions using experimental parameters (Sec. 5.1). **a** Spatial distribution of K atoms after collision using a 16×16 μm cell size. **b** Spatial distribution of the mean number of inter-cloud collisions per cell for K atoms. **c** Spatial distribution of Rb atoms after collision using a 16×16 μm cell size at the same time as **a**. **d** Spatial distribution of the mean number of inter-cloud collisions per cell for Rb atoms.

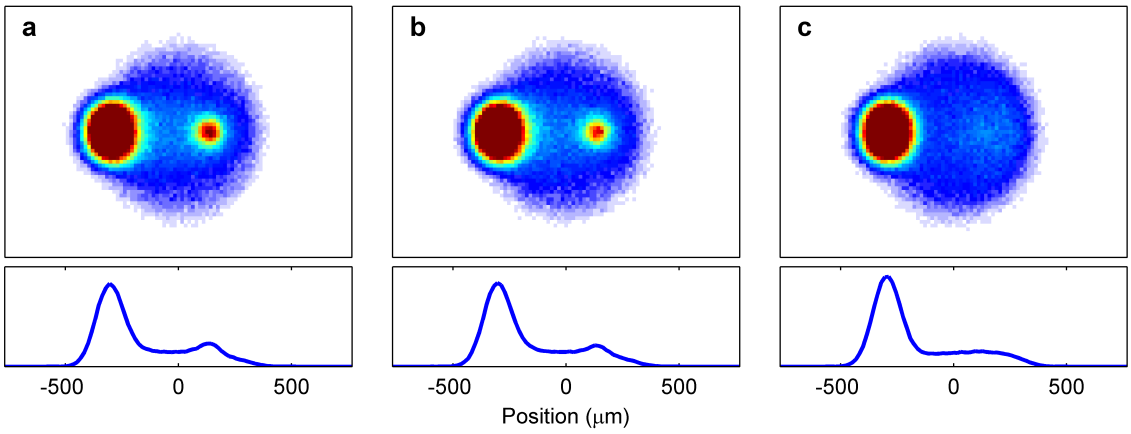

Figure 5.14: Simulated absorption images (top) and line density profiles (bottom) for ^{40}K after a collision at $E = 30$ μK for three different scenarios. **a** Parameters as determined in the experiment (see Sec. 5.1) with a cross section calculated from a coupled-channels model. **b** Same as **a** but with the Rb cloud size the same as the K cloud size. **c** Same as **a** but with an energy-independent cross section fixed to the value at $E = 30$ μK.

5.6 Conclusion

While Feshbach resonances have been a core component of ultracold atomic physics since nearly the inception of BEC, they have rarely been investigated outside of the near threshold regime. We have demonstrated that, using an appropriate collider, one can characterize these resonances at energies well above threshold where universal relationships do not necessarily hold. At these energies, we observe s-wave scattering halos that are complicated by the presence of secondary clouds which correspond to multiply scattered atoms. Their presence is dependent on the resonance lacking both a clear resonant feature as a function of energy and a centrifugal barrier that suppresses low energy collisions. Despite the presence of significant multiple scattering, the fraction of atoms scattered by the collision follows a pure Beutler-Fano profile which is uncomplicated by background energy dependencies. We use the characteristics of this profile to map out the properties of two Feshbach resonances as a function of energy and find that with suitable modification established model potentials describe well the energy-dependent scattering of the resonance. With reasonable improvements to the experiment, we expect to be able to probe narrower resonances at lower energy and test predictions of analytic theories [70].

Chapter 6

Epilogue: Quo vadis, optical collider?

This thesis had the primary goal of directly and precisely probing the scattering properties of atoms in the "cold" regime: between 0 and 2 mK. Improvements to the precision can always be made, and there are a number that are fairly obvious. The inherent energy width of our collider renders it ineffective at probing narrow scattering features or scattering features at low (< 10 μK) energies. This width is due solely to the thermal nature of the atoms, so if one can cool the atom clouds further, then the precision of the collider will be enhanced. The ideal limit would be to collide condensates with degenerate Fermi gases. However, one loses atoms rapidly as the temperature is lowered, so we need to either start with more atoms at a higher density or improve the signal-to-noise of our imaging system, or more preferably both. More atoms might be obtained by evaporatively cooling atoms in the magnetic quadrupole trap rather than the IP trap, as the density of atoms will be higher and cooling more efficient. Additionally, we might improve evaporative cooling in the optical dipole trap by fully implementing new evaporation techniques that we have developed[116]. Improved signal-to-noise on the images might be obtained using fluorescence imaging, or Rydberg tagging[166, 167], or more advanced image processing algorithms. Colder clouds will also allow shorter expansion times, which will yield denser scattering halos and improve the signal-to-noise. With such improvements, we can reasonably expect to improve our measurements of the widths and background phase shifts of the two Feshbach resonances in Chapter 5.

With a narrower energy width, we can probe Feshbach resonances closer to threshold while still retaining the advantages of having a distinct collision axis. In particular, the energy dependence of the s-wave Feshbach width, $\Gamma \propto E^{1/2}$, has not been measured directly, and given its ubiquity in the physics of s-wave Feshbach resonances, it seems prudent to do so.[1] While the ^{40}K^{87}Rb system may not be the best example of this behaviour, resonances

[1]The authors of [168] inferred the $E^{1/2}$ scaling from Feshbach molecule dissociation measurements, but did not measure the width directly.

in other systems such as homonuclear ^{87}Rb or ^{40}K are promising avenues for investigating this scaling. Additionally, by using condensates, we may be able to observe an analogue to "slow-light" in the propagation of light through an atomic medium: a so-called "slow-BEC" where the reduction in the group velocity of colliding BECs is caused by the coupling of atoms to molecules[169].

One particular advantage of having a well-defined collision axis is that we can directly observe the scattering halo. In this work, I focused only on s-wave Feshbach resonances. However, resonances can occur in channels with any partial wave ℓ. For example, there is a p-wave Feshbach resonance in ^{40}K^{87}Rb in the absolute ground state near 515 G. In experiments involving loss measurements, the p-wave nature of a Feshbach resonance is typically inferred by the splitting of the resonance into two peaks due to dipole-dipole coupling[170], or by comparing the resonance position to theoretical calculations. With our optical collider, we can directly determine the partial wave of a resonance by simply observing the scattering halo; in fact, we did just that in Fig. 6.1. This data was taken before

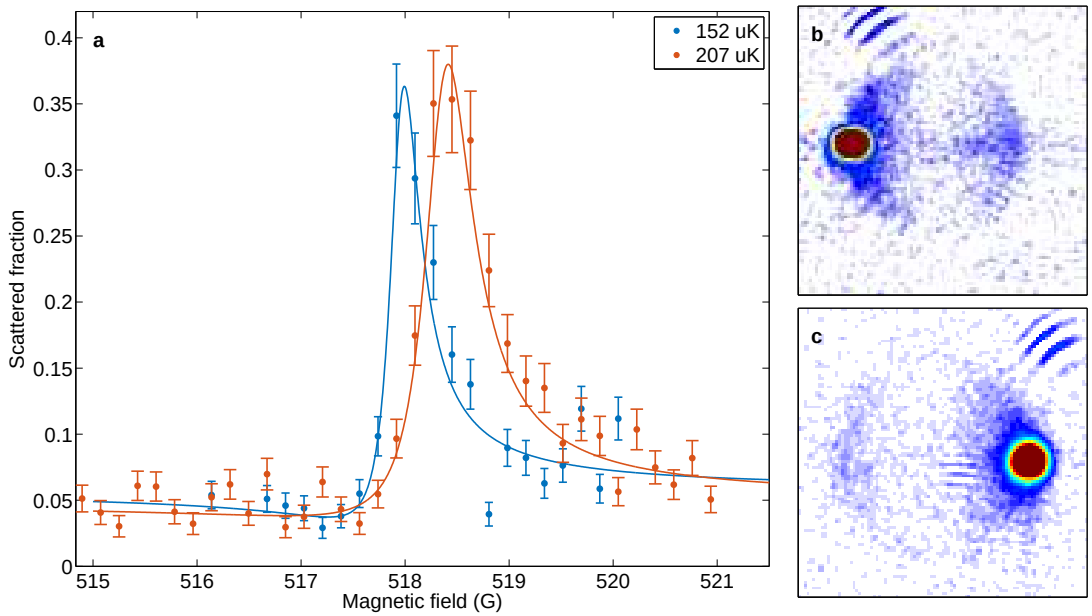

Figure 6.1: Observation and measurement of a p-wave Feshbach resonance in ^{40}K^{87}Rb. **a** Scattered fraction as a function magnetic field (uncalibrated). **b-c** Absorption images of K (**b**) and Rb (**c**) showing the p-wave nature of the Feshbach resonance.

we had a well-stabilized magnetic field, and only the two energies were measured. They show, however, the remarkable utility of the collider in resolving these features, which, due to an energy scaling similar to the Wigner threshold law in Eq. (2.112), are more difficult to detect and resolve at threshold. Future work in this direction will look more carefully at p-wave and possibly d-wave Feshbach resonances, which will allow us to compare to predictions regarding Feshbach resonances in the near-threshold regime. Higher-ℓ partial

waves can also be investigated in shape resonances; for example, there is an $\ell = 6$ shape resonance in the homonuclear ^{87}Rb system at 1900 μK and an $\ell = 4$ shape resonance in the ^{40}K^{87}Rb system at 1959 μK.[2]

One can imagine more exotic experiments. It is possible to generate spin entanglement in the collisions of identical particles[171], and we could look for spin correlations in the scattering halo[16, 46]. We could form weakly bound dimers using Feshbach resonances[146] and investigate atom-dimer collisions. This could also be a useful probe of Efimov physics[172], in addition to using atom-atom collisions as in [173]. Lastly, one could use multiple scattering effects similar to those seen in Sec. 5.5 to investigate interaction-based analogues[174] of Anderson localization[175, 176] and coherent backscattering[177].

In my opinion, the most fruitful and interesting experiments are yet to come.

[2]Both of these numbers come from coupled-channels calculations described in this thesis, although Dr. Eite Tiesinga predicted the $\ell = 6$ resonance first in a private communication with the Kjærgaard group.

Appendix A

Additional scattering theory

A.1 Proof of Rayleigh's formula

Given an expansion of a plane wave e^{ikz} in terms of Legendre polynomials, I want to find coefficients A_ℓ such that

$$e^{ikz} = \sum_{\ell=0}^{\infty} A_\ell P_\ell(\cos\theta) \tag{A.1}$$

where A_ℓ will depend on k and z. First, I let $u = \cos\theta$ and multiply both sides by $P_{\ell'}(u)$. I then integrate over u from -1 to 1 and use the orthogonality of Legendre polynomials[58]

$$\int_{-1}^{1} P_{\ell'}(u) P_\ell(u) du = \frac{2\delta_{\ell\ell'}}{2\ell+1}$$

to get

$$A_\ell = \frac{2\ell+1}{2} \int_{-1}^{1} P_\ell(u) e^{ikru} du.$$

The Legendre polynomials can be written using Rodrigues' formula[58]

$$P_\ell(u) = \frac{1}{2^\ell \ell!} \frac{d^\ell}{du^\ell} \left[(u^2-1)^\ell\right] \tag{A.2}$$

which, replacing $kr = q$, I can use to get

$$\begin{aligned} A_\ell &= \frac{2\ell+1}{2^{\ell+1}\ell!} \int_{-1}^{1} e^{iqu} \frac{d^\ell}{du^\ell} \left[(u^2-1)^\ell\right] du \\ &= \frac{2\ell+1}{2^{\ell+1}\ell!} F_\ell(q). \end{aligned}$$

Integrating by parts yields

$$F_\ell(q) = e^{iqu} \left[\frac{d^{\ell-1}}{du^{\ell-1}} \left\{(u^2-1)^\ell\right\}\right]_{-1}^{1} - iq \int_{-1}^{1} e^{iqu} \frac{d^{\ell-1}}{du^{\ell-1}} \left[(u^2-1)^\ell\right].$$

The polynomial $(u^2-1)^\ell$ has roots of order ℓ at $u = \pm 1$, but I am taking only $\ell - 1$ derivatives. Therefore, the resulting polynomial will have roots of order 1 at $u = \pm 1$, so

the boundary term must vanish. I can repeat integration by parts a total of ℓ times, which means

$$F_\ell(q) = i^\ell q^\ell \int_{-1}^{1} e^{iqu}(1-u^2)^\ell du$$

after switching the order of terms in the polynomial.

The next step uses the very handy identity

$$\int u^n e^{cu} du = \int \partial_c^n (e^{cu}) du = \partial_c^n \int e^{cu} du = \partial_c^n \left(\frac{e^{cu}}{c} \right)$$

which, when replacing $c = iq$, yields

$$\int_{-1}^{1} u^n e^{iqu} du = 2(-i)^n \partial_q^n \left(\frac{\sin q}{q} \right).$$

I now write $F_\ell(q)$ as

$$\begin{aligned} F_\ell(q) &= i^\ell q^\ell \int_{-1}^{1} e^{iqu}(1-u^2)^\ell du \\ &= i^\ell q^\ell \int_{-1}^{1} \sum_{k=0}^{\ell} \binom{\ell}{k} (-1)^k u^{2k} e^{iqu} du \\ &= 2i^\ell q^\ell \sum_{k=0}^{\ell} \binom{\ell}{k} (-1)^k (-i)^{2k} \partial_q^{2k} \left(\frac{\sin q}{q} \right) \\ &= 2i^\ell q^\ell \left(1 + \partial_q^2\right)^\ell \left(\frac{\sin q}{q} \right) \end{aligned}$$

which is a repeated differentiation using the operator $1 + \partial_q^2$. I will now recast this repeated differentiation. First, I let $f(q) = \sin q/q$, and note that

$$\left(1 + \partial_q^2\right)(qf) = 0$$

which implies that

$$\left(1 + \partial_q^2\right)^\ell (qf) = 0.$$

I will expand the powers of $1 + \partial_q^2$ in a binomial series again, but I first need to calculate the repeated derivatives of qf

$$\begin{aligned} \partial_q^n (qf) &= \sum_{m=0}^{n} \binom{n}{m} \partial_q^m (q) \partial_q^{n-m} (qf) \\ &= q\partial_q^n f + n\partial_q^{n-1} f. \end{aligned}$$

I now use this in the binomial expansion of $\left(1+\partial_q^2\right)^\ell(f)$:

$$\begin{aligned}
0 &= \left(1+\partial_q^2\right)^\ell (qf) \\
&= \sum_{k=0}^{\ell} \binom{\ell}{k} \partial_q^{2k}(qf) \\
&= q\sum_{k=0}^{\ell} \binom{\ell}{k} \partial_q^{2k} f + 2\sum_{k=1}^{\ell} \binom{\ell}{k} k\partial_q^{2k-1} f \\
&= q\sum_{k=0}^{\ell} \binom{\ell}{k} \partial_q^{2k} f + 2\ell\partial_q \sum_{k=0}^{\ell-1} \binom{\ell-1}{k} \partial_q^{2k} f \\
&= q\left(1+\partial_q^2\right)^\ell f + 2\ell\partial_q \left(1+\partial_q^2\right)^{\ell-1} f.
\end{aligned}$$

I can rearrange this to give a simple recurrence relationship

$$\left(1+\partial_q^2\right)^\ell f = -\frac{2\ell}{q}\partial_q \left(1+\partial_q^2\right)^{\ell-1} f$$

which implies that

$$\left(1+\partial_q^2\right)^\ell f = (-2)^\ell \ell! \left(\frac{1}{q}\partial_q\right)^\ell f. \tag{A.3}$$

Putting it all together, I have that

$$\begin{aligned}
A_\ell &= \frac{2\ell+1}{2^{\ell+1}\ell!} 2i^\ell q^\ell (-2)^\ell \ell! \left(\frac{1}{q}\partial_q\right)^\ell \left(\frac{\sin q}{q}\right) \\
&= (2\ell+1) i^\ell (-q)^\ell \left(\frac{1}{q}\partial_q\right)^\ell \left(\frac{\sin q}{q}\right).
\end{aligned} \tag{A.4}$$

The spherical Bessel function can be defined as[58]

$$j_\ell(q) = (-q)^\ell \left(\frac{1}{q}\partial_q\right)^\ell \left(\frac{\sin q}{q}\right) \tag{A.5}$$

which means that the expansion coefficients are

$$A_\ell = (2\ell+1) i^\ell j_\ell(kr) \tag{A.6}$$

which is precisely what I set out to prove.

A.2 Near threshold behaviour of partial waves

Using Eq. (2.38) I can write the threshold solution of the radial equation as

$$u_\ell(r) \overset{r\to\infty}{\propto} r^{\ell+1} - \frac{a_\ell^{2\ell+1}}{r^\ell} \tag{A.7}$$

for large r. The leading term $r^{\ell+1}$ is always present for potentials that are less singular than r^{-2} at the origin because it arises naturally from integrating Eq. (2.24) outwards from the origin. The next-to-leading term is not as universal, and it depends on the asymptotic properties of the potential itself. If the potential falls off as $V(r) \overset{r\to\infty}{\propto} r^{-\alpha}$, then the near threshold phase shifts given by Eq. (2.38) are only valid for[54]

$$\alpha > 2\ell + 3. \tag{A.8}$$

To see how this comes about, I assume that I have a potential that behaves asymptotically as

$$V_\alpha = \frac{C_\alpha}{r^\alpha} = \pm\frac{\hbar^2}{2m}\frac{\beta_\alpha^{\alpha-2}}{r^\alpha}$$

where I have defined the quantum mechanical length scale

$$\beta_\alpha = \left(\frac{2m|C_\alpha|}{\hbar^2}\right)^{1/(\alpha-2)},$$

which, for $\alpha = 6$, is twice the van der Waals length[63]. At threshold ($E = 0$) and for large r, the radial equation is

$$\left(-\partial_r^2 + \frac{\ell(\ell+1)}{r^2} \pm \frac{\beta^{\alpha-2}}{r^\alpha}\right) u_\ell(r) = 0 \tag{A.9}$$

where I have dropped the subscript β. This equation can be transformed into a Bessel-type equation using some substitutions. First, I define the function $w_\ell(r) = u_\ell(r)/\sqrt{r}$ which lets me rewrite Eq. (A.9) as

$$\left(r^\alpha\partial_r^2 + r^{\alpha-1}\partial_r + [\mp\beta^{\alpha-2} - r^{\alpha-2}(\ell(\ell+1) + \frac{1}{4})]\right) w_\ell(r) = 0.$$

I next define a new variable $z = ar^b$ which has partial derivatives related to r

$$\begin{aligned}\partial_r &= ab\left(\frac{z}{a}\right)^{1-1/b}\partial_z \\ \partial_r^2 &= ab(b-1)\left(\frac{z}{a}\right)^{1-2/b}\partial_z + a^2b^2\left(\frac{z}{a}\right)^{2-2/b}\partial_z^2,\end{aligned}$$

and I can substitute these derivatives into the equation for $w_\ell(r)$ to get

$$\left(z^2\partial_z^2 + z\partial_z + \frac{1}{b^2}\left[\mp\beta^{\alpha-2}\left(\frac{z}{a}\right)^{(2-\alpha)/b} - \ell(\ell+1) - \frac{1}{4}\right]\right) w_\ell(z) = 0.$$

To make the above into a Bessel-type equation, I need to have a coefficient z^2 in front of $w_\ell(z)$. Therefore, $(2-\alpha)/b = 2$ implying $b = (2-\alpha)/2$. Furthermore, I need the coefficient in front of the z^2 term to be unity, which means that

$$a = \frac{\alpha-2}{2\beta^{(\alpha-2)/2}}.$$

All this combined gives the equation

$$\left(z^2\partial_z^2 + z\partial_z + (\mp z^2 - \nu^2)\right) w_\ell(z) = 0 \tag{A.10}$$

with argument

$$z = \frac{2}{\alpha - 2}\left(\frac{\beta}{r}\right)^{(\alpha-2)/2}$$

and order

$$\nu = \frac{2\ell + 1}{\alpha - 2}.$$

For attractive cases, where $V_\alpha = -\frac{\hbar^2}{2m}\frac{\beta_\alpha^{\alpha-2}}{r^\alpha}$, I choose the positive sign in Eq. (A.10) and the solutions are regular Bessel functions $w_\ell(r) = J_\nu(z)$ and $w_\ell(r) = Y_\nu(z)$. For repulsive cases, with $V_\alpha = \frac{\hbar^2}{2m}\frac{\beta_\alpha^{\alpha-2}}{r^\alpha}$, I choose the negative sign which gives solutions as the modified Bessel functions $I_\nu(z)$ and $K_\nu(z)$ (obtained by considering only imaginary values of z). In both cases, the solution $u_\ell(r)$ is

$$u_\ell(r) = \sqrt{\frac{r}{\beta}}(A\mathcal{C}_\nu(z) + B\mathcal{D}_\nu(z))$$

where $\mathcal{C}_\nu(z)$ is either $J_\nu(z)$ or $I_\nu(z)$, and $\mathcal{D}_\nu(z)$ is either $Y_\nu(z)$ or $K_\nu(z)$ depending on whether the potential is attractive or repulsive, respectively. In either case, the limit $r \to \infty$ corresponds to $z \to 0$, which means that I can expand about $z = 0$ which gives

$$\mathcal{C}_\nu(z) \overset{z\to 0}{\sim} \frac{(z/2)^\nu}{\Gamma(1+\nu)}[1 + \mathcal{O}(z^2)]$$
$$\mathcal{D}_\nu(z) \overset{z\to 0}{\sim} \frac{\Gamma(\nu)}{2(z/2)^\nu}[1 + \mathcal{O}(z^2)].$$

Now, I also have

$$\left(\frac{z}{2}\right)^\nu = \left(\frac{1}{\alpha - 2}\right)^{(2\ell+1)/(\alpha-2)}\left(\frac{\beta}{r}\right)^{\ell+\frac{1}{2}}$$

and $z^2 \propto (\beta/r)^{\alpha-2}$, which means that the solution $u_\ell(r)$ has the behaviour

$$\begin{aligned} u_\ell(r) \overset{r\to\infty}{\propto} & A\left(\frac{r}{\beta}\right)^{1/2}\left(\frac{\beta}{r}\right)^{\ell+1/2}\left[1 + \frac{A'}{A}\left(\frac{r}{\beta}\right)^{\alpha-2}\right] \\ & + B\left(\frac{r}{\beta}\right)^{1/2}\left(\frac{r}{\beta}\right)^{\ell+1/2}\left[1 + \frac{B'}{B}\left(\frac{r}{\beta}\right)^{\alpha-2}\right] \\ u_\ell(r) \overset{r\to\infty}{\propto} & B\left(\frac{r}{\beta}\right)^{\ell+1} + A\left(\frac{\beta}{r}\right)^{\ell} + B'\left(\frac{\beta}{r}\right)^{\alpha-3-\ell} + A'\left(\frac{\beta}{r}\right)^{\ell+\alpha-2} \end{aligned} \tag{A.11}$$

for unknown coefficients A, A', B, and B'. When I determined the near-threshold behaviour of the phase shifts, I assumed that the lowest order term from the irregular free-particle solution was proportional to $1/r^\ell$. From Eq. (A.11) one can see that if $\ell > \alpha - 3 - \ell$, or

$$2\ell + 3 > \alpha \tag{A.12}$$

then the dominant term is not proportional to $1/r^\ell$ and I can no longer make the same statement about the near threshold behaviour of the phase shifts.

What can I say about the scattering phase shifts when $2\ell + 3 > \alpha$? For this I use the radial Lippman-Schwinger equation[54] to get the phase shift

$$\tan\delta_\ell = -\frac{2m}{\hbar^2 k^2}\int_0^\infty u_\ell^s(\rho) V\left(\frac{\rho}{k}\right) u_\ell(\rho) d\rho \tag{A.13}$$

with $\rho = kr$. For $k \to 0$, only the large r tail of the potential contributes to the integral, and I can replace the solution $u_\ell(\rho)$ with its free-particle form $u_\ell^s(\rho)$, where I have neglected the term $\tan\delta_\ell u_\ell^c(\rho)$ because $\delta_\ell \to 0$ for $k \to 0$. Making the substitutions, I get

$$\tan\delta_\ell \overset{k\to 0}{\sim} \mp(k\beta)^{\alpha-2}\int_0^\infty \frac{u_\ell^s(\rho)^2}{\rho^\alpha} d\rho \tag{A.14}$$

where the integral converges when, for small ρ, $2\ell + 2 - \alpha > -1$, or $2\ell + 3 > \alpha$. Therefore, when $2\ell + 3 > \alpha$ the phase shift scales as $\tan\delta_\ell \overset{k\to 0}{\sim} \mp(k\beta_\alpha)^{\alpha-2}$, and it depends only on the asymptotic behaviour of the potential and not on its short-range behaviour.

Appendix B

Theory of acousto-optic modulators

B.1 Wave equations

I start from Maxwell's equations in the absence of free charges and currents and in non-magnetic media

$$\begin{aligned}
\nabla \cdot \mathbf{D} &= 0 \\
\nabla \cdot \mathbf{B} &= 0 \\
\nabla \times \mathbf{E} &= -\dot{\mathbf{B}} \\
\nabla \times \mathbf{B} &= \mu_0 \dot{\mathbf{D}}
\end{aligned} \tag{B.1}$$

where $\mathbf{E}$ is the electric field, $\mathbf{B}$ is the magnetic field, and $\mathbf{D}$ is the electric displacement, which is defined by

$$\mathbf{D} = \epsilon_0 \mathbf{E} + \mathbf{P} \tag{B.2}$$

with $\mathbf{P}$ the electric polarization. All fields are functions of position $\mathbf{r}$ and time t. Calculating $\nabla \times \nabla \times \mathbf{E}$, I derive the wave equation for the electric field

$$\nabla^2 \mathbf{E} - \frac{1}{c^2}\ddot{\mathbf{E}} = \frac{1}{\epsilon_0 c^2}\ddot{\mathbf{P}} - \frac{1}{\epsilon_0}\nabla(\nabla \cdot \mathbf{P}). \tag{B.3}$$

In what follows, I will only consider the scalar wave case such that $\nabla \cdot \mathbf{P} = 0$ and $\mathbf{E} = E$. This is satisfied if I restrict the problem to the x-z plane and take the polarization to be in the y direction. The electric field is then a function of x, z, and t only: $E(\mathbf{r}, t) = E(x, z, t)$.

I define the space and time Fourier transforms as

$$\begin{aligned}
\hat{\mathcal{F}}_t f(t) &= \int_{-\infty}^{\infty} f(t) e^{i\omega t} dt \\
\hat{\mathcal{F}}_x f(x) &= \int_{-\infty}^{\infty} f(x) e^{-ikx} dx,
\end{aligned} \tag{B.4}$$

and I apply both to Eq. (B.3) to get the differential equation

$$\left(-k_x^2 + \partial_z^2 + \frac{\omega^2}{c^2}\right) E(k_x, z, \omega) = -\frac{\omega^2}{\epsilon_0 c^2} P(k_x, z, \omega). \tag{B.5}$$

I now assume that the medium is linear and isotropic so that I can define an electric susceptibility

$$\chi(\mathbf{r}, t) = \chi_0 + \chi_s(\mathbf{r}, t) \tag{B.6}$$

where χ_0 is the background susceptibility that is independent of time and space, and $\chi_s(\mathbf{r}, t) \ll \chi_0$ is a small deviation from the background due to the acoustic wave. The polarization is therefore

$$P(\mathbf{r}, t) = \epsilon_0 \chi_0 E(\mathbf{r}, t) + \epsilon_0 \chi_s(\mathbf{r}, t) E(\mathbf{r}, t) \tag{B.7}$$

which means that

$$P(k_x, z, \omega) = \epsilon_0 \chi_0 E(k_x, z, \omega) + \epsilon_0 \hat{\mathcal{F}}_x \hat{\mathcal{F}}_t [\chi_s(\mathbf{r}, t) E(\mathbf{r}, t)]. \tag{B.8}$$

The second term, being a Fourier transform of the product of functions, is equivalent to the double convolution

$$\hat{\mathcal{F}}_x \hat{\mathcal{F}}_t [\chi_s(\mathbf{r}, t) E(\mathbf{r}, t)] = \int_{-\infty}^{\infty} d\omega' \int_{-\infty}^{\infty} dk_x' \chi_s(k_x', z, \omega') E(k_x - k_x', z, \omega - \omega'). \tag{B.9}$$

Now, I assume that the acoustically induced susceptibility χ_s is a traveling wave in the medium

$$\chi_s(\mathbf{r}, t) = a e^{i\mathbf{q}\cdot\mathbf{r} - i\Omega t} + a^* e^{-i\mathbf{q}\cdot\mathbf{r} + i\Omega t} \tag{B.10}$$

where $q = |\mathbf{q}| = \Omega / v$ (with acoustic wave speed v) and $\mathbf{q} = q_x \hat{\mathbf{x}} + q_z \hat{\mathbf{z}}$. Then its Fourier transform is

$$\chi_s(k_x, z, \omega) = a e^{i q_z z} \delta(k_x - q_x) \delta(\omega - \Omega) + a^* e^{-i q_z z} \delta(k_x + q_x) \delta(\omega + \Omega) \tag{B.11}$$

and the double convolution reduces to

$$\int_{-\infty}^{\infty} d\omega' \int_{-\infty}^{\infty} dk_x' \chi_s(k_x', z, \omega') E(k_x - k_x', z, \omega - \omega') = a e^{i q_z z} E(k_x - q_x, z, \omega - \Omega) + a^* e^{-i q_z z} E(k_x + q_x, z, \omega + \Omega). \tag{B.12}$$

Let $n_0 = \sqrt{1 + \chi_0}$ be the background index of refraction. The wave equation is then

$$\left(\partial_z^2 + \frac{n_0^2 \omega^2}{c^2} - k_x^2\right) E(k_x, z, \omega) = -\frac{\omega^2}{c^2} \left[a e^{i q_z z} E(k_x - q_x, z, \omega - \Omega) + a^* e^{-i q_z z} E(k_x + q_x, z, \omega + \Omega) \right]. \tag{B.13}$$

To simplify Eq. (B.13), I define

$$E(k_x, z, \omega) = \tilde{E}(k_x, z, \omega) e^{i k_z z}$$

where $k_z = k_z(\omega, k_x) = \sqrt{n_0^2\omega^2/c^2 - k_x^2}$. I can then invoke the slowly-varying envelope approximation

$$\begin{aligned}\partial_z^2 E &= -k_z^2 \tilde{E} e^{ik_z z} + 2ik_z e^{ik_z}\partial_z \tilde{E} + e^{ik_z z}\partial_z^2 \tilde{E} \\ &\approx -k_z^2 \tilde{E} e^{ik_z z} + 2ik_z e^{ik_z}\partial_z \tilde{E}\end{aligned} \tag{B.14}$$

which amounts to dropping the second derivative term on $\tilde{E}$ compared to terms proportional to k_z and k_z^2. This approximation reduces the order of the differential equation Eq. (B.13) to one, which I can re-write as

$$\begin{aligned}&2ik_z\partial_z\tilde{E}(k_x, z, \omega) \\ &\quad = -\frac{\omega^2}{c^2}\Big[a\tilde{E}(k_x - q_x, z, \omega - \Omega)e^{iz(q_z + k_z(\omega-\Omega, k_x - q_x) - k_z(\omega, k_x))} \\ &\qquad + a^*\tilde{E}(k_x + q_x, z, \omega + \Omega)e^{iz(-q_z + k_z(\omega+\Omega, k_x+q_x) - k_z(\omega, k_x))}\Big].\end{aligned} \tag{B.15}$$

The exponential terms will quickly oscillate between positive and negative contributions to the electric field, so significant effects will only occur when the fields are phase-matched, which occurs when

$$k_z(\omega \pm \Omega, k_x \pm q_x) = k_z(\omega, k_x) \pm q_z. \tag{B.16}$$

Equation (B.16) is equivalent to the equation for energy and momentum conservation between collisions of a photon and a phonon

$$\mathbf{k}(\omega \pm \Omega) = \mathbf{k}(\omega) \pm \mathbf{q}(\Omega). \tag{B.17}$$

I now assume that the incident field is narrowly peaked around $k_x = 0$, so that I can treat the diffracted fields $\tilde{E}(k_x \pm q_x, z, \omega \pm \Omega)$ as separate fields. This will turn Eq. (B.15) into a set of coupled differential equations. I define

$$\tilde{E}_n(z) = \tilde{E}(nq_x, z, \omega + n\Omega) \tag{B.18}$$

and

$$k_{z,n} = k_z(\omega + n\Omega, nq_x).$$

The phase-matching condition Eq. (B.16) is then

$$k_{z,n+1} = k_{z,n} + nq_z.$$

Equation (B.15) becomes

$$\begin{aligned}2ik_z\partial_z\tilde{E}_n(z) = -\frac{(\omega + n\Omega)^2}{c^2}\Big[&a\tilde{E}_{n-1}(z)e^{iz(q_z + k_{z,n-1} - k_{z,n})} \\ &+ a^*\tilde{E}_{n+1}(z)e^{iz(-q_z + k_{z,n+1} - k_{z,n})}\Big].\end{aligned} \tag{B.19}$$

I choose $q_z = k_{z,1} - k_{z,0} = k_z(\omega+\Omega, q_x) - k_z(\omega, 0)$, which sets the exponent in the second term in Eq. (B.19) to zero. What about the first term? From the choice of q_z I have

$$q_z + k_z(\omega - \Omega, -q_x) - k_z(\omega, 0) = k_z(\omega + \Omega, q_x) + k_z(\omega - \Omega, -q_x) - 2k_z(\omega, 0)$$

which can be simplified by Taylor expanding $k_z(\omega + n\Omega, nq_x)$:

$$\begin{aligned} k_z(\omega + n\Omega, nq_x) &= \sqrt{\frac{n_0^2(\omega+n\Omega)^2}{c^2} - n^2 q_x^2} \\ &= \sqrt{\frac{n_0^2\omega^2}{c^2} + \frac{2n_0^2\omega\Omega}{c^2} + \frac{n_0^2 n^2\Omega^2}{c^2} - n^2 q_x^2} \\ &\approx \frac{n_0\omega}{c}\left(1 + \frac{n\Omega}{\omega} - \frac{n^2 q_x^2 c^2}{2n_0^2\omega^2}\right) \\ &= k_0\left(1 + \frac{n\Omega}{\omega} - \frac{n^2 q_x^2}{2k_0^2}\right) \end{aligned} \tag{B.20}$$

with the definition $k_0 = n_0\omega/c$. Ergo, the phase-matching term for the -1 order is equal to

$$k_z(\omega+\Omega, q_x) + k_z(\omega-\Omega, -q_x) - 2k_z(\omega, 0) = \frac{q_x^2}{2k_0} \approx \frac{q^2}{2k_0}.$$

In order to neglect this term it has to be much larger than the inverse of the typical length scale over which the $+1$ order changes. Similarly, the $+2$ order has a mis-match of

$$\frac{n_0\Omega}{c} - \frac{3q_x^2}{k_0} \approx -\frac{3q^2}{k_0}$$

which has the same requirement. For a typical AOM with $\Omega/(2\pi) = 80$ MHz, a sound velocity of 2000 m/s, and a laser with $\lambda = 1000$ nm the factor $q^2/k_0 \approx 2\pi/600\ \mu\text{m}^{-1}$. Typical AOM crystals are usually about 5-10 mm in length, so the assumption that these phase mis-matched terms cancel out is reasonable. Therefore, I assume that these terms, and all other non-phase-matched terms, can be neglected. The infinite system of equations reduces to just two:

$$\partial_z \tilde{E}_0(z) = \frac{i\omega a^*}{2k_{z,0}c^2}\tilde{E}_1(z) \tag{B.21a}$$

$$\partial_z \tilde{E}_1(z) = \frac{i(\omega+\Omega)a}{2k_{z,1}c^2}\tilde{E}_0(z) \tag{B.21b}$$

which can be reduced to a single second order equation for $\tilde{E}_1$:

$$\partial_z^2 \tilde{E}_1(z) = -M^2\tilde{E}_1(z) = -\frac{\omega^2(\omega+\Omega)^2}{4c^4 k_{z,0}k_{z,1}}|a|^2\tilde{E}_1(z). \tag{B.22}$$

Given that the initial condition is $\tilde{E}_1(0) = 0$, the solution is a sine function[1]

$$\tilde{E}_1(z) = -A\sin Mz$$

[1] I choose a negative sign to ensure that the phase of $\tilde{E}_0(z)$ does not change.

where the amplitude is determined by Eq. (B.21b):

$$-MA = \frac{i(\omega+\Omega)^2 a}{2k_{z,1}c^2}\tilde{E}_0(0).$$

Therefore, I have

$$\begin{aligned}\tilde{E}_1(z) &= -\frac{i(\omega+\Omega)}{\omega}\sqrt{\frac{k_{z,0}}{k_{z,1}}}\frac{a}{|a|}\tilde{E}_0(0)\sin Mz \\ &\approx -ie^{i\phi_a}\tilde{E}_0(0)\sin\left(\frac{k_0|a|}{2}z\right)\end{aligned} \tag{B.23}$$

where ϕ_a is the phase of a, $a = |a|e^{i\phi_a}$. The optical power in the diffracted beam is proportional to $|\tilde{E}_1|^2$, so

$$P_1(z) = P_0(0)\sin^2\left(\frac{k_0|a|}{2}z\right).$$

Assuming that $|a|^2$ is proportional to the acoustic power, the diffracted power is proportional to the acoustic power for small z.

Now I shall consider the situation where the acoustic wave is not a single frequency but is instead a periodic function. The induced susceptibility becomes

$$\chi_s(\mathbf{r},t) = \sum_m c_m e^{i\mathbf{q}_m\cdot\mathbf{r}-i\Omega_m t} + \text{c.c.} \tag{B.24}$$

where $\mathbf{q}_m$ has the same direction as the original $\mathbf{q}$ but now has a length $q_m = (\Omega+m\alpha)/v = q + mq_\alpha$ where α is the repetition frequency. Likewise, $\Omega_m = \Omega + m\alpha$. The double Fourier transform in Eq. (B.9) is now

$$\chi_s(k_x,z,\omega) = \sum_m c_m e^{iq_{z,m}z}\delta(k_x-q_{x,m})\delta(\omega-\Omega_m) + c_m^* e^{-iq_{z,m}z}\delta(k_x+q_{x,m})\delta(\omega+\Omega_m)$$

and the analog to Eq. (B.15) is

$$\begin{aligned}2ik_z\partial_z\tilde{E}(k_x,z,\omega) = -\frac{\omega^2}{c^2}\sum_m \Big[&c_m\tilde{E}(k_x-q_{x,m},z,\omega-\Omega_m)e^{iz(q_{z,m}+k_z(\omega-\Omega_m,k_x-q_{x,m})-k_z(\omega,k_x))} \\ &+ c_m^*\tilde{E}(k_x+q_{x,m},z,\omega+\Omega_m)e^{iz(-q_{z,m}+k_z(\omega+\Omega_m,k_x+q_{x,m})-k_z(\omega,k_x))}\Big].\end{aligned} \tag{B.25}$$

Under regular circumstances, the repetition frequency $\alpha \ll \Omega$ and $q_\alpha \ll q$, which means that if I have phase-matching for Fourier order $m = 0$ then I will have phase-matching for all m.[2] Additionally, only fields separated by q_x are coupled together, so all Fourier orders are independent. Therefore, I have the set of equations

$$\partial_z\tilde{E}_0(z) = \frac{i\omega^2}{2k_{z,0}c^2}\sum_m c_m^*\tilde{E}_{1,m}(z) \tag{B.26a}$$

$$\partial_z\tilde{E}_{1,m}(z) = \frac{i(\omega+\Omega_m)^2}{2k_{z,1,m}c^2}c_m\tilde{E}_0(z) \tag{B.26b}$$

[2] Within reason; I assume that the bandwidth of the modulated signal is small

where $\tilde{E}_{1,m}(z) = \tilde{E}(q_x + mq_\alpha, z, \omega + \Omega + m\alpha)$. Taking the derivative of Eq. (B.26a) and substituting with Eq. (B.26b), I have

$$\partial_z \tilde{E}_0(z) \approx -\frac{k_0^2}{4} \sum_m |c_m|^2 \tilde{E}_0(z) = -M^2 \tilde{E}_0(z)$$

where I have assumed that $\Omega, \alpha \ll \omega$. The above has the solution

$$\tilde{E}_0(z) = \tilde{E}_0(0) \cos Mz$$

from which I can arrive at

$$\tilde{E}_1(z) = -i \frac{c_m}{\sqrt{\sum_m |c_m|^2}} \tilde{E}_0(0) \sin Mz. \tag{B.27}$$

As would be expected in a linear theory, the power in each diffracted Fourier order is proportional to the relative power in each Fourier coefficient.

B.2 Optical dipole trap

The equations in Sec. 3.4 apply when the intensity is constant in time. In the experiment, the vertical trapping laser is derived from the diffracted order of an AOD which is then passed through an f-θ lens that maps angle to position. The slowly-varying (compared to the optical frequency) electric field amplitude at the focus of the f-θ lens is more appropriately described as

$$E(x, z, t) = E_0 \sum_n c_n e^{-\frac{(x-nx_0)^2}{w_x^2} - \frac{z^2}{w_z^2}} e^{in\alpha t} \tag{B.28}$$

where x_0 is proportional to the modulation frequency α, and the proportionality constant is determined by the geometry of the AOD-lens system. Since $I(\mathbf{r}, t) \propto |E(x, z, t)|^2$ the dipole potential calculated from Eq. (3.5) is

$$\begin{aligned} U(x, z, t) &= -U_0 \sum_{n,m} c_n c_m^* e^{-\frac{2z^2}{w_z^2}} e^{-\frac{(x-nx_0)^2}{w_x^2} - \frac{(x-mx_0)^2}{w_x^2}} e^{i(n-m)\alpha t} \\ &= -U_0 \sum_n |c_n|^2 e^{-\frac{2z^2}{w_z^2} - \frac{2(x-nx_0)^2}{w_x^2}} - U_0 \sum_{n,m\neq n} c_n c_m^* e^{-\frac{2z^2}{w_z^2}} e^{-\frac{(x-nx_0)^2}{w_x^2} - \frac{(x-mx_0)^2}{w_x^2}} e^{i(n-m)\alpha t} \\ U(x, z) &\approx -U_0 \sum_n |c_n|^2 e^{-\frac{2z^2}{w_z^2} - \frac{2(x-nx_0)^2}{w_x^2}} \end{aligned} \tag{B.29}$$

where the last line applies only when the modulation frequency α is much faster than the motion of the atoms in the trap. By defining the trap frequency to be

$$\omega_x^2 = \frac{1}{m} \partial_x^2 U(x, z) \Big|_{x=x_{\text{trap}}, z=0},$$

where x_{trap} is the location of the center of the approximate harmonic trap, I find that

$$\omega_x^2 = \frac{4U_0}{w_x^2} \sum_n |c_n|^2 e^{-\frac{2(x_{\text{trap}}-nx_0)^2}{w_x^2}} \left[1 - 4\frac{(x_{\text{trap}} - nx_0)^2}{w_x^2}\right]. \tag{B.30}$$

B.3 Frequency shift keying

All that is needed now to describe the optical potential generated by a periodically modulated AOM is to find the Fourier coefficients for a particular signal. Suppose that the signal is shifted between two frequencies ω_1 and ω_2, with repetition frequency α and period $T = 2\pi/\alpha$. There are two primary methods of performing this shifting: phase-continuous and phase-coherent. Figure B.1 illustrates the difference between the two methods. In

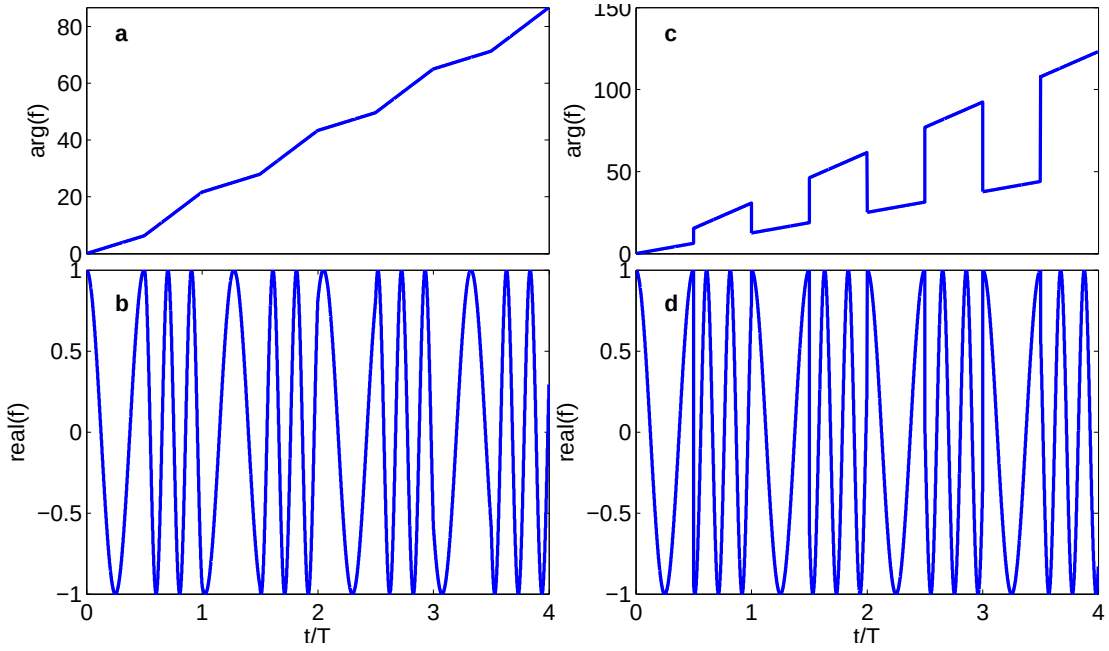

Figure B.1: Behaviour of the signal $f(t)$ and its phase $\arg(f)$ as a function of time for frequency shift keying. **a-b** Phase and real part of $f(t)$, respectively, as a function of time for phase-continuous shifting. **c-d** Phase and real part of $f(t)$, respectively, as a function of time for phase-coherent shifting.

phase-continuous shifting, the phase of the signal remains continuous as in Fig. B.1a; only the slope of the phase as a function of time changes. Phase-coherent driving, as in Fig. B.1c, switches between two independent phase ramps. Phase-continuous toggling results in continuous signals, unlike phase-coherent toggling, so there is reduced power in higher-frequency sidebands, although for the frequencies about which we are interested the difference is minor. We use phase-continuous toggling because it requires less information to be written to the FlexDDS system.

Phase-continuous frequency shift keying can be represented by the function

$$f(t) = \begin{cases} e^{i\omega_1(t-nT)+i\phi_1^{(n)}} & nT \le t < (n+\frac{1}{2})T \\ e^{i\omega_2(t-(n+\frac{1}{2})T)+i\phi_2^{(n)}} & (n+\frac{1}{2})T \le t < (n+1)T \end{cases} \tag{B.31}$$

where the phases $\phi_{1,2}^{(n)}$ have to be chosen to ensure that the signal's phase, and thus $f(t)$, is

continuous. This turns out to be easy, as $\phi_1^{(n)}$ is just the accumulated phase up until that time, which is $\phi_1^{(n)} = n\omega_1 T/2 + n\omega_2 T/2 = n\bar{\omega}T$ where $\bar{\omega} = \frac{1}{2}(\omega_1 + \omega_2)$ because the phase accumulates at each frequency for $T/2$ each cycle. We then have $\phi_2^{(n)} = \phi_1^{(n)} + \omega_1 T/2 = n\bar{\omega}T + \omega_1 T/2$. Therefore,

$$f(t) = \begin{cases} e^{i\omega_1(t-nT)+in\bar{\omega}T} & nT \le t < (n+\frac{1}{2})T \\ e^{i\omega_2(t-(n+\frac{1}{2})T)+in\bar{\omega}T+i\omega_1 T/2} & (n+\frac{1}{2})T \le t < (n+1)T \end{cases} \tag{B.32}$$

Now, $f(t)$ as defined is not periodic, so I cannot technically decompose it into a Fourier series. I can factor out a periodic part, however, if I factor out $e^{i\bar{\omega}t}$ from $f(t)$. Defining $\Delta = (\omega_1 - \omega_2)/2$, I have

$$f(t) = e^{i\bar{\omega}t} \begin{cases} e^{i\Delta(t-nT)} & nT \le t < (n+\frac{1}{2})T \\ e^{-i\Delta(t-(n+1)T)} & (n+\frac{1}{2})T \le t < (n+1)T \end{cases} \tag{B.33}$$

where the two cases together are periodic with period T. I can decompose the function $e^{-i\bar{\omega}t}f(t)$ into a Fourier series

$$e^{-i\bar{\omega}t}f(t) = \sum_m c_m e^{im\alpha t}$$

where the coefficients are

$$\begin{aligned} c_m &= \frac{1}{T}\int_0^T e^{-i\bar{\omega}t} f(t) e^{-im\alpha t} dt \\ &= \frac{1}{T}\int_0^{T/2} e^{i\Delta t - im\alpha t} dt + \frac{1}{T}\int_{T/2}^T e^{-i\Delta(t-T) - im\alpha t} dt \\ &= \frac{e^{i(\Delta - m\alpha)\frac{T}{4}}}{2}\text{sinc}\left[(\Delta - m\alpha)\frac{T}{4}\right] + e^{-im\pi}\frac{e^{i(\Delta - m\alpha)\frac{T}{4}}}{2}\text{sinc}\left[(\Delta + m\alpha)\frac{T}{4}\right] \\ &= \frac{e^{i(\Delta - m\alpha)\frac{T}{4}}}{2}\left(\text{sinc}\left[\frac{(\Delta - m\alpha)T}{4}\right] + e^{-im\pi}\text{sinc}\left[\frac{(\Delta + m\alpha)T}{4}\right]\right). \end{aligned} \tag{B.34}$$

These are exactly the coefficients that can be used in Eqs. (B.28)-(B.30).

Bibliography

[1] H. Geiger and E. Marsden. On a diffuse reflection of the α-particles. *Proceedings of the Royal Society A: Mathematical, Physical and Engineering Sciences*, **82**, 495–500, 1909.

[2] E. Rutherford. The scattering of α and β particles by matter and the structure of the atom. *Philosophical Magazine Series 6*, **21**, 669–688, 1911.

[3] C. E. Hecht. The Possible Superfluid Behaviour of Hydrogen Atom Gases and Liquids. *Physics*, **25**, 1159, 1959.

[4] W. C. Stwalley and L. H. Nosanow. Possible "New" Quantum Systems. *Physical Review Letters*, **36**, 910, 1976.

[5] D. G. Fried, T. C. Killian, L. Willmann, D. Landhuis, S. C. Moss, D. Kleppner, and T. J. Greytak. Bose-Einstein Condensation of Atomic Hydrogen. *Physical Review Letters*, **81**, 3811–3814, Nov 1998.

[6] M. Arndt, M. Ben Dahan, D. Guéry-Odelin, M. W. Reynolds, and J. Dalibard. Observation of a Zero-Energy Resonance in Cs-Cs Collisions. *Physical Review Letters*, **79**, 625–628, Jul 1997.

[7] T. Weber, J. Herbig, M. Mark, H.-C. Nägerl, and R. Grimm. Bose-Einstein Condensation of Cesium. *Science*, **299**(5604), 232–235, 2003.

[8] M. H. Anderson, J. R. Ensher, M. R. Matthews, C. E. Wieman, and E. A. Cornell. Observation of Bose-Einstein Condensation in a Dilute Atomic Vapor. *Science*, **269**(5221), 198–201, 1995.

[9] K. B. Davis, M. O. Mewes, M. R. Andrews, N. J. van Druten, D. S. Durfee, D. M. Kurn, and W. Ketterle. Bose-Einstein Condensation in a Gas of Sodium Atoms. *Physical Review Letters*, **75**, 3969–3973, Nov 1995.

[10] C. C. Bradley, C. A. Sackett, J. J. Tollett, and R. G. Hulet. Evidence of Bose-Einstein Condensation in an Atomic Gas with Attractive Interactions. *Physical Review Letters*, **75**, 1687–1690, Aug 1995.

[11] W. Pauli. Über den Zusammenhang des Abschlusses der Elektronengruppen im Atom mit der Komplexstruktur der Spektren. *Zeitschrift für Physik*, **31**, 373, 1925.

[12] B. DeMarco and D. S. Jin. Onset of Fermi Degeneracy in a Trapped Atomic Gas. *Science*, **285**(5434), 1703–1706, 1999.

[13] F. Schreck, G. Ferrari, K. L. Corwin, J. Cubizolles, L. Khaykovich, M.-O. Mewes, and C. Salomon. Sympathetic cooling of bosonic and fermionic lithium gases towards quantum degeneracy. *Physical Review A*, **64**, 011402, Jun 2001.

[14] C. Silber, S. Günther, C. Marzok, B. Deh, P. W. Courteille, and C. Zimmermann. Quantum-Degenerate Mixture of Fermionic Lithium and Bosonic Rubidium Gases. *Physical Review Letters*, **95**, 170408, Oct 2005.

[15] Z. Hadzibabic, C. A. Stan, K. Dieckmann, S. Gupta, M. W. Zwierlein, A. Görlitz, and W. Ketterle. Two-Species Mixture of Quantum Degenerate Bose and Fermi Gases. *Physical Review Letters*, **88**, 160401, Apr 2002.

[16] A. G. Truscott, K. E. Strecker, W. I. McAlexander, G. B. Partridge, and R. G. Hulet. Observation of Fermi Pressure in a Gas of Trapped Atoms. *Science*, **291**(5513), 2570–2572, 2001.

[17] A. Fetter and J. Walecka. *Quantum Theory of Many-Particle Systems*. McGraw-Hill, San Francisco, 1971.

[18] H. T. C. Stoof, M. Houbiers, C. A. Sackett, and R. G. Hulet. Superfluidity of Spin-Polarized ^{6}Li. *Physical Review Letters*, **76**, 10–13, Jan 1996.

[19] M. Houbiers, R. Ferwerda, H. T. C. Stoof, W. I. McAlexander, C. A. Sackett, and R. G. Hulet. Superfluid state of atomic ^{6}Li in a magnetic trap. *Physical Review A*, **56**, 4864–4878, Dec 1997.

[20] M. Houbiers, H. T. C. Stoof, W. I. McAlexander, and R. G. Hulet. Elastic and inelastic collisions of ^{6}Li atoms in magnetic and optical traps. *Physical Review A*, **57**, R1497–R1500, Mar 1998.

[21] K. M. O'Hara, S. R. Granade, M. E. Gehm, T. A. Savard, S. Bali, C. Freed, and J. E. Thomas. Ultrastable CO_2 Laser Trapping of Lithium Fermions. *Physical Review Letters*, **82**, 4204–4207, May 1999.

[22] K. M. O'Hara, S. L. Hemmer, M. E. Gehm, S. R. Granade, and J. E. Thomas. Observation of a Strongly Interacting Degenerate Fermi Gas of Atoms. *Science*, **298**(5601), 2179–2182, 2002.

[23] E. Tiesinga, B. J. Verhaar, and H. T. C. Stoof. Threshold and resonance phenomena in ultracold ground-state collisions. *Physical Review A*, **47**, 4114–4122, May 1993.

[24] H. Feshbach. Unified theory of nuclear reactions. *Annals of Physics*, **5**(4), 357 – 390, 1958.

[25] H. Feshbach. A unified theory of nuclear reactions. II. *Annals of Physics*, **19**(2), 287 – 313, 1962.

[26] U. Fano. Effects of Configuration Interaction on Intensities and Phase Shifts. *Physical Review*, **124**, 1866–1878, Dec 1961.

[27] S. Inouye, M. R. Andrews, J. Stenger, H.-J. Miesner, D. M. Stamper-Kurn, and W. Ketterle. Observation of Feshbach resonances in a Bose-Einstein condensate. *Nature*, **392**(6672), 151–154, 1998.

[28] V. Vuletić, A. J. Kerman, C. Chin, and S. Chu. Observation of Low-Field Feshbach Resonances in Collisions of Cesium Atoms. *Physical Review Letters*, **82**, 1406–1409, Feb 1999.

[29] T. Loftus, C. A. Regal, C. Ticknor, J. L. Bohn, and D. S. Jin. Resonant Control of Elastic Collisions in an Optically Trapped Fermi Gas of Atoms. *Physical Review Letters*, **88**, 173201, Apr 2002.

[30] G. Ferrari, M. Inguscio, W. Jastrzebski, G. Modugno, G. Roati, and A. Simoni. Collisional Properties of Ultracold K-Rb Mixtures. *Physical Review Letters*, **89**, 053202, Jul 2002.

[31] P. J. Leo, E. Tiesinga, P. S. Julienne, D. K. Walter, S. Kadlecek, and T. G. Walker. Elastic and Inelastic Collisions of Cold Spin-Polarized ^{133}Cs Atoms. *Physical Review Letters*, **81**, 1389–1392, Aug 1998.

[32] C. R. Monroe, E. A. Cornell, C. A. Sackett, C. J. Myatt, and C. E. Wieman. Measurement of Cs-Cs elastic scattering at T=30 μK. *Physical Review Letters*, **70**, 414–417, Jan 1993.

[33] E. P. Wigner. On the Behavior of Cross Sections Near Thresholds. *Physical Review*, **73**, 1002–1009, May 1948.

[34] B. DeMarco, J. L. Bohn, J. P. Burke, M. Holland, and D. S. Jin. Measurement of p-Wave Threshold Law Using Evaporatively Cooled Fermionic Atoms. *Physical Review Letters*, **82**, 4208–4211, May 1999.

[35] M. Gustavsson, E. Haller, M. J. Mark, J. G. Danzl, G. Rojas-Kopeinig, and H.-C. Nägerl. Control of Interaction-Induced Dephasing of Bloch Oscillations. *Physical Review Letters*, **100**, 080404, Feb 2008.

[36] A. Ludewig. *Feshbach Resonances in ^{40}K*. PhD thesis, University of Amsterdam, 2012.

[37] K. M. Jones, E. Tiesinga, P. D. Lett, and P. S. Julienne. Ultracold photoassociation spectroscopy: Long-range molecules and atomic scattering. *Reviews of Modern Physics*, **78**, 483–535, May 2006.

[38] K. Gibble, S. Chang, and R. Legere. Direct Observation of s-Wave Atomic Collisions. *Physical Review Letters*, **75**, 2666–2669, Oct 1995.

[39] R. Legere and K. Gibble. Quantum Scattering in a Juggling Atomic Fountain. *Physical Review Letters*, **81**, 5780–5783, Dec 1998.

[40] S. D. Gensemer, R. B. Martin-Wells, A. W. Bennett, and K. Gibble. Direct Observation of Resonant Scattering Phase Shifts and Their Energy Dependence. *Physical Review Letters*, **109**, 263201, Dec 2012.

[41] N. R. Thomas, N. Kjærgaard, P. S. Julienne, and A. C. Wilson. Imaging of s and d Partial-Wave Interference in Quantum Scattering of Identical Bosonic Atoms. *Physical Review Letters*, **93**(17), 173201, Oct 2004.

[42] C. Buggle, J. Léonard, W. von Klitzing, and J. Walraven. Interferometric Determination of the s and d-Wave Scattering Amplitudes in Rb87. *Physical Review Letters*, **93**(17), 173202, Oct 2004.

[43] A. S. Mellish, N. Kjærgaard, P. S. Julienne, and A. C. Wilson. Quantum scattering of distinguishable bosons using an ultracold-atom collider. *Physical Review A*, **75**(2), 020701, Feb 2007.

[44] D. Genkina, L. M. Aycock, B. K. Stuhl, H.-I. Lu, R. A. Williams, and I. B. Spielman. Feshbach enhanced s-wave scattering of fermions: direct observation with optimized absorption imaging. *New Journal of Physics*, **18**(1), 013001, 2016.

[45] R. A. Williams, L. J. LeBlanc, K. Jiménez-García, M. C. Beeler, A. R. Perry, W. D. Phillips, and I. B. Spielman. Synthetic partial waves in ultracold atomic collisions. *Science*, **335**(6066), 314–7, Jan 2012.

[46] A. Perrin, H. Chang, V. Krachmalnicoff, M. Schellekens, D. Boiron, A. Aspect, and C. I. Westbrook. Observation of Atom Pairs in Spontaneous Four-Wave Mixing of

Two Colliding Bose-Einstein Condensates. *Physical Review Letters*, **99**, 150405, Oct 2007.

[47] S. S. Hodgman, R. I. Khakimov, R. J. Lewis-Swan, A. G. Truscott, and K. V. Kheruntsyan. Solving the Quantum Many-Body Problem via Correlations Measured with a Momentum Microscope. *Physical Review Letters*, **118**, 240402, Jun 2017.

[48] N. Q. Burdick, A. G. Sykes, Y. Tang, and B. L. Lev. Anisotropic collisions of dipolar Bose-Einstein condensates in the universal regime. *New Journal of Physics*, **18**(11), 2016.

[49] A. Rakonjac. *A Versatile Collider for Ultracold Atoms*. PhD thesis, University of Otago, 2012.

[50] A. Rakonjac, A. B. Deb, S. Hoinka, D. Hudson, B. J. Sawyer, and N. Kjærgaard. Laser based accelerator for ultracold atoms. *Optics Letters*, **37**(6), 1085–7, Mar 2012.

[51] K. O. Roberts, T. Mckellar, J. Fekete, A. Rakonjac, A. B. Deb, and N. Kjærgaard. Steerable optical tweezers for ultracold atom studies. *Optics Letters*, **39**(7), 2012–5, 2014.

[52] H. R. Thorsheim, Y. Wang, and J. Weiner. Cold collisions in an atomic beam. *Physical Review A*, **41**, 2873–2876, Mar 1990.

[53] D. J. Griffiths. *Introduction to Quantum Mechanics*. Pearson Education, Inc., Upper Saddle River, NJ, 2005.

[54] H. Friedrich. *Scattering Theory*. Springer, New York, 2013.

[55] J. R. Taylor. *Scattering Theory*. Wiley, New York, 1972.

[56] R. G. Newton. *Scattering Theory of Waves and Particles*. Springer, New York, 1982.

[57] C. Cohen-Tannoudji, B. Die, and F. Laloë. *Quantum Mechanics*. Hermann, Paris, 1977.

[58] H. Margenau and G. M. Murphy. *The Mathematics of Physics and Chemistry*. D. Van Nostrand Company, Inc., New York, 1943.

[59] H. B. G. Casimir and D. Polder. The Influence of Retardation on the London-van der Waals Forces. *Physical Review*, **73**, 360–372, Feb 1948.

[60] M. Marinescu, J. F. Babb, and A. Dalgarno. Long-range potentials, including retardation, for the interaction of two alkali-metal atoms. *Physical Review A*, **50**, 3096–3104, Oct 1994.

[61] W. E. Boyce and R. C. DiPrima. *Elementary Differential Equations and Boundary Value Problems, 4th ed.* Wiley, New York, 1986.

[62] H. T. C. Stoof, J. M. V. A. Koelman, and B. J. Verhaar. Spin-exchange and dipole relaxation rates in atomic hydrogen: Rigorous and simplified calculations. *Physical Review B*, **38**, 4688–4697, Sep 1988.

[63] C. Chin, R. Grimm, P. Julienne, and E. Tiesinga. Feshbach resonances in ultracold gases. *Reviews of Modern Physics*, **82**, 1225–1286, Apr 2010.

[64] H. Beutler. Über Absorptionsserien von Argon, Krypton und Xenon zu Termen zwischen den beiden Ionisierungsgrenzen 2 P 3 2/0 und 2 P 1 2/0. *Zeitschrift für Physik A Hadrons and Nuclei*, **93**(3), 177–196, 1935.

[65] K. Kobayashi, H. Aikawa, S. Katsumoto, and Y. Iye. Tunable Fano system: A quantum dot embedded in an Aharonov-Bohm ring. *Physica E: Low-Dimensional Systems and Nanostructures*, **18**(1-3), 56–59, 2003. cited By 4.

[66] J. Nöckel and A. Stone. Fano resonances in transport across a quantum well in a tilted magnetic field. *Physical Review B*, **51**(23), 17219–17222, 1995. cited By 7.

[67] J. Falst, F. Capasso, C. Sirtori, K. West, and L. Pfeiffer. Controlling the sign of quantum interference by tunnelling from quantum wells. *Nature*, **390**(6660), 589–591, 1997. cited By 308.

[68] A. E. Miroshnichenko, S. Flach, and Y. S. Kivshar. Fano resonances in nanoscale structures. *Reviews of Modern Physics*, **82**, 2257–2298, Aug 2010.

[69] B. Gao. Zero-energy bound or quasibound states and their implications for diatomic systems with an asymptotic van der Waals interaction. *Physical Review A*, **62**, 050702, Oct 2000.

[70] P. S. Julienne and F. H. Mies. Collisions of ultracold trapped atoms. *Journal of the Optical Society of America B*, **6**(11), 2257, Nov 1989.

[71] J. M. Hutson. Feshbach resonances in ultracold atomic and molecular collisions: threshold behaviour and suppression of poles in scattering lengths. *New Journal of Physics*, **9**(5), 152, 2007.

[72] A. Pashov, O. Docenko, M. Tamanis, R. Ferber, H. Knöckel, and E. Tiemann. Coupling of the $X^1\Sigma^+$ and $a^3\Sigma^+$ states of KRb. *Physical Review A*, **76**, 022511, Aug 2007.

[73] M. Marinescu and L. You. Casimir-Polder long-range interaction potentials between alkali-metal atoms. *Physical Review A*, **59**, 1936–1954, Mar 1999.

[74] C. Strauss, T. Takekoshi, F. Lang, K. Winkler, R. Grimm, J. Hecker Denschlag, and E. Tiemann. Hyperfine, rotational, and vibrational structure of the $a^3\Sigma_u^+$ state of $^{87}Rb_2$. *Physical Review A*, **82**, 052514, Nov 2010.

[75] S. Falke, H. Knöckel, J. Friebe, M. Riedmann, E. Tiemann, and C. Lisdat. Potassium ground-state scattering parameters and Born-Oppenheimer potentials from molecular spectroscopy. *Physical Review A*, **78**, 012503, Jul 2008.

[76] F. H. Mies, C. J. Williams, P. S. Julienne, and M. Krauss. Estimating bounds on collisional relaxation rates of spin-polarized ^{87}Rb atoms at ultracold temperatures. *Journal of research of the National Institute of Standards and Technology*, **101**(4), 521, 1996.

[77] J. M. Gerton, C. A. Sackett, B. J. Frew, and R. G. Hulet. Dipolar relaxation collisions in magnetically trapped ^{7}Li. *Physical Review A*, **59**, 1514–1516, Feb 1999.

[78] D. Secrest. In R. B. Bernstein, editor, *Atom-Molecule Collision Theory: A Guide for the Experimentalist*. Plenum, New York, 1979.

[79] D. E. Manolopoulos. An improved log derivative method for inelastic scattering. *The Journal of Chemical Physics*, **85**(11), 6425–6429, 1986.

[80] E. Arimondo, M. Inguscio, and P. Violino. Experimental determinations of the hyperfine structure in the alkali atoms. *Reviews of Modern Physics*, **49**, 31–75, Jan 1977.

[81] D. Steck. Rubidium 87 D line data. http://steck.us/alkalidata/rubidium87numbers.1.6.pdf.

[82] T. G. Tiecke. Properties of Potassium. http://www.tobiastiecke.nl/archive/PotassiumProperties.pdf.

[83] National Institute for Standards and Technology. The NIST Reference on Constants, Units, and Uncertainty. http://physics.nist.gov/cuu/Constants/index.html.

[84] G. Audi, A. Wapstra, and C. Thibault. The Ame2003 atomic mass evaluation. *Nuclear Physics A*, **729**(1), 337 – 676, 2003. The 2003 NUBASE and Atomic Mass Evaluations.

[85] S. Knoop, T. Schuster, R. Scelle, A. Trautmann, J. Appmeier, M. K. Oberthaler, E. Tiesinga, and E. Tiemann. Feshbach spectroscopy and analysis of the interaction potentials of ultracold sodium. *Physical Review A*, **83**, 042704, Apr 2011.

[86] G. A. Bird. *Molecular Gas Dynamics and the Direct Simulation of Gas Flows*. Clarendon, Oxford, 1994.

[87] E. Cerboneschi, C. Menchini, and E. Arimondo. Monte Carlo simulations of Bose-Einstein condensation of trapped atoms. *Physical Review A*, **62**, 013606, 2000.

[88] H. Wu and C. J. Foot. Direct simulation of evaporative cooling. *Journal of Physics B: Atomic, Molecular, and Optical Physics*, **29**, 321, 1996.

[89] H. Wu, E. Arimondo, and C. J. Foot. Dynamics of evaporative cooling for Bose-Einstein condensation. *Physical Review A*, **56**, 560–569, Jul 1997.

[90] L. Verlet. Computer "Experiments" on Classical Fluids. I. Thermodynamical Properties of Lennard-Jones Molecules. *Physical Review*, **159**, 98–103, Jul 1967.

[91] W. H. Press, S. A. Teukolsky, W. T. Vetterling, and B. P. Flannery. *Numerical Recipes 3rd Edition: The Art of Scientific Computing*. Cambridge University Press, New York, NY, USA, 3 edition, 2007.

[92] M. A. Gallis, J. R. Torczynski, D. J. Rader, and G. A. Bird. Convergence behavior of a new DSMC algorithm. *Journal of Computational Physics*, **228**(12), 4532 – 4548, 2009.

[93] D. Guéry-Odelin, J. Söding, P. Desbiolles, and J. Dalibard. Strong evaporative cooling of a trapped cesium gas. *Optics Express*, **2**(8), 323–329, Apr 1998.

[94] A. C. J. Wade, D. Baillie, and P. B. Blakie. Direct simulation Monte Carlo method for cold-atom dynamics: Classical Boltzmann equation in the quantum collision regime. *Physical Review A*, **84**(2), 023612, August 2011.

[95] H. J. Lewandowski. *Coherences and correlations in an ultracold Bose gas*. PhD thesis, University of Colorado, 2002.

[96] H. J. Lewandowski, D. M. Harber, D. L. Whitaker, and E. A. Cornell. Simplified system for creating a Bose-Einstein condensate. *Journal of Low Temperature Physics*, **132**, 309, 2003.

[97] T. Mckellar. A Digital Frequency Source for Movement of Ultracold Atoms by Acousto-Optic Deflection. MSc thesis, University of Otago, 2014.

[98] K. Roberts. Construction and Characterization of a Steerable Optical Tweezer System. Honours thesis, University of Otago, 2013.

[99] C. N. Cohen-Tannoudji. Nobel Lecture: Manipulating atoms with photons. *Reviews of Modern Physics*, **70**, 707–719, Jul 1998.

[100] W. D. Phillips. Nobel Lecture: Laser cooling and trapping of neutral atoms. *Reviews of Modern Physics*, **70**, 721–741, Jul 1998.

[101] C. Cohen-Tannoudji. Atomic motion in laser light. In J. Dalibard, J.-M. Raimond, and J. Zinn-Justin, editors, *Les Houches 1990: fundamental systems in quantum optics*, chapter 1. Elsevier Science Publishes B. V., Amsterdam, 1992.

[102] W. D. Phillips. Laser cooling, optical traps and optical molasses. In J. Dalibard, J.-M. Raimond, and J. Zinn-Justin, editors, *Les Houches 1990: fundamental systems in quantum optics*, chapter 2. Elsevier Science Publishes B. V., Amsterdam, 1992.

[103] H. J. Metcalf and P. van der Straten. *Laser Cooling and Trapping*. Springer-Verlag, New York, 1999.

[104] A. Rakonjac, K. O. Roberts, A. B. Deb, and N. Kjærgaard. Note: Computer controlled rotation mount for large diameter optics. *Review of Scientific Instruments*, **84**(2), 026107, 2013.

[105] W. Ketterle, K. B. Davis, M. A. Joffe, A. Martin, and D. E. Pritchard. High densities of cold atoms in a dark spontaneous-force optical trap. *Physical Review Letters*, **70**, 2253–2256, Apr 1993.

[106] B. DeMarco. *Quantum Behavior of an Atomic Fermi Gas*. PhD thesis, University of Colorado, 2001.

[107] W. Petrich, M. H. Anderson, J. R. Ensher, and E. A. Cornell. Stable, Tightly Confining Magnetic Trap for Evaporative Cooling of Neutral Atoms. *Physical Review Letters*, **74**, 3352–3355, Apr 1995.

[108] W. Ketterle and N. J. van Druten. Evaporative Cooling of Trapped Atoms. *Advances in Atomic, Molecular, and Optical Physics*, **37**, 181, 1996.

[109] O. J. Luiten, M. W. Reynolds, and J. T. M. Walraven. Kinetic theory of the evaporative cooling of a trapped gas. *Physical Review A*, **53**, 381, 1996.

[110] K. B. Davis, M.-O. Mewes, and W. Ketterle. An analytical model for evaporative cooling of atoms. *Applied Physics B*, **60**, 155, 1995.

[111] M. J. Holland, B. DeMarco, and D. S. Jin. Evaporative cooling of a two-component degenerate Fermi gas. *Physical Review A*, **61**, 053610, Apr 2000.

[112] G. Modugno, G. Ferrari, G. Roati, R. J. Brecha, A. Simoni, and M. Inguscio. Bose-Einstein Condensation of Potassium Atoms by Sympathetic Cooling. *Science*, **294**(5545), 1320–1322, 2001.

[113] G. Roati, F. Riboli, G. Modugno, and M. Inguscio. Fermi-Bose Quantum Degenerate $^{40}\mathrm{K}-^{87}\mathrm{Rb}$ Mixture with Attractive Interaction. *Physical Review Letters*, **89**, 150403, Sep 2002.

[114] R. Grimm, M. Weidemller, and Y. B. Ovchinnikov. Optical Dipole Traps for Neutral Atoms. *Advances In Atomic, Molecular, and Optical Physics*, **42**, 95 – 170, 2000.

[115] D. Veberi. Lambert W function for applications in physics. *Computer Physics Communications*, **183**(12), 2622 – 2628, 2012.

[116] A. B. Deb, T. McKellar, and N. Kjærgaard. Optical runaway evaporation for the parallel production of multiple Bose-Einstein condensates. *Physical Review A*, **90**, 051401, Nov 2014.

[117] G. Reinaudi, T. Lahaye, Z. Wang, and D. Guéry-Odelin. Strong saturation absorption imaging of dense clouds of ultracold atoms. *Optics Letters*, **32**(21), 3143–3145, Nov 2007.

[118] P. Siddons, C. S. Adams, C. Ge, and I. G. Hughes. Absolute absorption on rubidium D lines: comparison between theory and experiment. *Journal of Physics B: Atomic, Molecular and Optical Physics*, **41**(15), 155004, Aug 2008.

[119] B. J. Sawyer. Dispersive Probing of Quantum State Preparation in Ultracold 87 Rb. MSc thesis, University of Otago, 2013.

[120] A. B. Deb, B. J. Sawyer, and N. Kjærgaard. Dispersive probing of driven pseudospin dynamics in a gradient field. *Physical Review A*, **88**, 063607, Dec 2013.

[121] B. J. Sawyer, A. B. Deb, T. McKellar, and N. Kjærgaard. Reducing number fluctuations of ultracold atomic gases via dispersive interrogation. *Physical Review A*, **86**, 065401, Dec 2012.

[122] B. J. Sawyer, M. S. J. Horvath, E. Tiesinga, A. B. Deb, and N. Kjærgaard. Dispersive optical detection of magnetic Feshbach resonances in ultracold gases. *Physical Review A*, **96**, 022705, Aug 2017.

[123] A. Marte. *Feshbach-Resonanzen bei Stößen ultrakalter Rubidiumatome*. PhD thesis, Technische Universität München, 2003. German only.

[124] W. Pauli. The Connection Between Spin and Statistics. *Physical Review*, **58**, 716–722, Oct 1940.

[125] R. Thomas, K. O. Roberts, E. Tiesinga, A. C. J. Wade, P. B. Blakie, A. B. Deb, and N. Kjærgaard. Multiple scattering dynamics of fermions at an isolated p-wave resonance. *Nature Communications*, **7**, 12069, May 2016.

[126] J. P. Gaebler, J. T. Stewart, J. L. Bohn, and D. S. Jin. p-Wave Feshbach Molecules. *Physical Review Letters*, **98**, 200403, May 2007.

[127] W. S. Watson and D. T. Stewart. Photoelectron angular distributions for argon and krypton in the 0-20 eV electron energy range. *Journal of Physics B: Atomic and Molecular Physics*, **7**(17), L466, 1974.

[128] G. R. Plattner and I. Sick. Coherence, interference and the Pauli principle: Coulomb scattering of carbon from carbon. *European Journal of Physics*, **2**(2), 109, 1981.

[129] R. Bracewell. *The Fourier Transform and Its Applications*. McGraw-Hill, New York, 1999.

[130] V. Dribinski, A. Ossadtchi, V. A. Mandelshtam, and H. Reisler. Reconstruction of Abel-transformable images: The Gaussian basis-set expansion Abel transform method. *Review of Scientific Instruments*, **73**(7), 2634, 2002.

[131] C. F. Ockeloen, A. F. Tauschinsky, R. J. C. Spreeuw, and S. Whitlock. Detection of small atom numbers through image processing. *Physical Review A*, **82**, 2010.

[132] N. Kjærgaard, A. S. Mellish, and A. C. Wilson. Differential scattering measurements from a collider for ultracold atoms. *New Journal of Physics*, **6**, 146–146, Oct 2004.

[133] A. C. J. Wade. Direct Simulation Monte Carlo Method for Cold Atom Dynamics : Boltzmann Equation in the Quantum Collision Regime. MSc thesis, University of Otago, 2012.

[134] M. S. Horvath, R. Thomas, E. Tiesinga, A. B. Deb, and N. Kjærgaard. Above-threshold scattering about a Feshbach resonance for ultracold atoms in an optical collider. *Nature Communications*, **8**, 452, 2017.

[135] P. Courteille, R. S. Freeland, D. J. Heinzen, F. A. van Abeelen, and B. J. Verhaar. Observation of a Feshbach Resonance in Cold Atom Scattering. *Physical Review Letters*, **81**, 69–72, Jul 1998.

[136] T. Bourdel, L. Khaykovich, J. Cubizolles, J. Zhang, F. Chevy, M. Teichmann, L. Tarruell, S. J. J. M. F. Kokkelmans, and C. Salomon. Experimental Study of the BEC-BCS Crossover Region in Lithium 6. *Physical Review Letters*, **93**, 050401, Jul 2004.

[137] M. Bartenstein, A. Altmeyer, S. Riedl, S. Jochim, C. Chin, J. H. Denschlag, and R. Grimm. Crossover from a Molecular Bose-Einstein Condensate to a Degenerate Fermi Gas. *Physical Review Letters*, **92**, 120401, Mar 2004.

[138] M. Greiner, C. A. Regal, and D. S. Jin. Emergence of a molecular BoseEinstein condensate from a Fermi gas. *Nature*, **426**(6966), 537–540, 2003.

[139] J. Kinast, S. L. Hemmer, M. E. Gehm, A. Turlapov, and J. E. Thomas. Evidence for Superfluidity in a Resonantly Interacting Fermi Gas. *Physical Review Letters*, **92**, 150402, Apr 2004.

[140] T. Kraemer, M. Mark, P. Waldburger, J. G. Danzl, C. Chin, B. Engeser, A. D. Lange, K. Pilch, A. Jaakkola, H.-C. Nägerl, and R. Grimm. Evidence for Efimov quantum states in an ultracold gas of caesium atoms. *Nature*, **440**(7082), 315–318, 2006.

[141] S. Knoop, F. Ferlaino, M. Mark, M. Berninger, H. Schöbel, H.-C. Nägerl, and R. Grimm. Observation of an Efimov-like trimer resonance in ultracold atomdimer scattering. *Nature Physics*, **5**(3), 227–230, 2009.

[142] G. Roati, C. D'Errico, L. Fallani, M. Fattori, C. Fort, M. Zaccanti, G. Modugno, M. Modugno, and M. Inguscio. Anderson localization of a non-interacting Bose-Einstein condensate. *Nature*, **453**(7197), 895–898, 2008.

[143] K. E. Strecker, G. B. Partridge, A. G. Truscott, and R. G. Hulet. Formation and propagation of matter-wave soliton trains. *Nature*, **417**(6885), 150–153, 2002.

[144] S. L. Cornish, S. T. Thompson, and C. E. Wieman. Formation of bright matter-wave solitons during the collapse of attractive Bose-Einstein condensates. *Physical Review Letters*, **96**(17), 1–4, 2006.

[145] S. T. Thompson, E. Hodby, and C. E. Wieman. Ultracold molecule production via a resonant oscillating magnetic field. *Physical Review Letters*, **95**(19), 1–4, 2005.

[146] C. A. Regal, C. Ticknor, J. L. Bohn, and D. S. Jin. Creation of ultracold molecules from a Fermi gas of atoms. *Nature*, **424**(6944), 47–50, 2003.

[147] I. Ferrier-Barbut, H. Kadau, M. Schmitt, M. Wenzel, and T. Pfau. Observation of Quantum Droplets in a Strongly Dipolar Bose Gas. *Physical Review Letters*, **116**(21), 1–6, 2016.

[148] T. Lahaye, J. Metz, B. Fröhlich, T. Koch, M. Meister, A. Griesmaier, T. Pfau, H. Saito, Y. Kawaguchi, and M. Ueda. D-Wave collapse and explosion of a dipolar bose-einstein condensate. *Physical Review Letters*, **101**(8), 1–4, 2008.

[149] T. Koch, T. Lahaye, J. Metz, B. Fröhlich, A. Griesmaier, and T. Pfau. Stabilization of a purely dipolar quantum gas against collapse. *Nature Physics*, **4**(3), 218–222, Mar 2008.

[150] S. L. Cornish, N. R. Claussen, J. L. Roberts, E. A. Cornell, and C. E. Wieman. Stable $^{85}\mathrm{Rb}$ Bose-Einstein Condensates with Widely Tunable Interactions. *Physical Review Letters*, **85**, 1795–1798, Aug 2000.

[151] T. Kraemer, J. Herbig, M. Mark, T. Weber, C. Chin, H. C. Nägerl, and R. Grimm. Optimized production of a cesium Bose-Einstein condensate. *Applied Physics B: Lasers and Optics*, **79**(8 SPEC. ISS.), 1013–1019, 2004.

[152] P. O. Fedichev, Y. Kagan, G. V. Shlyapnikov, and J. T. M. Walraven. Influence of Nearly Resonant Light on the Scattering Length in Low-Temperature Atomic Gases. *Physical Review Letters*, **77**, 2913–2916, Sep 1996.

[153] M. Theis, G. Thalhammer, K. Winkler, M. Hellwig, G. Ruff, R. Grimm, and J. H. Denschlag. Tuning the Scattering Length with an Optically Induced Feshbach Resonance. *Physical Review Letters*, **93**, 123001, Sep 2004.

[154] F. Ferlaino, C. D'Errico, G. Roati, M. Zaccanti, M. Inguscio, G. Modugno, and A. Simoni. Feshbach spectroscopy of a $\mathrm{K}-\mathrm{Rb}$ atomic mixture. *Physical Review A*, **73**, 040702, Apr 2006.

[155] P. O. Fedichev, M. W. Reynolds, and G. V. Shlyapnikov. Three-Body Recombination of Ultracold Atoms to a Weakly Bound s Level. *Physical Review Letters*, **77**, 2921–2924, Sep 1996.

[156] C. A. Regal, C. Ticknor, J. L. Bohn, and D. S. Jin. Tuning p-Wave Interactions in an Ultracold Fermi Gas of Atoms. *Physical Review Letters*, **90**, 053201, Feb 2003.

[157] A. Widera, O. Mandel, M. Greiner, S. Kreim, T. W. Hänsch, and I. Bloch. Entanglement Interferometry for Precision Measurement of Atomic Scattering Properties. *Physical Review Letters*, **92**, 160406, Apr 2004.

[158] M. S. J. Horvath. Energy dependent scattering of ultracold atoms about a Feshbach resonance. MSc thesis, University of Otago, 2016.

[159] S. Dürr, T. Volz, and G. Rempe. Dissociation of ultracold molecules with Feshbach resonances. *Physical Review A*, **70**, 031601, Sep 2004.

[160] T. Volz, S. Dürr, N. Syassen, G. Rempe, E. van Kempen, and S. Kokkelmans. Feshbach spectroscopy of a shape resonance. *Physical Review A*, **72**, 010704, Jul 2005.

[161] M. Greiner, C. A. Regal, J. T. Stewart, and D. S. Jin. Probing Pair-Correlated Fermionic Atoms through Correlations in Atom Shot Noise. *Physical Review Letters*, **94**, 110401, Mar 2005.

[162] C. Klempt, T. Henninger, O. Topic, M. Scherer, L. Kattner, E. Tiemann, W. Ertmer, and J. J. Arlt. Radio-frequency association of heteronuclear Feshbach molecules. *Physical Review A*, **78**, 061602, Dec 2008.

[163] F. Deuretzbacher, K. Plassmeier, D. Pfannkuche, F. Werner, C. Ospelkaus, S. Ospelkaus, K. Sengstock, and K. Bongs. Heteronuclear molecules in an optical lattice: Theory and experiment. *Physical Review A*, **77**, 032726, Mar 2008.

[164] J. Jiang, J. Mitroy, Y. Cheng, and M. Bromley. Effective oscillator strength distributions of spherically symmetric atoms for calculating polarizabilities and long-range atom-atom interactions. *Atomic Data and Nuclear Data Tables*, **101**, 158 – 186, 2015.

[165] J. Schuster, A. Marte, S. Amtage, B. Sang, G. Rempe, and H. C. W. Beijerinck. Avalanches in a Bose-Einstein Condensate. *Physical Review Letters*, **87**, 170404, Oct 2001.

[166] J. Tallant, K. R. Overstreet, A. Schwettmann, and J. P. Shaffer. Sub-Doppler magneto-optical trap temperatures measured using Rydberg tagging. *Physical Review A*, **74**, 023410, Aug 2006.

[167] L. Schnieder, W. Meier, K. H. Welge, M. N. R. Ashfold, and C. M. Western. Photodissociation dynamics of H_2S at 121.6 nm and a determination of the potential energy function of $SH(A^2\Sigma^+)$. *The Journal of Chemical Physics*, **92**(12), 7027–7037, 1990.

[168] T. Mukaiyama, J. R. Abo-Shaeer, K. Xu, J. K. Chin, and W. Ketterle. Dissociation and Decay of Ultracold Sodium Molecules. *Physical Review Letters*, **92**, 180402, May 2004.

[169] R. Mathew and E. Tiesinga. Controlling the group velocity of colliding atomic Bose-Einstein condensates with Feshbach resonances. *Physical Review A*, **87**, 053608, May 2013.

[170] C. Ticknor, C. A. Regal, D. S. Jin, and J. L. Bohn. Multiplet structure of Feshbach resonances in nonzero partial waves. *Physical Review A*, **69**, 042712, Apr 2004.

[171] L. Lamata and J. León. Generation of bipartite spin entanglement via spin-independent scattering. *Physical Review A*, **73**, 052322, May 2006.

[172] K. Kato, Y. Wang, J. Kobayashi, P. S. Julienne, and S. Inouye. Isotopic Shift of Atom-Dimer Efimov Resonances in K-Rb Mixtures: Critical Effect of Multichannel Feshbach Physics. *Physical Review Letters*, **118**, 163401, Apr 2017.

[173] Y. Wang, J. P. D'Incao, H.-C. Nägerl, and B. D. Esry. Colliding Bose-Einstein Condensates to Observe Efimov Physics. *Physical Review Letters*, **104**, 113201, Mar 2010.

[174] R. M. Kalas and D. Blume. Interaction-induced localization of an impurity in a trapped Bose-Einstein condensate. *Physical Review A*, **73**, 043608, Apr 2006.

[175] S. S. Kondov, W. R. McGehee, J. J. Zirbel, and B. DeMarco. Three-Dimensional Anderson Localization of Ultracold Matter. *Science*, **334**, 66–68, November 2011.

[176] J. Billy, V. Josse, Z. Zuo, A. Bernard, B. Hambrecht, P. Lugan, D. Clément, L. Sanchez-Palencia, P. Bouyer, and A. Aspect. Direct observation of Anderson localization of matter waves in a controlled disorder. *Nature*, **453**, 891–894, June 2008.

[177] F. Jendrzejewski, K. Müller, J. Richard, A. Date, T. Plisson, P. Bouyer, A. Aspect, and V. Josse. Coherent backscattering of ultracold atoms. *Physical Review Letters*, **109**, 1–5, November 2012.